TRITA-MEK
Technical Report 2004:07
ISNN 0348-467X
ISRN KTH/MEK/TR— 04/07-SE

SUPERSONIC FLOW SEPARATION WITH APPLICATION TO ROCKET ENGINE NOZZLES

by

Jan Östlund

June 2004
Technical reports from
Royal Institute of Technology
Department of Mechanics
S-100 44 Stockholm, Sweden

Akademisk avhandling som med tillstånd av Kungliga Tekniska Högskolan i Stockholm framlägges till offentlig granskning för avläggande av teknologie doktorsexamen torsdagen den 10 juni 2004 kl 10.00 i Kollegiesalen, Administrationsbyggnaden, Kungliga Tekniska Högskolan, Vallhallavägen 79, Stockholm.

Universitetsservice US-AB, Stockholm 2004

Jan Östlund 2004
Supersonic flow separation with application to rocket engine nozzles
Department of Mechanics, Royal Institute of Technology
SE-100 44 Stockholm, Sweden

ABSTRACT

The increasing demand for higher performance in rocket launchers promotes the development of nozzles with higher performance, which basically is achieved by increasing the expansion ratio. However, this may lead to flow separation and ensuing instationary, asymmetric forces, so-called side-loads, which may present life-limiting constraints on both the nozzle itself and other engine components. Substantial gains can be made in the engine performance if this problem can be overcome, and hence different methods of separation control have been suggested. However, none has so far been implemented in full scale, due to the uncertainties involved in modeling and predicting the flow phenomena involved.

In the present work the causes of unsteady and unsymmetrical flow separation and resulting side-loads in rocket engine nozzles are investigated. This involves the use of a combination of analytical, numerical and experimental methods, which all are presented in the thesis. A main part of the work is based on sub-scale testing of model nozzles operated with air. Hence, aspects on how to design sub-scale models that are able to capture the relevant physics of full-scale rocket engine nozzles are highlighted. Scaling laws like those presented in here are indispensable for extracting side-load correlations from sub-scale tests and applying them to full-scale nozzles.

Three main types of side-load mechanisms have been observed in the test campaigns, due to: (i) intermittent and random pressure fluctuations, (ii) transition in separation pattern and (iii) aeroelastic coupling. All these three types are described and exemplified by test results together with analysis. A comprehensive, up-to-date review of supersonic flow separation and side-loads in internal nozzle flows is given with an in-depth discussion of different approaches for predicting the phenomena. This includes methods for predicting shock-induced separation, models for predicting side-load levels and aeroelastic coupling effects. Examples are presented to illustrate the status of various methods, and their advantages and shortcomings are discussed.

A major part of the thesis focus on the fundamental shock-wave turbulent boundary layer interaction (SWTBLI) and a physical description of the phenomenon is given. This description is based on theoretical concepts, computational results and experimental observation, where, however, emphasis is placed on the rocket-engineering perspective. This work connects the industrial development of rocket engine nozzles to the fundamental research of the SWTBLI phenomenon and shows how these research results can be utilized in real applications. The thesis is concluded with remarks on active and passive flow control in rocket nozzles and directions of future research.

The present work was performed at VAC's Space Propulsion Division within the framework of European space cooperation.

Keywords: turbulent, boundary layer, shock wave, interaction, overexpanded, rocket nozzle, flow separation, control, side-load, experiments, models, review.

PREFACE

This thesis is based on the work contained in the following papers:

1. Mattsson[1] J, Högman U, and Torngren L
   ''A Sub-Scale Test Programme on Investigation of Flow Separation and Side-Loads in Rocket Nozzles''
   Proceedings of the 3rd European Symposium on Aerothermodynamics of Space Vehicles, ESA-ESTEC, Netherlands, November 24-26, 1998, ESA SP-426.

2. Östlund J and Bigert M
   ''A Subscale Investigation on Side-Loads in Sea Level Rocket Nozzles"
   35th AIAA/ASME/SAE/ASEE Joint Propulsion Conference and Exhibit, AIAA Paper 99-2759, June 1999.

3. Östlund J and Jaran M
   "Assessment of Turbulence Models in Overexpanded Rocket Nozzle Flow Simulations"
   35th AIAA/ASME/SAE/ASEE Joint Propulsion Conference and Exhibit, AIAA Paper 99-2583, June 1999

4. Östlund J, Damgaard T and Frey M
   "Side-Load Phenomena in Highly Overexpanded Rocket Nozzles"
   Accepted for publication in Journal of Propulsion and Power *(based on AIAA Paper 2001-3684 presented at 37th AIAA/ASME/SAE/ASEE Joint Propulsion Conference and Exhibit, which received "best paper" award)*.

5. Östlund J and Muhammad-Klingmann B
   "Supersonic Flow Separation with application to Rocket Engine Nozzles"
   Accepted in revised form for publication in Applied Mechanics Reviews

Relevant scientific publications not included in this thesis:

6. Mattsson[1] J
   "Separation Analysis in Conventional Bell Nozzles"
   In Proceedings of European Seminar on Rocket Nozzle Flows, CNES, Paris, 12-14 October 1998.

---

[1] Jan Östlund changed his name from Jan Mattsson in January 1999

7. Mattsson[1] J
"Analysis of Flow Separation in Viking Nozzle"
In Proceedings of European Seminar on Rocket Nozzle Flows, CNES, Paris, 12-14 October 1998.

8. Mattsson[1] J
"Subscale Testing of Flexible Nozzles"
In Proceedings of European Seminar on Rocket Nozzle Flows, CNES, Paris, 12-14 October 1998.

9. Mattsson[1] J
"Aeroelastic Modelling of Side Loads in Nozzles"
In Proceedings of European Seminar on Rocket Nozzle Flows, CNES, Paris, 12-14 October 1998.

10. Hagemman G, Terhardt M, Frey M, Reijasse P, Onofri M, Nasuti F and Östlund J
"Flow Separation and Side-Loads in Rocket Nozzles"
4th International Symposium on Liquid Space Propulsion, March 12-15, 2000, DLR Lampoldshausen

11. Östlund, J, Damgaard T and Frey M
"Side-Load Phenomena in Highly Overexpanded Rocket Nozzles"
37th AIAA/ASME/SAE/ASEE Joint Propulsion Conference and Exhibit, AIAA Paper 2001-3684, July 2001.

12. Östlund J
"Flow Processes in Rocket Engine Nozzles with Focus on Flow Separation and Side-Loads"
Licentiate Thesis, TRITA-MEK 2002:09, Department of Mechanics, Royal Institute of Technology, Stockholm, Sweden, 2002.

In addition, the work includes results reported by this author in numerous classified technical notes at VAC, ESA/ESTEC and CNES.

ACKNOWLEDGEMENTS

This work has been carried out at the Space Propulsion Division at Volvo Aero Corporation in Trollhättan within the GSTP program and the framework of the European Flow Separation Control Device (FSCD) working group. I would like to express my sincere thanks and appreciation to my supervisor Dr. Barbro Muhammad-Klingmann (Royal Institute of Technology), without whose guidance and support this work would not be possible. I would like to thank my close colleagues Dr. Lars Ljungkrona and Dr. Manuel Frey for their suggestions, remarks and inspiring discussions. Valuable help and suggestions from many people at Volvo Aero Corporation are appreciated and special thanks to those working at the Business Unit Nozzles. I would like to acknowledge all the FSCD members, especially Dr. G Hagemann, Dr. M Terhardt (ASTRIUM), Dr. M Pons, Dr. P Vuillermoz (CNES), R Stark (DLR), Dr. R Schwane (ESTEC), Mr. L Torngren (FOI), Dr. Ph Reijasse (ONERA), Dr. Ph James (SNECMA) and Dr. Alziary de Roquefort (University of Poitiers) for the fruitful cooperation in this field. Last but not least I thank my wife Anna for her encouragement and understanding.

This work has been supported through grants from Volvo Aero Corporation and the Swedish Research Council for Engineering Sciences (TFR contract 285-98-717). These sources of support are gratefully acknowledged.

CONTENTS

INTRODUCTION

The valuable services offered by today's satellites are many and varied. They include more secure air traffic control, accurate weather reports, timely warnings of environmental hazards as well as a wider choice of television programs and improvements in health care.

All these services we now take for granted and tend to forget that they would not exist if we did not have rocket launchers capable of placing satellites accurately into space.

Rocket Fundamentals

The rocket is a device that stores its own propellant mass and expels this mass at high velocity to provide a reaction force, the thrust. As the rocket contains all the propellant itself, it is independent of its environment and, hence, can operate in empty space. There are two groups of rocket propellants, liquids and solids. Many spacecraft launchers involve the use of both types of rockets, for example the solid rocket boosters attached to liquid-propelled rockets. Solid rockets are generally simpler than liquid, but they cannot be shut down once ignited. Liquid engines may be shut down after ignition and conceivably could be re-ignited.

The basic principle driving a rocket engine is the famous Newtonian principle that "to every action there is an equal and opposite reaction." A rocket engine is throwing mass in one direction and benefiting from the reaction that occurs in the other direction as a result, see Figure 1a.

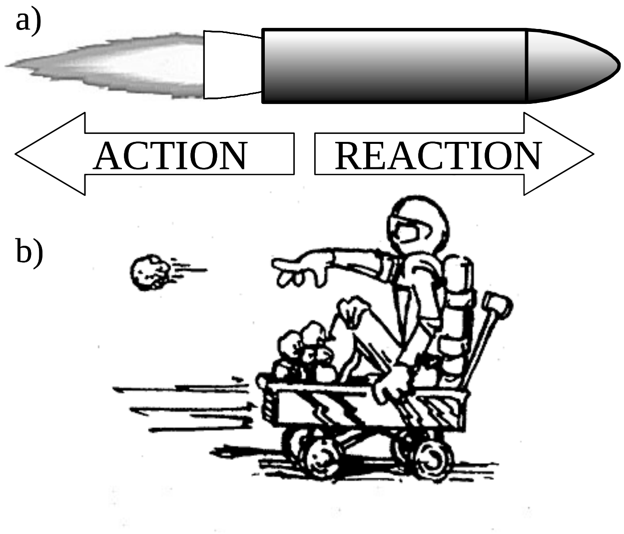

Figure 1. The basic principle of momentum exchange.
a) Rocket, b) One person-rocket (Courtesy cartoon of Humble *et al.* [1])

This concept of "throwing mass and benefiting from the reaction" can be hard to grasp at first, because that does not seem to be what is happening. Rocket engines seem to be about flames and noise and pressure, not "throwing things". To get a better picture we consider an astronaut throwing rocks out of the back of a wagon, see Figure 1b. The astronaut uses his muscles to accelerate the rocks in one direction, leading to an equal but opposite force on the wagon that pushes it in the opposite direction. The thing that controls the speed at which the wagon moves away is the weight of the rocks that he throws and the amount of acceleration that he applies to it. From Newton’s Second Law, we know that the force on an object is equal to the rate of change of momentum, so the momentum thrust is

$$F_m = \frac{dm}{dt} v_e = \dot{m} v_e \tag{1}$$

where $\dot{m}$ is the mass flow rate and v_e is the exit or exhaust velocity of the propellant. If the astronaut wants to generate more thrust, he has two options: increase the mass or increase the velocity of the rock. He can throw a heavier rock or throw a number of rocks one after another (increasing the mass), or he can throw the rock faster. But that is all that he can do.

A rocket engine is generally throwing mass in the form of a high-velocity gas. The engine throws the mass of gas out in one direction in order to get a reaction in the opposite direction. The mass comes from the weight of the propellants that the rocket engine uses. In a liquid rocket engine the propellants (fuel and oxidizer) are injected in to a combustion chamber where it is mixed and burned. Typically, the combustion chamber is a constant diameter duct with sufficient length to allow complete combustion of the propellants before the nozzle accelerates the gas products, see Figure 2. The nozzle is said to begin at the point where the chamber diameter begins to decrease.

Simply stated, the nozzle uses the temperature (T_0) and pressure (p_0) generated in the combustion chamber to create thrust by accelerating the combustion gas to a high supersonic velocity (see Figure 2). The nozzle exit velocity (v_e) that can be achieved is governed by the nozzle expansion ratio ε, defined as the ratio between the nozzle exit area and throat area, $\varepsilon = A_e/A_t$.

In addition to the momentum thrust, there are pressure forces acting on the rocket system. Combining the momentum and pressure thrust, the total thrust *(F)* produced by the rocket engine can be expressed as

$$F = \dot{m} v_e + \left(p_e - p_a \right) A_e \tag{2}$$

where p_e and A_e are the pressure and cross section area at the nozzle exit, and p_a is the ambient pressure.

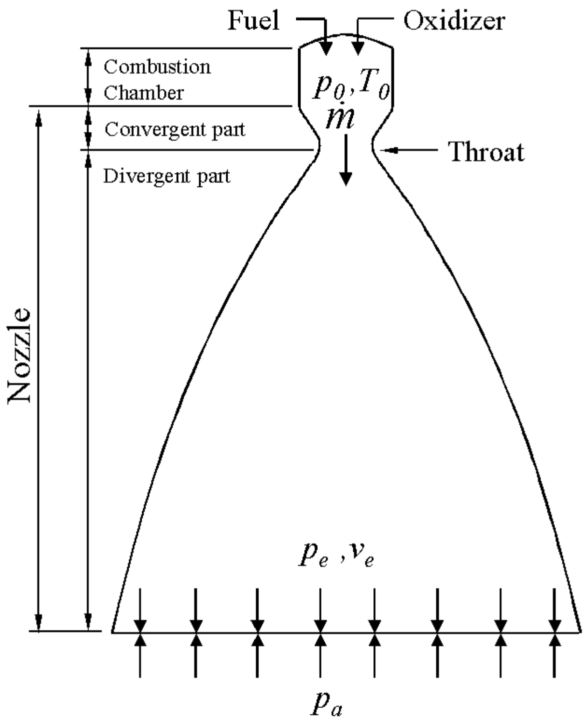

Figure 2. Definition of nozzle.

Besides the thrust, the specific impulse, I_{sp}, is an important parameter characterizing a rocket engine. The specific impulse is defined as[2]

$$I_{sp} = \frac{F}{\dot{m}} = v_e + \frac{(p_e - p_a)}{\dot{m}} A_e \tag{3}$$

which is a measure of how well a given propellant flow rate is transformed into thrust**.**

When inspecting Eq. (2) or Eq. (3), we get the impression that maximizing the exit pressure and velocity would maximize the performance for a given flow rate. If exit pressure and velocity were uncoupled this would be true. However, the nozzle exit pressure and velocity are very closely and adversely coupled through the amount of nozzle expansion. Since the flow is supersonic, the exit velocity will increase and exit pressure decrease as ε is increased and vice versa as ε is decreased. It can be shown that optimum performance is obtained if the nozzle exit pressure is equal to the atmospheric pressure, $p_e = p_a$, i.e. for adapted (or ideally expanded) flow. This is illustrated in Figure 3**,** which shows how the specific

[2] Sometimes g_0=9.81 (m/s^2) is included in the denominator to make the performance value independent of the used unit system, i.e. the unit for I_{sp} changes from a velocity (m/s) to a time (s).

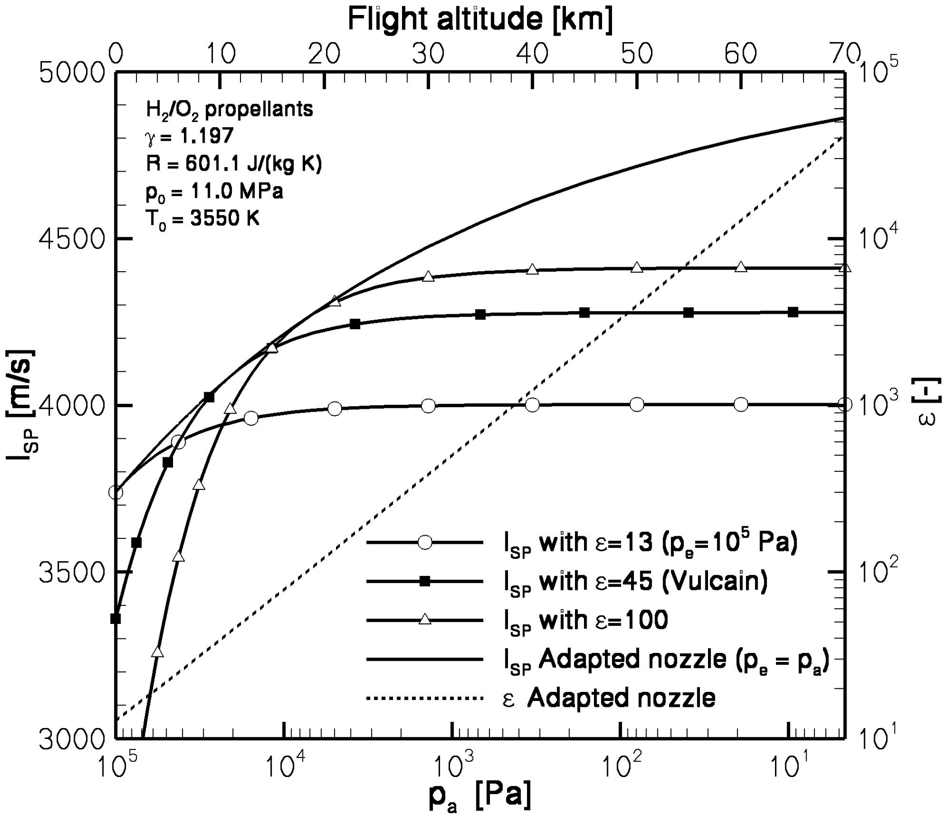

Figure 3. Performance versus ambient pressure.

impulse varies with ambient pressure (or flight altitude) for given chamber conditions equal to that of the Vulcain engine[3]. The solid lines show the specific impulse, the ones with symbols are for nozzles with fixed expansion ratio, and the one without symbols for an adaptable nozzle (able to change ε to adapt the exit pressure to the ambient pressure). The dashed line shows the corresponding expansion ratio of the adaptable nozzle. With a nozzle expansion ratio of ε=45, the flow becomes ideally expanded at an altitude of 10 km. From ground level up to this altitude the flow is overexpanded, i.e. $p_a > p_e$, while it is underexpanded ($p_a < p_e$) at higher altitudes. The flow patterns in the exit jet for the different regimes are illustrated by the numerical Schlieren pictures of Figure 4.

So far we have only described how a rocket engine is working and nothing has been said about the demands a rocket launcher need to fulfill and how it is done.

[3] The Vulcain engine is used as the core stage engine on the European Ariane 5 launcher.

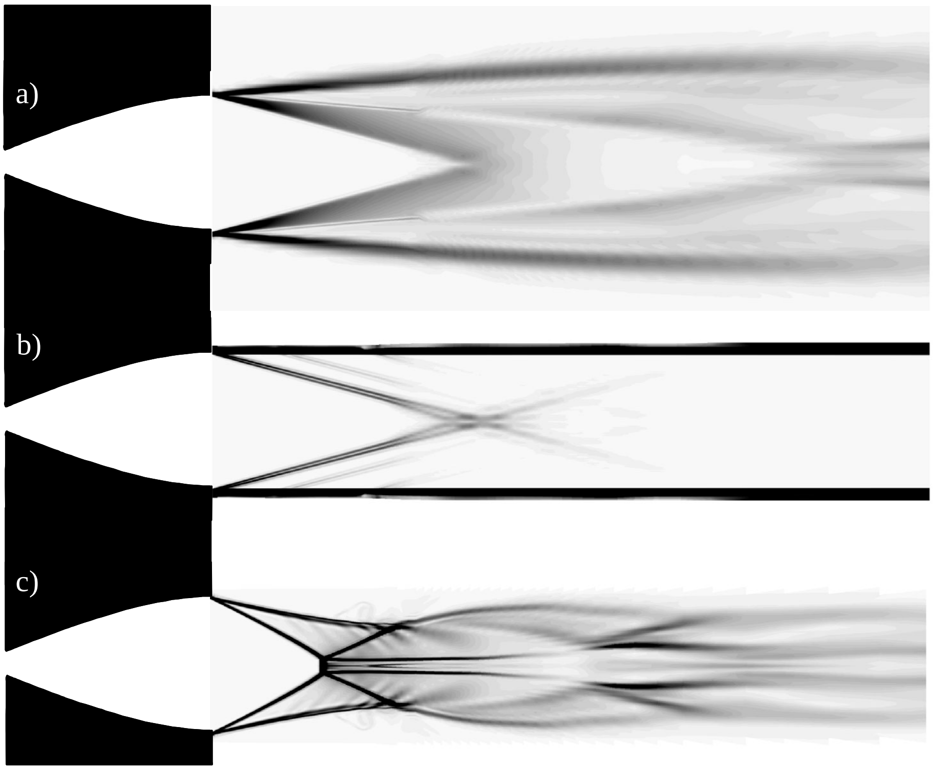

Figure 4. Numerical Schlieren pictures of flow at exit of a Mach 4 nozzle.
a) Under- (p_e/p_a=2), b) Ideal (p_e/p_a=1) and c) Over- (p_e/p_a=0.3) expanded flow.

To escape from Earth's atmosphere a launcher has to travel at least 150 km at a speed of more than 7.9 km per second. If the velocity were less the launcher would not be able to escape the Earth's gravitational attraction and if a satellite were put into lower orbit it would be pulled back into the Earth's atmosphere and rapidly burn up. When sorting out all parameters it will be found that weight is all-important. The heavier the payload the more fuel the launcher has to carry to ensure liftoff. More fuel means bigger tanks and yet more weight. A delicate balance has to be found between the weight of the launcher and ensuring that it has enough fuel and power to accelerate fast enough to reach its orbit before falling to the ground. For this reason, most launchers have three stages, each stage dropping away once it has fulfilled its purpose. In this way launchers become progressively lighter and require less fuel. The launcher can either use serial staging, i.e. where the subsequent stage starts to operate first when the launcher jettisons the previous stage, or parallel staging where two stages operates simultaneously.

The Main Design Issue of Core Stage Engine Nozzles

Most of today's launch vehicles, e.g. the American Space Shuttle, the European Ariane 5 launcher and the Japanese H-2 launcher, use parallel staging with two or more strong solid rocket boosters and a liquid core stage engine. The latter is ignited at ground to increase the reliability of the launcher and operates up to high altitudes, where the ambient pressure is close to vacuum. During take-off and the first phase of flight, the strong boosters make up most of the thrust, whereas the contribution of the core stage is comparably small. After booster separation, which usually takes place in altitudes where the ambient pressure is very low, the core stage alone accelerates the launcher. This is illustrated in Figure 5, which shows a typical flight sequence of a Geostationary Transfer Orbit mission for Ariane 5. With this type of staging, the vacuum performance of the core stage engine has a considerable influence on the payload, whereas its sea-level impulse is of minor importance (see Figure 3). The performance of rocket engines is highly dependent on the aerodynamic design of the expansion nozzle, the main design parameter being the area ratio as shown above. An obvious way to enhance the payload of such launchers is hence to increase the area ratio of the core engine nozzle, however, this will at the same time reduce the nozzle exit pressure.

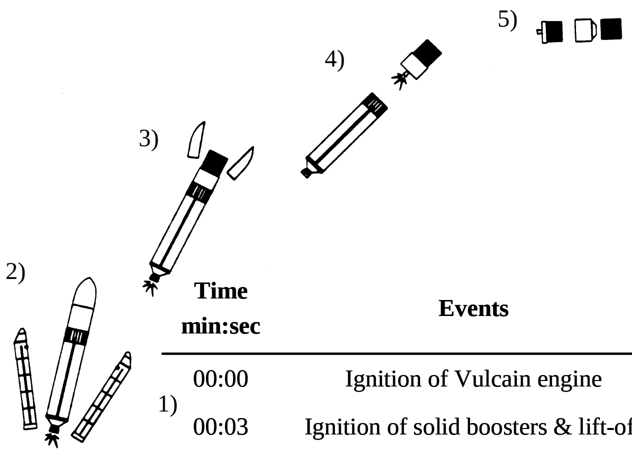

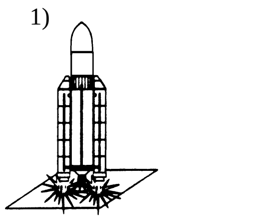

	Time min:sec	**Events**	**Altitude km**
1)	00:00	Ignition of Vulcain engine	0
	00:03	Ignition of solid boosters & lift-off	0
2)	02:06	Solid booster jettisioning	56
3)	03:04	Fairing jettisioning	106
4)	09:52	Core stage flight end Stage separation & 3rd stage ignition	141
5)	23:10	3rd stage flight end Orientation & payload separation	1077

Figure 5. Typical flight sequence of an Ariane 5 GTO mission. (Adopted from Isakowitz [2])

If a rocket engine is operated with the ambient pressure considerably higher than the nozzle exit pressure, the flow will not be fully attached, but separated from the nozzle wall. Flow separation in rocket nozzles is undesired because it can lead to high dynamic loads, which can damage the nozzle and end-up with a serious failure of the launcher. The most well known of these loads being the so called side-load, that has attracted the attention of many researchers. In order to prevent flow separation and side-loads, the core stage nozzles of today's launch vehicles use area ratios that are far below the optimum, but ensure full-flowing and thus safe function at sea-level conditions. Hence, allowing flow separation in the core stage engine with reduced side-loads would considerably improve the launcher's payload and thereby meeting the increasing demands from the satellite market.

One possible solution of the described problem is to adapt the nozzle contour during the flight to the changes of ambient pressure as shown in Figure 3. Attempts in this direction, however, have not yet been successful due to weight and mechanical complexity of such adapting devices.

Another approach is to introduce so called Flow Separation Control Devices (FSCD), by which high area ratio nozzles can be operated at separated condition at high ambient sea-level pressure without severe loads, thereby obtaining an improved overall performance. The feasibility of such devices is presently the objective of demonstration tests [3]. The main reason why such devices do not yet exist in full scale is that several basic questions regarding the nature of the flow separation phenomena and corresponding side-loads remain to be answered, which means that basic research is needed.

Undesirable Effects Associated with Flow Separation

Flow separation is a natural phenomenon as well as an engineering problem of fundamental importance in numerous industrial applications. It occurs in a wide range of flow regimes - laminar or turbulent, incompressible or compressible, subsonic or supersonic. In most cases it is an undesirable phenomenon because it is associated with large energy losses, or - as is the case in rocket engine nozzles - high levels of unsteady lateral forces, the so-called side-loads. Other examples where flow separation is present are cars and ducts in the subsonic regime, and in the supersonic regime missiles, airbreathing transatmospheric vehicles and spacecraft.

When a supersonic flow is exposed to an adverse pressure gradient it adapts to the higher-pressure level by means of a shock wave system. Basically, separation occurs when the turbulent boundary layer cannot negotiate the adverse gradient imposed upon it by the inviscid outer flow. Thus, flow separation in any supersonic flow is a process involving complex shock wave boundary layer interactions (SWBLI).

The interaction of shock waves with turbulent boundary layers can pose significant problems in the design of high-speed vehicles. When the flow is separated, large fluctuating pressure loads occur and can have characteristic frequencies close to the resonant frequencies of vehicle structural components. Interactions can arise from a variety of sources such as surfaces protuberances (wing-body junctures, antennae), abrupt turning of the high-speed flow (engine inlets, deflected elevons), and incident shocks originating from other parts of the vehicle. Since these types of loads are severe, always present during flight and cannot be avoided, it has been extensively studied in the last fifty years in order to understand and find ways to predict and reduce the loads.

Compared to the massive work focused on dynamic loads generated by SWBLI in external flow, the number of studies performed on internal flow separation in rocket nozzles has been meager in the past, see e.g. Refs. [4-31]. As a consequence the understanding of rocket nozzle flow separation and the ensuing side-load phenomena was limited when this project was initiated in 1997. The main reason is that flow separation and side-loads in rocket nozzles became a serious issue first in the 1970's when the development of the American Space Shuttle was initiated, i.e. the first launcher using parallel staging with a high performance core stage engine. Further, a core stage engine nozzle can be designed so that flow separation is avoided at nominal sea level steady-state operation. Thereby limiting the period of time with flow separation in the nozzle to the start-up (and shut-down) transient of the engine.

The following milestones give a historically perspective of the understanding of the side-load phenomena

1. **1970's development of the American Space Shuttle Main Engine (SSME):** Experimental studies are performed by Nave & Coffey [4] to investigate flow separation and the side-load phenomena in rocket nozzles for obtaining SSME design information. For the first time measurement results of side-loads become public available. It is observed that the flow separation and side-load characteristics are different in the full-scale and the sub-scale model engine tests. In contrast to the full-scale tests a transition between two different separations patterns, from "Free Shock Separation" (FSS) to "Restricted Shock Separation" (RSS), are observed in the model tests. In FSS the flow separates from the wall and continuous as a free stream. In RSS the flow separates and reattaches to the wall forming a small-restricted region with recirculating flow. It is also found that this flow phenomenon includes a hysteresis effect, i.e. the transition from FSS to RSS and from RSS back to FSS does not occur at the same operational condition. Further, significant side-loads are

obtained in both the FSS and RSS region, whereas the side-load activity is at a minimum in the hysteresis region. No explanation is given why the model nozzles features both separation patterns whereas the full-scale engine only has FSS.

2. **1974:** According to Schmucker, side-loads in rocket engine nozzles are due to asymmetric fluctuations of the separation line. He purposed a quasi-static side-load model based on a tilted separation line assumption, i.e. an asymmetric pressure distribution, which is acting over an effective area [5]. Schumcker's correlates his model with the side-load data by Nave & Coffey [4].
3. **1980's development of the European core stage engine Vulcain:** Schmucker side-load model is used in the design work.
4. **1981 SSME fuel feed line failure investigation**: Unexpectedly large loads during SSME engine start and cutoff transients cause fatigue failure of the fuel feed line. Larson *et al.* [6] conduct cold gas tests to investigate the side-load activity at the nozzle exit of a sub-scale SSME nozzle. With help of fluctuating wall pressure measurements and high-speed Schlieren movies of the flow, they find that the cause of the failure is due to unsteady flow separation at the nozzle exit. It is observed that the flow separates from and reattaches to the wall at the nozzle exit in a cyclic manner with a frequency of 100 Hz. It is the first time this phenomenon is reported and Larson *et al.* does not correlate theses observations with the appearance of RSS found in the earlier sub-scale tests performed by Nave & Coffey [4].
5. **1989 first Vulcain engine test:** Unexpected high levels of side-loads are observed. It is concluded that the Schmucker model is too simple.
6. **1994:** Pekkari claims that side-loads in rocket engine nozzles are due aeroelastic instability [8-9]. Based on an aeroelastic model, Pekkari conclude that the "model results are qualitatively as well as quantitatively consistent with Vulcain test results".
7. **1996:** Dumnov reports that side-loads are due to random pressure fluctuations, similar to those observed in external SWBLI [7]. Dumnov proposes a dynamic side-load model based on a generalized pressure fluctuation function. The application of the model to Russian rocket nozzles gives reasonable agreement between measured and predicted side-load. However, the model cannot reproduce the side-load feature of the Vulcain nozzle.
8. **1997-1998 Sub-scale testing of a Vulcain nozzle:** Mattsson *et al.* [32] investigates the flow separation and side-load phenomena in a sub-scaled Vulcain nozzle. They re-discover the FSS-RSS transition. They also find that a significant side-loads pulse is generated during the FSS-RSS transition inside the nozzle. Further, a second side-load peak is observed as the RSS is converted to FSS at the nozzle exit. The findings initiate a renewed interest of RSS phenomenon. Possible

aeroelastic effects are also investigated by changing the mechanical stiffness of the model nozzle. Mattsson [33] find that the aeroelastic coupling effects are not as strong as Pekkari anticipated. However, Mattsson also shows that a significant aeroelastic amplification of side-loads can occur in weak nozzle structures. These conclusions later becomes more public available through the work by Östlund *et al.* [3, 34].

9. **1998:** Frey *et al.* [35] shows that the appearance of RSS is closely linked to the internal shock generated in non-ideal nozzles, such as the thrust optimized Vulcain and SSME nozzle.
10. **1999:** Based on the recent findings, Terhardt *et al.* [36] re-evaluates Vulcain test data. The re-evaluation confirms that the transition between separation patterns observed in the Vulcain sub-scale tests by Mattsson *et al.* [32] also are the key driver for the large side-loads experienced in the Vulcain rocket engine.
11. **1999-present date:** Thanks to the focused work aimed to investigate flow separation and side-load origins, performed by the author and other European researchers during recent years [37-39], a major break-through regarding the physical understanding of nozzle dynamics has been done. Today we know that the problem of side-loads is substantially more complex than previously realized. Side-loads are generated not by one but by a variety of physical mechanisms, depending on nozzle contour type, mechanical structure and ambient conditions.

Development Logic for Nozzle Design

The positive results obtained during recent years concerning separation and side-load behavior are the fruit of combined analytical, numerical and experimental efforts, where CFD has been employed to support the design of test models, and tests have furnished input for refinement of CFD-methods, thus achieving a physical understanding of the flow processes that would not have been possible only a generation ago.

A schematic of the development loop is shown in Figure 6. A design loop usually begins with a contour layout, where the Method Of Characteristics (MOC) and/or other CFD methods are used to optimize the aerodynamic performance for a given design specifications (e.g. length, area ratio, weight etc). The next step is to verify, and if necessary modify, the design so as to meet specified load requirements. For this it is necessary to know pressure and temperature loads acting on the wall, but it is also necessary to assess internal flow field, in order to predict the flow regime at each given operational conditions. This is done using a combination of numerical and experimental methods. CFD methods are usually calibrated and validated in a specific flow regime, and hence may only give reliable results as

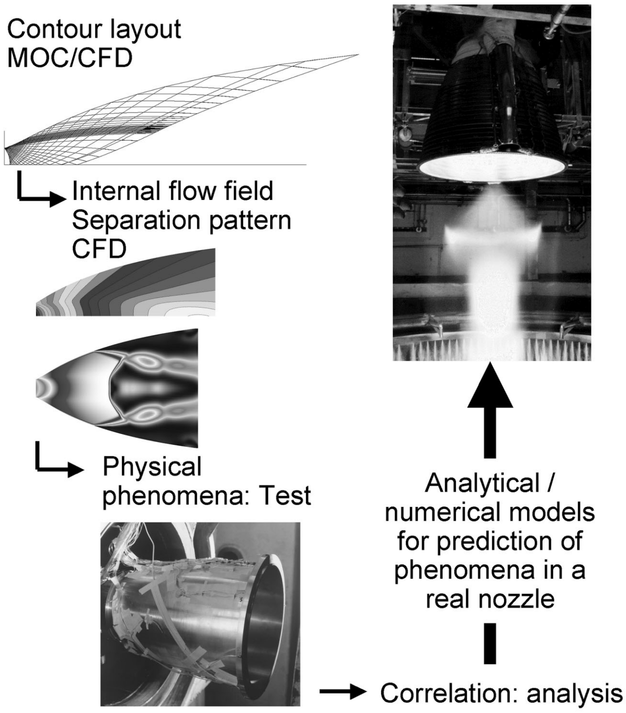

Figure 6. Logic of nozzle development.

long as the flow remains within the same regime. It is therefore imperative to perform hardware tests in order to verify that the nozzle flow actually lies within this regime. Most test methods, on the other and, can only access wall properties and hence experimental results on the internal nozzle flow field are usually not available. Flow measurements and visualization therefore need to be used interactively with CFD in order to draw conclusions concerning the physical mechanisms at work. In this process, the engineer will arrive at generalized correlations, which serve to evaluate a given design. A last step will be to apply these to the full-scale nozzle operating with real combustion gases on the rocket engine, which may require yet another loop of interaction between test, CFD and analysis.

Figure 7 shows some typical test configurations and how they relate to the full-scale engine nozzle in terms of complexity of the setup versus representativity of the obtained results. Which type of test to perform will depend on the stage of development, i.e. whether one is interested in general results of a fundamental character or data for a specific design.

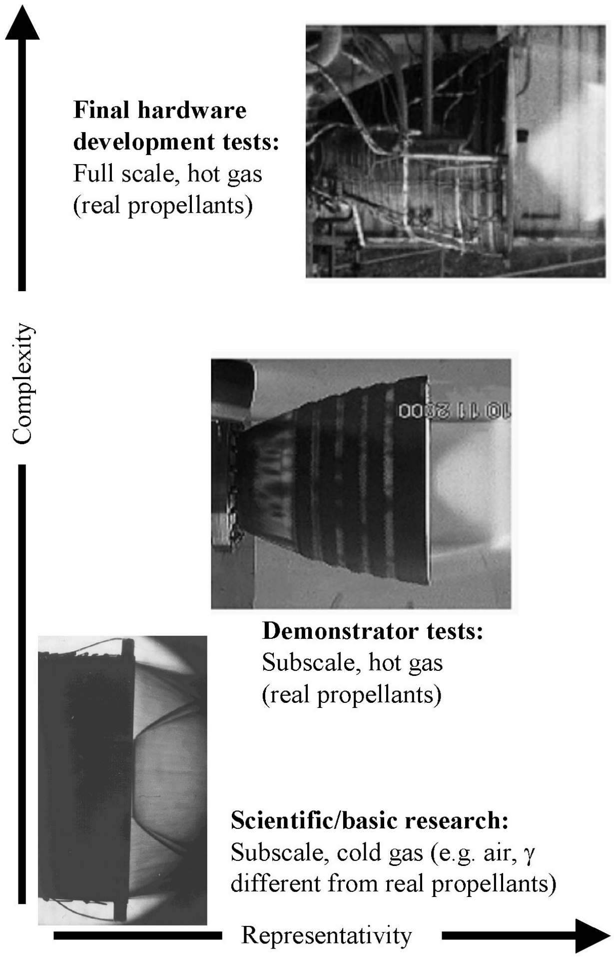

Figure 7. Subscale model testing.

Subscale model experiments are basically of two kinds:

(i) Hot gas tests, using gases with the same physical properties as a full-scale propellant gas. This allows for a simple geometric scale-down, leaving dynamical parameters unchanged. This type of sub-scale tests was performed e.g. during the development of the Vulcain engine [40] and also recent in demonstrator test of a radiation cooled C/SiC nozzle extension [41]. In both of these cases, the test model was a complete scale-down of the Vulcain nozzle. As expected the separation characteristics in the scaled nozzles [40, 41] showed close agreement with the Vulcain nozzle [36,42]. For instance, the transition of the separation pattern inside the nozzle from FSS to RSS and the transition from RSS to FSS at the exit of the nozzle occurred at the same operation conditions as in the Vulcain nozzle.

However, the test and instrumentation cost for this kind of test is high, and the high temperature imposes severe limitations on the measurement equipment that can be used. The obtainable information is further restricted by the test duration time, which is usually short due to test rig limitations. It is therefore necessary to complement with wind tunnel testing, where the test duration can be significantly increased.

(ii) Cold gas tests, using e.g. air ($\gamma = 1.4$) instead of hot gas propellants (e.g. $\gamma \approx 1.2$ for engines operated with H_2-O_2), are a relatively inexpensive alternative, allowing for more extensive testing, and parameter variation. The draw-back is that it is no longer possible to separate geometrical and dynamical parameters, since all gasdynamical quantities are functions of both Mach number and γ. In this case CFD is indispensable as a tool to define appropriate test models as well as making meaningful test evaluations. The main challenge in such tests is to reproduce the actual behavior of a nozzle run with hot propellants.
In the present context, the main scaling requirement is that the model nozzle should have similar separation and side-load characteristics as the original. This means that the essential features of the interior flow field must be reproduced, while maintaining a similar wall pressure distribution. These requirements cannot be simultaneously fulfilled, if the gas used to operate the model does not have the same γ as in the real nozzle as shown by Östlund [37]. Nevertheless, direct scaling from cold to hot flows is possible within certain limits if the cold-gas contouring is done very carefully and if the right values are used for normalization [37]. Of course, cold-gas test results can always be used to understand the physical phenomena and establish prediction tools, which can be applied to hot full-scale applications [37,41].

In the following sections the current authors contribution to the understanding and modeling of supersonic flow separation and the ensuing side-load phenomenon in rocket engine nozzles is presented.

SUMMARY OF PAPERS

Building of knowledge regarding flow separation and side-loads has been a continuous process at Volvo Aero Corporation (VAC) since 1993, when the Flow Separation Control working (FSC) group was formed with CNES, SNECMA and ASTRIUM[4].

VAC performed focused studies on the topic within the GSTP/FSC program, 1996-1999, under a contract with the European Space Agency (ESA) and the Swedish National Space Board (SNSB). This included sub-scale testing of rocket nozzles at the modified hypersonic wind tunnel HYP500 at the Aeronautical Research Institute of Sweden (FFA)∗, in order to investigate the aerodynamic and aeroelastic behavior of a parabolic contour with and without FSCD inserts. The present author has been actively involved in the VAC/FSCD activities since 1997, being in charge of the test design (including design of model contours), hardware set-up and instrumentation, as well as test logic and evaluation of test results. In Paper I a description of the GSTP test program is given, together with discussion and analysis of the obtained test results.

In the subsequent FSCD-program since 1998, under contract with Swedish National Space Board (SNSB) and Centre National d'Études Spatiales (CNES), flow separation and side-loads have been studied analytically and experimentally in sub scale test campaigns and this work is partly presented in Paper II. This work was performed in co-operation with FOI, CNES, SNECMA, ONERA, LEA, DLR and ASTRIUM [38-39].

Throughout the work, CFD-computations have been extensively used for designing the models. They are indispensable for a qualitative understanding of the physics and flow phenomena, and hence provide a necessary input for setting up model descriptions and making meaningful evaluations. During the initial phase of the GSTP program, CFD studies were performed in order to investigate the capability of some standard RANS models for predicting flow separation in nozzles. These studies showed that all standard 2-equation models tested severely failed to predict this type of flow field. To cure the apparent anomaly in the RANS simulations an ad hoc realizability correction was introduced, which showed to improve the prediction. These predictions are compared with test data in Paper I. Based on these experiences a new study was initiated together with FFA to assess the influence of different corrections. The result from this work is presented in Paper III. Besides this work, an overview and analysis of the most commonly used corrections of RANS models is given in Paper V.

---

[4] is now a part of EADS Space Transportation

∗ is now a part of the Swedish Defence Research Agency (FOI)

Nozzle	Base Contour	ε	Nozzle Picture	Description/Test objectives
VolvoS1	Parabolic contour	20	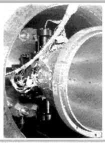	This nozzle was designed with the geometrical definition of the Vulcain nozzle as a model. The primary objectives were to investigate the separation and side-load behaviour in a Vulcain like nozzle. More specific objectives were to study the influence of different structural response of the nozzle on the side load magnitude and investigate the degree of aeroelastic coupling.
VolvoS2	Parabolic contour	20.8	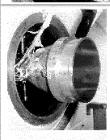	S2 was dedicated to investigating the same h/w as S1 with an applied extension. The nozzle length was increased with approximately 25 %. The extension was made in such a way that the pressure gradient was relatively high in the extension. The chief objective was to study the impact on the end-effect side load peak.
VolvoS3	Parabolic contour	18.2	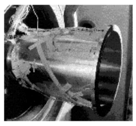	This nozzle is a more refined scaling of the Vulcain nozzle compared with S1. The idea was here not only to duplicate the nozzle wall geometry, pressure and Mach number profile, but also to imitate the internal flow-field. As the chemistry is completely different, hydrogen / oxygen vs. air, it is impossible to get identical flow patterns. The contour was however made to have the same wall pressure profiles and Mach number distribution and the internal shock as close as possible to the Vulcain.
VolvoS4	Parabolic Polygon	18.2	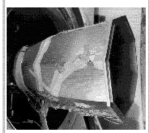	The Polygon nozzle is a patented Volvo invention. The aim of the Polygon nozzle is to have a design with a side load reduction relative to a normal axi-symmetric nozzle. The shape is three-dimensional, see the figure. This Polygon nozzle has an identical base-line contour as S3. The nozzle was made as an octagon with the polygonisation starting at the predicted position for the separation pattern transition. The objective was to evaluate the degree of side-load reduction with this concept.
VolvoS5	Parabolic contour (VolvoS3) + Positive pressure gradient on the second bell	18.2	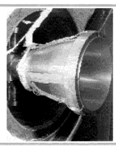	S5 is a Dual-Bell nozzle, i.e. another FSC concept. This is a well-known nozzle type since several decades. Actual testing with separation has however been very limited and side load measurements were lacking when these test where performed. The contour of S5 is equal to S3 in the first upstream section. This constitutes the first bell. The dual-bell contour used for this nozzle is then designed according to the principle of positive pressure-gradient in the second bell. This means that the separation front in theory will travel directly from the start of the second bell out to the exit during the start transient.
VolvoS6	Truncated Ideal Contour (TIC)	20.7	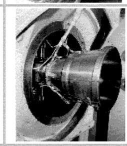	S6 is a truncated ideal contoured nozzle, i.e. from a different familly of contours compared with S1-S5. This type of nozzle has no internal shock why it only features free shock separation. The primary objectives were to investigate the separation and side-load behaviour in this type of nozzle.
VolvoS6 short	Truncated Ideal Contour (TIC), same contour as VolvoS6	13.9	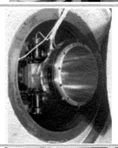	This is a shorten S6 nozzle. The objective was to investigate the influence of changes in the geometry downstream of the separation on the separation location and corresponding side-load.
VolvoS7	High Pressure Gradient (HPG)	24.6	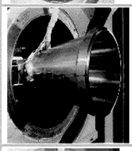	In nozzles with an internal shock it exist a driving mechanism for transition between two different separation patterns. However, the contour can be design such as this transition is suppressed. Hence, it will only be free shock separation in the nozzle. With the S7 nozzle this type of design was demonstrated.
VolvoS7 short	High Pressure Gradient (HPG)	20.3	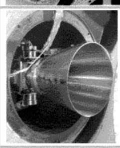	This is a shorter version of the S7 nozzle. The objective was to investigate the influence of the downstream geometry on the separation and side-load.
VolvoS8	HPG with film injection	22.1	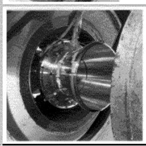	The S8 nozzle is a HPG contour with film injection. This nozzle was designed to have similar flow properties regarding mass flow rate and film injection pressure ratio as the film cooled Vulcain 2 and Vulcain 2+ nozzle. The objective was to study the impact of film injection on separation and side-loads.

Table 1. Sub scale nozzles tested by VAC at FFA's HYP500 facility.

Within the frame of the FSCD-program, VAC performed new sub-scale nozzle tests at FFA's test facility in Stockholm. In the FSCD program VAC has tested eight different nozzle concepts, which are listed in Table 1. Three potential origins of side-loads have been observed and investigated - namely the pressure fluctuations in the separation and recirculation zone due to the unsteadiness of the separation location, the transition of separation pattern and the aeroelastic coupling. In Paper IV, all three mechanisms are described in detail, and methods are presented to calculate their magnitude and pressure ratio of occurrence. In Paper V the nozzle flow separation phenomena is put in a wider perspective. This paper gives an introduction to the physical background, and an overview of methods of research, modeling and prediction, and important achievements, starting with boundary-layer interactions in basic configurations and then proceeding to the more complex case of rocket engine nozzles.

PAPER 1

Mattsson J (changed name to Östlund 1999), Högman U and Torngren L
''A Sub-Scale Test Programme on Investigation of Flow Separation and Side-Loads in Rocket Nozzles'', In *Proceedings of the 3rd European Symposium on Aerothermodynamics of Space Vehicles*, ESA-ESTEC, Netherlands, November 24-26, 1998, ESA SP-426

Significance of work

This paper gives a description of a subscale test program aimed to investigate the flow separation and side-load phenomenon in parabolic bell shaped rocket nozzles. The tested nozzle was a subscale model of the Vulcain nozzle. The results show that there is a transition of separation pattern in the nozzle, from the free-shock separation (FSS) to the restricted shock separation (RSS) pattern. This type of transition was observed already in the 1970's by Nave & Coffey [4]. However, in this work it was shown, for the fist time, that these transitions also are the origin of two distinct side-load peaks. This conclusion was the ignition for intensive research of the phenomenon both within and outside Europe. Further subscale experiments were performed within different FSCD test campaigns [3,43,44] as well as recent Japanese experiments [45], which confirmed this mechanism for side-loads in TOP and CTIC nozzles (both of which have an internal shock). In addition, re-evaluation of test results of the Vulcain rocket engine confirmed this mechanism as key driver for side-loads during both start-up and shut-down [36].

Division of work by authors

Jan Mattsson has been in charge of the test design, hardware set-up and instrumentation, as well as test logic and evaluation of test results. The tests were performed at FOI by Lars Torngren and his colleges. The work was led by Ulf Högman. The paper was written by Jan Mattsson. The work was performed within the ESA/ESTEC General Support Technology Program and has partly been presented by (i) Torgny Stenholm: Flow separation control activities at Volvo and SEP, ESA Advanced Nozzle Workshop, University of Rome, 14-15 October, 1997. (ii) Jan Mattsson: Subscale Testing of Flexible Nozzles, In Proceedings of European Seminar on Rocket Nozzle Flows, CNES, Paris, 12-14 October 1998.

PAPER 2

Östlund J and Bigert M
''A Subscale Investigation on Side-Loads in Sea Level Rocket Nozzles"
Presented at 35th AIAA/ASME/SAE/ASEE Joint Propulsion Conference and Exhibit, AIAA Paper 99-2759, June 1999

Significance of work

This paper gives a description of test objectives, results and conclusions of a subscale test program aimed to investigate the flow separation and side-load phenomenon in rocket nozzles with Flow Separation Control (FSC) or side-load reduction devices. The designed test set-up is unique in the sense that it resembles the bending mode of a real rocket nozzle. The influences of the degree of freedom of the nozzle motion and the bending resistance on the side-load magnitude were studied with the use of exchangeable torsions springs. Mainly two types of FSC nozzles were tested, i.e. a polygon shaped and a Dual-bell nozzle respectively. This work was the first actual side-load reduction demonstration with FSC concepts in a rig test. It was also the first work that showed that there can be both aerodynamic and aeroelastic drivers for the side-load. Further, a verified analytical model for the prediction of the transition of separation pattern from FSS to RSS is given in the paper. This model in parallel with the model by Frey *et al.* [42], were the first models aimed for prediction of this phenomenon.

Division of work by authors

Jan Östlund has been in charge of the test design, hardware set-up and instrumentation, as well as test logic and evaluation of test results. The work was led by Mikael Bigert. The paper was written by Jan Östlund and Mikael Bigert.

PAPER 3

Östlund J and Jaran M
"Assessment of Turbulence Models in Overexpanded Rocket Nozzle Flow Simulations", Presented at 35th AIAA/ASME/SAE/ASEE Joint Propulsion Conference and Exhibit, AIAA Paper 99-2583, June 1999

Significance of work

In this work it is shown that the choice of turbulence model has a significant influence on the simulated flow field in an overexpanded rocket nozzle. It is found that without corrections, standard two-equation turbulence models fails to predict the measured separation characteristics in the nozzle. The main source of the apparent anomaly in these simulations are located, namely the unphysical production of turbulent energy (P_k) encountered at shocks. It is shown that the results can be improved when a physical limiter of P_k is introduced. It is also shown that further improvements can be obtained with the use of a weakly nonlinear realizability correction, which limits the value of the eddy viscosity.

Division of work by authors

This work was initiated by Jan Östlund. The simulations were carried out by Matias Jaran under supervision of Jan Östlund. The paper was written by Jan Östlund and Matias Jaran.

PAPER 4

Östlund J, Damgaard T and Frey M
"Side-Load Phenomena in Highly Overexpanded Rocket Nozzles"
Accepted for publication in Journal of Propulsion and Power

Significance of work

This paper gives an overview of different side-loads mechanisms observed in the VAC nozzle test campaigns. Three main types of side-loads have been observed due to: (i) random pressure fluctuation, (ii) transition in separation pattern and (iii) aeroelastic coupling. All these three types are described and exemplified by test results together with analysis. A new approach for detection of the separation zone in nozzles is proposed based on general characteristics of the unsteady separated flow. It is shown that the dynamic separation process in rocket nozzles is very similar to the one observed in generic test cases. Hence, the intermittency of the nozzle flow can be described in similar manner as in generic test cases. Methods to translate aerodynamic forces to mechanical loads or vice versa are outlined. This includes solving a forced response problem for stationary and random forces and using pulse excitation theory for sudden and distinct forces. A major part of the work is devoted to the more complex case, i.e. when the separated nozzle flow interacts with the mechanical system. For the first time, an aeroelastic model for separated nozzle flow is presented and verified with test results. It is shown that the aeroelastic model is capable to predict the aeroelastic behavior experienced in the tests and that aeroelastic effects can be significant in week nozzle structures.

Division of work by authors

Jan Östlund performed analysis and simulations. The results were discussed with Tomas Damgaard and Manuel Frey. The paper was mainly written by Jan Östlund. The paper is based on Östlund J, Damgaard T and Frey M, "Side-Load Phenomena in Highly Overexpanded Rocket Nozzles", 37th AIAA/ASME/SAE/ASEE Joint Propulsion Conference and Exibit, AIAA Paper 2001-3684, July 2001.

PAPER 5

Östlund J and Muhammad-Klingmann B
"Supersonic Flow Separation with application to Rocket Engine Nozzles"
Accepted in revised form for publication in Applied Mechanics Reviews

Significance of work

This paper describes the current status of analytical, experimental and numerical research on shock-wave-boundary-layer interactions (SWBLI), where, however, emphasis is placed on the rocket-engineering perspective. The essential viscous-inviscid interaction phenomena are explained in detail on the basis of analytical arguments. Fundamentals of SWBLI are reviewed. Subsequently the paper focuses on rocket-nozzle design issues and the fluid-mechanics phenomena affecting these. The paper also connects the industrial development of rocket engine nozzles to the fundamental research of the SWBLI phenomenon and show how these research results can be utilized in real applications. Aspects of scaling, testing and CFD modeling, which are specific for supersonic combustive flows, are highlighted. The paper is concluded with remarks on active and passive flow control in rocket nozzles and directions of future research.

Division of work by authors

This paper is based on the Licentiate Thesis by Jan Östlund, "Flow Processes in Rocket Engine Nozzles with Focus on Flow Separation and Side-Loads", Licentiate Thesis TRITA-MEK 2002:09, Royal Institute of Technology, Department of Mechanics, Stockholm, Sweden, 2002. The paper was written by Jan Östlund and Barbro Muhammad-Klingmann.

REFERENCES

[1] Humble R W, Henry G N and Larson W J (1995), *Space propulsion analysis and design*, McGraw-Hill, Inc., ISBN-0-07-031329-6.

[2] Isakowitz S J (1991), *International reference guide to space launch systems*, AIAA Technical Publications, Washington DC.

[3] Östlund J and Bigert M (1999), A subscale investigation on side-loads in sea level rocket nozzles, *35th Joint Propulsion Conference and Exhibit*, AIAA Paper 99-2759.

[4] Nave L H and Coffey G A (1973), Sea-level side-loads in high area ratio rocket engines, *9th Propulsion Conference*, AIAA Paper 73-1284.

[5] Schmucker R (1973), Flow processes in overexpanding nozzles of chemical rocket engines (In German), Report TB-7,-10,-14, Technical University Munich, Munich.

[6] Larson E, Ratekin G, O´Connor G (1981), Structural response of the SSME fuel feedline to unsteady shock oscillations, *52nd Shock and Vibration Symposium*, New Orleans.

[7] Dumnov G E (1996), Unsteady side-loads acting on the nozzle with developed separation zone, *32nd Joint Propulsion Conference and Exhibit,* AIAA Paper 96-3220.

[8] Pekkari L-O (1993), Aeroelastic stability of supersonic nozzles with separated flow, *29th Joint Propulsion Conference and Exhibit,* AIAA Paper 93-2588.

[9] Pekkari L-O (1994), Aeroelastic analysis of side-loads in supersonic nozzles with separated flow, *30th Joint Propulsion Conference and Exhibit*, AIAA Paper 94-3377.

[10] Salikuddin M (1992), Unsteady pressures on exhaust nozzle interior surfaces – empirical correlations for prediction, *14th DGLR/AIAA Aeroacoustics Conference*, Proceedings. Vol. 2 (A93-19126 05-71), Bonn, Deutsche Gesellschaft fuer Luft- und Raumfahrt, pp. 873-881.

[11] Darren R and Hidalgo H (1995), Fluctuating pressure analysis of a 2-d SSME nozzle air flow test, *In its Thirteenth Workshop for Computational Fluid Dynamic Applications in Rocket Propulsion and Launch Vehicle Technology*, (SEE N96-29750 11- 34) pp. 723-743.

[12] Foster C and Cowles F (1949), Experimental study of gas flow separation in overexpanded exhaust nozzles for rocket motors, JPL Progress Report 4-103, Jet Propulsion Lab., California Inst. of Tech., Pasadena, CA.

[13] Green L (1953), Flow separation in rocket nozzles, *ARS Journal*, **23**(1).

[14] Summerfield M, Foster C and Swan W (1954), Flow separation in overexpanded supersonic exhaust nozzles, *Jet Propulsion*, **24**.

[15] Campbell C and Farley J (1960), Performance of several conical convergent-divergent rocket type exhaust nozzles, NASA TN D-467, NASA Lewis Research Center, Cleveland OH.

[16] Schilling T W (1962), Flow separation in rocket nozzle, M. S. Thesis, University of Buffalo, New York.

[17] Kalt S and Badal D (1965), Conical rocket nozzle performance under flow separated condition, *Journal of Spacecraft and Rockets*, **2**(3).

[18] Arens, M and Spiegler E (1963), Shock-Induced boundary layer separation in overexpanded conical exhaust nozzles, *AIAA Journal*, **1**(3).

[19] Sunley H and Ferriman D (1964), Jet separation in conical nozzles, *Journal of the Royal Aeronautical Society*, **68**.

[20] Lawrence R A (1967), Symmetrical and unsymmetrical separation in supersonic nozzles, Research report 67-1, Southern Methodist University, Dallas.

[21] Chen C, Chakravarchy S and Hung C (1994), Numerical investigation of separated nozzle flows, *AIAA Journal*, **32**(9).

[22] Nasuti F and Onofri M (1996), Viscous and inviscid vortex generation during nozzle flow transients, *34th Aerospace Sciences Meeting & Exhibit*, AIAA Paper 96-0076.

[23] NASA (1976), NASA space vehicle design criteria (chemical propulsion), liquid rocket engine nozzles, NASA SP-8120, Lewis Research Center, Cleveland OH.

[24] Crocco L and Probstein R (1964), The peak pressure rise across an oblique shock emerging from a turbulent boundary layer over a plane surface, Princeton University, Princeton NJ.

[25] Carriere P (1966), Comments on computational methods of viscous effects in propulsion nozzles (In French), *DGRR/WGLR Symposium*, also published as ONERA TP 408.

[26] Carrière P, Sirieix M and Solignac J-L (1968), Propértiés de similitude des phénomènes de décollement laminaires ou turbulents en écoulemnt supersonique non uniforme, *12th International Congress of Applied Mechanics*, Stanford University, Stanford, also ONERA TP N° 659F.

[27] Lewis J E, Kubota T and Lees L (1968), Experimental investigation of supersonic laminar, two-dimensional boundary layer separation in a compression corner with and without wall cooling, *AIAA Journal*, **6**, 7-14.

[28] Dumnov G E, Nikulin G Z, Voinov A L and Zyuzin V I (1995), Nozzle flow separation and unsteady side-loads, *Conference on Propulsive Flows in Space Transportation System*, pp. 798-816.

[29] Kudryavtsev V M (1975), Fundamentals of theory and calculations of liquid rocket engines (In Russian), Moscow High School, Moscow.

[30] Malik T I and Tagirov R K (1988), A semiempirical method for calculating separated turbulent flow in a conical Laval nozzle in the reexpansion mode (In Russian), *Akademiia Nauk SSSR, Izvestiia, Mekhanika Zhidkosti i Gaza* , 60-66.

[31] Tuovila W J and Land N S (1968), Experimental study of aeroelastic instability of overexpanded rocket nozzle extensions, NASA TN D-4471, Langley Research Center, Langely Station, Hampton, Va.

[32] Mattsson J (changed name to Östlund 1999), Högman U and Torngren L (1998), A sub-scale test programme on investigation of flow separation and side-loads in rocket nozzles, *Proceedings of the 3rd European Symposium on Aerothermodynamics of Space Vehicles*, ESA SP-426, 373-378.

[33] Mattsson J (changed name to Östlund 1999) (1998), Subscale testing of flexible nozzles, *In Proceedings of European Seminar on rocket nozzle flows*, CNES, Paris.

[34] Östlund J, Damgaard T, Frey M (2001), Side-load phenomena in highly overexpanded rocket nozzles, *37th AIAA/ASME/SAE/ASEE Joint Propulsion Conference and Exhibit,* AIAA Paper 2001-3684.

[35] Frey M and Hagemann G (1998), Status of flow separation prediction in rocket nozzles, *34th Joint Propulsion Conference and Exhibit,* AIAA Paper 98-3619.

[36] Terhardt M, Hagemann G and Frey M (1999), Flow separation and side-load behaviour of the Vulcain engine, *35th Joint Propulsion Conference and Exhibit*, AIAA Paper 99-2762.

[37] Östlund J (2002), Flow processes in rocket engine nozzles with focus on flow separation and side-loads, Licentiate Thesis TRITA-MEK 2002:09, Royal Institute of Thechnology, Stockholm, Sweden

[38] Hagemman G, Terhardt M, Frey M, Reijasse P, Onofri M, Nasuti F and Östlund J (2000), Flow separation and side-loads in rocket nozzles, *4th International Symposium on Liquid Space Propulsion*.

[39] Frey M, Ryden R, Aziary de Roquefort T, Hagemann G, James P, Kachler T, Reijasse P, Schwane R and Stark R (2002), European cooperation on flow separation control, *4th International Conference on Launcher Technology "Space Liquid Propulsion"*.

[40] Stanke H (1986), Test report on the results on HM60-subscale test series 3, Vulcain Ne Project Report HM RT 110 0000 501, MBB, Ottobrun.

[41] Hagemann G, Alting J and Preclik D (2001), Scalability discussion for rocket nozzle flows based on subscale and full-scale testing, *4th European Symposium on Aerothermodynamics for Space Vehicles*.

[42] Frey M and Hagemann G (1999), Flow separation and side-loads in rocket nozzles, *35th Joint Propulsion Conference and Exhibit,* AIAA Paper 99-2815.

[43] Frey M, Stark, R, Cieaki H K, Quessard F and Kwan W (2000), Subscale nozzle testing at the P6.2 test stand, *36th Joint Propulsion Conference and Exhibit*, AIAA Paper 2000-3777.

[44] Reijasse P, Servel P and Hallard R (1999), Synthesis of the 1998-1999 ONERA works in the FSCD working group, ONERA RTS 49/4361 DAFE/Y, ONERA, Châtillon-sous-Bagneux.

[45] Tomita T, Takahashi M, Ueda S, Tamura H and Aoki K (2001), Visualization of the formation of separation bubbles on a bell-shaped nozzle surface in relation to serious side-load, *37th Joint Propulsion Conference and Exhibit,* AIAA Paper 2001-3559.

Paper 1

A SUB SCALE TEST PROGRAMME ON INVESTIGATION OF FLOW SEPARATION AND SIDE LOADS IN ROCKET NOZZLES

J. Mattsson[1], U. Högman[2], L. Torngren[3]

[1]Volvo Aero Corporation, SE-461 81 Trollhättan, Sweden, Phone: +46 520 93735, Fax: +46 520 98578, VAC.JNMN@MEMO.volvo.se

[2]Volvo Aero Corporation, SE-461 81 Trollhättan, Sweden, Phone: +46 520 94946, Fax: +46 520 98578, VAC.UFHN@MEMO.volvo.se

[3]FFA, SE-161 11 Bromma, Sweden, Phone: +46 8 63410450, Fax: +468 6341072, tnl@ffa.se

ABSTRACT

An important factor limiting the performance optimisation of a rocket engine is the loads induced by unsymmetrical and unsteady flow separation in the nozzle extension during launch. Within the ESA/ESTEC General Supporting Technology Programme (GSTP) the flow separation phenomenon in a rocket nozzle with corresponding side load features has been investigated in sub scale wind tunnel tests. In the present paper, results from this testing are presented and discussed. First, the used test facility, hardware and logic are presented. Results from the test and associated analysis are discussed. The results from the testing demonstrate that the rig is capable of simulating flow separation and side loads in flexible nozzles. Two different steady state separation patterns are prevailing in the test nozzle. Further, numerical simulation of the flow separation with state of the art-turbulence-modelling results in good agreement with the experimental data. The separation pattern, point of separation and the wall pressure behind the separation point have been successfully predicted.

Key words: Nozzle; Over-expanded Flow; Flow Separation; Side load; Test

1. INTRODUCTION

Some rocket engines suffer severe dynamic loads during operation at chamber pressures below the design pressure. This operational condition typically occurs during the start-up and throttle down process of the rocket motor at sea level. These loads can sometimes be of such a magnitude that they present life-limiting constraints on thrust chamber components as well as on the thrust vector control system. The source of these loads is generally attributed to the instationary nature of the partially detached and partially attached flow that occurs during operation of the thrust chamber at over-expanded conditions.

The most well known of these dynamic loads that have received attention in the literature is the so called side-load[1,2]. Side loads have been observed during start-up of over-expanded sea-level liquid propellant rocket engines as well as during ignition and the staging of a multi-stage solid propellant rockets[3,4,5]. Due to the severe complications experienced due to too high levels of side-loads, it is one of the most important features in sea-level nozzle design. It has e.g. been taken into account for the contour definition for the Vulcain 2 nozzle extension[6].

The traditional design approach for bell type nozzles is to design the nozzle contour and area ratio such that attached flow and low levels of side-loads are guaranteed at nominal operation at high ambient pressure, sea level conditions. Further, the structure is designed robust enough to withstand the side-loads during the throttling up and down process. The reduced performance under vacuum ambient condition and the corresponding weight penalty with a robust design is accepted with this design approach. Increasing demands for improved launcher performance, however, push the development of new concepts. One possible solution is to adapt the nozzle contour during the flight to the changes of ambient and chamber pressure. Attempts in this direction, however, have so far not been successful due to the weight and mechanical complexities of such devices. By introducing so called Flow Separation Control Devices (FSCD), high area ratio nozzles can be operated at separated condition at sea level without severe loads, and an improved overall performance is obtained. The feasibility of such devices is under demonstration. The main reason why such devices do not yet exist in full scale is that several basic questions regarding the nature of separation phenomena and the corresponding side-loads remain to be answered.

Within the Flow Separation Control (FSC) programme at Volvo Aero Corporation (VAC) the flow separation phenomenon in sea level rocket nozzles with corresponding side load features have been investigated. In the course of the work, detailed aerodynamic and aeroelastic sub scale testing have been performed in the modified hypersonic wind tunnel HYP500 at the Aeronautical Research Institute of Sweden (FFA) under

Proceedings of the Third European Symposium on Aerothermodynamics for Space Vehicles, 24th-26th November 1998, ESTEC, Noordwijk, The Netherlands, ESA SP-426, December 1998

a contract with the European Space Agency (ESA). In the present paper results from this testing are presented and discussed.

2. GSTP TEST PROGRAMME

The primary objectives of the GSTP FSC programme were to study the side load and separation behaviour in a sub scaled rocket nozzle.

More general test objectives were:

1) Study the influence of different structural response of the test nozzle on the side load magnitude and investigate the degree of aeroelastic[7,8] coupling.
2) Define the separation characteristics of the nozzle.
3) Measure nozzle vibrations.
4) Establish statistical data base on side loads
5) Provide data for calibration of design tools with respect to flow separation and side loads.

The GSTP FSC testing was performed during the period 12 August 1997 to 21 January 1998 in the modified hypersonic wind tunnel HYP500 at FFA and allowed successful completion of the test objectives.

2.1 TEST CONFIGURATIONS

The testing was performed with a bell-shaped sub-scale rocket nozzle mounted in the modified HYP500 wind tunnel, Figure 1. The test nozzle was designed to resemble the separation and structure response characteristics of the Vulcain nozzle[9]. Because the nozzle model is operated with air instead of hot propellant gases the shape and expansion ratio differs from the Vulcain nozzle. The main parameters of the model nozzle are shown in Table 1.

Table 1. Main parameters of model nozzle.

Parameter	*Value*	*Dimension*
Area ratio (ε)	*20*	-
Nozzle length (L)	350	mm
Throat radius (r_t)	33.54	mm
Nozzle exit radius (r_{exit})	150	mm
Design feeding pressure (P_0)	5.0	MPa
Design feeding temperature (T_0)	450	K
Feeding gas	Air	-

The nozzle consists mainly of two parts, one fixed part mounted to the downstream flange of the wind tunnel and one flexibly hinged part, see Figure 2. The flexible part is free to move in one plane perpendicular to the test section viewing direction and the motion simulates the throat bending mode of a real rocket nozzle. The bending resistance is simulated with exchangeable torsion springs. A photo of the reference hardware with the different parts can be found in Figure 3.

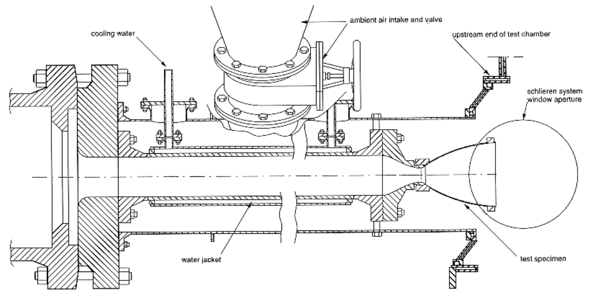

Figure 1. Schematic side view of the flexible hinged test nozzle in FFA tunnel HYP 500.

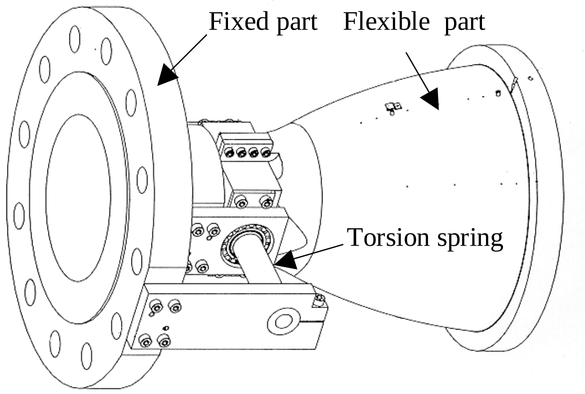

Figure 2. Side view of model nozzle assembly.

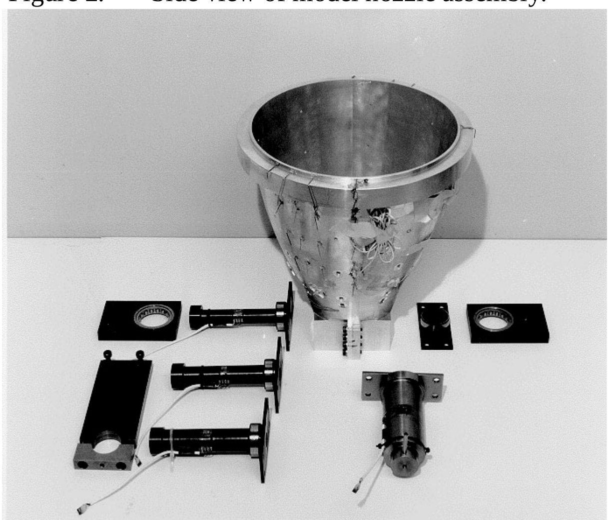

Figure 3. Photo of used hardware.

In order to investigate the influence of structural response and aeroelastic coupling[7,8] on the side load, five different torsion spring set-ups were used. The resulting natural oscillating frequencies of the bending mode are listed in Table 2 for the different set-ups.

Table 2. Resulting natural oscillating frequencies of the bending mode for the different spring set-ups.

Spring name	*Super weak*	*Weak*	*Medium*	*Stiff*	*Rigid*
Natural frequency [Hz]	25,2	36,3	45,0	57,5	120

2.2 INSTRUMENTATION

The quantities that were measured during the test campaign were:

- Nozzle side load
- Nozzle wall static pressure
- Nozzle wall dynamic pressure
- Nozzle wall vibrations
- Feeding pressure
- Feeding temperature
- Static pressure in test cell
- Dynamic pressure in test cell
- Schlieren visualisation of flow field

A summary of the nozzle instrumentation and the transducer locations is found in Figure 4.

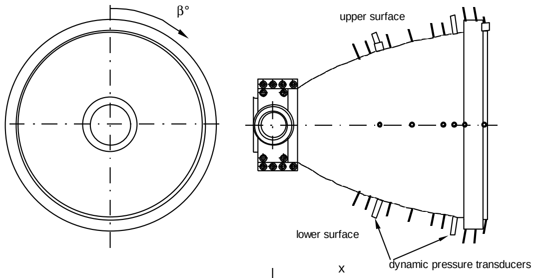

Pressure tap locations	
x (mm)	β (°)
140	0, 180
157.5	0, 180
175	45, 270
192.5	0, 180
227.5	0, 45, 180, 270
262.5	0, 180
280	0, 45, 180, 270
297.5	45, 270
315	0, 45, 180, 270
332.5	0, 180
350	0, 45, 180, 270

Dynamic pressure transducer locations	
x (mm)	β (°)
175	0, 180
297.5	0, 180

Accelerometer locations	
x (mm)	β (°)
175	0*
350	0*

* as close to β=0 as possible

Figure 4. Instrumentation of model nozzle.

The main jet wall pressure was measured with a total number of 30 static pressure taps in the nozzle. The transducers were positioned both in axial lines in order to measure the steady state separation point and in circumferential lines in order to see possible asymmetry of the flow. Four fast response pressure transducers on the nozzle wall were used in an attempt to trace the pressure fluctuations connected with unsteady separation.

The side load was measured with strain gauge bridges mounted on the torsion springs. Corresponding nozzle dynamic behaviour was recorded with two accelerometers located at the middle of the nozzle and at the exit.

In addition to the numerical data, a Schlieren system was used to visualise the flow downstream of the nozzle exit. The Schlieren system was equipped with a beam splitter and both a camera for photographic film and a high-speed video camera with 500 frame/sec. were used simultaneously.

2.3 TEST SEQUENCES

Mainly three different types of test sequences with three different objectives were used during the testing:

1) To investigate the steady state separation of the nozzle flow, test sequences with stepwise variation of the feeding pressure were used. The runs were performed with increasing pressure and at different pressure levels, which were held constant for at least 10 sec. The test cell pressure was held constant to atmospheric pressure during the test. A typical test run is shown in Figure 5.

2) To study the stochastic variation in side loads during start and stop transients a numbers of start-up and shut down sequences were used. In these tests the feeding pressure was increased rapidly from atmospheric pressure to a maximum feeding pressure which guaranteed full flowing condition, then followed by a throttling down again to atmospheric conditions. The test cell pressure was held constant to atmospheric pressure during the test, Figure 5.

3) To assess the impact of the Reynolds number and the ambient pressure on the separation, test sequences with variation of the test cell pressure were used, Figure 5.

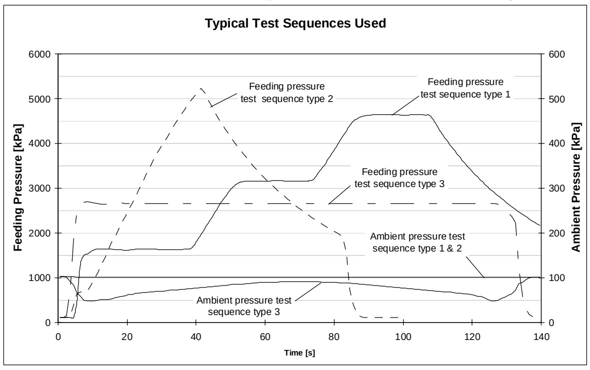

Figure 5. Typical test sequences used.

In all test sequences performed the test model was supplied with preheated pressurised dry air through the wind tunnel circuit. The air was preheated in order avoid condensation. The operation capabilities of the wind tunnel used during the testing are listed in Table 3.

Table 3. Used operation capabilities of the wind tunnel.

Parameter	*Value*
Mass flow rate	Up to 36 kg/s
Feeding pressure	Up to 5.3 MPa
Feeding air temperature	450-500 K
Test cell static pressure	50–100 kPa

3. TEST RESULTS

Typical steady-state wall pressure data are shown in Figure 6 for 11 different operational conditions, feeding to ambient pressure ratio ranging from about 10 to 50. The data have been averaged over 4 seconds, the wall pressure normalised with the feeding pressure and the axial location from the throat are normalised with the nozzle length.

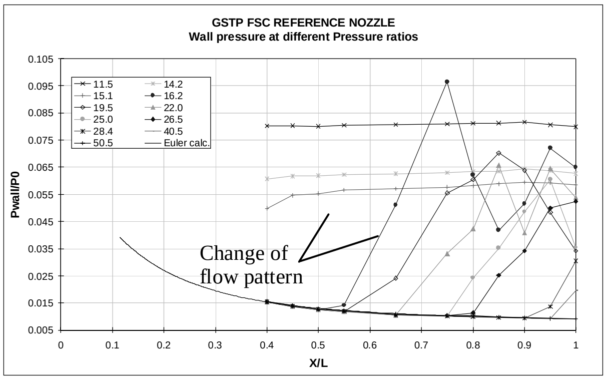

Figure 6. Wall pressure profiles in the model nozzle, experimental data FFA.

As can be noted in the figure the wall pressure profile features are subjected to a drastic change when the pressure ratio between the feeding and ambient pressure is increased above 15. This is explained by a transition of the flow separation pattern.

At a pressure ratio below 15, the separation profile follows the classical concept of nozzle separation often labelled ”free-shock” separation. In Figure 7 the flow field pattern predicted with CFD and the prevailing wall pressure in the nozzle at a pressure ratio of 14 is shown. From the figure we can conclude that at free shock separation the wall pressure rises nearly to ambient pressure in a very short distance. The source of this rise is due to the oblique shock originating from the separation point. Downstream the steep pressure gradient region, the wall pressure increases slowly to almost ambient pressure.

In Figure 8 we can see the corresponding picture of the flow pattern inside the nozzle at a pressure ratio of 16. As can be observed the flow first separates from the wall and that the pressure exceeds the ambient pressure downstream the separation point. The oblique shock wave emerging from the boundary layer is reflected by the Mach disc, which almost completely covers the nozzle cross section. Because of the reflection, the flow reattaches and the nozzle appears to be full flowing. The oscillatory behaviour of the wall pressure is caused by the expansion and compression waves interacting with the supersonic jet boundaries to match the ambient air.

This kind of flow behaviour was first reported within the J2-S cold flow test programme and the separation and reattachment flow pattern was denoted ”restricted shock” separation after Nave and Coffey[2]. Due to the scale and the use of cold air as feeding gas a wide-spread assumption was made that this flow process could only occur in sub-scale cold flow nozzles[1]. However, recent investigations of full-scale nozzles have shown that restricted shock separation occurs both in the SSME and the Vulcain nozzle[10,11,12]. The similarity between the GSTP, J2-S, SSME and the Vulcain nozzle is that they are all parabolic nozzles of Rao type[13,14], with an internal shock induced in the throat region.

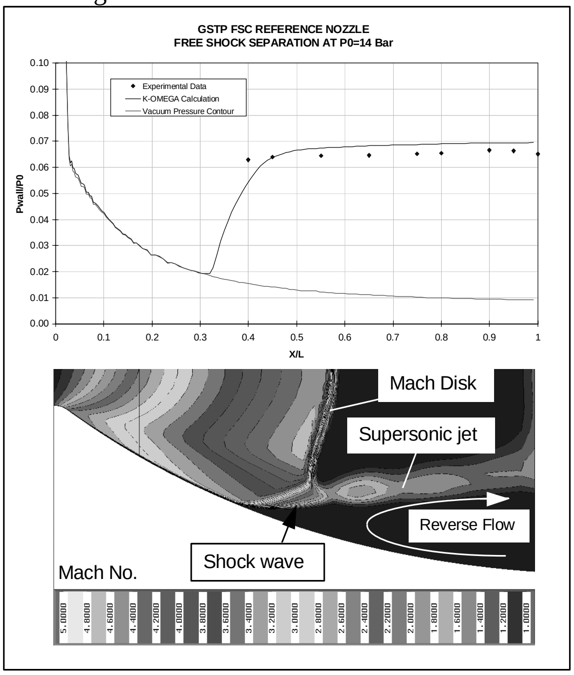

Figure 7. Free shock separation in model nozzle, experimental data FFA.

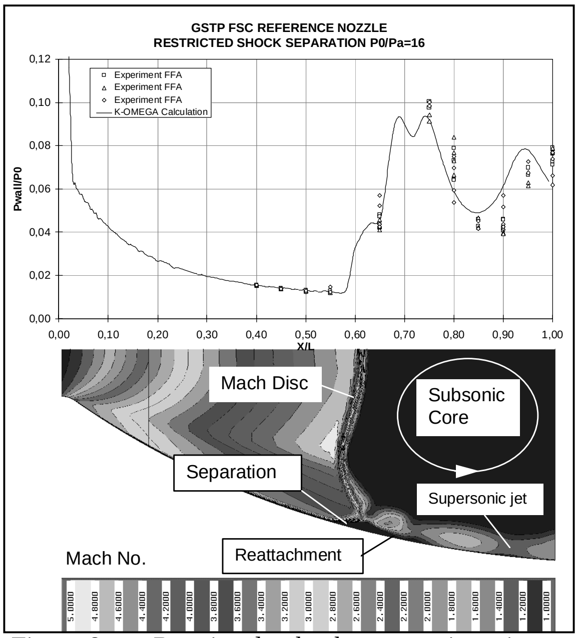

Figure 8. Restricted shock separation in model nozzle, experimental data FFA.

For the numerical flow field analysis presented in Figure 7-8 an in-house structured multi-block Navier-Stokes solver, VOLSOL[15], with a modified k-ω turbulence model was used. As can be concluded from the figures, CFD is capable of predicting the separation phenomenon. Good agreement can be seen between the calculations and the experimental data when considering the prediction of the separation point and the wall pressure down stream the separation point.

When representing the separation characteristics graphically the method of plotting the ratio between the separation pressure, p_{sep}, and the plateau pressure, p_p, behind the separation point versus the inviscid Mach number at the separation point is widely adopted [1]. The motivation of this method emerges from the physical reasoning that the pressure ratio over the oblique separation shock is only a function of the Mach number and the specific heat ratio. In Figure 9, a summary of the separation characteristics for the GSTP nozzle can be found together with the Schmucker separation criterion[1]. This is the most widely used separation criterion today in the European space industry.

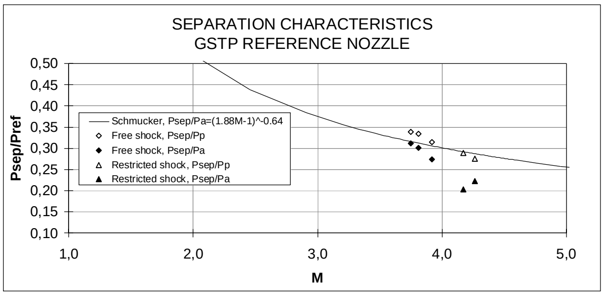

Figure 9. Separation characteristics of the GSTP nozzle.

In the figure the measured separation pressure has been normalised with either the plateau pressure behind the shock or the ambient pressure for comparison. In the case of free shock separation the plateau pressure behind the shock is often roughly approximated as being equal the ambient pressure. This neglects the fact that the pressure recovery to ambient pressure consists of two independent mechanisms, flow separation and recirculation. When considering restricted shock separation this approximation is even coarser. The flow in the separated region is enclosed by supersonic flow and the scatter of the data when using the ambient pressure as the reference pressure indicates this. In the GSTP nozzle the ratio between the plateau pressure and the ambient pressure is of the order 0.9 in the free shock case and varies between 0.7 and 0.85 for the restricted shock case depending on the position of the separation point. This indicates that the Schumcker criterion is far too simple as it tries to account for all pressure recovery effects in one single formula, see above. There is thus a need of an improved criterion that simulates all the different recovery phenomena separately.

A time record of the measured side load torque during a start up and shut down process is shown in Figure 10. Two different distinct load peaks can be identified both during start up and shut down.

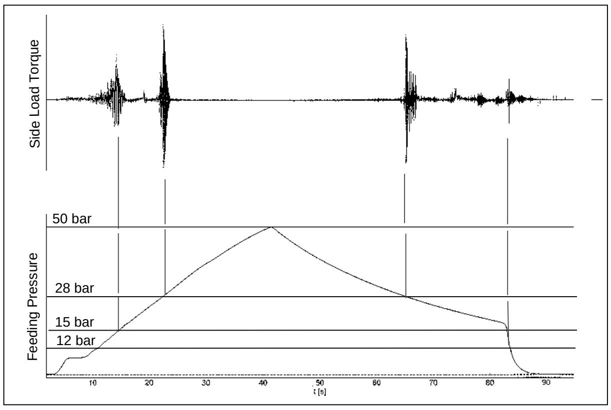

Figure 10. Time record of the measured side load torque during start up and shut down.

In Figure 11 and Figure 12 these data are given in terms of percent of peak measured loads versus the feeding to ambient pressure ratio for the start up and shut down transient respectively.

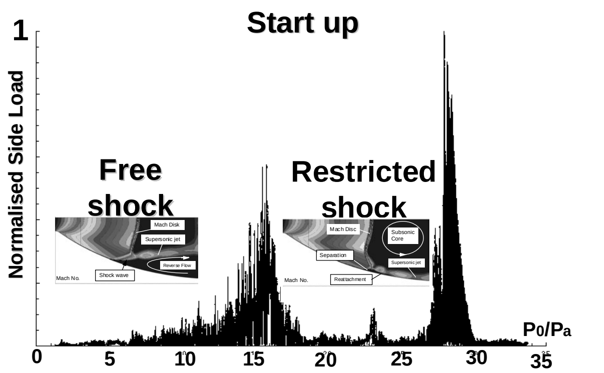

Figure 11. Normalised side load torque vs. feeding to ambient pressure ratio, start up.

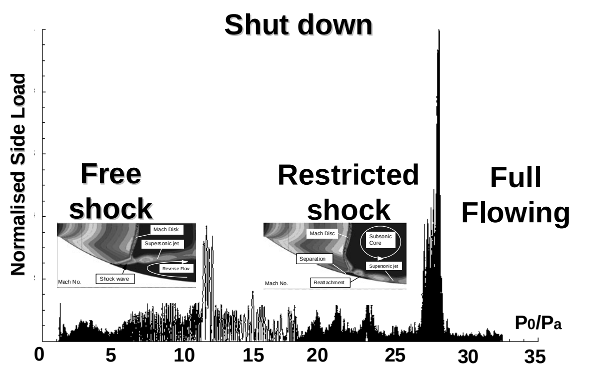

Figure 12. Normalised side load torque vs. feeding to ambient pressure ratio, shut down.

As indicated in the figures it is one significant load peak at a pressure ratio of about 15 and second at a pressure ratio of 28 during the start transient. Corresponding side load peaks during the throttle down occurs at pressure ratio of 12 and 28. The low pressure side load peak is obviously coupled to the transition of the separation pattern. The different values of the pressure ratio for the low pressure peak during throttling up and down indicates a hysteresis effect of the transition phenomenon. The two side load peaks and the hysteresis effect were also experienced in the J2-S sub-scale test[2].

From the high speed video recording of the flow pattern at the exit it can be seen that the flow starts to pulsate when the downstream leg of the λ shock, i.e. the reattachment point, is close / intersects the nozzle exit. This happens at a pressure ratio of 25. At this point the flow becomes highly unstable, it separates from and reattaches to the wall in a cyclic manner until the increase of the feeding pressure is enough to move the downstream leg of the λ shock totally out of the nozzle, which corresponds to a pressure ratio of 30. It is obvious that the second side load peak is connected to this end effect. This kind of unsteady flow process with a restricted shock separation converted to a free shock separation at the nozzle exit was also experienced in the SSME nozzle[10,16]. It was concluded that this effect was the reason for the failure of the SSME fuel feed line.

4. SUMMARY AND CONCLUSIONS

A sub scale test programme on the investigation of flow separation and side load experienced in rocket nozzles has been carried out. The used test facility, hardware and logic have been presented and the results from the test and associated analysis discussed. The results from the testing demonstrate that the rig and model hardware is capable of simulating the flow separation and the associated side load phenomena experienced in real rocket nozzles. The two main flow fields found in the over-expanded nozzle featured separation from the wall without reattachment at lower feeding pressure (free shock separation) and with reattachment at higher feeding pressure (restricted shock separation). The free shock separation remained to a higher feeding pressure during the start-up phase and the restricted shock separation tended to remain when the driving pressure was lowered. This accounts for a hysteresis effect. It was concluded that the phenomena with two different flow separation regimes occur in parabolic nozzles of Rao type with an internal shock emerging from the throat region. The two significant side load peaks observed are generated during transition between the separation patterns. Further, numerical simulation of the flow separation with state-of-the-art turbulence modelling results in a very good agreement with the experimental data. The separation pattern, point of separation and the wall pressure behind the separation point have been successfully predicted.

ACKNOWLEDGMENTS

The authors wish to express their appreciation to the European Space Agency and the Swedish National Space Board for the financial and technical support of this work.

REFERENCES

1. R. H. Schmucker, “Flow processes in overexpanded chemical rocket nozzles, Part 1: Flow separation”, NASA TM-77396.
2. L. H. Nave and G. A. Coffey, “Sea level side loads in high area ratio rocket engines”, AIAA 73-1284
3. J. M. Bowyer, G. W. Krieter and R. E. Peterson, “An investigation of the Side Force that is Sometimes Observed in Rocket Motor Start-Up”, AIAA78-1045.
4. G. D. Luke and D. E. Adams, ”Use of Nozzle Trip Rings to Reduce Nozzle Separation Side Loads During Staging”, AIAA-92-3617.
5. G. L. Romine, “Nozzle Flow Separation”, AIAA Journal Vol.36, No. 9, September 1998.
6. M. Bigert, T. Stenholm and T. Sätmark, “Technology for the Film-Cooled Nozzle of the Vulcain Engine”, IAF-98-S.3.05
7. L.-O. Pekkari, “Aeroelastic Stability of Supersonic Nozzles with Separated Flow”, AIAA 93-2588.
8. L.-O. Pekkari, “Aeroelastic Analysis of Side Loads in Supersonic Nozzles with Separated Flow”, AIAA 94-3377.
9. T. Stenholm et al., “The Vulcain Extension and its Evaluation”, ISTS 98-a-1-08.
10. T.-S. Wang, C. Dumas, “Numerical Study of the SSME Nozzle Flow Fields During Transient Operations- A comparison of the Animated Results with Test”, 11th Workshop for CFD Applications in Rocket Propulsion, Alabama April 22, 1993.
11. M. Frey and G. Hagemann, “Status of Flow Separation Prediction in Rocket Nozzles”, AIAA 98-3619.
12. M. Terhardt, M. Bigert. “Vulcain Testing Analysis ANE Test Results”, European Seminar on Rocket nozzle Flows, CNES, France, October 1998.
13. G.V.R Rao, “Exhaust Nozzle Contours for Optimum Thrust”, Jet Propulsion, pp.377-382, June 1958.
14. G.V.R. Rao, “Approximation of Optimum Thrust Nozzle Contours”, ARS Journal, p. 561, June 1960.
15. R. Ryde’n and P. Groth, “Volsol V2.6 user’s Guide”, VAC Report 9970-1857, Volvo Aero Corporation.
16. E. W. Larson et al.,”Structural Response of the SSME Fuel Feedline to Unsteady Shock Oscillations”, 52nd Shock and Vibration Symposium , New Orleans, Lousiana 21-29 October 1981.

Paper 2

AIAA-99-2759

A Sub Scale Investigation on Side Loads in Sea Level Rocket Nozzles

J. Östlund

M. Bigert

Space Propulsion

Volvo Aero Corporation

S-461 81 Trollhättan, Sweden

35th AIAA/ASME/SAE/ASEE
Joint Propulsion Conference & Exhibit
June 20-24, 1999 / Los Angeles, California

A SUB SCALE INVESTIGATION ON SIDE LOADS IN SEA LEVEL ROCKET NOZZLES

Jan Östlund [##]
Mikael Bigert

Volvo Aero Corporation
Space Propulsion Division
SE-461 81 Trollhättan
Sweden
(E-mail: vac.jnos@memo.volvo.se, vac.mbig@memo.volvo.se)

Abstract

The challenge of designing first stage rocket engine nozzles is made more difficult by the unstable loads during the start-up and sea level rig testing. These side loads are a key issue for the nozzle designed. In order to understand this and to be able to optimise the future designs, Volvo is currently working with a broad program. With both tests and analysis. The program started within the GSTP framework in 1997 and is presently continuing as a National program closely co-ordinated with our European partners.

Up to June 1999, not less than 7 test campaigns have been carried out, all at the facilities of FFA in Stockholm. The paper describes the objectives of these tests together with results and conclusions.

In parallel work is ongoing to understand the side loads, their nature and the factors influencing their size. Analytical models have been developed and correlated to the test results.

The future potential of the knowledge generated in this program is very high since the side load reduction design will be a powerful instrument in increasing the performance of the next generations sea level nozzles.

Nomenclature

Abbreviations / Physics	
ANE	Advanced Nozzle Extension
FSC	Flow Separation Control
FSCD	Flow Separation Control Device
FSS	Free Shock Separation.
LEA	Laboratoires d'Etudes Aérodynamiques
NE	Nozzle Extension
P	Pressure
R	Radius
RSS	Restricted Shock Separation.
TEG	Turbine Exhaust Gases
x	Axial position
Index	
cc	Combustion Chamber
ns	Normal shock

: Jan Östlund changed his name from Mattson in April 1999

Introduction

Some rocket engines suffer severe dynamic loads during operation at chamber pressures below the design pressure. These operational conditions typically occur at start-up and shut-down or at off nominal operation of the engine. These loads can sometimes be of such a magnitude that they present life limiting constrains on thrust chamber components as well as on the thrust vectoring control system. The source of such loads are generally attributed to the instationary nature of the partially detached and partially attached flow that occurs during the operation of the thrust chamber at pressure below design pressure.

The most well known of these dynamic loads that have received attention in the literature is the so called side-load. Side loads have been observed during start-up of over-expanded sea-level liquid propellant rocket engines as well as during the staging of a multi-stage solid propellant rockets. Due to the severe complications experienced due to too high levels of side-loads the side-load is one of the most important features in sea-level nozzle design and has e.g. been guiding the contour definition for the Vulcain 2 nozzle extension.

The traditional design approach for bell type nozzles is to design the nozzle contour and area ratio such that attached flow and low levels of side-loads is guaranteed at nominal operation at high ambient pressure, sea level conditions. Further, the structure is designed robust enough to withstand the side-loads during the throttling up and down. The reduced performance under vacuum ambient condition and the corresponding weight penalty with a robust design is accepted with this design approach. Increasing demands for improved launcher performance, however, push the development of new concepts. To decrease the separation margin at sea level will yield clear performance benefits /4/. One possible solution is to adapt the nozzle contour during the flight to the changes of ambient and chamber pressure. Attempts in this direction, however, have not been successful due to the weight and mechanical complexities of such devices. By introducing so called Flow Separation Control Devices (FSCD), high area ratio nozzles can be operated at separated condition at sea level without severe loads, and an improved overall performance is obtained. The feasibility of such devices are under demonstration. The main reason why such devices do not yet exist in full scale is that several basic questions regarding the nature of separation phenomena and the corresponding side-loads remain to be answered. The side load phenomena has recently received new attention in Europe /1/ and /8/.

Volvo programs for side load investigations

Within the Flow Separation Control programme at Volvo Aero Corporation (VAC) the flow separation phenomena in sea level rocket nozzles with corresponding side load features has been investigated. In the course of the work detailed aerodynamic and aero-elastic sub scale testing has been performed in the modified hypersonic wind tunnel HYP500at the Aeronautical Research Institute of Sweden (FFA) under contract with European Space Agency (ESA) and Swedish National Space Board (SNSB).

The first program was within the GSTP of ESA /1/, where a great number of tests were run in 1997.

A continuation was started in 1998 within the frame of the so-called Vulcain 2+ program at Volvo. Here, the activities have been coordinated with similar programs in France and Germany. A European FSCD Working Group has been created for technical co-operation between CNES/SEP/Dasa/DLR/ONERA/LEA/FFA and Volvo. The Vulcain 2+ program is focussed on coming sea level engine generations with drastically improved performance.

The present plans include several more test campaigns to be carried out during the year 1999.

GSTP test campaigns 1997

The tested nozzle consisted mainly of two parts, one fixed part mounted to the downstream flange of the wind tunnel and one flexible hinged part. The nozzle throat radius is about 33 mm. The flexible part was suspended with a flexible joint permitting motion in only one plane and the motion simulated the throat bending mode of a real rocket nozzle. The bending resistance was simulated with five different exchangeable torsion springs in order to investigate the influence of the structure response on the side load amplitude and possible aero-elastic coupling. The ratio in stiffness between the stiffest and the weakest spring was 25. To conclude whether the resulting side-load was measured or not with the flexible joint with one degree of freedom a test with a universal joint suspension permitting bending in all directions around the throat was also performed. With this test, both the side load level and direction of the load could be measured. A number of start-up and shutdown transients, were performed with these test configurations to achieve statistical information of the side-load behaviour.

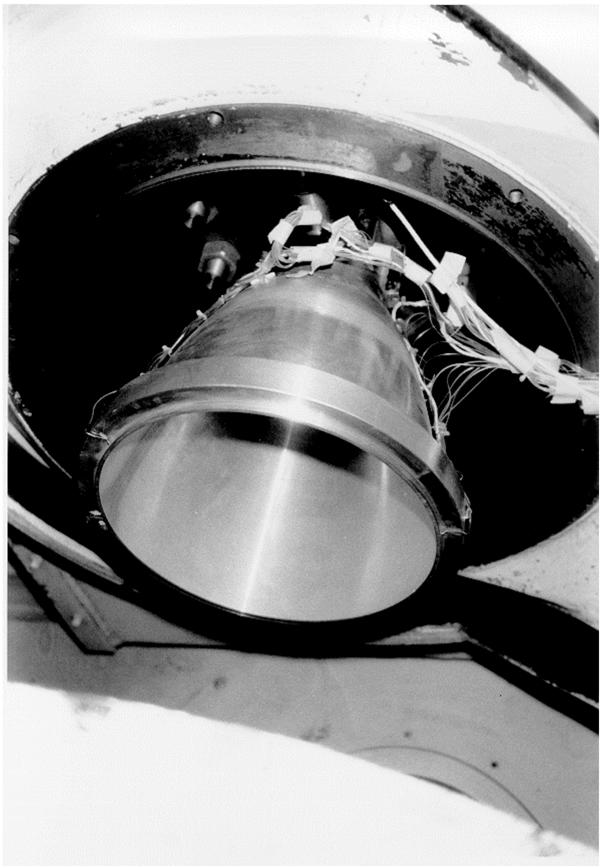

Figure 1 : GSTP nozzle installed in rig

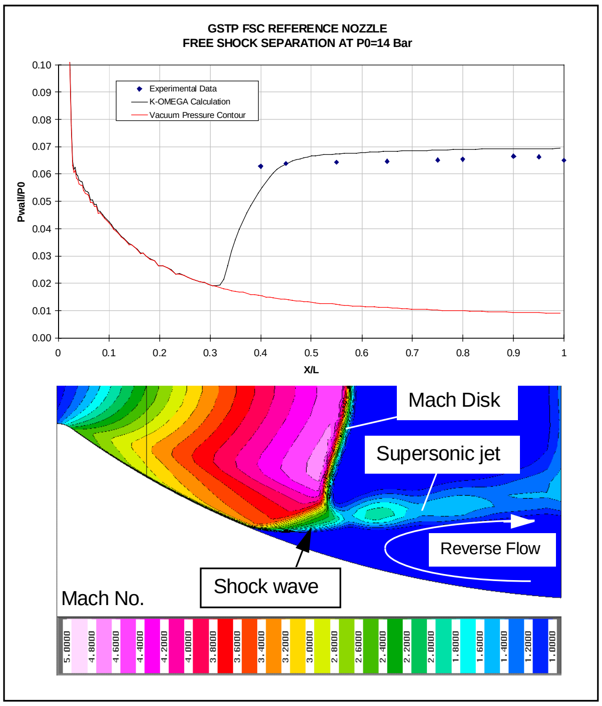

Figure 2 : Free shock separation in GSTP nozzle, CFD simulations compared with test results.

Two significant side-load peaks were identified both during the start-up and the throttle down sequence for all the different spring set-ups. The analysis shows that the low thrust level side-load peak is due to a transition between two radically different overall flow topologies, from free shock separation to restricted shock separation during start-up and the reversed order during shutdown, and a related flow hysteresis effect.

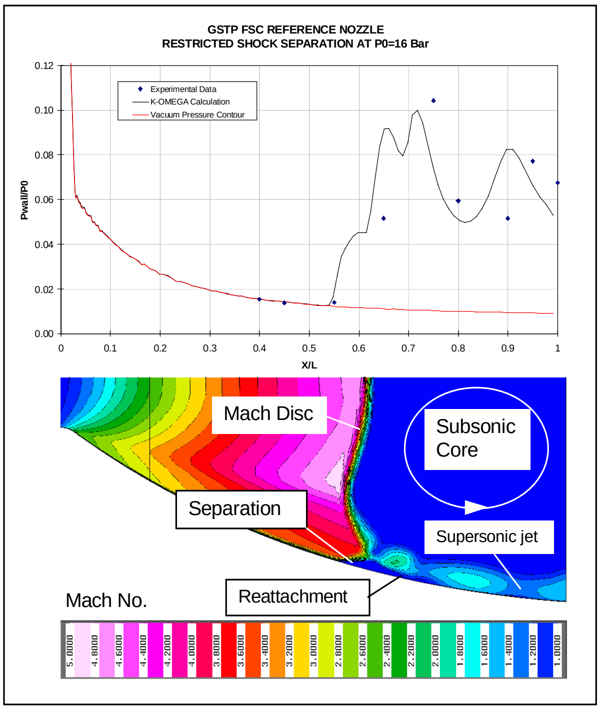

Figure 3 : Restricted shock separation in GSTP nozzle, CFD simulations compared with test results.

The high thrust level peak is connected to an end separation phenomenon. No significant influence of the spring stiffness could be seen on the side-load level for the low thrust level peak. For the high thrust level peak the side-load levels decreased with decreased spring stiffness but the trend is suddenly interrupted by the weakest spring system which experience the highest side-loads. With aeroelastic theory it is shown that the weakest spring system is aeroelastically unstable whereas the aeroelastic coupling is considered weak for the other spring systems, explaining the obtained features, see the chapter about aero-elastic analysis.

The observed side-load features in the sub-scale test show good agreement with available full-scale test experience.

After the GSTP was finished, a new phase was started with further investigations. The focus was now less on aero-elasticity and more on aerodynamic loads.

Logic for a continued program

The FSC program was now continued with more sub-scale testing. The logic was to investigate the most interesting phenomena that had been identified before:

- The influence of the degrees of freedom for the nozzle movement at the throat. The GSTP tests were done with hinging in only one axis.
- The importance of extending the nozzle contour.
- The adaptation of the nozzle contour to have similarity in internal flow field with Vulcain NE.
- The application of a three-dimensional FSC device
- The investigation of a discontinuity in the angle, a dual-bell contour.

Two-directional cardan tests

In order to demonstrate the importance of the degrees of freedom, the hardware used in the GSTP campaign was equipped with a cardan. This made it possible to have movements in both perpendicular directions at the throat. The arrangement is shown in the picture below:

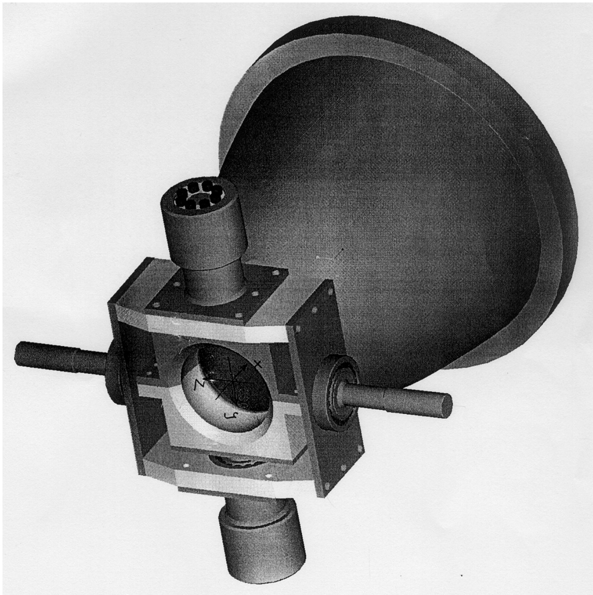

Figure 4: GSTP nozzle equipped with cardan.

The cardan made it possible to measure the side load torques in both directions. There was thus no loss of information, as it had been in the GSTP testing where only one direction was possible. In theory, the amplitude in an infinite series would be $2^{0.5}$ higher than for a one-directional side load. In the tests, the amplification varied between 1.2 and 1.9 : It was clear that the loads had random direction and that no direction was preferred. The conclusion was to use the cardan for all subsequent testing.

Extended contour tests

The next campaign was dedicated to investigating the same h/w with an applied extension. The nozzle length was increased with approximately 25 %. The extension was made in such a way that the pressure gradient was relatively high in the extension.

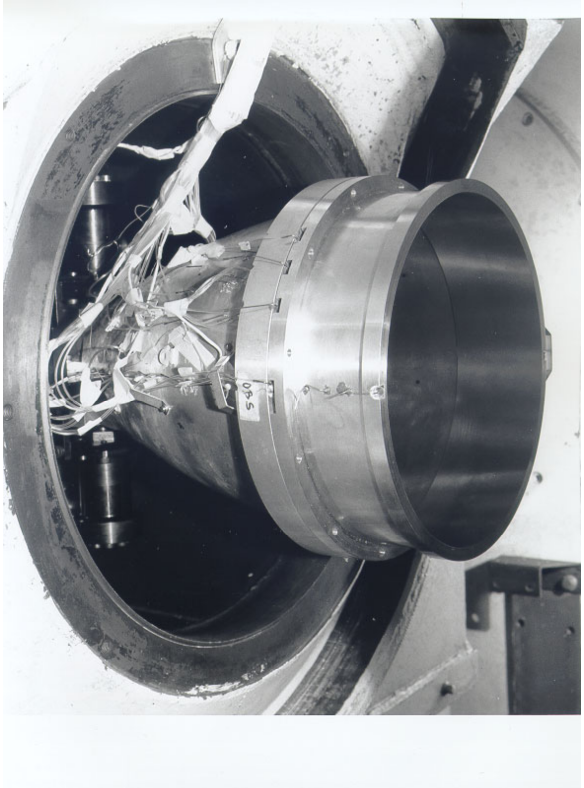

Figure 5: GSTP nozzle with extension in rig.

The chief objective was to study the impact on the end-effect side load peak. A small number of tests were carried out but the conclusion was very clear: The actual end-effect in the extension was almost extinguished due to the high pressure gradient.

New reference tests

The GSTP nozzle was designed with the geometrical definition of the Vulcain NE as a model. However, a more refined analysis was now employed in order to create a new reference nozzle. The idea was here not only to duplicate the nozzle wall geometry and pressure profile, but also to imitate the internal flow-field.

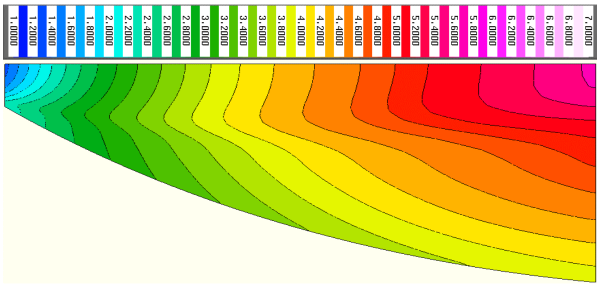

Figure 6 : Vulcain inner Mach number contours

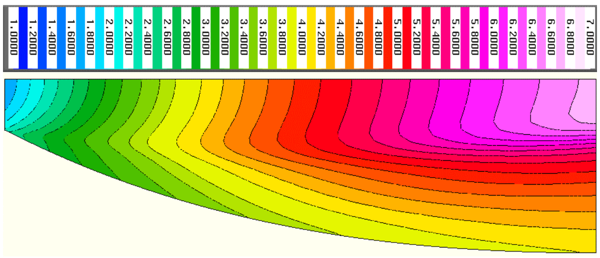

Figure 7 : V2+ sub-scale reference inner Mach number contours

As the chemistry is completely different, hydrogen / oxygen vs. air, it is impossible to get identical flow patterns. The contour was however made to have the same pressure profiles and the internal shock as close as possible to the Vulcain. The nozzle length was also increased to about 520 mm. The side load behaviour in the tests was close to the Vulcain case.

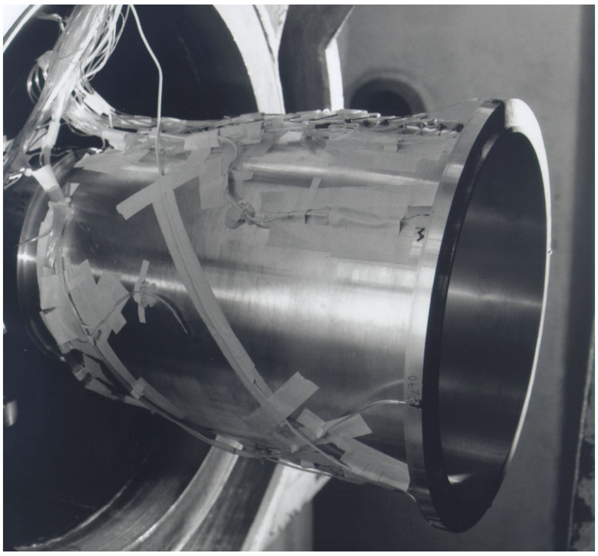

Figure 8 : Sub-scale Reference nozzle installed in rig

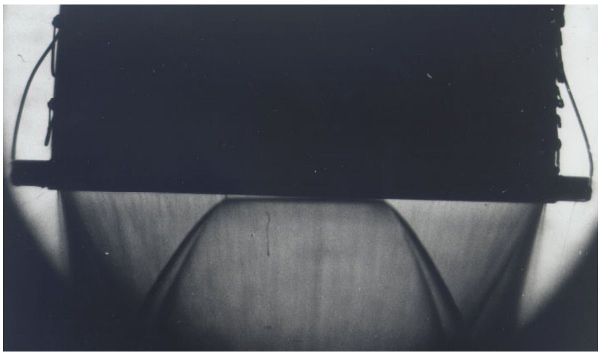

Figure 9: Schlieren picture: Reference of nozzle exit at full-flowing conditions

Polygon nozzle

The Polygon nozzle is a patented Volvo invention. The aim of the Polygon nozzle is to have a design with a side load reduction relative to a normal axi-symmetric nozzle. The shape is three-dimensional, see the figure below. The number of sides is envisaged to be 7-11. There is only a very small performance loss due to the asymmetry. The polygonisation can be done in several ways, depending on for which axial positions the effect is desired. Of high interest is also the transition from the circular to the polygon cross-section.

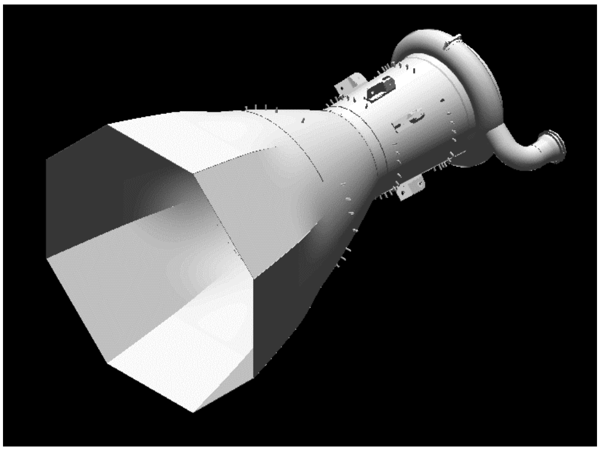

Figure 10 : Polygon nozzle, example on Viking-engine

There are three different side load reduction mechanisms that can be acting, depending on the exact design and the application.

- Stochastic circumferential flow pattern disruption. The polygon corners will act as a kind of structure-breaker leading to splitting of the separation flow pattern in circumferential direction. If the correlation in circumferential direction is indeed important for this part of the side load, it seems probable that asymmetry can give a reduction.
- Pressure difference and instability length being out of phase. When studying the resulting pressure field in the circumferential direction, it is seen that there is a phase difference between the pressure difference between attached and separated flow and the separation front instability length. This will lead to an aerodynamic side load decrease if a Schmucker-type model /5/ approach is used.
- Uneven separation leading to aero-elastic stabilisation. The aero-elastic model, such as described in /2/ was used for estimating the side load reduction of the polygon concept as a possible FSC concept. The fundamental reason for the side load reduction was the spreading-out of the separation line. When it reaches the exit, there is a smoother transition as only part of the separation line lies inside the nozzle at one time. This yields aero-elastic stability. This effect will depend very much on the design of the polygonisation in order to be efficient. The structure of the polygon can also have a stabilising effect in itself.

In the GSTP program, a second campaign was done in 1997 with polygon inserts. There were eight inserts put inside the GSTP nozzle exit to achieve asymmetric pressure distribution. These were attached at the exit, to reduce the side load stemming from the end-effect. Although the number of tests with comparable stiffness was not high, three, an average side load decrease of about 20% was recorded. The figure below shows that the pressure became highly three-dimensional in the tests.

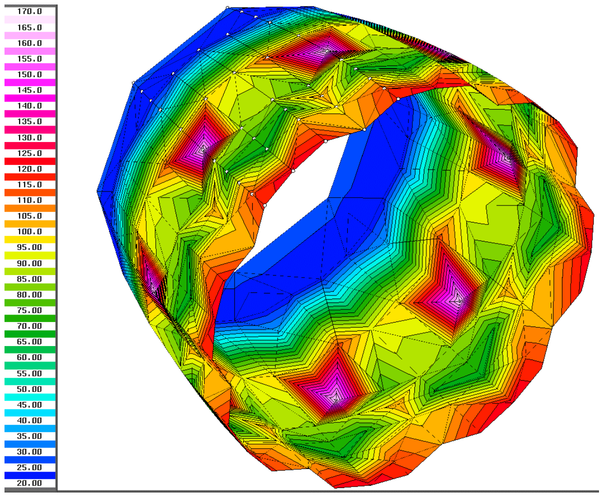

Figure 11 : Measured wall pressure distribution in GSTP nozzle with polygon inserts.

Polygon nozzle tests

Based on the experience from the GSTP activities in 1997 and 1998, a continued testing was carried out with a Polygon nozzle at FFA in late 1998. In order to have a complete comparability, the Polygon nozzle had an identical base-line contour as the Reference. The nozzle was made as an octagon with the polygonisation starting at the predicted position for the separation pattern transition.

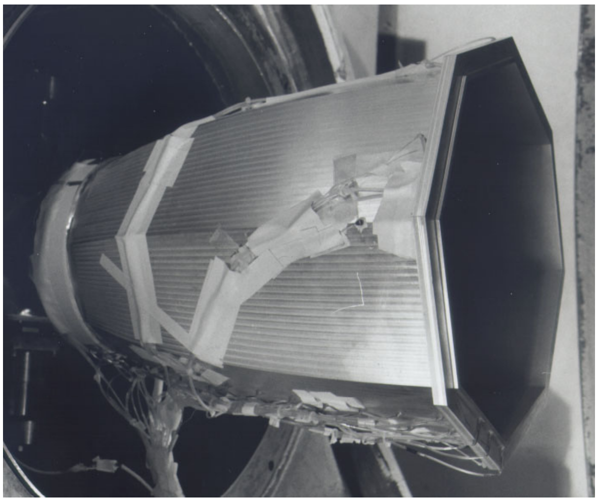

Figure 12 : Sub-scale Polygon nozzle installed in rig

The nozzle was run in 12 tests with good results. Extensive pressure measurements made a three-dimensional pressure mapping possible. The corners can be compared with the facets, defined as the point on each side with the smallest radius. In-between there is a mean point, in this case a 11.25 degrees. The mean point corresponds to the contour of the Reference axi-symmetric nozzle. Below is a plot of the pressures:

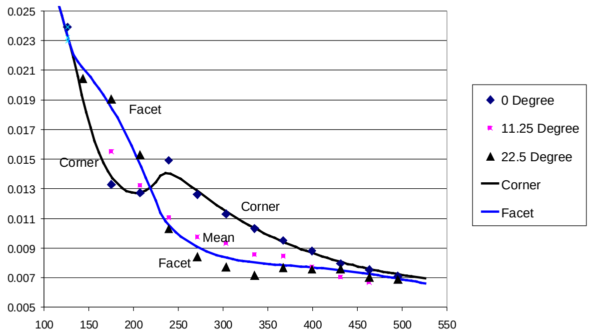

Figure 13 : Pressure measurements (bar) vs. axial coordinate (mm) compared with Navier-Stokes predictions for Polygon nozzle, full-flowing

The measured values are noted with squares, diamonds or triangles, whereas the CFD predictions are drawn as simple lines. As can be seen, the 3D-Navier Stokes predictions were very accurate. After the polygonisation has started the pressure drops rapidly in the corner, due to the larger radius. After a relatively short axial distance, the three-dimensional effect start to act however. This means that there is a flow towards the corners, and the pressure in the corner is increased. This leads to the pressure being lower on the facet than in the corner after some distance. Towards the exit, the pressures are balanced, and there is no effect from the polygon. Another illustration of the 3D-flow is shown below:

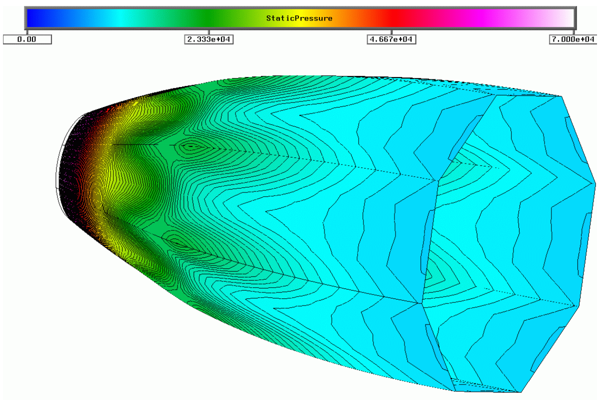

Figure 14 : CFD simulation of 3D wall pressure on Polygon nozzle

This simulation can be compared with the measured pressure distribution shown below. The flow features are very well predicted by the 3D Navier-Stokes simulation.

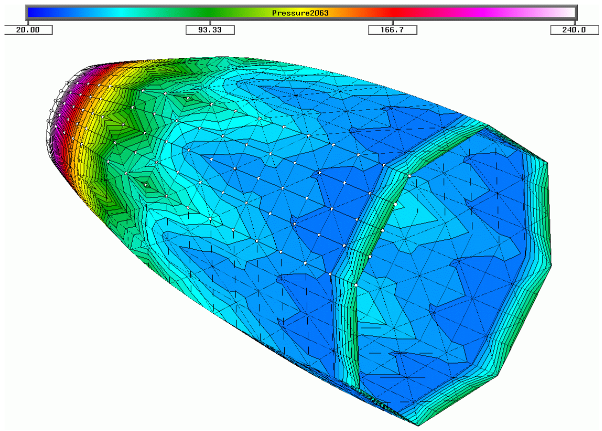

Figure 15 : Visualisation of measured wall pressures on Polygon nozzle

In order to get a feeling for the three-dimensional flow, it is also interesting to study the complex shock pattern at the exit:

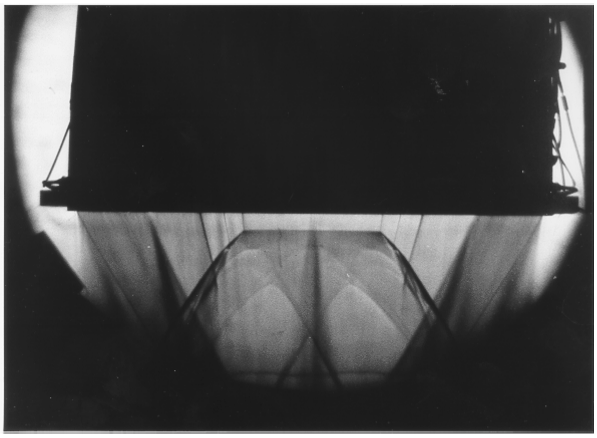

Figure 16 : Schlieren picture: Polygon nozzle exit at full-flowing conditions

The objective of the design was to have a side load reduction of the first side load peak, stemming from the transition between free-and restricted-shock separation. This is the critical side load for Vulcain-type nozzles. The goal was achieved conclusively after 10 tests, as both the mean, the median and the maximum side load was reduced with around 30%. This is the first actual side load reduction demonstration with an FSC concept in a rig test.

Dual-Bell nozzle tests

Another very interesting FSC concept is the Dual-Bell. This is a well-known nozzle type since several decades.. Actual testing with separation has however been very limited. In the testing described in /7/, for instance, separation and start transients are described, but no side load measurements were mentioned. The contour of the Volvo sub-scale Dual-Bell is equal to the reference in the first upstream section. This constitutes the first bell. The dual-bell contour used for this nozzle is then designed according to the principle of positive pressure-gradient in the second bell. This means that the separation front in theory will travel directly from the start of the second bell out to the exit during the start transient. Below is shown a CFD-simulation of the nozzle flow

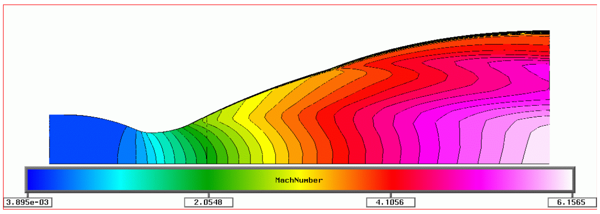

Figure 17 : Internal Mach number in Dual-Bell nozzle.

A shock emanating from the start of the second bell can be noted, although it is quite weak. The angle deviation from the first to the second bell is only about 5 deg. This was enough to assure a considerable pressure drop.

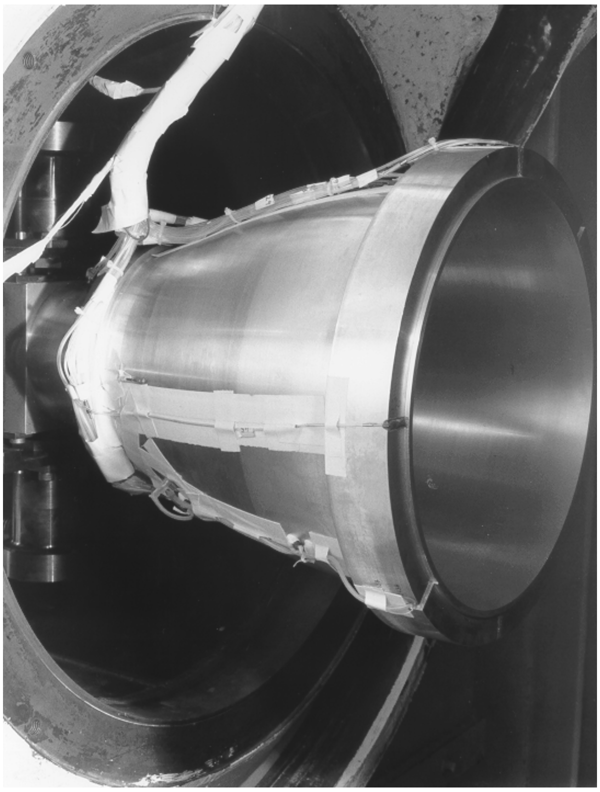

Figure 18 : Dual-Bell nozzle installed in rig (second bell starts at beginning of darker section)

A test campaign of 12 tests were run at FFA with the Dual-Bell nozzle in April 1999. The dual-bell operation functioned according to prediction as can be seen in the figure below. The positive pressure-gradient on the second bell has been achieved.

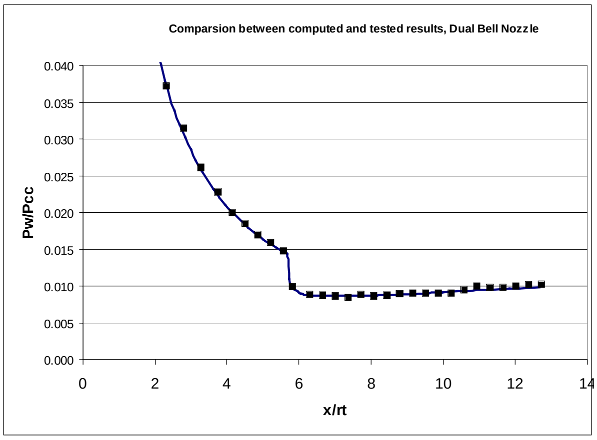

Figure 19 : Analytical and measured pressure profiles, dual-bell nozzle.

The flow pattern is very interesting. In the figure below, the complex pattern downstream of the nozzle during full-flowing operation can be seen.

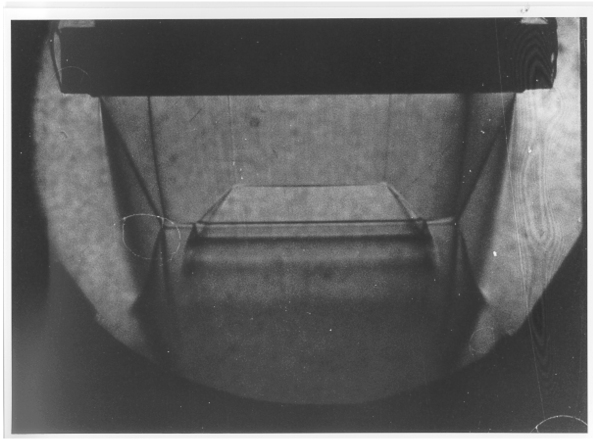

Figure 20 : Schlieren picture at exit for full-flowing conditions, dual-bell nozzle.

The transition during start-up from the first to the second bell was very rapid. The jump was made in about 5% of the total transient time. The end-effect was almost completely extinguished at the start-up. The side loads corresponding to the separation pattern at the start-up were about 30 % smaller than the separation pattern transition side loads for the Reference nozzle. The end-effect side load at the shut-down stands for the highest torque level. The restricted shock separation is only stable for the shut-down.

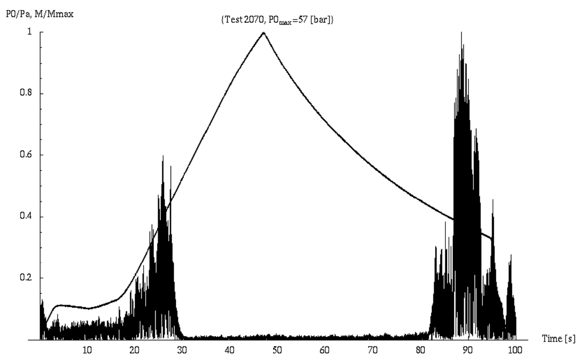

Figure 21 : Side load torques measured in test with Dual-Bell nozzle

The testing performed so far is summarised in the table below:

Campaign	Performed
GSTP 1 /1/	1997
GSTP / Polygon inserts /1/	1997
VolvoS1 / GSTP w. cardan	1998
VolvoS2 / GSTP w. extension.	1998
VolvoS3 / V2+ Ref.	1998
VolvoS4 / V2+ Polygon	1998
VolvoS5 / V2+ Dual-Bell	1999

Table 1 : Sub-scale testing in FSC program

Analytical model, aero-elastic coupling

The study of the closed-loop effects of jet separation has not been attacked vigorously due to the complexities involved in generating accurate asymmetric dynamic models of the nozzle-engine support system, the jet boundary layer separation, and interaction at the boundary of the two subsystems. A technique for handling these difficult coupling problems has been developed by Pekkari, /2/. The model is very useful for checking whether aero-elastic instability is present in the case of separated nozzle flow coupled to bending or pendulum modes. By simplifying the relations described in /2/ the following relation can be derived for the aero-elastic coupling :

$$\left(\frac{\Omega}{\omega}\right)^2 = 1 - \left.\frac{(P_a - P_{sep})\rho_\infty \cdot u_\infty^2}{-\left(\frac{\partial P_\infty}{\partial x}\right)\sqrt{M_\infty^2 - 1}} \cdot \frac{r\pi(x \cdot Cos\tau + rSin\tau)}{K_m m L^2 \omega^2}\right]_{x_{sep0}}$$

There is stability if the second term of the right hand side in the equation is lower than unity. If the contrary is the case, the equation will have a non-zero imaginary part in the solution, and there will be instability. The theory was applied to the GSTP nozzle case. The different spring cases were compared for the bending mode. The only spring that was unstable in the model was the “super-weak” one. This was also found to correspond to the actual behaviour in the tests.

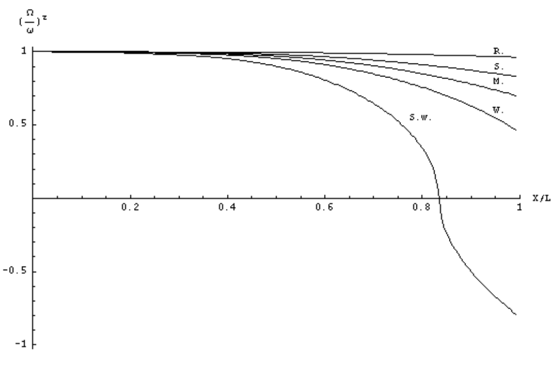

Figure 22 : Analytical aeroelastic stability for the different spring setups, S.W. =Super Weak, W. = Weak, M.=Medium, S.=Stiff and R.=Rigid spring respectively

Analytical model, separation transition

In parallel to the experimental investigations, an analytical model to predict separation transition has been created. The eventual objective is to create at Volvo an engineering model that can be used for accurate side load predictions. So far, in Europe, the Schmucker model /5/ has been used for predictions for sea-level nozzles. This model has however its shortcomings, as it does not take into account all the phenomena involved, as the separation transition. In the frame of the FSCD group, Volvo and DLR have been working with analytical models for predictions of side load transitions based on internal flow parameters.

The first aim of the Volvo model was to correctly predict when the transition from Free Shock Separation to Restricted Shock Separation takes place. It is important to know for which chamber pressure this side load peak will occur. This is interesting as this value tends to vary quite little, as opposed to the side load magnitude which has a considerable scatter.

Investigation made with sophisticated CFD tools and various turbulence models applied to Navier-Stokes calculations showed that it was difficult to find a general model that would give good agreement for many different cases. The present model is therefore based on inviscid 2D flow field calculations. By studying the internal flow field and the momentum balance, it has been possible to set an exact criterion for when the transition will take place.

The first step has been to make refined predictions of separation pressure, both for free- and restricted shock separation. These separation criteria come from both experimental and analytical work /1/. It is well known that the separation pressure for the restricted shock separation at a given chamber pressure will be below the one for free shock separation. This means that the restricted shock separation front will be located further downstream. The separation lines for the free- and restricted shock separation can then be plotted as chamber pressure versus axial position to follow them travelling downstream. By including the normal-shock position for the nozzle centreline, the occurrence of transition can be simulated when comparing the positions. Although this model is quite rough and in an early stage of development, it can still give a good measure of the momentum balance. The chamber pressure for transition from free to restricted shock separation is assumed to be proportional to the chamber pressure when the restricted shock separation is at the same position as the normal shock on the centreline.

$Pcc_{,transition} = K\ Pcc_{,(x,rss=x,ns)}$

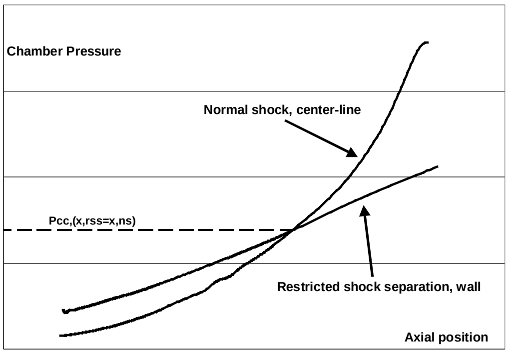

Figure 23 : Principle, transition model

After the transition has taken place, the back-pressure starts to increase again for the separation. This means that the separation position starts to move again towards the free shock separation position. When it approaches the same curve as for free shock separation , there is an actual transition again to free shock, and the second side load peak occurs, the end-effect.

The model can also take injected secondary film into account, as is used in the ANE demonstrator or Vulcain 2 NE. The Volvo film-cooling model /3 / is here used to calculate the separation characteristics which are influenced by the film-injection. The first version of this model has been tested for a number of cases with very good results:

Case	Pcc for transition: predicted / actual
Vulcain NE	0.88
ANE Demo	0.87
GSTP	0.97
V2+ Ref.	0.90
V2+ Polygon	1.00
V2+ Dual-Bell	0.92
J2s sub-scale	0.90
SSME	0.94
LEA Subscale parabolic contour /6/	1.00

Table 2 : Volvo-model for predicting at which Pcc there is an FSS to RSS transition.

One interesting feature is that the model also correctly predicts the absence of transition to Restricted Shock Separation. This will be the case when an Ideal Contour is used, as with, for instance, the Viking or the Russian RD-0120 nozzle.

Presently, the model is being extended to also be able to predict the magnitude of the side loads, taking also the mechanical characteristics into account.

Future plans

The studies of FSC and side-load reductions will continue with the following goals:

- Demonstration of further side load reduction experimentally
- Continued development of engineering side load model
- Studies of the physical nature of different types of separation and the origin of the side loads
- Application of theories to design of sea-level nozzles

Conclusions

The side loads are among the dimensioning loads for the sea-level rocket engine nozzles. To understand these loads is a central theme when designing optimised nozzles. The investigations at Volvo of side loads have lead to a number of interesting results:

- One side load peak for thrust-optimised nozzles stems from the transition from free to restricted shock separation
- This side load can be reduced by Flow Separation Control or side-load reduction devices. Two types, Polygon and Dual-bell have been tested with positive results.
- There are impacts on the side loads from the degrees of freedom, the pressure gradients and the stiffness of the nozzle.
- There can be both aerodynamic and aero-elastic drivers for the side loads
- The occurrence of the separation transition can be predicted by analytical means

Acknowledgements

The authors firstly wish to thank the Swedish National Space Board for their support which has made the program possible. We also like to thank the personnel at FFA that has worked with the test programs, in particular Lars Torngren and Johan Agrell. Further, we would like to thank ESA and CNES and our other partners in Europe; DLR, Dasa ONERA and SEP for the fruitful technical discussions we have had. For the invention of the Polygon nozzle concept, this was achieved largely due to the work of Dr Lars-Olof Pekkari and Jan Häggander at Volvo. Last, but not least, we would like to thank the rest of the Nozzle team at Volvo in our continued efforts to design optimum nozzles.

References

/1/ A Sub-scale Test Program on Investigation of Flow Separation and Side Loads in Rocket Nozzles
J.Mattsson et.al, ESA-SP-426, Dec 1998

/2/ Aeroelastic Analysis of Side Loads in Supersonic Nozzles with Separated Flow
L.O.Pekkari AIAA 94-3377

/3/ Technology for the Film-Cooled Nozzle of the Vulcain 2 Engine
M.Bigert et al. IAF-98-S.3.05

/4/ Nozzle and Turbine Impact on Launcher Performance
M Bigert, AIAA 94-3380

/5/ Status of Separation Prediction in Liquid Propellant Rocket Nozzles
R.H.Schmucker NASA TM X-68490

/6/ Measurements of side loads in an overexpanded parabolic nozzle,
S.Girard, T.Alziary de Roquefort, Laboratoires d'Etudes Aérodynamiques, Université de Poitiers, UMR CNRS 6609.

/7/ Dual-Bell Altitude Compensating Nozzles
M.Horn,S.Fischer Rocketdyne, NASA 94-23057

/8/ Status of Flow Separation Prediction in Rocket Nozzles
M.Frey, G.Hagemann, AIAA 98-3619

Paper 3

AIAA 99–2583

ASSESSMENT OF TURBULENCE MODELS IN OVEREXPANDED ROCKET NOZZLE FLOW SIMULATIONS

Jan Östlund
Volvo Aero Corporation, SE-46181, Trollhättan, Sweden
Mattias Jaran
The Aeronautical Research Institute of Sweden, Box 11021, SE-16111 Bromma, Sweden

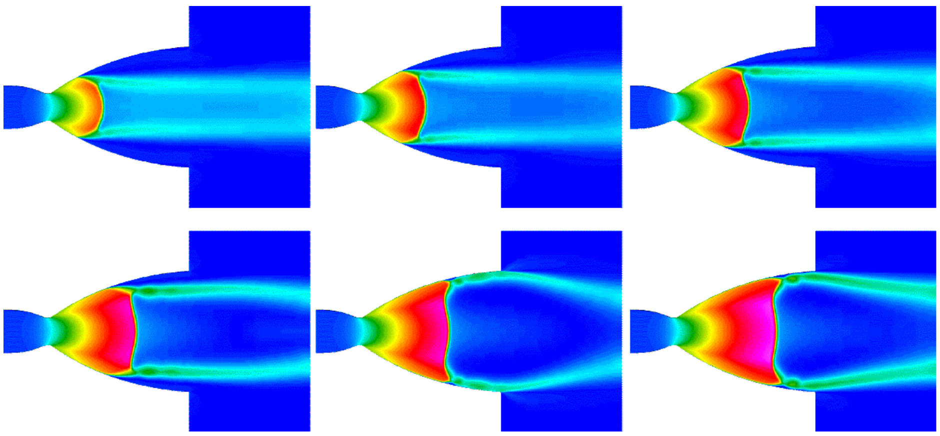

35th AIAA/ASME/SAE/ASEE Joint Propulsion Conference & Exhibit
June 20-23, 1999/Los Angeles, CA

ASSESSMENT OF TURBULENCE MODELS IN OVEREXPANDED ROCKET NOZZLE FLOW SIMULATIONS

Jan Östlund*
Volvo Aero Corporation, SE-46181, Trollhättan, Sweden

Mattias Jaran†
The Aeronautical Research Institute of Sweden,Box 11021, SE-16111 Bromma, Sweden

A report is given on the initial validation of Navier-Stokes predictions of turbulent, separated flow in an overexpanded bell nozzle. The CFD predictions are compared to sub-scale wind tunnel test data using a scaled Vulcain nozzle. The test chamber pressure has been varied to simulate the shock hysteresis region of start-up and shut-down. The suitable choice of turbulence model, boundary conditions and CFD solution procedure is investigated by comparison to measured wall pressure data. The details of the turbulent fields of the four investigated turbulence models are compared, as well as its effect on the boundary layers, shocks and separation locations.

Nomenclature

M	Mach number
P	Pressure, Pa
T	Temperature, K
x, y, z	Cartesian axes, m
u, v, w	Velocity in x,y,z, m/s
V	Velocity m/s
k	Turbulent kinetic energy, m^2/s^2
ρ	Density, kg/m^3
ω	Specific dissipation rate, 1/s
μ_t	Eddy-viscosity, kg/ms^3
P_k	Production of turb. kin. en.
D_k	Dissipation of turb. kin. en.
EVM	Eddy viscosity model
SST	Menter shear stress transport model
BSL	Menter base line model
KWL	Wilcox k-ω model with limiter
KWS	Standard Wilcox k-ω model
FSS	Free shock separation
RSS	Restricted shock separation

Subscripts

w	Wall
amb	Ambient condition
s	Stagnation condition

Introduction

Background

SOME rocket engines suffer severe dynamic loads during operation at chamber pressures below the design pressure. This operational condition typically occurs during the start up and throttle down process of the rocket motor at sea level. These loads can sometimes be of such a magnitude that they present life limiting constraints on thrust chamber components as well as on the thrust vector control system. The source of these loads is generally attributed to the in stationary nature of the partially detached and partially attached flow that occurs during operation of the thrust chamber at overexpanded conditions.

The most well known of these dynamic loads that have received attention in the literature is the so called side load.[1] [2] Side loads have been observed during start up of overexpanded sea level liquid propellant rocket engines as well as during ignition and the staging of a multi stage solid propellant rockets.[3] [45] Due to the severe complications experienced with high levels of side loads, it is one of the most important features in sea level nozzle design. It has e.g. been taken into account for the contour definition for the Vulcain 2 nozzle extension.[6]

The traditional design approach for bell type nozzles is to design the nozzle contour and area ratio such that attached flow and low levels of side-loads are guaranteed at nominal operation at high ambient pressure, sea level conditions. Further, the structure is designed robust enough to withstand the side loads during the throttling up and down process. The reduced performance under vacuum ambient condition and the corresponding weight penalty with a robust design, is accepted with this design approach. Increasing demands for improved launcher performance, however, push the development of new concepts. One possible solution is to adapt the nozzle contour during flight to the changes of ambient and chamber pressure. At-

*Aero Design Engineer, Space Propulsion Division. Jan Östlund changed his name from Mattsson in Jan 1999.

†Research Scientist, Computational Aerodynamics Department.

tempts in this direction, however, have so far not been successful due to the weight and mechanical complexities of such devices. By introducing so called Flow Separation Control Devices (FSCD), high area ratio nozzles can be operated at separated condition at sea level without severe loads, and an improved overall performance is obtained. The feasibility of such devices is under demonstration. The main reason why such devices do not yet exist in full scale is that several basic questions regarding the nature of separation phenomena and the corresponding side loads remain to be answered.

Within the Flow Separation Control (FSC) program at Volvo Aero Corporation (VAC) the flow separation phenomenon in sea level rocket nozzles with corresponding side load features have been investigated. In the course of the work, detailed aerodynamic and aeroelastic sub scale testing have been performed in the modified hyper sonic wind tunnel HYP500 at the Aeronautical Research Institute of Sweden (FFA), under a contract with the European Space Agency (ESA) and the Swedish National Space Board (SNSB).[7,8] Steady state axisymmetric CFD analyses of the sub scale tests were performed in parallel with the experimental investigations. The analysis revealed a significant change of flow separation pattern at specific pressure ratios in close relation to the points where unsteady side loads were found in the experiments. The change in flow pattern in the calculations showed considerable hysteresis with regard to the pressure at which it occurred, and when increasing or decreasing the driving pressure, see illustrating figure (1). This was in accordance with the experimental findings.

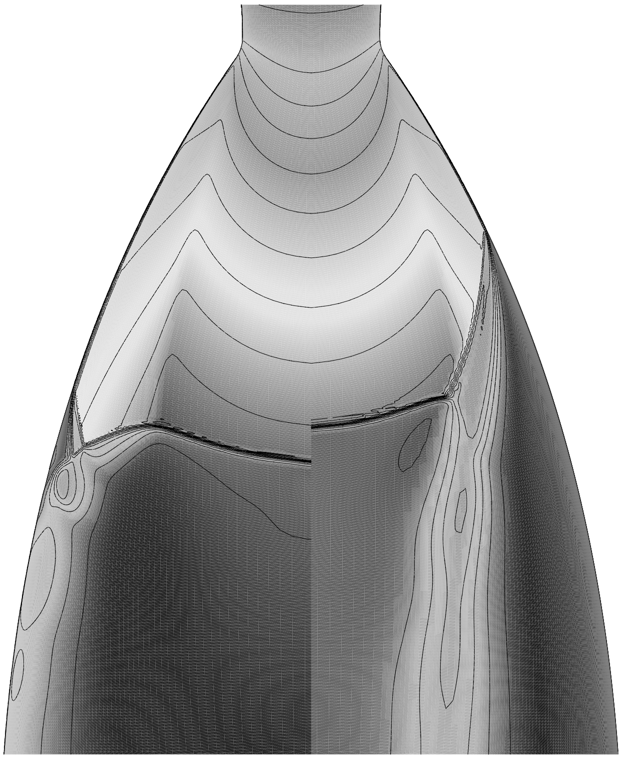

Fig. 1 Illustration of free shock separation (right) and restricted shock separation (left) in the hysteresis region, at a pressure ratio (P_s/P_{amb}) of twelve.

Separated Nozzle Flow Physics

The flow in an overexpanded nozzle is of mixed supersonic/subsonic type with shocks interacting with the nozzle wall boundary layers and a nearly inviscid core flow. The internal shock structures and shock wave/boundary layer interactions produce strong adverse pressure gradients which may give rise to separated, recirculating flow. As reported by Mattsson[7] the two main flow field types found in the present over expanded nozzle feature separation from the wall without reattachment at lower driving pressures, labeled free shock separation (FSS), or with reattachment at higher driving pressures, labeled restricted shock separation (RSS). The solution with free shock separation remains to higher driving pressures during the start up phase and the restricted shock separation solution tend to remain when the driving pressure is lowered. This accounts for the hysteresis effect found in the experiments as well as in the computations, see figure (1).

When starting the nozzle and increasing the chamber pressure (P_s), at first the flow is separated in the free shock separation mode. In the free shock separation regime the flow separates from the wall and the wall pressure rises to a plateau pressure, close to the ambient pressure. The source of this rise is due to the oblique shock originating from the separation point. Downstream the steep pressure gradient region, in the open recirculating zone, the wall pressure increases slowly to almost ambient pressure. As P_s is increased, the hysteresis region is entered, and the flow stays in the free shock separation mode. At the limit were the hysteresis region is exited, the separation pattern changes to restricted shock separation and a closed recirculation zone is formed. The plateau pressure in this closed recirculation bubble is lower than the plateau pressure in the open recirculating zone in the free shock separation case, and a jump of the separation point in the downstream direction occurs. Due to the reattachment of the flow, the wall pressure features an oscillating behavior with values above the ambient pressure. This irregular behavior is caused by the expansion and compression waves, which interacts with the supersonic jet boundaries to match the ambient air. The sudden change of the separation pattern from free to restricted shock separation is connected to significant side loads for the nozzle.

The restricted separation mode itself is stable until the reattachment point reaches the nozzle exit, where a second peak in side load has been found, due to an unsteady phenomena named the end effect. The end effect takes place as the recirculating zone open up and the plateau pressure behind the separation shock is suddenly increased, as ambient air is sucked in to the nozzle. This pressure increase forces the separation point to move upstream with a subsequent closing of the recirculating zone, again. This procedure repeats its self until the triple point between the separation shock and the internal oblique shock has been transported out of the nozzle.

When decreasing P_s, the same phenomena can be observed but in reversed order. However, the flow stays in restricted separation mode until the lower limit of the hysteresis region is encountered where the transition from restricted to free shock separation takes place.

This entire phenomena have been found in both full scale and cold flow sub scale rocket nozzles of Rao-type.[7] The existence of two different separation topologies is thus a consequence of the chosen contouring method, and not the nozzle size or the working gas.

In the present investigations, an emphasis has been placed on the role of the turbulence modeling in simulating separated nozzle flows as described above. An in depth investigation has been performed to assess the influence of inflow turbulence levels, in the free stream and in the shock regions. Also, a comparison to experimental data for three different driving pressures, in and outside the hysteresis region, is presented.

Numerical Method

The Solver

The simulations have been performed using the EURANUS[9] code developed under contract by the European Space Agency, by FFA, VUB in Brussels and other cooperation partners. EURANUS is a finite volume code for the Reynolds-averaged Navier-Stokes equations. At present the code incorporates a number of turbulence models. Emphasis has been put on the improvement and validation of the code for computing flows including turbulent separation. A number of different schemes may be selected for the spatial discretization. For the present calculations second order central differences were used for the main equations and a second order upwind scheme for the turbulent equations. Solutions to the steady state problems are usually obtained with Runge-Kutta time stepping, with local time stepping, multigrid and residual implicit smoothing used to accelerate convergence.

Turbulence Modeling

Different turbulence models have been tested, all Eddy Viscosity Models (EVM) based on the Boussinesq hypothesis, which is used to close the Reynolds averaged Navier-Stokes equations. Eddy viscosity models are the industrial standard models, today. Many models have been proposed and a few have become widely accepted. We have focussed on the k-ω class of models because of their known ability to predict pressure gradient flows and the success of some of its variants, notably the Menter SST model, to predict flow separation in other cases.

Since the purpose was to test different models, with different turbulence modeling, the following models were selected. As a reference, and for being very well known, the Wilcox[10] k-ω model. The k-ω model was also used together with a limiter on the production for the turbulent kinetic energy, see equation (2) to try to assess the influence of that type of limiter, see figure (2) for an illustration. Furthermore, two models developed by Menter[11] were added. His BSL and SST models differ by the boundary layer treatment. The SST model includes a limiter on the ratio of production to dissipation (P_k/D_k) in the boundary layer. This makes the boundary layer more likely to separate, since it can take less strain. Both models include the so called cross diffusion term that should make the boundary layer insensitive to the free stream ω. Both models also include a limiter on the production of the turbulent kinetic energy in the free stream.

Turbulent Production Limiter

Different codes have different limiters on the production of turbulent kinetic energy. One common type of limiter, that is also specified in the two Menter models,[11] is to limit the production (P_k) by the dissipation (D_k). Menter's models have

$$P_k = \min(P_k, 20 \cdot D_k). \tag{1}$$

As discussed above, the Wilcox k-ω model has been used in these simulations together with a limiter on P_k. The limiter was proposed by Wallin,[12] and worked well for this type of problem.

$P_k = \min(P^{EVM}, P^{LIM})$, where

$$P^{LIM} = \rho K \sqrt{\frac{P^{EVM}}{\mu_t}}. \tag{2}$$

For the Wilcox k-ω model, this limiter is not active for $P^{EVM} < \epsilon/C_\mu$, which implies that the limit would not be active for $P_k/D_k < 10$, and hence not interfere with the prediction capability of the model in general.

Geometry

If the nozzle length,[6] from throat to exit is used as a scaling factor and set to unity, then the dimensions of the computational geometry is as follows. The length of the inlet channel is about 4, and the purpose of it is to isolate the nozzle from the inflow boundary condition. At the nozzle exit, the height of the expansion chamber is three times the height of the nozzle. The upper boundary of the expansion chamber has a thirty degree positive angle with the symmetry axis, this is so that an inflow boundary condition can be used with a small velocity in the x direction only. The expansion chamber length is at about 10 in the units defined above.

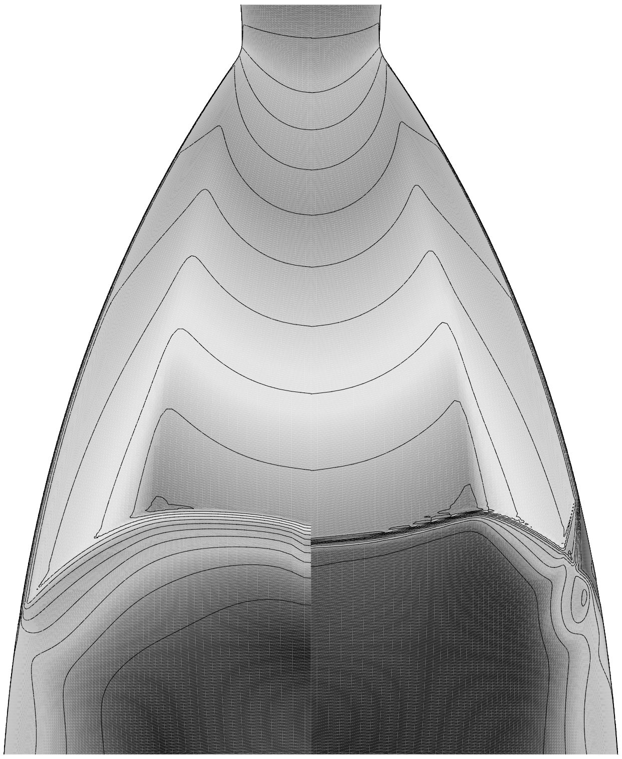

Fig. 2 Illustration of restricted shock separation, with (right) and without (left) turbulent production limiter, at a pressure ratio (P_s/P_{amb}) of 16.2.

Boundary Conditions

In this paper the atmospheric conditions were 290 K, and 0.10 MPa. The stagnation conditions in the nozzle were 500 K, and 0.60, 1.20, and 1.62 Mpa. The turbulence level at the inlet were varied as in table (1), and for the comparison to the experimental data, k=0.01, and ω=500, was selected. Air was used as the driving gas, as in the wind tunnel experiments, for all simulations.

The simulations are treated as axisymmetric, with a three degree opening angle. Symmetry boundary conditions are used at the symmetry planes. A singular polar line is used at the symmetry axis, which imposes the flow direction to be along the symmetry axis. Stagnation conditions are used at the nozzle inlet, where the direction of the flow is imposed and the turbulent quantities are not allowed to fluctuate. An adiabatic wall is used at the channel wall, leading to the nozzle inlet, where the nozzle wall also is treated as adiabatic. The nozzle wall thickness, at the nozzle exit, is modeled as an adiabatic wall with a wall thickness of about one fifth of the nozzle throat radius. The external inflow boundary condition is of the Riemann invariant type, with atmospheric conditions and about 50 m/s in inflow velocity. At the outflow, an extrapolation boundary condition is used. The reason for not using a lower inflow velocity is strictly practical from a numerical point of view. During the start up sequence, the flow could get reversed at the outlet, since an extrapolation boundary condition was used there. There should be no influence on the nozzle flow by this procedure, so the simulations are as if the nozzle was stationary.

Results & Discussion

Grid Convergence

Three grids were studied for the purpose of showing grid convergence. The grids are multigrid multiples of each other, and have the resolution 101·37, 201·73, and 401·145 in the nozzle. Outside the nozzle about the same amount of nodes are spent additionally.

The grids were designed so that even the coarsest grid would be able to resolve the relevant flow structure. Only very minor differences exist between the medium and fine grid solutions. Still, it turned out that a three level multigrid solution method on the fine grid used about the same computer time as a single grid method on the medium grid, where a three level multigrid method did not converge well.

Since no additional computer cost permitted runs at a finer grid level, it was decided to do so. Hence, all quantitative simulations have been performed on the fine grid with a three level multigrid method.

Sensitivity to Turbulent Inflow Conditions

A series of simulations were conducted to investigate the sensitivity to, and establish, reasonable turbulent inflow conditions. A test matrix was set up, and ran at free separation conditions with a pressure ratio (P_s/P_{amb}) of six.

Table 1 Test matrix to determine correct turbulent inflow conditions.

Std k-ω	Limited k-ω	Menter SST
k=0.01, ω=500	k=0.01, ω=500	k=0.01, ω=500
k=0.10, ω=500	k=0.10, ω=500	k=0.10, ω=500
k=1.00, ω=500	k=1.00, ω=500	k=1.00, ω=500

It was decided to check the inflow conditions at a station half way between the start of the converging section of the nozzle and the nozzle throat, on a grid line from the symmetry axis to the nozzle wall. At this location, a turbulent boundary layer has been established and the flow is accelerating towards the throat. Also, the nozzle inlet was extended far upstream, so that the nozzle was well isolated from the inflow boundary condition.

In general, the influence of the free stream turbulence level was small, for the pressure ratio investigated. No significant influence was found, except for the levels of μ_t in the free stream, see figure (7a). These are high due to the higher levels of turbulent kinetic energy, specified in table (1), which is shown in figure (7e).

Other global measures, such as the velocity profiles in figure (7d) or the turbulent variables in figures (7b - 7c) showed little or no scattering between cases. For example, the main difference in the peak turbulent kinetic energy (k) over all tested models and inflow conditions was about ten percent. The dissipation rate (ω) showed very little difference between cases as seen in figure (7c).

It has been reported[13] that the standard k-ω model suffers from an unphysical free stream sensitivity when it comes to ω. From the results in the present simulations, no significant influence is found physical or not, see figure (7c). Simply, in a complex flow like this, the downstream development of ω cannot be controlled by a realistic variation of the inflow boundary condition.

For the quantitative comparison to experimental data, the lowest values of the turbulent intensity were chosen, since they produce the most physically correct looking eddy viscosity distribution, see figure (7a).

Sensitivity to Shock Modeling

For the test cases in table (1), the modeling over the shock waves were investigated. The results were established by looking at the variation along the center line of the nozzle.

From figure (8c), it is seen that the turbulent kinetic energy grows dramatically over the shock for the standard Wilcox k-ω model, which has no turbulent production limiter. Behind the shock, a turbulent fluctuation $u' \sim \sqrt{k}$ is of the same order of magnitude as the main flow u velocity, which is unrealistic.

As a consequence, the eddy viscosity (μ_t) in figure (8b) also grow to high levels. The eddy viscosity stays at a high level in the nozzle, behind the shock. Outside the nozzle the levels of μ_t increase again. From figure (2) it is seen what happens inside the nozzle for the very high level of μ_t, present in the simulations with no production limiter. The shock is smeared out and the flow behind it has no real structure, since the μ_t levels do not drop, as mentioned.

Finally, it is seen in figure (8a), that the point of separation from the nozzle wall is influenced by the production limiter. The two models based on the Wilcox k-ω model, separate at different locations. The model with the limiter separates just upstream of the one without. For this driving pressure, the separation is of free shock separation type for all models, as it should be, and the difference most likely lies in the way the shock and the back pressure is resolved. For the restricted separation type, the flow field is different and it is more obvious from figure (2) why the separation is late.

The present results clearly show the importance of a limited production of turbulent kinetic energy over the shock. From a simple analysis[12] it can be shown that the turbulent production over a shock for an EVM is almost unlimited and grid dependent. As shown by the behavior of the models incorporating a limiter, a more realistic result is feasible. Also, a strong shock is just the place were a turbulent production limiter will have an influence, and hence the actual limit of the highest possible production makes a difference. The actual values of the limiters have not been investigated here, but obviously a limiter is needed to produce reasonable results.

Comparison to Experimental Data

A complete engine cycle has been simulated. Hence, the driving pressure was increased from a low starting level to the level where a full flowing nozzle is achieved. Then, the driving pressure was decreased as during a shut down. This ramping was made in small steps, and the solution was fully converged for each pressure level. Inflow turbulent conditions are specified as the lowest turbulence intensity in table (1), and the fine grid is used.

Results are shown for three different driving pressures in figures (3 - 6). In figures (4 - 5), the hysteresis phenomenon is shown with two different flow fields at one driving pressure. As the figures show, only the Menter SST model was able to capture the correct separation type during the pressure increase and decrease. Still, the pressure in the supersonic jet, downstream of the separation, show some difference compared to the experimental data, meaning that the model only give qualitatively correct results.

All of the other models fail to predict the free shock separation mode at Ps/P_{amb}=12. Ordering the models in a descending order, the BSL model performed second best, followed by the Wilcox k-ω model with the turbulent production limiter, and last the standard Wilcox k-ω model. The BSL model generally separates before the k-ω models, see figure (3), and therefore is closer to the experiments. The reason for the earlier separation is not clear at the present. The limited k-ω model performs reasonable to, in the sense that it can reproduce the details of the flow, to some degree. The standard k-ω model should not be used in simulations with shocks.

In general, the free and restricted shock separation modes are set up by the respective location of the point of separation and the location of the main normal shock.[8] The influences on the location of the main, almost normal, shock are the surrounding pressure, and if any, the pressure in the closed recirculation area behind the shock. These pressure levels are generally modeled almost the same by different models. What does differ more, is the location of the point of separation. As have been pointed out in this paper, relatively small changes to an existing model can improve the ability to predict separation. Improved separation prediction has also proven effective for predicting the correct separation type in the present nozzle.

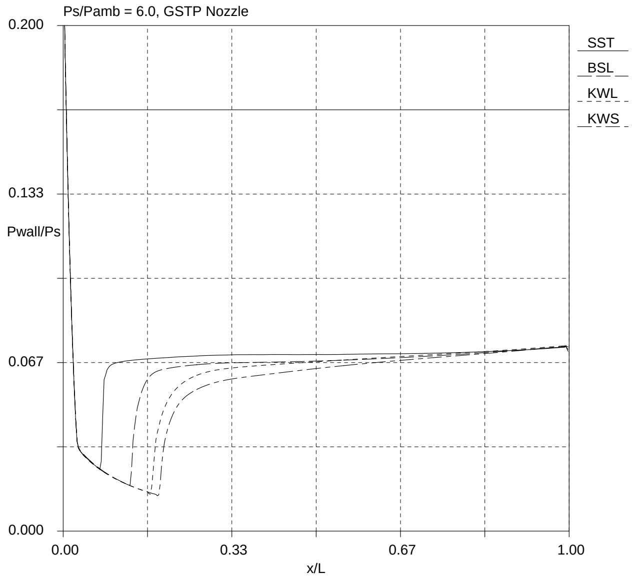

Fig. 3 Free shock separation for a pressure ratio (P_s/P_{amb}) of 6.

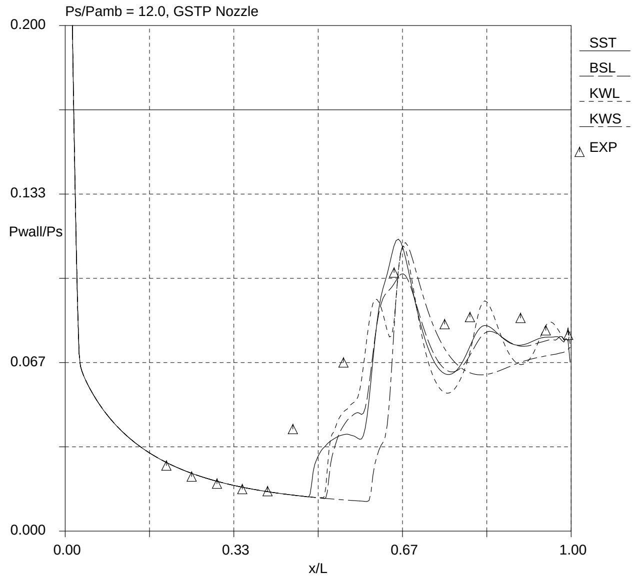

Fig. 5 Restricted shock separation for a pressure ratio (P_s/P_{amb}) of 12.

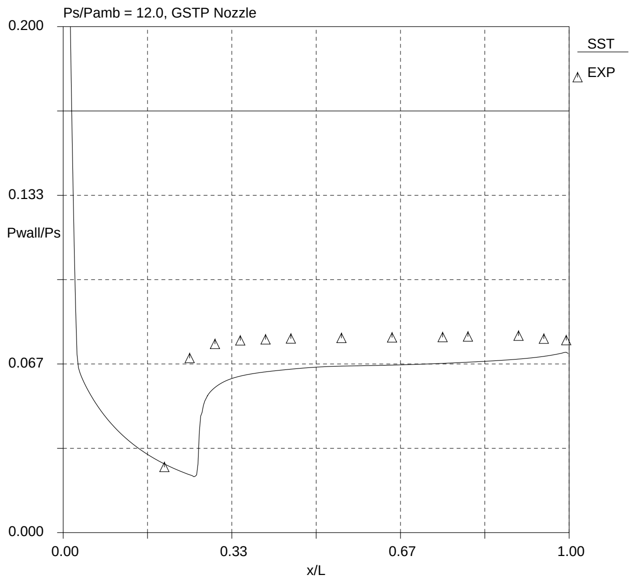

Fig. 4 Free shock separation for a pressure ratio (P_s/P_{amb}) of 12.

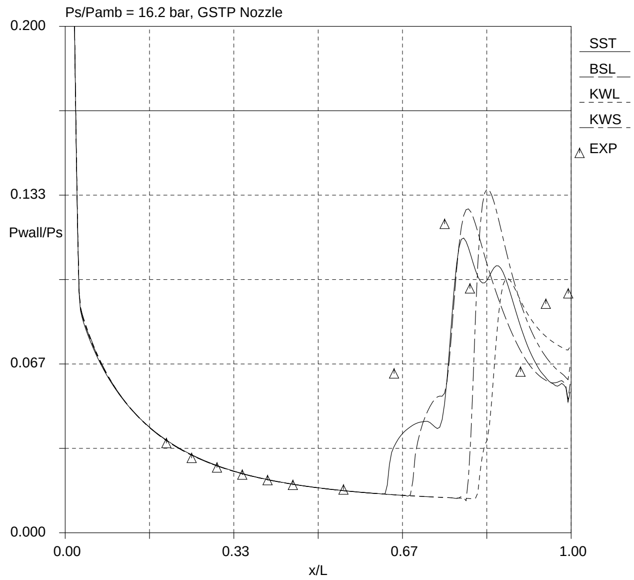

Fig. 6 Restricted shock separation for a pressure ratio (P_s/P_{amb}) of 16.2.

Conclusions

The results in this paper show that it is possible to predict the separation pattern in the present rocket nozzle, reasonably well, as it is started and closed, using standard two equation turbulence models and steady state methodology.

Most important is to have a physical limiter on the production of turbulent kinetic energy over the shocks. Without the limiter, the turbulent fluctuations behind the shock will contain as much energy as the main flow. This generates high levels of the eddy viscosity which will destroy the flow structure behind the shock.

The inflow conditions did not have an influence on the global variables, like the velocity profiles, the turbulent kinetic energy (in the boundary layer), or the turbulent dissipation rate (in the boundary layer). Also, no influence on the point of separation or on the locations of the shocks were found. Hence, the inflow conditions are not of primary importance.

It is shown, together with the references, that key to getting the correct results is the point of separation from the nozzle wall. It is most likely the point of separation that determines the structure of the flow, and hence a model with good separation qualities should be preferred.

Acknowledgment

The authors are grateful to the European Space Agency (ESA/EsTEC), the Swedish National Space Board (SNSB), and the Aeronautical Research Institute of Sweden (FFA) for supporting this work under contract.

Also, the following persons deserve an extra thank you for help and support in different ways; Mr. Schwane at ESA, Mr. Högman at VAC, Mr. Torngren, Mr. Wallin, and Mr. Lindblad, all at FFA.

References

[1]Schmucker, R. H., "Flow processes in overexpanded chemical rocket nozzles, Part 1: Flow separation," NASA TM–77396.

[2]Nave, L. H. and Coffey, G. A., "Sea level side loads in high area ratio rocket engines," AIAA Paper 73–1284, 1973.

[3]Bowyer, J. M., K. G. W. and E., P. R., "An investigation of the Side Force that is Sometimes Observed in Rocket Motor Start-Up," AIAA Paper 78-1045, 1978.

[4]Luke, G. D. and Adams, D. E., "Use of Nozzle Trip Rings to Reduce Nozzle Separation Side Loads During Staging," AIAA Paper 92-3617, 1992.

[5]Romine, G. L., "Nozzle Flow Separation," *AIAA Journal*, Vol. 36, No. 9, 1998.

[6]Bigert, M. Stenholm, T. and Sätmark, T., "Technology for the Film-Cooled Nozzle of the Vulcain Engine," IAF-98-S.3.05.

[7]Mattsson, J. Torngren, L. and Högman, U., "A Sub Scale Test programme on investigation of flow separation and side loads in rocket nozzles," *Third European Symposium on Aerothermodynamics for Space Vehicles*, ESTEC, Nordwijk, The Netherlands, Nov. 1998.

[8]Östlund, J. and M., B., "A Sub Scale Investigation on Side Loads in Sea Level Rocket Engines," AIAA Paper 99–2479, Jun. 1999.

[9]Rizzi, A., Eliasson, P., Lindblad, I., Hirsch, C., Lacor, C., and Hauser, J., "The Engineering of Multiblock/Multigrid Software for Navier-Stokes Flows on Structured Meshes," *Computers Fluids*, Vol. 31, 1993, pp. 341–367.

[10]Wilcox, D. C., *Turbulence Modeling for CFD*, No. ISBN 0–9636051–0–0, DCW Industries Inc, 1993.

[11]Menter, F. R., "Zonal Two Equation k-ω Turbulence Models for Aerodynamic Flows," AIAA Paper 93–2906, Jul. 1993.

[12]Wallin, S., "Personal communication, to be published in," *AVTAC/DEL/FFA/D3.2C3*, May 1999, pp. 13–14.

[13]Menter, F. R., "Influence of Freestream Values on k-ω Turbulence Model Predictions," *AIAA Journal*, Vol. 30, No. 6, 1993, pp. 1657–59.

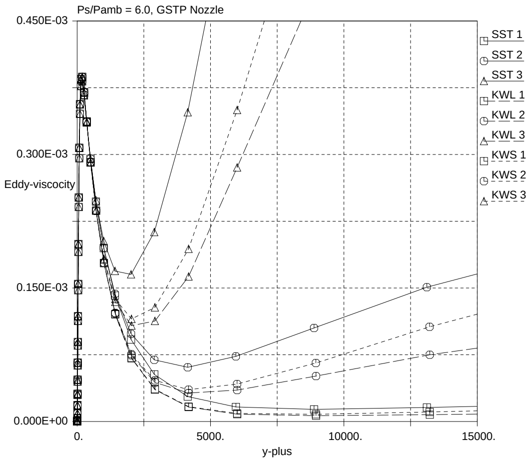

a) **Eddy viscosity (μ_t). Turbulence levels as defined in table (1) and models as defined in the Nomenclature.**

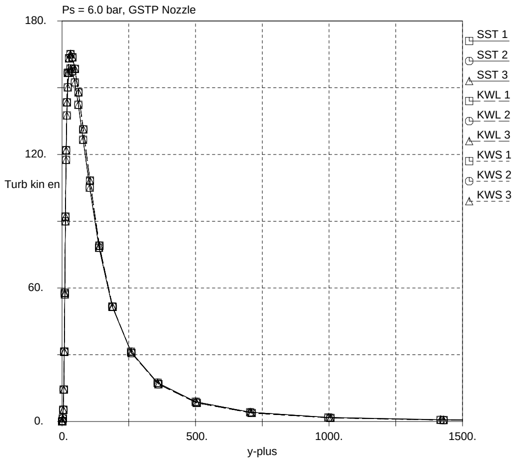

b) **Turbulent kinetic energy (k). Turbulence levels as defined in table (1) and models as defined in the Nomenclature.**

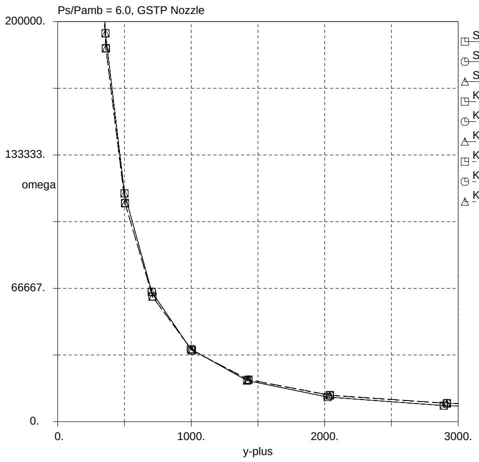

c) **Turbulent dissipation rate (ω). Turbulence levels as defined in table (1) and models as defined in the Nomenclature.**

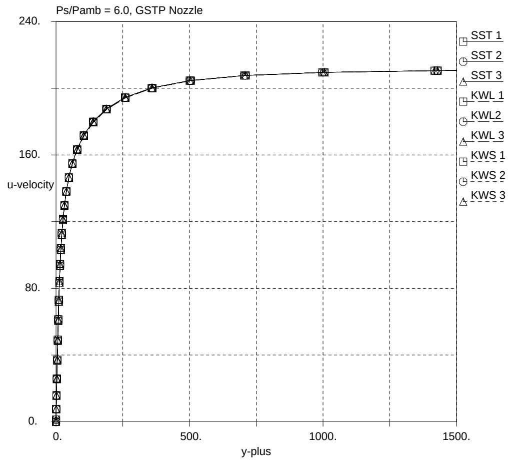

d) **U velocity profiles. Turbulence levels as defined in table (1) and models as defined in the Nomenclature.**

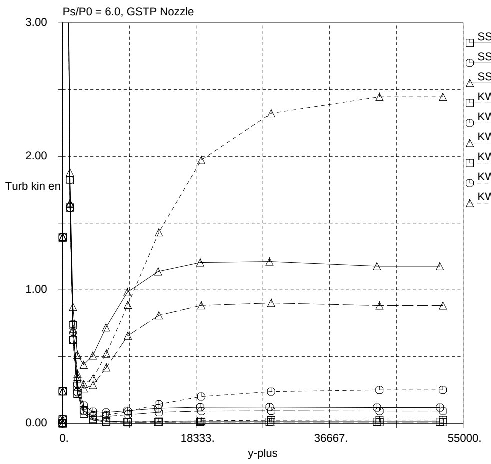

e) **Turbulent kinetic energy (k). Turbulence levels as defined in table (1) and models as defined in the Nomenclature.**

Fig. 7 Evaluation of different turbulent inlet conditions.

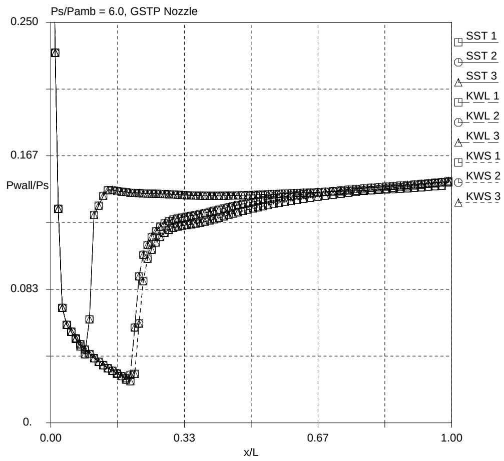

a) Wall pressure, indication point of separation. Turbulence levels as defined in table (1) and models as defined in the Nomenclature.

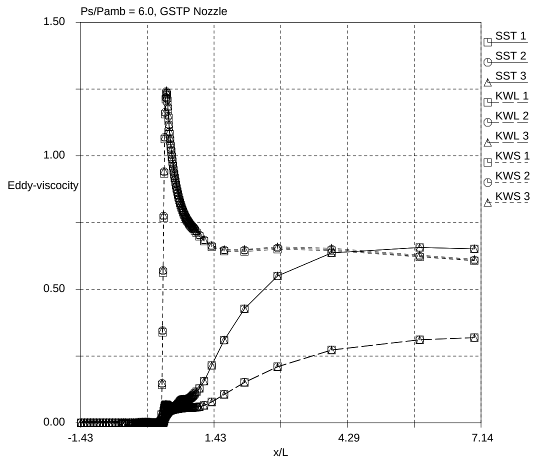

b) Eddy viscosity (μ_t) on centerline. Turbulence levels as defined in table (1) and models as defined in the Nomenclature.

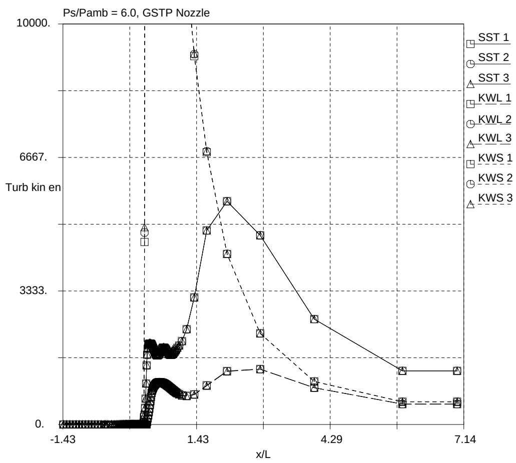

c) Turbulent kinetic energy (k) on centerline. Turbulence levels as defined in table (1) and models as defined in the Nomenclature.

Fig. 8 Evaluation of turbulent variables over the shock on the centerline.

Paper 4

JOURNAL OF PROPULSION AND POWER
Vol. 20, No. 2, March–April 2004 (Tentative)

Side-Load Phenomena in Highly Overexpanded Rocket Nozzles

Jan Östlund*
Volvo Aero Corporation, S-461 81 Trollhättan, Sweden, Royal Institute of Technology, S-144 00 Stockholm, Sweden
and
Tomas Damgaard† and Manuel Frey‡
Volvo Aero Corporation, S-461 81 Trollhättan, Sweden

The operation of rocket engines in the overexpanded mode, that is, with the ambient pressure considerably higher than the nozzle exit wall pressure, can result in dangerous lateral loads acting on the nozzle. These loads occur as the boundary layer separates from the nozzle wall and the pressure distribution deviates from its usual axisymmetric shape. Different aerodynamic or even coupled aerodynamic/structural mechanic reasons can cause an asymmetric pressure distribution. A number of subscale tests have been performed, and three potential origins of side loads were observed and investigated, namely, the pressure fluctuations in the separation and recirculation zone due to the unsteadiness of the separation location, the transition of separation pattern between free-shock separation and restricted-shock separation, and aeroelastic coupling, which indeed cannot cause but do amply existing side loads to significant levels. All three mechanisms are described in detail, and methods are presented to calculate their magnitude and pressure ratio at which they occur.

Nomenclature

B = normalized pressure shift coefficient
C = separation point shift coefficient
F = force
F' = differential force
f = frequency
J = mass of inertia
k = stiffness
L, l = length
M = Mach number or torque
m = mass
n = off-design ratio
$\boldsymbol{n}$ = wall normal vector
p = pressure
q = nondimensional variable
r = radius
S = surface
s = arc length
t = time
t_1 = pulse-duration time
u, v = velocity
$\boldsymbol{w}$ = wall displacement
x = axial position
$\boldsymbol{x}$ = vector of location
y = horizontal position
z = vertical position
γ = specific heat ratio
δ = boundary layer
δ^* = displacement thickness
ε = area ratio or intermittence factor
θ = tilt angle
ρ = density
σ = rms value
τ = period time or wall angle
τ_w = wall friction
φ = azimuth
ψ = pressure shift coefficient
ω, Ω = angular frequency

Subscripts

a = aerodynamic or ambient
e = exit
ff = full flowing
i = interaction
m = measured or mechanical
max = maximum
n = natural
p = plateau
r = recirculating
s = separation
t = throat
w = wall
y = horizontal
0 = undisturbed flow state or stagnation condition

Presented as Paper 2001-3684 at the Side load phenomena in highly overexpanded rocket nozzles, Joint Propulsion conference in Salt Lake City, 8 July 2001; received 11 June 2003; revision received 3 December 2003; accepted for publication 3 December 2003.

*Research Engineer, Engineering Department Nozzles, Space Propulsion Division; Ph.D. Student, Department of Mechanics; jan.ostlund@volvo.com.

†Research Engineer, Engineering Department Nozzles, Space Propulsion Division; tomas.damgaard@volvo.com.

‡Research Engineer, Engineering Department Nozzles, Space Propulsion Division; manuel.frey@volvo.com.

Introduction

THE performance of a rocket engine is strongly influenced by the characteristics and function of its nozzle extension. The characteristics of a conventional nozzle under vacuum conditions are well understood, and under this condition, design tools are available. However, during operation at highly overexpanded conditions, the rocket nozzle will be exposed to dynamic loads due to uncontrolled flow separation. These loads can sometimes be of such a magnitude that they present life-limiting constraints on thrust chamber components, as well as on the thrust vectoring control system.

The increasing demand for higher performance in rocket launchers promotes the development of nozzles with higher performance and, hence, larger area ratio. In a high area ratio nozzle, the flow will not be fully attached, but separated during testing at sea-level condition and during the first phase of the actual flight. In a nozzle that is not full flowing, the separation line will move toward the nozzle exit when the chamber to ambient pressure ratio increases.

Different kinds of dynamic loads occur in the nozzle when the flow is separated. The most well-known of these dynamic loads, which has received attention in the literature, is the so called side load. To avoid damage from these loads, a deeper understanding of the phenomena involved is needed.

A focused work dedicated to the investigation of the flow separation phenomena in rocket nozzles and corresponding side loads was initiated in 1997.[1] In the course of this work, numerous subscale tests were performed in the modified hypersonic wind tunnel HYP500 at the Aeronautical Research Institute of Sweden (FFA) (now a part of the Swedish Defence Research Agency) in Stockholm.[1–3] Heated air was used as driving gas to avoid condensation. Dynamic and static wall pressure measurements were performed together with schlieren video recording to characterize the flowfield. The subscale models consist mainly of two parts: one fixed part mounted to the downstream flange of the wind tunnel and one hinged part (Fig. 1). The hinged part is fastened by a cardan, permitting the nozzle to move in two directions (Fig. 2). The side-load torque is measured around the nozzle throat in the cardan by strain gauges located on the torsion springs, and this motion simulates the throat-bending mode of a real rocket nozzle. Each of the different nozzle concepts tested was equipped with a stiffener ring at the nozzle exit to receive approximately the same eigenfrequency in all of the nozzle concepts. An overview of the nozzles analyzed is shown in Fig. 3.

In the test campaigns, three main types of side loads have been observed due to 1) random pressure fluctuation, 2) transition of separation pattern, and 3) aeroelastic coupling. All three types are described and exemplified by test results together with analysis in this paper. A fourth type of side loads, which is due to the influence of the external flow, is not addressed here.

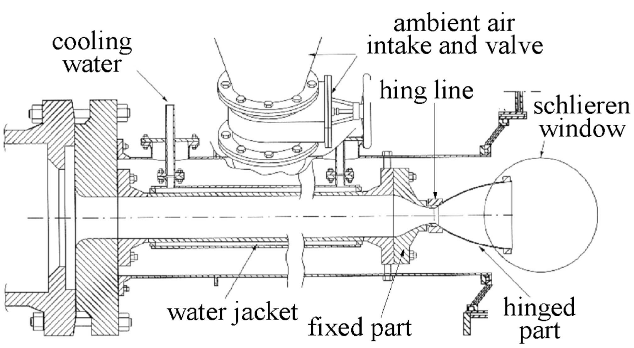

Fig. 1 Schematic side view of the cardan hinged test nozzle in FFA tunnel HYP 500.

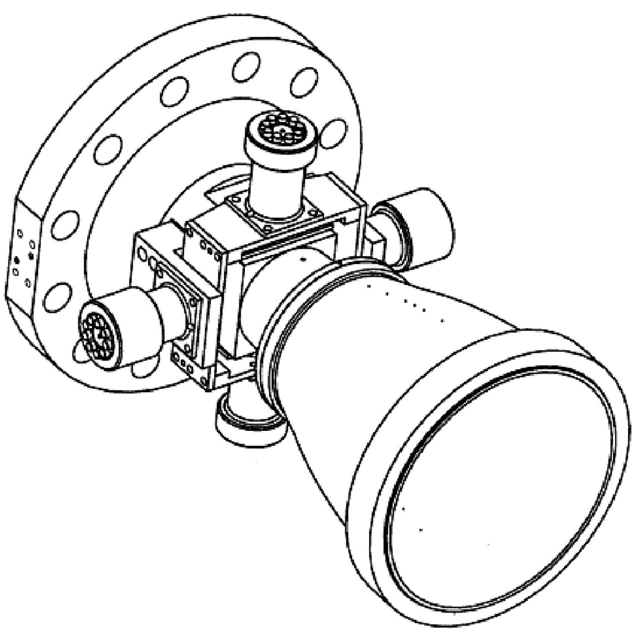

Fig. 2 Test nozzle with cardan suspension.

a) Volvo S1 parabolic contour, $\varepsilon = 20$

c) Volvo S6 Truncated ideal contour, $\varepsilon = 20.7$

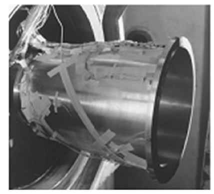

b) Volvo S3 parabolic contour, $\varepsilon = 18.2$

d) Volvo S7 short high-pressure gradient, $\varepsilon = 20.3$

Fig. 3 Subscale nozzles tested by VAC at FFA's HYP500 facility.

Side Loads Created by Random Pressure Fluctuations

Flow separation in supersonic flows is, of course, not limited to the field of rocket nozzles. When a supersonic flow meets a forward-facing step, a ramp, or an incident shock, the pressure rise in the boundary layer can be strong enough to cause flow separation. From basic experiments with exactly these configurations, it is known that the boundary-layer separation in turbulent supersonic flows is not a stationary process, even if the main flow is stationary.[4,5] Instead, the separation line and the shock resulting from the deflection of the flow show a highly instationary behavior, which seems to be triggered by the major scales of turbulence and also influences the recirculation region downstream.[6]

In rocket nozzles, basically the same phenomena can be observed. However, the separation location is not fixed by geometrical properties of the test configuration as in the earlier cases, but results mainly from the ratio of wall pressure to ambient pressure.

It is useful to describe the off-design condition as

$$n = p_{e,\mathrm{ff}}/p_a \tag{1}$$

where $p_{e,\mathrm{ff}}$ is the theoretic nozzle exit wall pressure for a full-flowing nozzle and p_a is the ambient pressure.

As an example, static wall pressure measurements from a truncated ideal nozzle (Volvo S6 in Fig. 3) are shown in Fig. 4. As expected, the separation point moves out of the nozzle when the off-design ratio n is increased towards unity, that is, the degree of overexpansion is reduced.

Based on the static wall pressure development, the flow can be divided in three regions. As shown in Fig. 5, upstream of the point of minimum static wall pressure (usually indexed i), the boundary layer is attached, and its behavior corresponds to a full-flowing nozzle. The following region of steep pressure rise, which ends at a certain plateau (often indexed p), is usually referred to as separation or interaction zone. In this region, the whole separation process take place, that is, thickening of boundary layer and physical flow separation (indexed s) at the zero wall friction point, $\tau_w = 0$. The last portion of the nozzle, where the flow is fully separated, shows a weak pressure rise until a wall pressure slightly below the ambient pressure is reached at the nozzle exit plane. This last portion is referred to as the recirculation zone.

When the dynamic behavior of the wall pressure is examined rather than the static behavior, interesting features of the flow can be observed. Figure 6 shows pressure signals in different parts of the separation zone, and Figure 7 shows the corresponding statistical moments. In Fig. 7, the axial positions correspond to $M = 3.8$

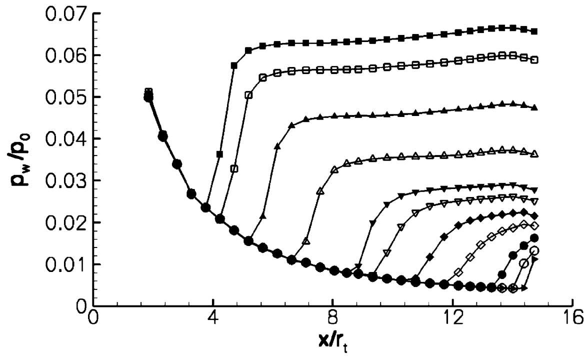

Fig. 4 Static wall pressure measurements in the S6 nozzle for different operational conditions, $n = 0.04$–0.24.

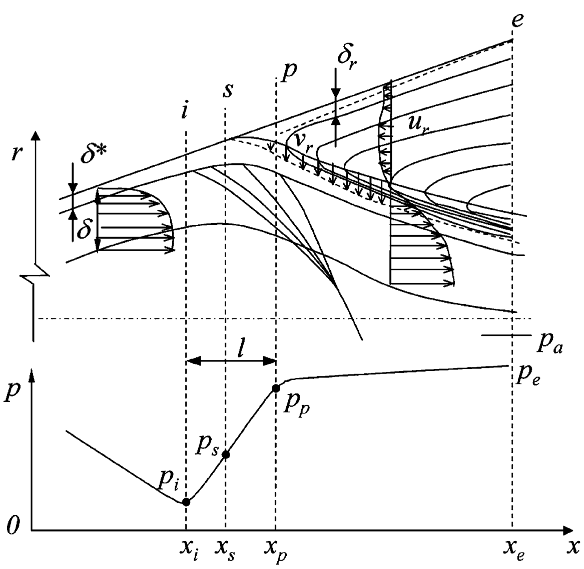

Fig. 5 Schematic of FSS.

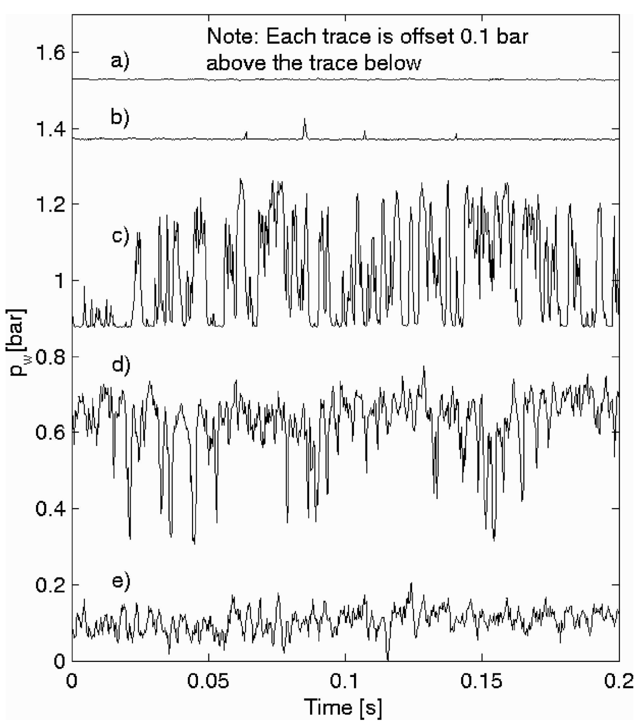

Fig. 6 Pressure signals at different positions through the separation zone in the Volvo S7 short nozzle; measurements made during down ramping of p_0.

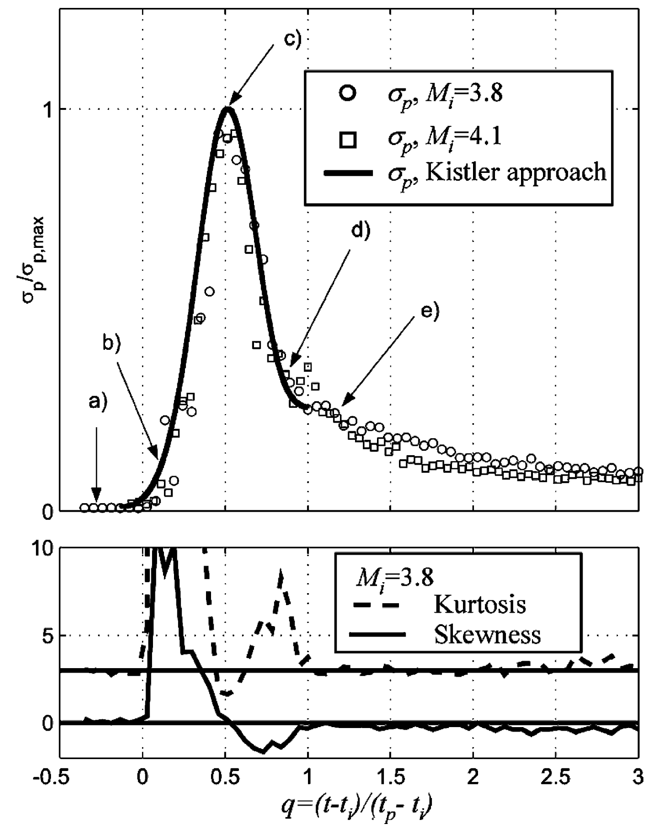

Fig. 7 Statistical evaluation of pressure signal at two different axial locations in the Volvo S7 short nozzle during down ramping of p_0: top, standard deviation values and bottom, skewness and kurtosis.

and $M = 4.1$ in the full-flowing nozzle. Each symbol is based on 800 samples collected during 0.2 s. The data were obtained at transient operation of the Volvo S7 short nozzle (Fig. 3). During down-ramping of the chamber pressure, the separation zone moves over the transducers during the time t_p–t_i, where the subscripts i and p refer to the start of the separation zone and the plateau point, respectively. Because the ramping is slow compared to the typical timescale of the pressure fluctuations, the variation of σ_p over time can be interpreted as the streamwise evolution by defining a nondimensional coordinate $q = (t - t_i)/(t_i - t_p)$. Figure 7 shows this behavior for two pressure transducers located at different axial positions. As can be seen, the two curves in Fig. 7 (representing the normalized standard deviation of the measured pressure signals) coincide, which proves that this generalization is valid. Outside the separation zone (signals a and e, Fig. 7), the pressure fluctuations follow a Gaussean distribution, with skewness near zero and the kurtosis equal to three. In contrast, the separation zone is characterized by high intermittency: at the beginning with a positive skewness (Fig. 7, signal c) and toward the end with a negative skewness (Fig. 7, signal d). In fact, the onset of high values of skewness and kurtosis (flatness) constitutes an accurate criterion for detecting the beginning and end of the separation zone.

The explanation of the obtained feature, first given by Kistler,[4] is that the flow is intermittent. In the separation zone, the pressure jumps back and forth between the mean pressure levels p_i and p_p due to a fluctuation of the separation point, and at each pressure level, the pressure oscillates with an amplitude characteristic of that level, that is, $\sigma_{p,i}$ and $\sigma_{p,p}$, respectively.

According to Kistler,[4] the wall pressure signal near the separation can be modeled as a step function, with the jump location, that is, the shock wave, moving over some restricted range. When ε is defined as the fraction of time that the plateau pressure region is acting over the point of interest, that is, an intermittence factor, the mean pressure at a given axial position x can be expressed as

$$p(x) = \varepsilon(x) p_p + [1 - \varepsilon(x)] p_i \tag{2}$$

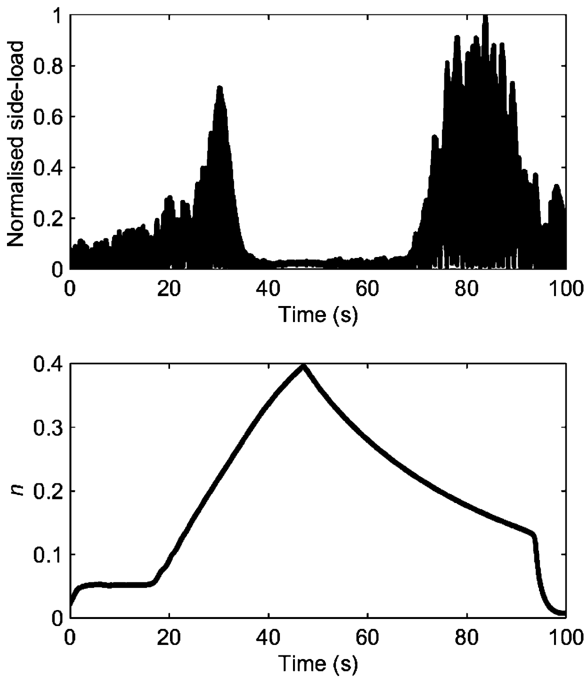

Fig. 8 Side loads created in a nozzle with random pressure pulsation.

and the mean-square fluctuation around the mean pressure becomes

$$\sigma_p^2(x) = \underbrace{\overbrace{\varepsilon[1-\varepsilon](p_p - p_i)^2}^{\text{Shock motion}}}_{\text{Low freq. part}} + \underbrace{\overbrace{\varepsilon\sigma_{p,p}^2}^{\text{Shear layer}} + \overbrace{[1-\varepsilon]\sigma_{p,i}^2}^{\text{Boundary layer}}}_{\text{High freq. part}} \qquad (3)$$

Erengil and Dolling[7] showed, on the basis of ramp flow data, that the error function gives a good fit to the distribution of ε over the interaction region. This means that the position of the separation shock has a Gaussian distribution within this region.

The comparison in Fig. 7 with pressure rms values calculated with a refined Kistler approach (see Ref. 8) shows that the intermittence model gives correct results and can be applied to separated nozzle flows.

The pressure fluctuations have a random character, but show a clear correlation both in space and time. Therefore, they cause deviations from the axisymmetric flow and, hence, can produce forces perpendicular to the nozzle axis. Figure 8 shows those forces as a function of test time and operational condition for the Volvo S6 nozzle. Dumnov[9] presented a methodology to calculate the size of such forces based on the measurement of correlations both in time and space. This method is well suited to predict side loads in conical or truncated ideal nozzles.

Note that the earlier described side load, which results from random pressure fluctuations, is an aerodynamic force that acts on the dynamic system of the nozzle or the engine. To calculate the system response, that is, strains, deformations, and movements, it is necessary to solve a forced-response problem. The same holds true if the aerodynamic side load should be extracted from measurements: Because only the system response can be measured, a recalculation of the aerodynamic force is necessary, which requires the precise knowledge of the system's dynamic behavior. One possibility to do this is to determine the system's transfer function.[13] This procedure was also used to calculate the aerodynamic side loads from test data recorded at the HYP500 rig.

Side Loads Created by Transition of Separation Pattern

The classic, well-documented case of flow separation in nozzles is the free shock separation (FSS), where the flow continues as free-jet downstream of the separation point and does not reattach to the nozzle wall (Fig. 5). In nozzles with an internal shock that induces a cap shock pattern,[3] for example, compressed truncated ideal contours, parabolic contours, and directly optimized nozzles, a second separation pattern can occur. It is characterized by a reattachment of the separated flow to the nozzle wall and commonly referred to as restricted shock separation (RSS).[1,3,10,11] Two well-known full-scale nozzles where RSS occurs are the Vulcain and the space shuttle main engine (SSME) nozzle.

In the subscale testing, this behavior is detected in the parabolic nozzles Volvo S1 (Fig. 9) and Volvo S3. Numerical simulation was done using an in-house code that used the Menter[12] shear stress transport (SST) turbulence model. Figure 10 shows the side forces for the S1 nozzle, which are dominated by the changes in separation pattern.

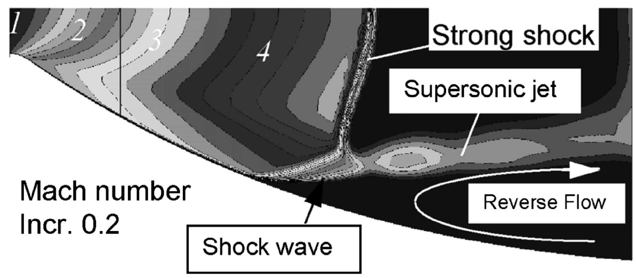

a) FSS at $n = 0.13$

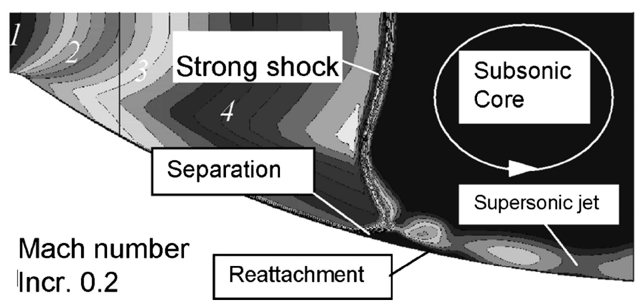

b) RSS at $n = 0.15$

Fig. 9 Volvo S1 nozzle at start-up.

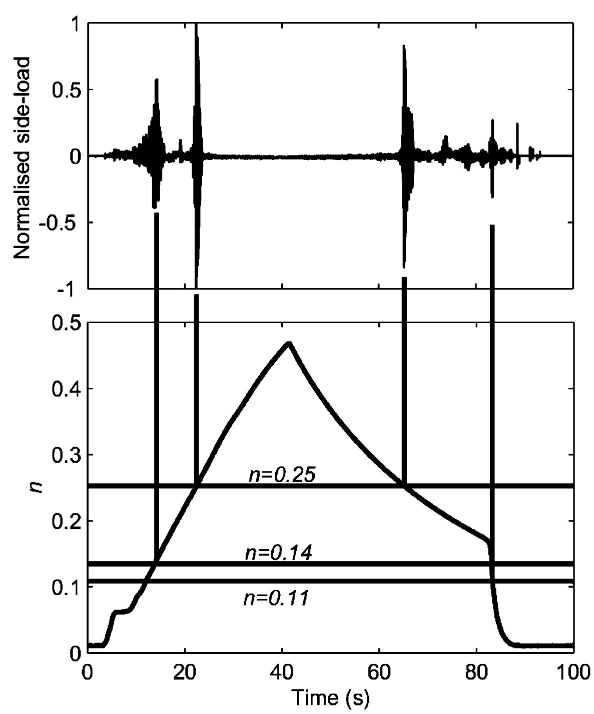

Fig. 10 Side loads created in the parabolic S1 nozzle due to transition in separation pattern.

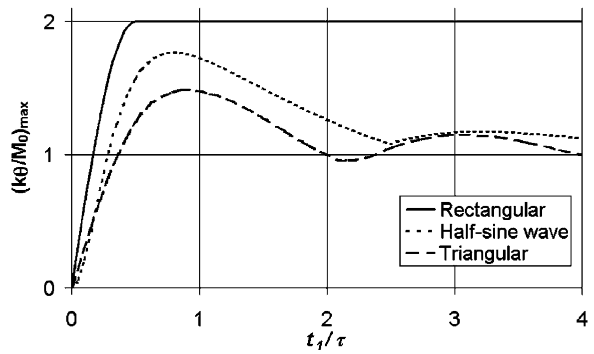

Fig. 11 SRS for different pulse shapes.

During startup, a transition from FSS to RSS occurs at an off-design ratio of $n = 0.14$ (Fig. 10). This rapid unsymmetrical transition creates a side-load impulse acting on the nozzle structure. Because of the short duration of the aerodynamic side load, the pulse excitation theory[13] can be used when evaluating the mechanical load. With this theory, the dynamic response factor, that is, the amplification of the applied load due to the dynamic system, is less than two for any single pulse. The most critical pulse is the single square wave because it contains the highest energy that any single pulse of defined strength and length can have. Figure 11 shows the shock response spectrum (SRS) for a single square wave together with the SRS for the half-sine wave and triangular pulse. The half-sine and the triangular pulse are often good approximations to real pulse shapes, for example, the load created by the aforementioned transition from FSS to RSS. If the transition time t_1 and the natural period of the mechanical eigenmode τ are known, the dynamic response factor can be obtained from Fig. 11.

The second side-load peak at $n = 0.25$ is created as the reattachment point reaches the nozzle exit and the closed separation bubble opens to ambient. The ambient pressure, which is higher than the pressure in the closed separation bubble, pushes the separation point upstream, which can result in a renewed reattachment of the flow to the wall and a downstream movement of the separation point. This process can recur periodically until the nozzle pressure ratio has been increased sufficiently and, thus, causes a continuously pulsating force on the nozzle. In contrast to the FSS–RSS transition side load described earlier, which was treated by the pulse excitation theory, the second peak should be treated as a forced response phenomenon. If the mechanical eigenfrequency of the system is close to the aerodynamic side-load frequency, it can lead to a severe side-load amplification and, thus, fatigue of mechanical components. The failure of an SSME fuel feed line was explained by this phenomenon.[14]

Different models have been proposed for the prediction of the aerodynamic load due to the transition between separation patterns (Hagemann et al.[10]). The basic idea in all proposed models is the same: It is assumed that the transition does not occur in a symmetric way. A worst-case assumption is that during this transition, one-half of the nozzle experiences free-shock separation while there is restricted-shock separation at the opposite half. Of course, the wall pressure distribution for the two different separation patterns is not the same; hence, a lateral force is produced. The side sload is then calculated from the momentum balance over the entire nozzle surface area. The key point for predicting the side-load level correctly is first to predict the operational condition where the transition from FSS to RSS takes place and second to calculate the corresponding FSS and RSS flow conditions. This can be done with computational fluid dynamics (CFD) or semi-empirical models or a combination of both (Hagemann et al.[10]).

Aeroelastic Stability

In highly aeroelastic cases, a significant amplification of the side load can occur as the flow interacts with the mechanical structure. The study of aeroelastic effects in separated nozzle flows is rather complex, requiring dynamic models of the mechanical nozzle–engine support system and the flow separation, as well as the coupling between these two. A technique for handling these difficult coupling problems was proposed by Pekkari[15,16] in the early 1990s. The model consists of two main parts, the first dealing with the equation of motion of the thrust chamber as aerodynamic loads are applied and a second part modeling the change of the aerodynamic loads due to the elastic deformation of the wall contour. In the original work by Pekkari, the pressure shift due to the deformation of the wall is determined by using the linearized supersonic flow theory. However, experience has shown that this theory significantly overpredicts the pressure shift when it is applied to internal nozzle flow, and therefore, a modified approach is proposed here, where the pressure shift is extracted from three-dimensional Euler simulations. This modified model predicts the aeroelastic stability and the modification of eigenfrequencies due to aeroelastic effects, as well as the transient behavior during startup and shutdown of the nozzle. Different mechanical eigenmodes can be treated, however, from side load point of view, the aeroelastic behavior of the bending mode is the most relevant one.

In the following section, the applied aeroelastic theory will be described, and results will be compared to the Volvo S1 and S6 cold-gas subscale tests (Fig. 3). Thanks to the simple test setup, the mechanical system can be described analytically (in contrast to real rocket engine cases, which require a complex finite element model analysis) and the basic model assumptions can, thus, be verified separately.

Geometry

The coordinate system implemented and the definition of the nozzle motion is shown in (Fig. 12).

The model nozzle is mounted on a flexible joint or cardan with stiffness k located at the throat. Here, θ is the tilt angle between the nozzle centerline and the combustion chamber centerline. L is the nozzle length from the throat to the exit, m the mass, and J_y the mass of inertia around the y axis. Also, τ is the local contour angle with respect to the nozzle centerline, and $r(x)$ is the local radius of the nozzle at the axial location x. Furthermore, $\boldsymbol{w}$ describes the displacement of the nozzle wall. The circumferential location is denoted by the angle φ, and p, M, u, ρ are the freestream flow properties along the wall.

Equation of Motion

Following the analysis of Pekkari,[15,16] the system is considered as quasi static with respect to the flow, that is, the characteristic

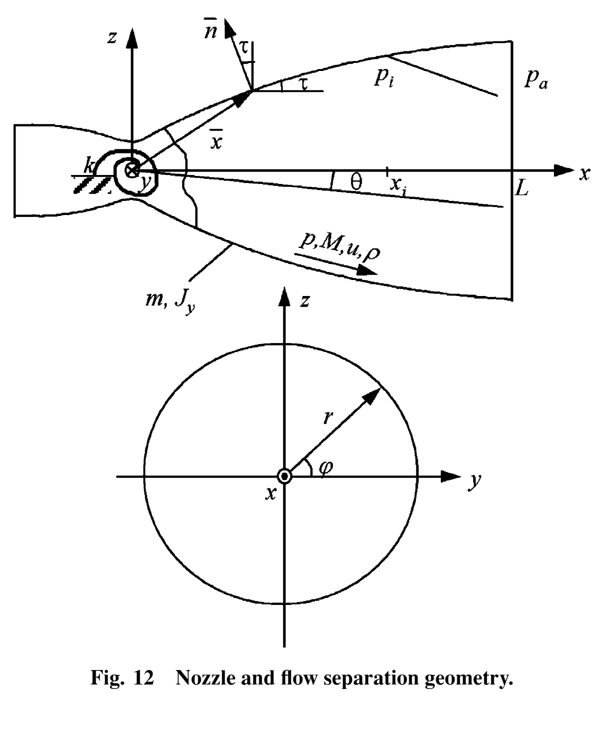

Fig. 12 Nozzle and flow separation geometry.

timescales of the flow are considered to be an order of magnitude faster than the characteristic timescales of the mechanical system.

In the y direction, the equation of motion for the bending of the nozzle by an angle θ, without considering damping, is

$$J_y\ddot{\theta} = M_m(\theta) + M_a(\theta) \tag{4}$$

M_m is the mechanical torque, that is, the restoring torque of the spring in the nozzle suspension,

$$M_m = -k\theta \tag{5}$$

and M_a is the y component of the aerodynamic torque induced by the pressure load onto the nozzle wall, neglecting any wall friction,

$$\boldsymbol{M}_a(\theta) = \oiint \boldsymbol{x} \times \{p[\boldsymbol{w}(\theta), x] - p_a\} \cdot \boldsymbol{n}\,\mathrm{d}S \tag{6}$$

Here, $\boldsymbol{n}$ is the wall surface normal vector as indicated in Fig. 12, and $\boldsymbol{x}$ is the corresponding vector of location,

$$\boldsymbol{n} = \{-\sin\tau, \cos\tau\cos\varphi, \cos\tau\sin\varphi\} \tag{7}$$

$$\boldsymbol{x} = \{x, r(x)\cos\varphi, r(x)\sin\varphi\} \tag{8}$$

Eigenfrequency

The equation of motion for the mechanical system alone, that is, the nozzle without flow, is derived by putting the considered harmonic amplitude motion solution

$$\theta \sim e^{i\omega t} \tag{9}$$

into Eq. (4) and leaving out the aerodynamic torque M_a,

$$J_y\ddot{\theta} = M_m(\theta), \qquad -J_y\omega^2\theta = -k\theta \tag{10}$$

From Eq. (10), the eigenfrequency is found as

$$\omega^2 = k/J_y \tag{11}$$

This frequency can be found with hammer tests. Now, a nozzle with flow and, thus, with aerodynamic load M_a is considered, again assuming the motion to be purely harmonic,

$$\theta \sim e^{i\Omega t} \tag{12}$$

Introducing Eq. (12) in (4) and dividing by Eq. (11) gives

$$-J_y\Omega^2\theta = -k\theta + M_a, \qquad (\Omega/\omega)^2 = 1 - [M_a(\theta)/k\theta] \tag{13}$$

The analysis of Eq. (13) shows that, when $M_a/k\theta < 0$, the aeroelastic torque acts to restore the nozzle to its nominal position, that is, the system becomes stiffer than the mechanical structure itself and the frequency of the eigenmode is shifted to a higher frequency, that is, $(\Omega/\omega)^2 > 1$.

The analysis of Eq. (13) also shows that, when $M_a/k\theta \in [0, 1]$, the aeroelastic torque acts in the same direction as the displacement of the nozzle wall, that is, the system becomes weaker than the mechanical structure itself and the frequency of the eigenmode is shifted to a lower frequency, that is, $(\Omega/\omega)^2 \in [0, 1]$.

Finally, analysis of Eq. (13) shows that, when $M_a/k\theta > 1$, the unconditionally stable eigenmode becomes aeroelastically unstable, that is, $(\Omega/\omega)^2 < 0$, and the displacement of the nozzle will start to grow exponentially.

Aerodynamic Load

To calculate the aerodynamic load and the associated frequency shift, the wall pressure distribution of the deformed nozzle must be known. As in the original model by Pekkari,[15,16] the pressure upstream of the separation point x_i is assumed to be the pressure of the attached boundary layer, but taking into account the asymmetric deformation. Downstream of the separation point, a pressure recovery occurs, and the pressure gradually approaches the ambient pressure. However, the model presented here assumes this pressure to be equal to the ambient pressure p_a for simplicity and clarity,

$$p(\boldsymbol{w}, \boldsymbol{x}) = \begin{cases} p(x) + p_0\Psi(\boldsymbol{w}, \boldsymbol{x}), & x \le x_i \\ p_a, & x > x_i \end{cases} \tag{14}$$

Here $p(x)$ is the axisymmetric wall pressure in the undeformed nozzle. The second term in the pressure upstream of the separation line is the disturbance of the wall pressure due to the deformation of the nozzle contour, that is,

$$\Psi(\boldsymbol{w}, \boldsymbol{x}) = [p(\boldsymbol{w}, \boldsymbol{x}) - p(x)]/p_0 \tag{15}$$

where p_0 is the stagnation pressure.

The location of the separation point is considered to be given by a separation criterion of Summerfield type:

$$p_i/p_a = \text{const} \tag{16}$$

In the original work by Pekkari, the pressure shift, ψ, was calculated with the use of the small perturbation theory (SPT), that is,

$$\Psi(\boldsymbol{w}, \boldsymbol{x}) = \frac{\rho u^2}{p_0\sqrt{M^2 - 1}}\frac{\partial w}{\partial s} = B\frac{\partial w}{\partial s} \tag{17}$$

Here $w = \boldsymbol{w} \cdot \boldsymbol{n}$ is the normal displacement of the nozzle wall surface and s is the arc length along the wall in the axial direction; thus, for small deflections, $\partial w/\partial s$ is the angle of deformation. B is the normalized pressure shift coefficient, which expresses the change in pressure with the wall deformation. However, experience has shown that SPT overpredicts the pressure shift in deformed nozzles. Therefore, a modified approach is proposed,[3] where the normalized pressure shift coefficient B is extracted from three-dimensional Euler simulations:

$$B(x) = \frac{\Psi(\boldsymbol{w}, \boldsymbol{x})}{\partial w/\partial s} = \frac{p(\boldsymbol{w}, \boldsymbol{x}) - p(x)}{p_0\partial w/\partial s} \tag{18}$$

A test was performed where the S1 nozzle was statically deformed by 1 deg to verify the simulation results. In Fig. 13, the measured and the calculated wall pressure profile are shown for the undeformed and deformed S1 nozzle, respectively. As can be seen in

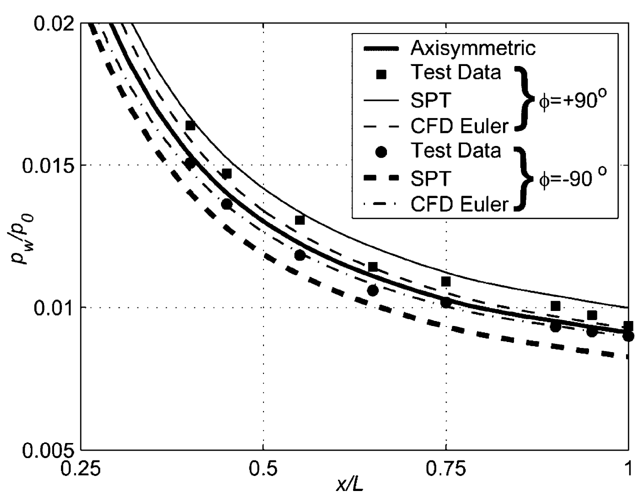

Fig. 13 Measured and calculated wall pressure in the S1 nozzle statically deflected by 1 deg.

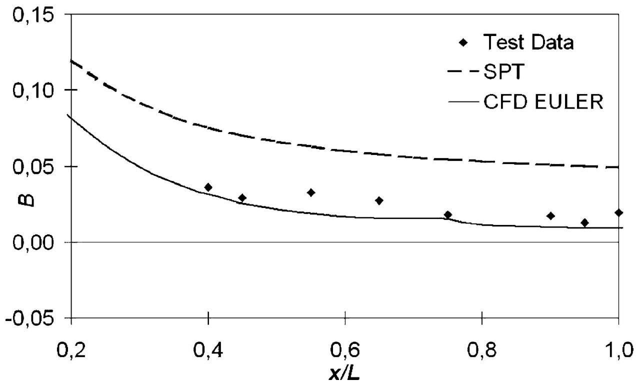

Fig. 14 Comparison between calculated and measured normalized pressure shift coefficient *B* in the S1 nozzle.

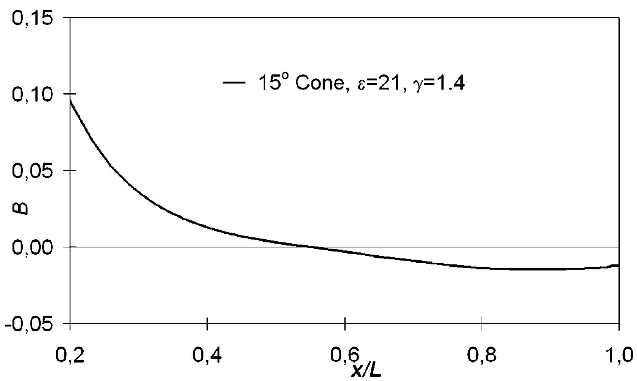

Fig. 15 Normalized pressure shift coefficient in conical nozzle.

Fig. 13, there is good agreement between the CFD prediction and the measured wall pressure, whereas SPT overpredicts the pressure shift considerably.

This effect can be seen even more clearly in Fig. 14, which shows the corresponding normalized pressure shift coefficient B. The SPT method overpredicts the pressure shift coefficient by approximately a factor of four for this case. The CFD predictions, on the other hand, show close agreement with the experimental data and, thus, validate the use of Euler simulations for calculating the pressure shift coefficient.

Note that the deviation of the wall pressure due to bending around the throat is highly dependent on the nozzle contour itself. As shown in Refs. 11 and 17, the secondary flow effects due to the uneven flow distribution around the circumference in a conical nozzle are so strong that the pressure deviation trend even reverses itself: On the side with higher flow angles, where more expansion is expected, the wall pressure in some portions of the nozzle is even higher than on the opposite side. This finding has been confirmed by our own numerical simulations and underscores the necessity of case-sensitive methods. See Fig. 15 and note the negative value of B.

Linearized Aerodynamic Load

A simple relation can be found by linearizing the aerodynamic torque around the initial location of the separation line in the undeformed nozzle, x_{i0}. Expanding the wall pressure for attached flow around x_{i0} gives

$$p(x_i) = p(x_{i0}) + \frac{\mathrm{d}p}{\mathrm{d}x}(x_i - x_{i0}) + \cdots \tag{19}$$

Equation (14) written at the axial station x_i is

$$p(\boldsymbol{w}, \boldsymbol{x}) = p(x) + p_0 B \left.\frac{\partial w}{\partial s}\right|_{x = x_i} \tag{20}$$

The separation pressure $p(\boldsymbol{w}, \boldsymbol{x})$ at $x = x_i$, approximated for the deformed wall contour by Eq. (20), will be the same as the separation pressure $p(x_{i0})$ for the undeformed wall contour included in Eq. (19). The separation line is, therefore, defined by

$$p(x_{i0}) = p(\boldsymbol{w}, \boldsymbol{x})|_{x = x_i} \tag{21}$$

which gives

$$p(x_i) - \frac{\mathrm{d}p}{\mathrm{d}x}(x_i - x_{i0}) = p(x_i) + p_0 B \left.\frac{\partial w}{\partial s}\right|_{x = x_i}$$

$$x_i - x_{i0} = \left[B \Big/ -\frac{\mathrm{d}}{\mathrm{d}x}\frac{p(x)}{p_0}\right] \left.\frac{\partial w}{\partial s}\right|_{x = x_i} = C \left.\frac{\partial w}{\partial s}\right|_{x = x_i} \tag{22}$$

where

$$C = B \Big/ -\frac{\mathrm{d}}{\mathrm{d}x}\frac{p(x)}{p_0}$$

which expresses the change of the separation point with the nozzle wall deformation.

The differential aerodynamic pressure force per circumferential fraction due to a small wall displacement may be written as

$$\mathrm{d}\boldsymbol{F}'_a(\boldsymbol{w}) = \boldsymbol{n}(p_i - p_a)(x_i - x_{i0})r\,\mathrm{d}\varphi = \boldsymbol{n}(p_i - p_a)C\frac{\partial w}{\partial s}r\,\mathrm{d}\varphi \tag{23}$$

When the differential force is integrated along the separation line a round the circumference, the aerodynamic pressure force is

$$\boldsymbol{F}_a(\boldsymbol{w}) = \oint_{l_{\mathrm{sep}}} \boldsymbol{F}'_a\,\mathrm{d}l = (p_i - p_a)\oint_{l_{\mathrm{sep}}} \boldsymbol{n}C\frac{\partial w}{\partial s}\,\mathrm{d}l\bigg|_{x = x_{i0}} \tag{24}$$

The corresponding aerodynamic torque is

$$\boldsymbol{M}_a(\boldsymbol{w}) = (p_i - p_a)\oint_{l_{\mathrm{sep}}} \boldsymbol{x} \times \boldsymbol{n}C\frac{\partial w}{\partial s}\,\mathrm{d}l\bigg|_{x = x_{i0}} \tag{25}$$

The change of the nozzle wall slope at different circumferential locations φ due to a small tilt angle θ of the nozzle can be expressed as

$$\frac{\partial w}{\partial s} \approx \theta \sin\varphi \tag{26}$$

When this and

$$\oint_{l_{\mathrm{sep}}} \ldots \mathrm{d}l \approx \int_0^{2\pi} \ldots r(x_{i0})\,\mathrm{d}\varphi \tag{27}$$

are used for small wall deformations, the aerodynamic torque can be expressed as

$$\boldsymbol{M}_a(\theta) \approx \{0, M_a, 0\}$$

$$M_a(\theta) = (p_a - p_i)Cr\pi(x\cos\tau + r\sin\tau)\theta|_{x = x_{i0}} \tag{28}$$

When Eq. (28) is substituted in Eq. (13), the frequency shift, linearized around the initial location of the separation line, is obtained as

$$(\Omega/\omega)^2 = 1 - [(p_a - p_i)Cr\pi(x\cos\tau + r\sin\tau)/k]|_{x = x_{i0}} \tag{29}$$

Typical Model Results

The general features of the aeroelastic model are best visualized by applying it to the Volvo S1 test case. The resulting natural oscillating frequencies of the bending mode are listed in Table 1 for the different spring setups used. The frequencies were determined by performing a ping test on the test article in the test facility. A more detailed description of the test program is presented in Ref. 1.

With the use of Eq. (29), the aeroelastic stability of the S1 nozzle can be calculated for the different spring setups. Such a calculation is presented in Fig. 16, with $p_i/p_a = 0.25$ and B from an Euler calculation according to Fig. 4. It can be seen that the only aeroelastically unstable system is the S1 nozzle with the superweak spring for $x_i/L > 0.8$.

The aeroelastically stable system will almost behave like a regular forced response system, that is, the closer the mechanical eigenfrequencies are to the frequencies of the aerodynamic load, the higher the generated loads. The exception is that a small shift of the system eigenfrequency and a corresponding small amplification of the forced response load will occur. The frequency shift and the size of the aeroelastic side-load amplification depend on the degree of coupling. For the weak, medium, stiff, and rigid spring setups considered here, the coupling is weak and the aeroelastic effect can almost be neglected.

For the aeroelastically unstable system, on the other hand, a significantly higher side-load magnitude can be expected compared to the classic forced response theory due to the aeroelastic instability. When the separation enters the section of the nozzle that is unstable, the displacement of the nozzle will start to grow exponentially. At the same time, the separation line will be displaced accordingly. The nonlinear growth of the nozzle displacement will saturate as parts of the separation line start to move out of the nozzle, that is, parts of the nozzle becomes full flowing, when the displacement becomes sufficiently high. This can be seen in the nonlinear stability relation (13), shown in Fig. 17 for tilt angles $\theta = 0.1$ and $\theta = 2.6$ deg. For comparison, the linearized stability relation (29) is also included in Fig. 17.

If we study the nonlinear stability relation for the S1 nozzle more carefully (Fig. 17), we can see that the aeroelastic instability occurs at $n = 0.25$. When n is increased further, the nozzle will become full flowing at $n \approx 0.27$, and the system becomes stiffer than the mechanical structure itself, that is, $(\Omega/\omega)^2 > 1$, because the aerodynamic torque now acts to stabilize the nozzle.

Table 1 Resulting natural oscillating frequencies of the bending mode for the different spring setups with the Volvo S1 nozzle

Spring	Natural frequency, Hz
Superweak	25.2
Weak	36.3
Medium	45.0
Stiff	57.5
Rigid	120

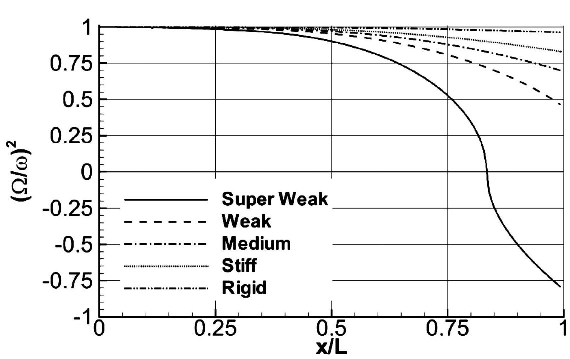

Fig. 16 Aeroelastic stability of the S1 nozzle for the different spring setups.

Table 2 Measured side-load magnitude vs frequency ratio between exciting load and mechanical system, peak at $n = 0.24$

Spring	ω_a/ω_n	M/M_{max}
Rigid	0.8	0.66
Stiff	1.7	0.63
Medium	2.2	0.48
Weak	2.8	0.45
Superweak	3.9	1

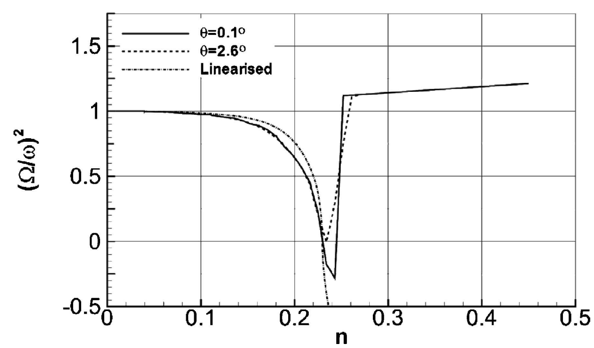

Fig. 17 Aeroelastic stability relation for the S1 nozzle hinged with the superweak spring.

Comparison with Experimental Data

In the following text, the presented model for the prediction of aeroelastic effects will be validated with respect to amplitude and frequency by comparing the model results to experimental data for the Volvo S1 nozzle and the Volvo S6 nozzle, respectively.

Volvo S1 Nozzle

Table 2 shows the measured side load at $n = 0.24$, obtained with the different spring setups. Schlieren videos show that the side load at this pressure ratio is connected to an oscillation of the whole separation shock system with a frequency of about $f_a = 100$ Hz ($\omega_a = 2\pi f_a$) near the nozzle exit.[3] When the aeroelastically stable systems (rigid to weak spring) are examined, the measured load decreases with decreasing spring stiffness, which can be explained by the classic forced response theory: The highest response is reached with the system's eigenfrequency f_n ($\omega_n = 2\pi f_n$) closest to the exciting frequency. However, the trend of decreasing response with increasing distance from the exciting frequency is clearly interrupted for the superweak spring. This behavior can be explained by aeroelastic amplification, and indeed, aeroelastic instability was predicted for the S1 nozzle with the superweak string in the preceding paragraph.

Volvo S6 Nozzle

In Fig. 18 the predicted frequency shift in the S6 nozzle is compared to experimental data. The experimental frequency shift of the eigenmode has been determined by applying the Welch method[18] for power spectral analysis on the measured steady-state side load at different constant pressure ratios. The sampling time was at least 8 s for each case to achieve sufficient frequency resolution. The frequency shift [Eq. (13)] for the S6 nozzle has been calculated with a tilt angle $\theta = 0.1$ deg, $p_i/p_a = 0.2$, and B extracted from an Euler calculation.

As indicated in Fig. 18, the theory predicts almost the same frequency shift as observed in experiments. The discrepancy is mainly due to the fact that both structural and gasdynamic damping was neglected in this analysis. Inclusion of damping in the analysis would increase the frequency shift, and the prediction should move closer to experimental data. However, the influence of the damping is only significant during steady-state operation, whereas during short

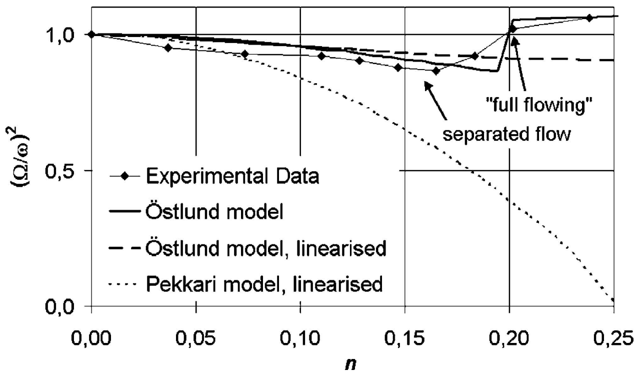

Fig. 18 Comparison between measured and calculated frequency shift for S6 nozzle.

transient phases, such as a rocket engine startup, the damping plays a minor role. Because damping plays a minor role, the simplification in the analysis becomes more valid.

Because of the simple separation model used, the sudden increase of the frequency is predicted somewhat later compared to experimental data. The gradient of the predicted frequency shift is also steeper compared with the experimental data. However, this is only a reflection of the single and very small tilt angle ($\theta = 0.1$ deg) used for calculating the frequency shift. In Fig. 17, it can be seen that the predicted gradient will be reduced for larger tilt angles. The increased system frequency observed in the experiments, when the nozzle becomes full flowing, is also well captured with the model.

In Fig. 18, the linearized frequency shift [Eq. (29)] calculated with the Östlund and Pekkari approaches are also shown to visualize how the frequency shift is overpredicted when determining B with SPT [cf. Eqs. (17 and 18)].

Pekkari[15,16] concluded in his work that the aeroelastic model results were qualitatively as well as quantitatively consistent with Vulcain side-load test results. As shown earlier, the aeroelastic coupling in the bending mode is not as strong as Pekkari anticipated. Today, we know that the high Vulcain side loads are caused by a transition between different separation patterns and not due to an aeroelastic phenomenon. Nevertheless, the experimental data as well as the modified model presented in this work show that aeroelastic effects can amplify the original side load and that the aeroelastic amplification is significant in weak nozzle structures. It has also been shown that the aeroelastic amplification is highly dependent on the nozzle contour.

The current work has only focused on aeroelastic effects coupled to the side-load phenomenon and not on possible aeroelastic instability of nozzle shell buckling modes. In recent tests of a flexible thin-walled ideal nozzle, Brown et al. found indications of a self-excited vibration loop coupling the ovalization mode to the flow separation.[19] So far, the mechanism for the observed response has not been clarified, and Brown et al. suggest that the lines laid down by Pekkari[15,16] should be followed.

Conclusions

Side-load phenomena in highly overexpanded rocket nozzles have been investigated with the help of extensive subscale testing at FFA. The starting point for side-load analysis is a deep understanding of the flow separation behavior in a rocket nozzle. Three different kinds of side loads have been analyzed.

The first kind of side loads analyzed are those created by random pressure fluctuations. When the pressure rise in the boundary layer is strong enough, the flow separates from the nozzle wall. This kind of flow separation can be seen in several basic flow experiments, for example, where a supersonic flow meets a forward-facing step. It can be seen that the boundary-layer separation in turbulent supersonic flows is not a stationary process, even if the main flow is stationary. Both the static and dynamic wall pressure behaviors have been studied. It has been shown in this paper that the behavior of the dynamic wall pressure constitutes a suitable criterion for detecting the beginning and end of the separation zone by analyzing the skewness and the kurtosis of its distribution. Furthermore, an error function approach was used for the prediction of pressure fluctuations in the separation zone.

The second kind of side loads analyzed are those created by transition of separation pattern. In nozzles with an internal shock that induces a cap shock pattern,[3] for example, compressed truncated ideal contours, parabolic contours, and directly optimized nozzles, a second separation pattern can occur. It is characterized by a reattachment of the separated flow to the nozzle wall and commonly referred to as RSS.[1–3,10,11] In the subscale test program performed, RSS was observed in the parabolic nozzles S1 and S3.

It is the rapid unsymmetrical transition that creates a side-load impulse acting on the nozzle structure. Because of the short duration of the aerodynamic side load, the pulse excitation theory[13] has been used when evaluating the mechanical load.

The third kind of side loads analyzed are those created by aeroelastic coupling. The model proposed by Pekkari[15,16] in the early 1990s has been analyzed and modified. Three-dimensional Euler simulations have been used, instead of small perturbation theory, when calculating the normalized pressure shift in a deflected nozzle. These new simulations have been compared with subscale test results of the deflected S1 and S6 nozzle and found to have good agreement. It has also been shown that the aeroelastic coupling can be significant in weak nozzle structures.

Acknowledgments

This work was funded by the Swedish National Space Board (SNSB) in the framework of the European Flow Separation Control Device (FSCD) program. The authors wish to thank SNSB for the funding and the members of the FSCD group for the fruitful technical discussions. Furthermore, special thanks are also extended to Lars Torngren and Johan Agrell at the Aeronautical Research Institute of Sweden for their excellent work with the experimental setup, manufacturing, and testing of the subscale nozzles.

References

[1]Mattsson (Östlund), J., Högman, U., and Torngren, L., "A Sub-scale Test Program on Investigation of Flow Separation and Side Loads in Rocket Nozzles," ESA-SP-426, Dec. 1998.

[2]Östlund, J., and Bigert, M., "A Subscale Investigation on Side-Loads in Sea Level Rocket Nozzles," AIAA Paper 99-2759, June 1999.

[3]Östlund, J., "Flow Processes in Rocket Engine Nozzles with Focus on Flow Separation and Side-Loads," Licentiate Thesis TRITA-MEK 2002:09, Dept. of Mechanics, Royal Inst. of Technology, Stockholm, 2002.

[4]Kistler, A., "Fluctuating Wall Pressure under a Separated Supersonic Flow," *Journal of the Acoustical Society of America*, Vol. 36, No. 3, 1964, pp. 543–550.

[5]Coe, C., Chyu, W., and Dods, J., "Pressure Fluctuations Underlying Attached and Separated Supersonic Turbulent Boundary Layers and Shock Waves," AIAA Paper 73-996, Oct. 1973.

[6]Adams, N. A., "Direct Simulation of the Turbulent Boundary Layer Along a Compression Ramp at $M = 3$ and $Re = 1685$," *Journal of Fluid Mechanics*, Vol. 420, 2000, pp. 47–83.

[7]Erengil, M. E., and Dolling, D. S., "Correlation of Separation Shock Motion with Pressure Fluctuations in the Incoming Boundary Layer," *AIAA Journal*, Vol. 29, No. 11, pp. 1868–1877.

[8]Barter, J. W., and Dolling, D. S., "Prediction of Fluctuating Pressure Loads Produced by Shock-Induced Turbulent Boundary Layer Separation," AIAA Paper 96-2043, June 1996.

[9]Dumnov, G. E., "Unsteady Side-Loads Acting on the Nozzle with Developed Separation Zone," AIAA Paper 96-3220, 1996.

[10]Hagemann, G., Terhardt, M., Frey, M., Reijasse, P., Onofri, M., Nasuti, F., and Östlund J., "Flow Separation and Side-Loads in Rocket Nozzles," 4th International Symposium on Liquid Space Propulsion, March 2000.

[11]Frey, M., "Behandlung von Strömungsproblemen in Raketendüsen bei Überexpansion," Ph.D. Dissertation Univ. of Stuttgart, Stuttgart, Germany, http://elib.uni-stuttgart.de/opus/volltexte/2001/800.

[12]Menter, F. R., "Zonal Two Equation k–ω Turbulence Models for

Aerodynamic Flows," AIAA Paper 93-2906, July 1993.
[13]Harris, C. M., and Crede, C. E., *Shock and Vibration Handbook*, McGraw–Hill, New York, 1976.
[14]Larson, E. W., Ratekin, G. H., and O'Connor, G. M., "Structural Response of the SSME Fuel Feedline to Unsteady Shock Oscillations," 52nd Shock and Vibration Symposium, 21–29 Oct. 1981.
[15]Pekkari, L.-O., "Aeroelastic Stability of Supersonic Nozzles with Separated Flow," AIAA Paper 93-2588, June 1993.
[16]Pekkari, L.-O., "Aeroelastic Analysis of Side-Loads in Supersonic Nozzles with Separated Flow," AIAA Paper 94-3377, June 1994.
[17]Kwan, W., "Aeroelastic Effects on a Bended Conical Nozzle," German Aerospace Research Center, DLR, Internal Rept. DLR-IB 645-2001-06, 2001.
[18]Welch, P. D., "The Use of Fast Fourier Transform for the Estimation of Power Spectra: A Method Based on Time Averaging over Short, Modified Periodograms," *IEEE Transactions on Audio Electroacoustic*, Vol. AU-15, June 1967, pp. 70–73.
[19]Brown, A. M., Ruf, J., Reed, D., and D'Agostino, M., "Characterization of Side Load Phenomena Using Measurement of Fluid/Structure Interaction," AIAA Paper 2002-3999, July 2002.

Paper 5

Accepted in revised form for publication in Applied Mechanics Reviews

Supersonic flow separation with application to rocket engine nozzles

J Östlund

Volvo Aero Corporation, S-461 81 Trollhättan, Sweden
Department of Mechanics, Royal Institute of Technology
S-144 00 Stockholm, Sweden ; jan.ostlund@volvo.com

B Muhammad-Klingmann

Department of Mechanics, Royal Institute of Technology
S-144 00 Stockholm, Sweden ; barbro@mech.kth.se

Abstract

The past decade has seen a qualitative advancement of our understanding of physical phenomena involved in flow separation in supersonic nozzles, in particular the problem of side-loads due to asymmetrical pressure loads, which constitutes a major restraint in the design of nozzles for satellite launchers. The development in this field is to a large extent motivated by the demand for high performance nozzles in rocket engineering. The present paper begins with an introduction to the physical background of shock-boundary-layer interactions in basic 2D configurations, and then proceeds to internal axisymmetric nozzle flow. Special attention is given to past and recent efforts in modeling and prediction, turning physical insight into applied engineering tools. Finally an overview is given on different technical solutions to the problem if separation and side-loads, discussed in the context of rocket technology.

NOMENCLATURE

Abbreviations

AM	Altitude Mode
CFD	Computational Fluid Dynamics
CTIC	Compressed Truncated Ideal Contour
CTPC	Compressed Truncated Perfect Contour
DNS	Direct Numerical Simulation
DOF	Degree of Freedom
FPSP	Fast Pressure Sensitive Paint
FSCD	Flow Separation Control Devices
FSS	Free Shock Separation
IR	Infrared Radiometry
LES	Large Eddy Simulation
MOC	Method of Characteristics
PIV	Particel Image Velocimetry
PSP	Pressure Sensitive Paint
RANS	Reynolds Averaged Navier-Stokes
RSS	Restricted Shock Separation
SM	Sea-level Mode
SPT	Small Perturbation Theory
SSLC	Shear Sensitive Liquid Crystals
SSME	Space Shuttle Main Engine
SWBLI	Shock-Wave Boundary Layer Interaction
TIC	Truncated Ideal Contour
TOC	Thrust Optimized Contour
TOP	Thrust Optimized parabolic Contour
TTM	Two Threshold Method
URANS	Unsteady Reynolds Averaged Navier-Stokes
2D	Two-dimensional
3D	Three-dimensional

Symbols

A	area
A_0 A_r A_s	turbulence model coefficients
C	separation point shift coefficient
C_μ	turbulence model coefficient
C_f	skin friction
D, d	diameter
F	force; thrust; generalized wall pressure function
f	frequency
f_1 , f_2	dimensionless functions used in the free interaction theory
$\mathcal{F}$	Fourier transform
$G(f)$	power spectral density
h	height
$H(f)$	transfer function
I	start of interaction
I_{sp}	specific impulse
J_y	mass of inertia around the y-axis
k	stiffness; coefficient; turbulent kinetic energy
L,l	length
$\dot{m}$	mass flow rate
m	mass
M	Mach number, torque
n	off-design pressure ratio: p_e/p_a
$\vec{n}$	wall normal vector
p	pressure
P	plateau point
q	dynamic pressure
R	gas constant; reattachment point
r	radius
Re	Reynolds number
s	non-dimensional length; arc length; dimensionless mean strain rate
S	surface; strain; separation point
S_{ij}	strain-rate tensor
Sr	Strouhal number
T	temperature
t	time
t_1	transition time
U, u	velocity
V, v	velocity
$\vec{w}$	wall displacement
W	spectral correlation function
x, y, z	cartesian-coordinates
$\vec{x}$	vector of location

Greek letters

α	angle
$\alpha_v, \bar{\alpha}_v$	turbulence model coefficients
β	shock angle

γ	specific heat ratio	geo	geometrical
δ	boundary-layer thickness	*i*	start of interaction
δ^*	displacement thickness	*ij*, *kk*	tensor indices
ε	area ratio; intermittence factor; turbulent dissipation	*max*	maximum
		min	minimum
ζ	damping coefficient	*m*	mechanical; measured
η	efficiency	*r*	recovery, reattachment
θ	bending, contour or flow angle; momentum thickness	*ref*	reference
		p	plateau
μ	dynamic viscosity	*s*	separation
ν	Prandtl-Meyer function	*SL*, *sl*	side-load
ρ	density	*sh*	shock
σ	RMS-value	*rec*	recirculating
τ	shear stress; wall angle; period	*t*	throat, turbulent
φ	circumferential angle	*td*	downstream throat
Ω,ω	angular frequency; specific dissipation rate	*w*	wall
		∞	free stream value
Ω_{ij}	rotation tensor	0	stagnation condition; initial
$\bar{\varpi}$	dimensionless vorticity invariant		

Subscript

a	ambient, aerodynamic
c	calculated
E,*e*	exit
E/A	conditional ensemble-averaged value

Superscripts

'	fluctuating
—	average value
$\rightarrow$	vector
^	Fourier transformed variable
~	normalized value

1 INTRODUCTION

The performance of rocket engines is highly dependent on the aerodynamic design of the expansion nozzle, the main design parameters being the contour shape and the area ratio.

The nozzle is the part of the rocket engine extending beyond the combustion chamber, see Figure 1. Typically, the combustion chamber is a constant diameter duct into which propellants are injected, mixed and burnt, for a sufficiently long time to allow complete combustion of the propellants before the nozzle accelerates the gas products. The nozzle is said to begin at the point where the chamber diameter begins to decrease.

Simply stated, the nozzle uses the stagnation temperature (T_0) and pressure (p_0) generated in the combustion chamber to induce thrust by accelerating the combustion gas to a high supersonic velocity (see Figure 1). For a given stagnation state, the nozzle exit velocity (v_e) that can be achieved is governed by the nozzle expansion ratio ε, defined as the ratio between the nozzle exit area and throat area, $\varepsilon = A_e/A_t$.

The thrust, F, produced by the nozzle can be expressed as

$$F = \dot{m} v_e + \left(p_e - p_a \right) A_e \tag{1}$$

where $\dot{m}$ is the mass flow through the nozzle and, v_e, p_e and A_e are the velocity, pressure and cross section area at the nozzle exit, and p_a is the ambient pressure. Optimum thrust is

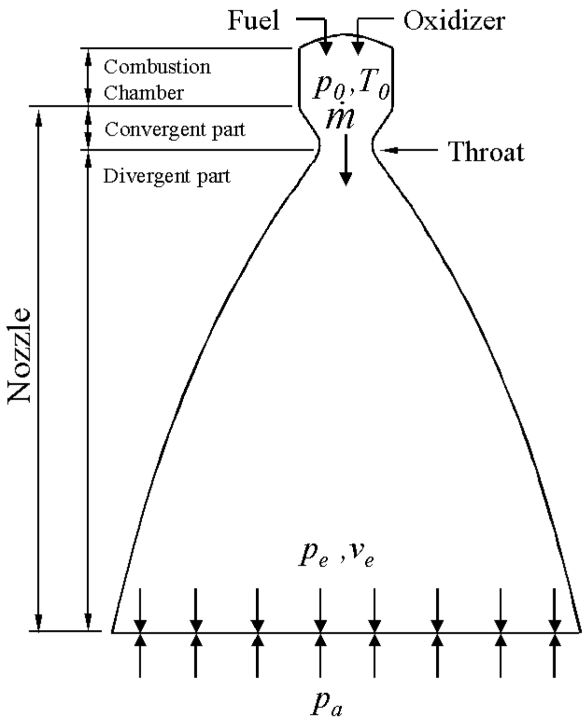

Figure 1. Definition of nozzle.

obtained when the nozzle exit pressure is adapted to the atmospheric pressure, p_e=p_a (so-called adapted or ideally expanded flow).

Performance is usually measured in terms of the so-called specific impulse, I_{sp}, defined as $F/\dot{m}$ [1], which is a measure of how well a given propellant flow rate is transformed into thrust**.**

Figure 2 shows how the specific impulse varies with flight altitude for given chamber conditions equal to that of the Vulcain engine, which is used as the first stage engine on the European Ariane 5 launcher [1]. The solid line without symbol is for ideally expanded nozzle flow, and the lines with symbols are for a nozzle with fixed expansion ratio. With a nozzle expansion ratio of ε=45, the flow becomes ideally expanded at an altitude of 10.000 m. From ground level up to this altitude the flow is overexpanded, i.e. $p_a > p_e$, while it is underexpanded ($p_a < p_e$) at higher altitudes.

It is obvious from Figure 2 that there is much to be gained in terms of performance, if the nozzle could adapt to the change of ambient pressure during ascent to give ideally expanded flow at all altitudes. However, for internal nozzles, this can only be achieved if the expansion ratio is continuously varied during fight, by varying either the throat or contour exit area. Different mechanical devices have been suggested for this purpose, but they are quite complex, heavy and difficult to cool, and have so far only been demonstrated

[1] Sometimes g_0=9.81 (m/s^2) is included in the denominator to make the performance value independent of the used unit system, i.e. the unit for I_{sp} changes from a velocity (m/s) to a time (s).

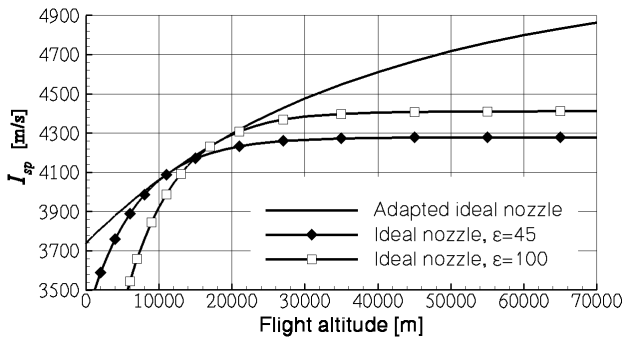

Figure 2. Performance versus altitude.

in experimental set-ups. Present day rocket engineering is still based on traditional bell-shaped nozzles with a fixed ε, chosen as a compromise taking into consideration performance and stability requirements throughout the flight trajectory.

Another possibility is to allow the nozzle to operate in a state of flow separation. In principle, a first or main stage rocket nozzle could be designed for much higher area ratios than those commonly used today, thereby achieving higher performance at high altitudes, where the main part of the trajectory takes place. However, this results in a significant overexpansion at sea level, which causes the flow to separate, generating large unsteady asymmetric forces – so-called side-loads –, which reduce the lifetime and safety margin of the rocket.

While the design of bell type nozzles under full flowing (attached flow) conditions is well supported by accurate and validated tools, the prediction of separation and side-loads is still an area open for research. With the present status of engineering, stable operation cannot be guaranteed unless the nozzle is fully attached at sea level, and one is therefore forced to accept a high degree of underexpansion at high altitude. If the level of side-loads could be reduced – or at least accurately predicted – this would allow for nozzles with higher ε, i.e. less underexpansion and hence higher vacuum performance. Figure 2 demonstrates this for a hypothetical nozzle with ε=100.

Different so-called Flow Separation Control Devices (FSCD) have been suggested during the past decade, most of which are based on reducing the side-loads by inhibiting the movement of the separation line. Some of these ideas are briefly reviewed in Sec. 10. The feasibility of such devices is presently the object of demonstration tests [2]. The main reason why such devices do not yet exist in full scale is that several basic questions regarding the nature of the flow separation phenomena and corresponding side-loads remain to be answered.

One thing that has become clear in this process is that the problem of side-loads is substantially more complex than previously realized. Side-loads are generated by a variety of physical mechanisms, depending on nozzle contour type, mechanical structure and ambient conditions. The first step towards reliable prediction of side-loads is therefore a correct assessment of which physical mechanisms are at work in a given situation. Focused work in this direction has been carried out during recent years by the joint European FSCD

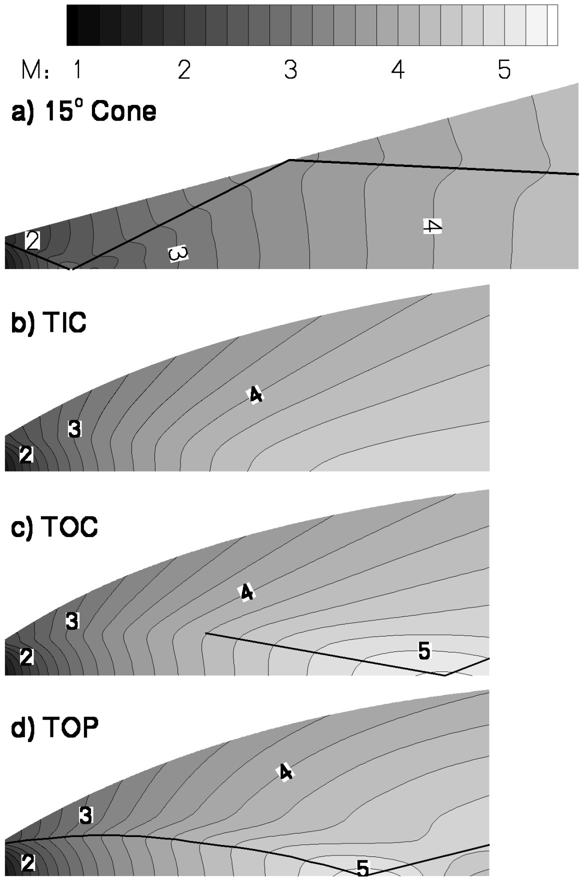

Figure 3. Mach number distribution in a 15° conical, TIC, TOC, TOP nozzle with ε=43.4 (From top to bottom). The thick line indicates the approximate position of the internal shock.

group[2] [3]. Valuable contributions have also been made by researchers in the Russian space industry during the past decade. In combination with the solid basis laid by US researchers in the past, these recent findings have led to a major break-through regarding the physical understanding of nozzle dynamics.

The objective of the present paper is to give an overview of phenomena involved in nozzle flow separation, along with some ideas on how to construct models and prediction tools based on a physically correct understanding of the origin of side-loads. The paper is organized as follows: Sec. 2 describes the characteristics of attached nozzle flow, depending on contour type. Sec. 3 and 4 present the basic physical phenomena, first for different generic cases of plane 2D geometries, then for curved axisymmetric internal nozzle flow. The present state-of-the-art concerning modeling and prediction of flow

[2] Research group with members from industry (ASTRIUM, SNECMA, Volvo Aero Corporation) and institutes (CNES, ESA, DLR, FOI, KTH, ONERA, LEA Poitiers), which investigates flow separation and side-load origins in nozzles by means of experiments and numerical analyses.

separation and side-loads in rocket engine nozzles is presented in Sec. 5, while Sec. 6 describes the phenomenon of aeroelastic instability, which needs to be considered under certain conditions. Aspects of scaling, testing and CFD modeling, which are specific for supersonic combusting flows, are highlighted in Sec. 7-9 respectively. Finally, Sec. 10 and 11 discuss the potential of modern concepts for flow separation control and directions of future research.

2 PHYSICS OF FULL FLOWING SUPERSONIC NOZZLES

2.1 Nozzle contour types and flow field

The final design of a rocket nozzle configuration depends on a number of considerations, such as performance requirements, maximum acceptable engine mass, limitations on the main dimensions, cooling performance, lifetime considerations, manufacturing methods, etc. Detailed examination of all these aspects requires knowledge in several engineering fields, not considered in this work. However, it should be pointed out that one of the most basic demands in the design loop of a real rocket nozzle is to minimize the weight. With increasing nozzle weight, a number of problems arise. The nozzle will be more difficult to handle and fabricate. The loads and power required for gimbaling (vector control) and moving the engine increase, and thereby the weight and complexity of the thrust vectoring system etc. It is therefore necessary to keep the nozzle length or surface area at a minimum. The main gas dynamic problem lies in optimally contouring the nozzles in order to maximize efficiency and the main design methods will be outlined below. Analysis of rocket nozzle flows includes radiative heat loss, chemical reactions due to incomplete combustion, and chemical properties of the exhaust gases. However, a detailed description of these aspects is not the topic of the current work.

From a purely inviscid point of view, nozzle contours can be classified into different types, each producing its own specific internal flow field. It is essential for the designer to understand these features, since the internal flow field determines the flow separation and side-load behavior. Figure 3 shows examples of the Mach number distribution in some of the most common nozzle types, which will be discussed below.

2.1.1 The initial expansion region

The inviscid hyperbolic Euler equations are usually solved using the method of characteristics (MOC) [6], which produces a design with particular physical characteristics. In the present-day rocket nozzle community, this is the most commonly used method for generating nozzle contours. The basis in all MOC design methods is the kernel, which is determined by the initial expansion that occurs along the throat contour TN, see Figure 4. The throat is usually designed as a circular arc. Using a transonic-flow analysis, an initial data line, TO, with a Mach number slightly greater than unity can be defined at the throat. Given the flow condition along TO and the solid boundary TN, a kernel flow field TNKO can be generated with the method of characteristics. Since the flow downstream of TO is supersonic, the kernel is entirely determined by the throat conditions, and this in turn determines the character of the downstream flow field.

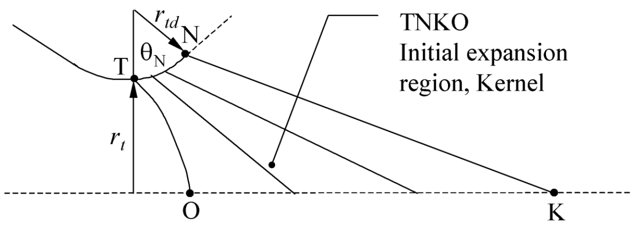

Figure 4. Initial expansion region, kernel.

2.1.2 *The conical nozzle*

The conical nozzle, Figure 3a, has historically been the most common contour for rocket engines since it is simple and usually easy to fabricate. The exhaust velocity of a conical nozzle is essentially equal to the one-dimensional value corresponding to the expansion ratio, except that the flow direction is not axial all over the exit area. Hence, there is a performance loss due to the flow divergence.

Assuming conical flow at the exit, Malina [4] showed that the geometrical efficiency is

$$\eta_{geo} = \frac{1+\cos\alpha}{2} \tag{2}$$

where α denotes the nozzle cone half angle. The length of the conical nozzle can be expressed as

$$L_{\alpha^\circ,cone} = \frac{r_t\left(\sqrt{\varepsilon}-1\right)+r_{td}\left(\sec\alpha-1\right)}{\tan\alpha} \tag{3}$$

Typically, cone half angles can range between 12° to 18°. A common compromise is a half angle of 15°. A 15° conical nozzle is often used as a reference in comparing lengths and performance of other types of nozzles. A term often used when designing bell nozzles is the “percent bell”. The phrase refers to the length of the nozzle compared to a 15^{o} half-angle conical nozzle with the same ε.

Extensive nozzle research was performed by German scientists in the late 1930’s and early 1940’s [5]. Taking into account all aspects of design, they found no significant advantage in using more complex contours. However, this holds only for nozzles with low expansion ratios like that of the V-2 rocket [1]. Due to its high divergence losses, the conical nozzle is nowadays mainly used for short nozzles like solid rocket boosters and small thrusters, where simple fabrication is preferred over aerodynamic performance.

2.1.3 *Ideal nozzle*

An ideal nozzle is a nozzle that produces an isentropic flow (i.e. without internal shocks), and gives a uniform exit velocity. Such a nozzle contour can be designed using the method of characteristics (MOC). Figure 5 shows a sketch of the flow in an ideal nozzle.

After the initial expansion TN, the contour NE turns the flow in the axial direction. TN also defines the Mach number at K, which is equal to the design Mach number obtained at the exit. With the characteristic line NK defined and the condition that the characteristic

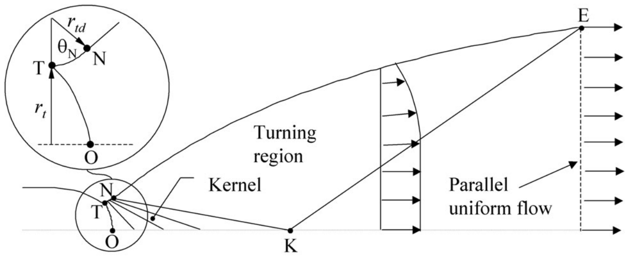

Figure 5. Basic flow structures in an ideal nozzle.

line KE is a uniform exit characteristic it is possible to use MOC to construct the streamline between N and E, which patches the flow to become uniform and parallel at the exit and thus complete the nozzle design.

2.1.4 Truncated Ideal Contoured nozzles (TIC)

The ideal nozzle is extremely long and is therefore not suitable for rocket applications. The huge length is necessary to produce a one-dimensional exhaust profile. However, since the thrust contribution from the last part of the contour is negligible due to the small wall slope, a more practical rocket nozzle is obtained by truncating the contour. Such a contour is called truncated ideal contour (TIC). The truncation can be made quite far upstream. As long as the kernel region is not truncated, a TIC nozzle will have a central part where the exit velocity profile is uniform and parallel, and will only be divergent in a region close to the wall, Figure 5. As an example the Mach number distribution in a TIC nozzle is shown in Figure 3b. Examples of TIC nozzles are the LR-115, Viking and RD-0120 nozzle used on the American Saturn C-1, European Ariane 4 and the Russian Energia launcher respectively [1].

Ahlberg *et al.* [7] proposed a graphical technique for selecting optimum nozzle contours from a family of TIC nozzles. With this method, a set of ideal nozzle contours is synthesized in a plot together with lines representing constant surface area, exit diameter, length and vacuum thrust coefficient respectively, as illustrated in Figure 6a. The contour shapes are computed using MOC (which assumes inviscid flow), however in calculating the thrust coefficient all losses are taken into account. Figure 6b shows how to use the graph to select the most efficient nozzle shape and truncation point within given constraints, such as expansion ratio (or exit radius), length and surface area (which affect weight). The bow-shaped curves are curves of constant thrust (C_F). Point A in Figure 6b is where the highest iso-C_F curve is tangent to a line of constant exit radius. The nozzle shape and truncation length corresponding to this point give the highest possible thrust for a given exit radius. Similarly, one finds the highest iso-C_F curve tangent to a line of given surface area in B, and to a line of given length in C. Point D is the tangent point between an iso-C_F curve and a nozzle contour, showing where to truncate a given nozzle shape to obtain the highest performance if no other constraints are given. If it is made longer, C_F will decrease due to viscous losses. In most practical situations however, length and weight limitations will prompt the choice of a much shorter nozzle.

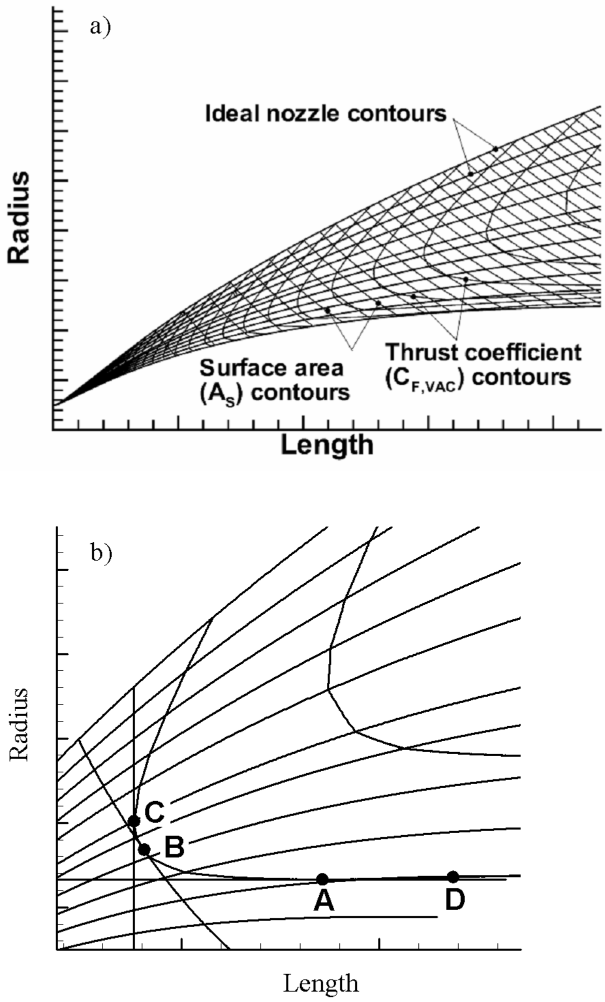

Figure 6. a) Ideal nozzle contours, b) Truncation point to obtain maximum performance for a given constraint on expansion ratio (A), surface area (B) or length (C).

2.1.5 Thrust optimized contoured nozzles (TOC)

A direct and elegant approach of designing nozzle contours is the calculus of variations. Guderley & Hantsch [8-9] formulated the problem of finding the exit area and nozzle contour to produce the optimum thrust, for prescribed values of the nozzle length and the ambient pressure. However, the method was not widely adopted until a simplified solution method was presented by Rao [10]. Therefore the obtained nozzle contour is often labeled a Rao nozzle in the west. In Russia this nozzle type is better known as a Shmyglevsky nozzle since Shmyglevsky [11-14] independently formulated the same method in Russia. The basic idea of the Rao-Shmyglevsky nozzle, or the thrust-optimized contour (TOC) as

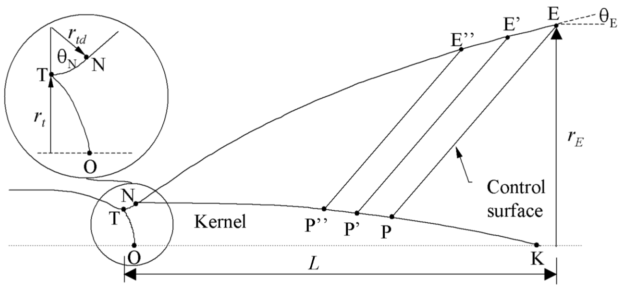

Figure 7. Thrust optimized nozzle contour.

it is sometimes called, is illustrated in Figure 7. First, a kernel flow is generated with MOC, for a variety of θ_N and a given throat curvature r_{td}. For given design parameters (such as wall exit Mach number and ε or nozzle length and ε) the points P and N can now be found by satisfying the following conditions concurrently:

1. Mass flow across PE equals the mass flow across NP.
2. The resulting nozzle gives maximum thrust.

By using the calculus of variations, these conditions are formulated as specific relations that must be fulfilled along PE and NP see e.g. Reference [10].

Once N and P are known, the kernel line TNKO is fixed, and the contour line NE is constructed in the following manner: By selecting points P', P'', etc. along line NK, a series of control surfaces P'E', P''E'', etc. can be generated to define E', E'', etc. along the contour NE.

It should be noted that the method produces a shock free flow in the region NPE governing the wall pressure. If point P is equal to point K, the nozzle is by definition an ideal nozzle. However, when P≠K a more drastic turning of the flow is obtained compared with an ideal nozzle, and weak compression waves formed in region NPE will coalesce into a right running shock downstream of the control surface PE. This is illustrated in Figure 3c, which shows the Mach number distribution in a TOC nozzle and the approximate position of the internal shock.

The TOC nozzle has a significant increase in geometric efficiency compared with a 15° half-angle conical nozzle with the same expansion ratio see e.g. Huzel & Huang [15]. The corresponding length is in general between 80%-100% of the conical one.

2.1.6 Parabolic bell nozzles (TOP)

Since the computation leading to the TOC nozzle is rather complicated and the resulting contour can only be described by a co-ordinate list, Rao [16] proposed a skewed parabolic-geometry approximation to the TOC nozzle from the inflection point to the nozzle exit

$$\left(\frac{r}{r_t}+b\frac{x}{r_t}\right)^2+c\frac{x}{r_t}+d\frac{r}{r_t}+e=0 \qquad (4)$$

Such nozzles are often referred as Thrust Optimized Parabolic (TOP) nozzles. With a skewed parabola the nozzle contour is entirely defined by the five independent variables

r_{td}, θ_N, L, r_E, and θ_E, see Figure 7. By freely varying these parameters, any type of parabolic contour can be generated, but any parabolic contour is not necessarily a faithful approximation to a TOC, and may in fact result in serious performance losses. It is a common misunderstanding that any parabolic bell nozzle of 80% length can replace a 15° conical nozzle to yield increased performance, however, this is not generally the case. Rao [17] examined nozzles with an expansion ratio of ε=100 and found that an arbitrarily chosen parabolic nozzle of 80% length yielded only 0.07% higher inviscid specific impulse than the conical one. He also showed that this parabolic contour could be replaced with a much smaller TOC nozzle, with the same length and performance but a much smaller expansion ratio, ε=80.

In Figure 3d the Mach number distribution in a parabolic-geometry approximation to the TOC nozzle in Figure 3c is shown. The flow conditions along the wall are almost equal and the performance is only slightly less then the TOC nozzle. There is however one main difference between the two nozzle flows. At the point N where the circular arc is continued with the parabolic curve, the discontinuity in contour curvature generates compression waves that coalesce into an internal shock upstream of the last left running characteristic line. In a TOC nozzle this shock is formed downstream of the last left running characteristic line and hence has no influence of the wall pressure. In contrast, in a TOP nozzle the internal shock appears upstream of this characteristic line (see the comparison between TOP and TOC nozzle in Figure 3) and hence affects the flow properties at the wall, given a slightly higher wall pressure at the nozzle exit. This feature of TOP nozzles has proven to be useful for sea level nozzles where a margin against flow separation is important. For this reason the Vulcain and the SSME nozzle (used on the European Ariane 5 launcher and the American Space Shuttle respectively [1]), were designed with parabolic contours. The initial contour design of the SSME was actually a TOC. However, with this design the wall pressure at the exit would be about 31 % of the ambient pressure at sea level, i.e. in a range where past experience showed that nozzle flow separation is likely to occur. In order to avoid problems with flow separation, an additional margin in exit pressure was sought. A parametric study of different TOP contours then resulted in a contour where the additional flow turning (and the accompanying internal shock) resulted in a pressure increase of 24% at the nozzle exit, and hence an acceptable flow separation margin, at a cost of only 0.1% in nozzle efficiency compared with the initial TOC design.

2.1.7 Compressed Truncated Ideal Contoured nozzles (CTIC)

In 1966 Gogish [18] suggested a method to design extremely short nozzles. The idea is to compress a TIC nozzle. He suggested that such a compressed truncated ideal contour (CTIC) might have higher performance than a TOC nozzle for the same envelope. A CTIC nozzle – or a compressed truncated perfect contour (CTPC) as it is sometimes labeled – is obtained by compressing a TIC nozzle linearly in the axial direction to the desired nozzle length. This produces a discontinuity in the nozzle slope, which can be eliminated by a cubic equation, which smoothly connects the linearly compressed curve with the initial circular curve. The above procedure yields a nozzle that has a more rapid initial expansion followed by a more severe turn back, as compared to the TIC nozzle. As a consequence, strong right-running compression waves will propagate from the compressed contour into the flow field. If the compression is strong enough, the characteristic lines will coalesce and form a right running oblique shock wave. The shock wave will increase the static pressure as the flow crosses the shock wave. If the shock wave lies near the nozzle wall, the pressure along the wall will be increased, thus increasing the nozzle thrust. This effect is the mechanism Gogish considered when he suggested that the compressed nozzle might yield higher performance than a TOC nozzle. However, as the study by Hoffman [19] showed, this is not the case. Hoffman found that the TOC nozzle is superior to the CTIC nozzle. For some designs, however, the difference in performance was quite small indicating that an optimum CTIC nozzle is certainly a good propulsive nozzle. As an example the LE7A, used on the Japanese H-IIA launcher [1], is a CTIC nozzle.

2.1.8 Directly optimized nozzles

The classical design methods described above are inviscid. The hyperbolic Euler equations are usually solved using MOC, which produces a design with particular physical characteristics. After completing the inviscid design, a boundary layer correction is added to compensate for the viscous effects. In the present-day rocket nozzle community, this is still the most commonly used method for generating nozzle contours and determining loads and performances.

However, modern advances in computational technology allow scientists nowadays to use Navier-Stokes (N-S) solvers in parallel with direct optimization techniques in the design loop. Direct optimization based on N-S-solvers makes it possible to include the different types of losses (such as viscous losses, kinetic losses, etc.) in the calculation rather than just accounting for them *a posteriori*. The drawback is that the solution is not based on any physical knowledge about the flow field. Since the contour derived with this method deviates from an ideal contour, compression waves will be generated, which may converge to form an internal shock inside the nozzle in the same way as in TOP or CTIC nozzles. A compromise is to implement direct optimization in MOC-based codes such as TDK [20]. However, in conventional first stage rocket engine nozzles, direct optimization gives only a marginal improvement compared to traditional “optimization” of the Alhlberg-type – typically the performance gain does not exceed 0.1% [21-22]. In other words, the choice of contouring method has in fact little influence on the performance of conventional nozzles.

However, this is not the case for all types of rocket nozzles. For engines operating on metal-containing fuels (liquid or solid), high expansion ratio nozzles can at present only be contoured by direct optimization methods, since the Rao-Smyglevsky or the Ahlberg method do not rule out the precipitation of metal oxide particles on nozzle walls, and the consequent loss of specific impulse, eroding and destroying the contour [23-24]. Another example where direct optimization must be used is for low Reynolds number nozzles (such as small satellite thrusters), since the classical approach with a boundary layer correction of an inviscid designed contour breaks down when the viscous effects are dominant [25].

One advantage with direct optimization is that it would, in principle, be possible to include any number of criteria, e.g. separation margin and side-load limits, in the optimization process, provided that mathematical descriptions of these phenomena are available. Such schemes do not exist today, but will become feasible as reliable methods for separation and side-load prediction are developed.

2.1.9 Concluding remarks

It should be mentioned that the choice of contour type depends upon the application, i.e. if the nozzle is to be used as an upper-stage, first-stage or booster nozzle etc. For first-stage nozzles, which operate from sea level to high altitudes, this difference is essential since the internal shock discussed above has a strong influence on the global shock pattern of the exhaust plume and determines the flow separation shock pattern and the side-load behavior of the nozzle, see Sec. 4 and 5. If upper-stage engines are not used for stage separation there is no considerable flow separation at start up, hence the choice of contour has a much smaller importance.

2.2 Shock patterns in over- and underexpanded nozzle flow

As discussed in the introduction, the flow issuing from the nozzles is only ideally expanded or adapted to the surrounding flow when the pressure of the surrounding atmosphere is equal to the pressure of the nozzle jet. Most part of the operational time of a rocket engine, the supersonic discharge from the nozzle occurs under off-design conditions, where the nozzle exit pressure, p_e, differs from that of the atmosphere, p_a. Here both overexpansion of the gas in the nozzle ($p_e<p_a$) and underexpansion ($p_e>p_a$) are possible. In both cases this results in a system of compression and expansion waves around the exiting jet, with consequent density discontinuities, which gradually achieve a match between the pressure in the jet and the pressure of the surrounding medium. It is customary to describe the conditions for off-design supersonic discharge by the degree of departure from the theoretical value, which is given as the ratio between the nozzle design exit pressure to the pressure in the surrounding medium

$$n = p_e / p_a \tag{5}$$

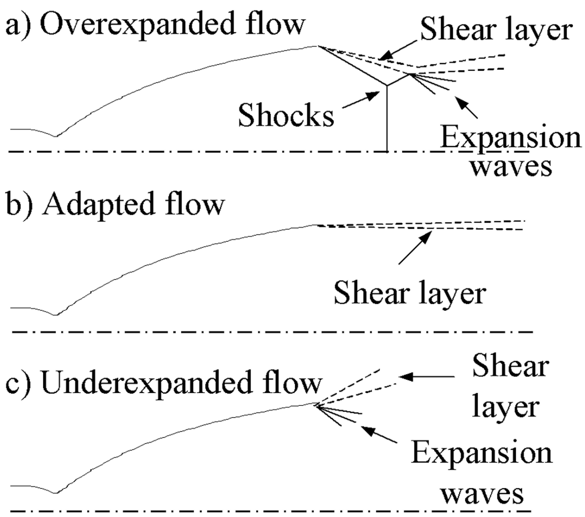

Figure 8. Illustration of exhaust plume patterns at different operational conditions.

An illustration of the exhaust plume patterns at underexpanded ($n>1$), adapted ($n=1$) and at overexpanded -but not separated flow - condition ($n<1$) is given in Figure 8. The actual shape of the overexpansion shock pattern depends on the nozzle contour type (internal flow field) and degree of overexpansion.

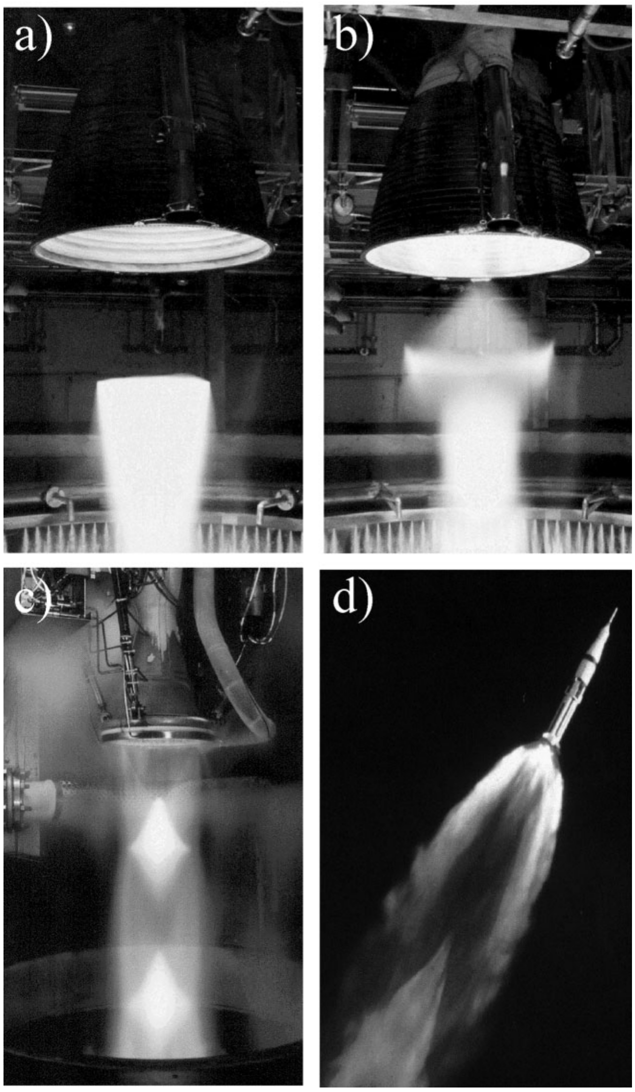

Figure 9. Exhaust plume patterns. Overexpanded flow: a) Vulcain, with classical Mach disc. b) Vulcain, with cap-shock pattern. c) RL10-A5, with apparent regular reflection. Underexpanded flow: d) Saturn 1-B photographed during launch. From Hagemann *et al.* [27]. (Courtesy photos: SNECMA, CNES, NASA).

2.2.1 *Exhaust plume patterns*

Nozzles of high performance rocket engines in use for first- or main stage propulsion, e.g. the American SSME, the European Vulcain, or the Japanese LE-7, operate from sea-level with one bar ambient pressure up to near vacuum. At ground level, such engines operate in an overexpanded flow condition with an ambient pressure higher than the nozzle exit pressure. As the ambient pressure decreases during ascent, the initially overexpanded exhaust flow passes through a stage where it is equal to the ambient pressure, and then finally becomes underexpanded.

Figure 9 and Figure 10 shows photographs of nozzle exhaust flows during these two types of off-design operation.

In the case of overexpanded flow, the exhaust flow adapts to the ambient pressure through a system of oblique shocks and expansion waves, which leads to the characteristic barrel-like form of the exhaust plume. Different shock patterns in the plume of overexpanded rocket nozzles have been observed, the classical Mach disc, Figure 9a, the cap-shock pattern, Figure 9b and the apparent regular shock reflection at the centerline, Figure 9c.[3] At high altitudes, the underexpansion of the flow results in a further expansion of the exhaust gases behind the rocket as impressively illustrated in Figure 9d, taken during a Saturn 1-B launch.

In ideal and TIC nozzles, a transition between Mach disc and the apparent regular shock reflection can be observed as the degree of overexpansion is decreased [28]. This is because a nozzle flow with a small overexpansion is able to adapt to the ambient pressure without forming a strong shock system (i.e. the Mach disc).

The difference between the Mach disc and cap-shock pattern is shown schematically in Figure 10. The cap-shock pattern is only observed in nozzles featuring an internal shock, such as TOC, TOP and CTIC nozzles. Figure 9b proves the existence of the cap shock pattern in the exhaust plume of the Vulcain nozzle, which has a parabolic contour [29-31]. This is the pattern which first appears at the nozzle exit during start up. Upon increasing the combustion chamber pressure, the flow becomes less overexpanded. At some point the internal shock intersects the centerline and a transition to a Mach disc pattern takes place, see Figure 9a and Figure 11.

Recent sub-scale experiments performed within the European FSCD group also confirmed the stable existence of the cap shock pattern in the plume of parabolic sub-scale rocket nozzles [2, 32-34].

Figure 10a-c show Schlieren images of the exhaust plume of parabolic sub-scale nozzles tested at DLR, ONERA, and FOI. For comparison, the exhaust plume of a truncated ideal nozzle is also shown where the classical Mach disc is clearly visible.

The above described shock patterns are not only an exhaust plume phenomenon. They also exist inside the nozzle at highly overexpanded flow conditions, when the jet is separated from the nozzle wall. As will be shown later in Sec. 4 and 5, the different shock patterns determine the characteristics of the nozzle separation and side-loads.

---

[3] In case of axisymmetrical flow, a pure regular reflection at the centreline is not possible. Instead, a very small normal shock exists at the centerline.[26]

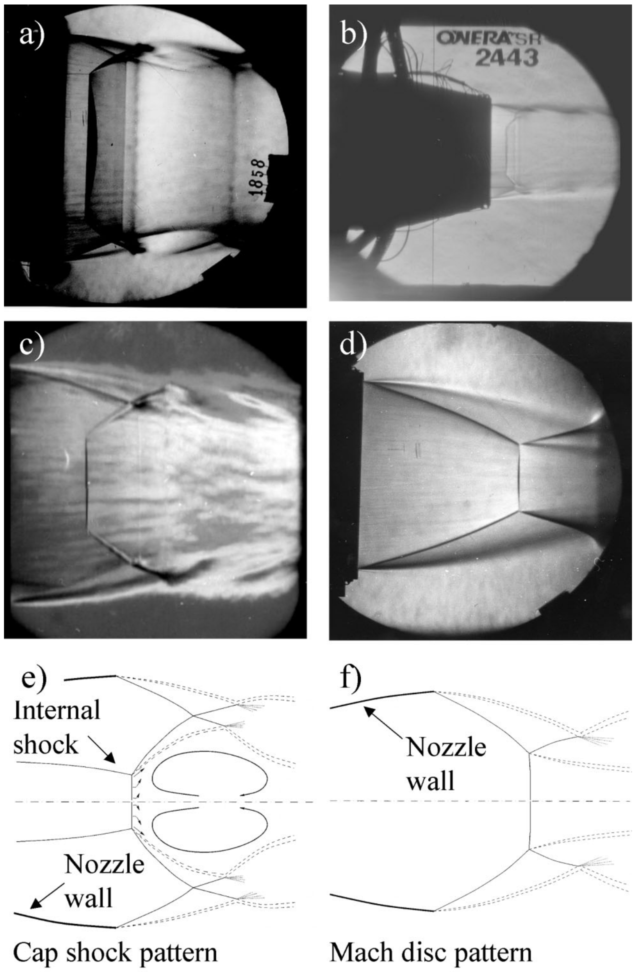

Figure 10. Exhaust plume patterns for subscale nozzles. Parabolic nozzles with cap-shock pattern: a) VOLVO S1. b) TOP ONERA. c) P6 TOP DLR. d) TIC nozzle with Mach disc: VOLVO S6. e) sketch of cap shock pattern. f) sketch of Mach disc pattern. (Courtesy photos: DLR and ONERA)

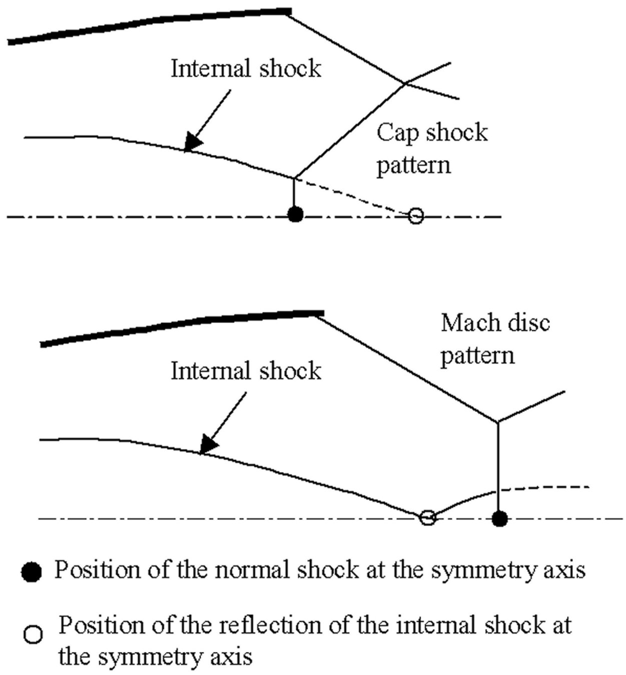

Figure 11. Illustration of transition between cap shock and Mach disc pattern: The transition occurs when the normal shock hits the reflection point of the internal shock at the symmetry axis.

3 SHOCK-WAVE TURBULENT BOUNDARY LAYER INTERACTION

When a supersonic flow is exposed to an adverse pressure gradient it adapts to the higher-pressure level by means of a shock wave system. Basically, separation occurs when the turbulent boundary layer cannot withstand the adverse gradient imposed upon it by the inviscid outer flow. Thus, flow separation in any supersonic flow is a process involving complex Shock Wave Boundary Layer Interactions (SWBLI). SWBLI is an intrinsically unsteady and three-dimensional phenomenon, which may generate large fluctuating forces on the structure. In the following we will first discuss observations and basic models for determining the mean pressure distribution in the separation zone, and thereafter some observations concerning the fluctuating pressure field.

3.1 Basic interactions

Shock wave boundary layer interaction has been extensively studied in the last fifty years with the help of basic experiments, see e.g. References [35-81]. Three nominally basic configurations involving interaction between a shock wave and a turbulent boundary layer in supersonic flows, which have been studied extensively, are represented schematically in Figure 12. In all of these cases, the incoming flow is a uniform stream along a flat plate.

The first and conceptually most simple configuration is the wedge (or ramp) flow. Here, a discontinuity in the wall direction is the origin of a shock wave through which the supersonic flow undergoes a deflection equal to the ramp angle α, Figure 12a.

The second type is separation induced by a step of height *h* facing the incoming flow, see Figure 12b. Such an obstacle provokes separation of the flow at point *S*. The rapid pressure rise accompanying separation gives rise to a shock wave emanating from a place very close to the separation point *S*, and a separated zone develops between the separation point *S* and the step.

The third type is separation caused by the impingement of an oblique shock on a smooth wall, see Figure 12c. The incident shock causes a deflection of the incoming flow, and a reflected shock is formed, as the downstream flow tends to become parallel to the wall.

It has been shown in many experiments, that the upstream part of the shock / boundary

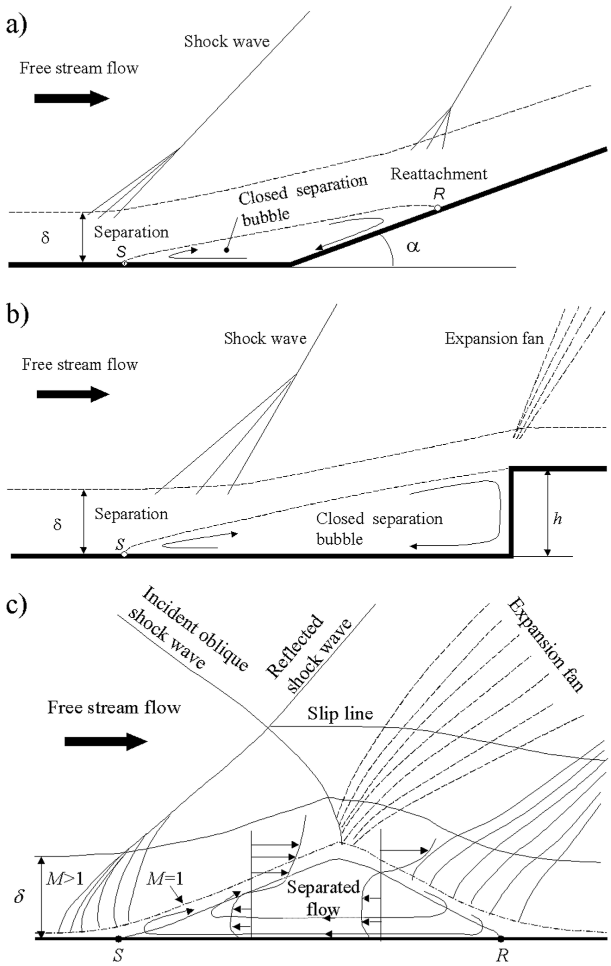

Figure 12. Basic shock/boundary layer interactions in supersonic flow. a) Ramp flow, b) Step induced separation and c) Shock reflection, adopted from Delery *et al*. [82].

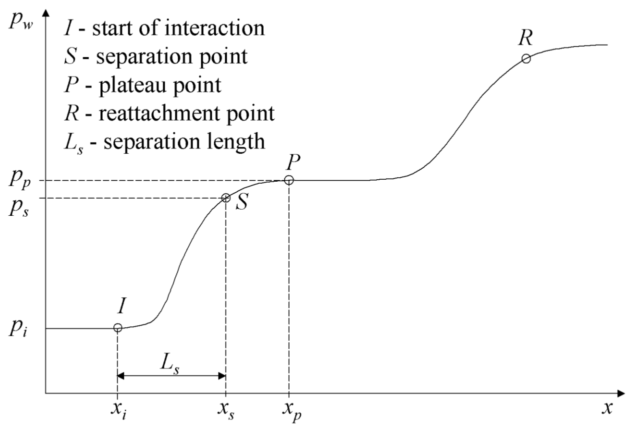

Figure 13. Typical static wall pressure distribution observed in ramp, shock reflection and step flow; adopted from [52, 83].

layer interaction is nearly independent of the cause of separation, whether it is a solid obstacle or an incident shock wave [36,39,82]. In fact the features of the static wall pressure for the above different experimental configurations are the same, and are illustrated in Figure 13. The wall pressure has a steep rise shortly after the beginning of the interaction at *I*. The flow separates from the wall at point *S*, located a distance L_s from *I*. If the separated flow scale is large enough, the wall pressure then gradually approaches a plateau with almost constant pressure, labeled the plateau pressure p_p. The extent of this plateau reflects the size of the closed recirculation bubble, and p_p thus corresponds to the wall pressure in the bubble. A second pressure rise can be observed as the reattachment point at *R* is approached. These characteristics are independent on the downstream geometry, as already mentioned, everything happens as if the flow were entirely determined by its properties at the onset of the interaction.

3.2 The concept of free interaction

This observation of a general form of the pressure distribution over the interaction region led Chapman *et al*. [39] to formulate the concept of free interaction. They considered flow separation caused by the interaction between the boundary layer formed in a plane, adiabatic, supersonic uniform flow and a shock wave. The Mach number M_i and the pressure p_i define the inviscid uniform flow. The skin friction coefficient (C_f), the displacement thickness (δ^*) etc. define the local characteristics of the boundary layer. The deflection angle of the mean flow in the streamwise direction is called θ, see Figure 14.

Chapman *et al.* made two assumptions about the flow in the interaction domain:

1. The flow structure follows a law of similarity
2. The deviation of the external non-viscid flow corresponds precisely to the displacement effect of the boundary layer.

By integrating the simplified boundary layer momentum equation at the wall

$$\frac{\partial \tau_w}{\partial y} = \frac{\partial p_w}{\partial x} \tag{6}$$

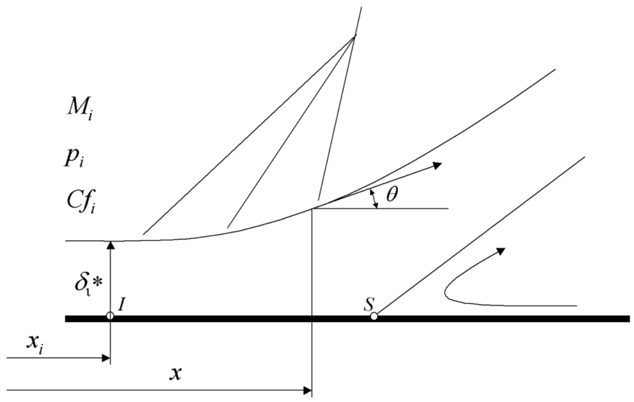

Figure 14. Flow separation in uniform flow, notations.

from $x=x_i$ (see Figure 14), Chapman found the streamwise wall pressure evolution could be written in a generalized form as

$$F(s) = \sqrt{f_1 \cdot f_2} = \sqrt{\frac{p-p_i}{q_i}\frac{\nu(M_i)-\nu(M)}{C_{fi}}} \tag{7}$$

Where $s=(x-x_i)/l$, l is a length scale characterizing the extent of the domain, q_i is the dynamic pressure, ν is the Prandtl Meyer function and $f_1(s)$ and $f_2(s)$ are non-dimensional functions characterizing the outer streamline deflection and the pressure rise respectively. C_{fi} is the skin friction coefficient at point I, where the interaction begins. Chapman then expressed the variation of $\nu(M_i)$-$\nu(M)$ as a function of $(p-p_i)/q_i$, linearised for small pressure changes $p-p_i$ (see e.g. Shapiro [6] p. 436) and finally obtained

$$F(s) = \frac{p-p_i}{q_i}\sqrt{\frac{\sqrt{M_i^2-1}}{2C_{fi}}} \tag{8}$$

The function $F(s)$ is assumed to be a universal function, independent of Mach number and Reynolds numbers, to be determined from experiments. Figure 15 shows the generalized wall pressure correlation function $F(s)$ obtained by Erdos & Pallone [84]. The axial distance from the onset of the interaction has been normalized with the separation length i.e., $l=L_s=x_s-x_i$. In the original work by Erdos & Pallone the distance to the pressure plateau of the extended separated flow was used as the characteristic length scale i.e., $l=L_p=x_p-x_i$. From the figure the following particular values of F can be found, $F_s=F(s=1)=4.22$ at the separation point (S) and $F_p=F(s=4)=6.00$ at the plateau point (P).

Chapman also showed that the characteristic length l could be expressed as

$$\frac{l}{\delta_i*} = \frac{F(s)}{\nu(s=0)-\nu(s)} \cdot \sqrt{\frac{f_1(s)}{f_2(s)}} \tag{9}$$

At the separation point S (s=1), this relation can be evaluated as

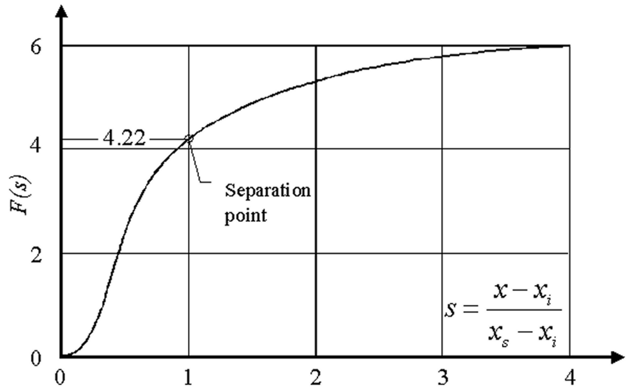

Figure 15. Generalized wall pressure correlation function *F(s)* for uniform turbulent flow, by Erdos & Pallone [84].

$$\frac{L_s}{\delta_i *} = k \frac{F_s}{\nu_i - \nu_s} \tag{10}$$

or in linearised form as

$$\frac{L_s}{\delta_i *} = k \sqrt{\frac{2}{C_{fi}\sqrt{M_i^2 - 1}}} \tag{11}$$

Here k is the value of $\sqrt{f_1 / f_2}$ evaluated at s=1. From different experiments an average value of k=0.37 has been obtained [82]. However, the experimental data have a significant scatter around this value, k=0.27–0.57 has been observed, presumably due to the difficulty of accurately determining the separation length, which in turbulent flows is very short, typically a few boundary layer thicknesses.

3.2.1 Separation criteria based on free interaction theory

The free interaction theory can be used to establish separation criteria for supersonic flow. The best known is the type of criteria first proposed by Erdos & Pallone [84] 1962. They determined the critical pressure rise between the pressure p_r at location $s=r$ and p_i (s=0) by assuming that the separation occurs when the pressure jump p_r/p_i is

$$\frac{p_r}{p_i} = 1 + F_r \gamma M_i^2 \sqrt{\frac{C_{fi}}{2\sqrt{M_i^2 - 1}}} \tag{12}$$

This equation is obtained by rewriting Eq. (8) and using the fact that the dynamic pressure can be written as

$$q_i = \tfrac{1}{2}\rho_i u_i^2 = \tfrac{1}{2} p_i \gamma M_i^2 \tag{13}$$

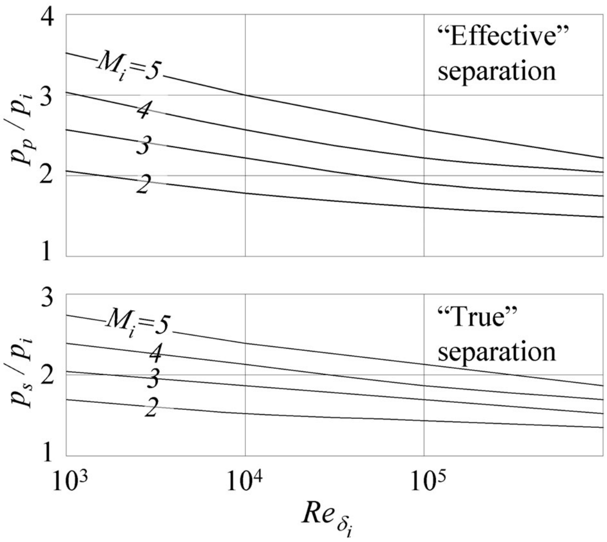

Figure 16. Separation pressure obtained with the free interaction theory for uniform flow. "Effective separation": F=6 (point P); "True separation" (point S): F=4.22. (from Östlund [85])

The pressure rise, corresponding to "true" incipient separation (point S in Figure 13) is obtained with $F_r=F_s=4.22$, while the "effective" incipient separation (point P in Figure 13) is obtained with $F_r=F_p=6.0$. The "true" incipient separation point (F_r=4.22) corresponds to the first appearance of a tiny separation bubble, while the "effective" incipient separation (F_r=6.0) corresponds to a stage where the separation bubble has reached a size large enough to produce a significant change in the flow field. The latter (which is the value used by Erdos & Pallone) is most important for practical applications.

Figure 16 shows how separation pressure at these two points vary with Mach and Reynolds numbers. The curves are obtained from Eq. (12), using the relation between Re_δ and C_f for turbulent boundary layer on a flat plate.

From Figure 16, we can draw some general conclusions concerning the pressure rise at the separation (p_p/p_i or p_s/p_i) obtained with the free interaction theory:

- The pressure rise increases when the Mach number is increased.
- The pressure rise decreases when the skin friction coefficient decreases (corresponding to an increase of the Reynolds number).

Both of these tendencies have been confirmed by experiments performed at low to moderate Reynolds numbers, and the criteria in Eq. (12) also correlate experimental data well in the range $Re_{\delta i} < 10^5$ and Mach numbers $M_i < 5$.

However, in several experiments performed at higher Reynolds numbers ($Re_{\delta i} > 10^5$) it has been observed that the pressure rise (p_p/p_i or p_s/p_i) tends to become independent of the Reynolds number and even to slightly increase with it. As an example, Zukoski [49] made a series of experiments on step flows at $Re_{\delta i} > 10^5$ with M_i varying between 1.4-6.0, and found that the pressure rise at high Reynolds numbers depended only on the upstream Mach number M_i as

$$\frac{p_s}{p_i} = 1 + 0.73\frac{M_i}{2} \tag{14}$$

$$\frac{p_p}{p_i} = 1 + \frac{M_i}{2} \tag{15}$$

Hence there appears to be a change of tendency in both *Re* and Mach number behavior as these parameters becomes large. An explanation for this behavior may be that, as the Reynolds number increases, the viscous sublayer occupies a smaller part of the entire boundary layer, and it becomes far thinner than the subsonic layer. These facts combine to make the pressure propagation in a high Reynolds number boundary layer an essentially inviscid process.

3.2.2 Prediction of the separation length

Viscous parameters also influence the separation length L_s, i.e. the distance between the point where the wall pressure starts to rise to the point where the flow actually separates. Experiments on ramp flows have shown that in turbulent flow the separation length is very

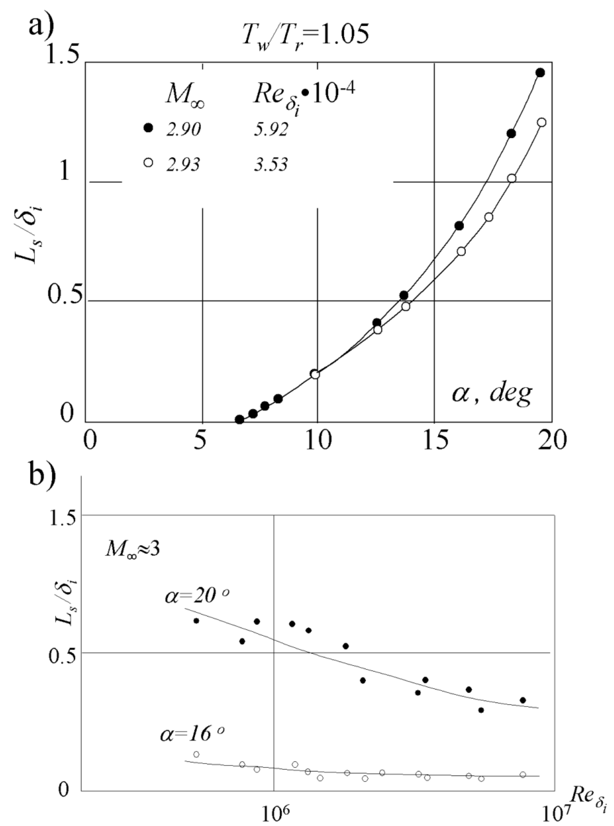

Figure 17. Influence of Reynolds number and ramp angle on separation length a) at low to moderate $Re_{\delta i}$ L_s/δ_i increases with *Re*, data from Spaid & Frishett [58] b) at high $Re_{\delta i}$ L_s/δ_i decreases with *Re*, data from Settles [44].

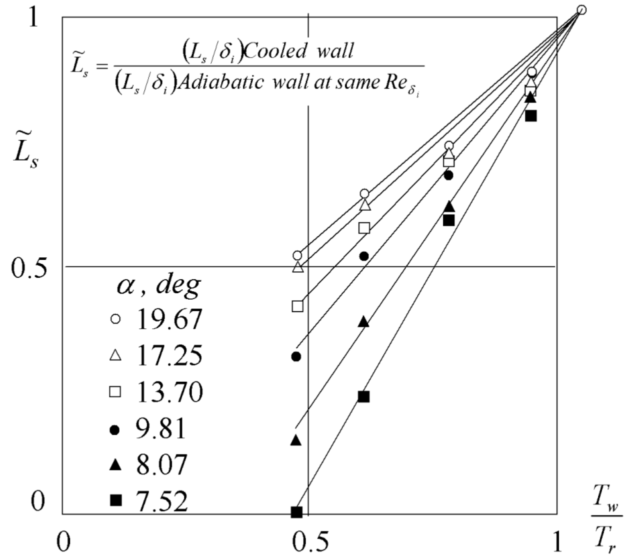

Figure 18. Influence of wall cooling on the separation length in a ramp flow. M_i=2.9, ramp angles 7.52°≤ α ≤ 19.7°, $2.18 \circ 10^4 \le Re_{\delta i} \le 5.92 \circ 10^4$ and $0.474 \le T_w/T_r \le 1.05$ (data from Spaid & Frishett [58])

short, L_s/δ_i is of order 1, compared to the laminar case where the separation length is far larger than the incoming boundary layer thickness [82]. For turbulent flow the influence of the Reynolds number on the separation length can be divided in two regions. For low or moderate Reynolds number ($Re_{\delta i} < 10^5$) L_s increases with increasing Reynolds and Mach number (see Figure 17a), in agreement with the free interaction theory. Whereas at high Reynolds number ($Re_{\delta i} > 10^5$), several investigators have found that the separation length tends to become independent of the Reynolds number and even to decrease with it, as indicated in Figure 17b. This change in behavior at $Re_{\delta i} \approx 10^5$ can be explained by the fact that the shape of the velocity profile is dependent on Reynolds number and that a fuller velocity profile has a higher resistance against separation. At low to moderate Reynolds numbers the velocity "fullness" initially decrease with increasing Reynolds number, but at higher Reynolds number the opposite behavior occurs, see e.g. Johnson & Bushnell [86].

Another parameter that influences the separation length is the heat transfer. The cooling effect can be seen in Figure 18, where $\tilde{L}_s$ is plotted versus T_w/T_r based on experimental data from Spaid & Frishett [58]. $\tilde{L}_s$ is the ratio between L_s/δ_i when heat transfer is present and L_s/δ_i with adiabatic flow evaluated at the same $Re_{\delta i}$. As indicated in the figure, wall cooling decreases the separation distance. This reduction of $\tilde{L}_s$ with decreasing wall temperature can be explained with the help of the free interaction theory. When reducing T_w/T_r (T_r is the wall recovery temperature), the skin friction coefficient will increase and according to Eq. (11) this provokes a decrease of L_s. Another interpretation of the reduction of $\tilde{L}_s$ is that an overall contraction of the interaction domain is obtained due to a thinning of the subsonic layer, as the temperature level and thus the speed of sound near the wall becomes lower.

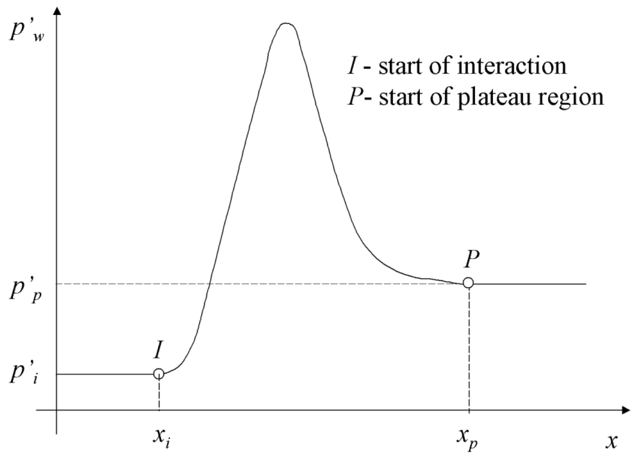

Figure 19. Typical distribution of the fluctuating pressure in the interaction region near separation [62-63,69].

3.3 Unsteadiness and 3-dimensional effects

In the previous section we only looked at the mean properties of shock induced separation. The unsteady pressure behavior has been the topic of a number large of studies [59-81,87-88], some of which are discussed in more detail below.

3.3.1 Kistler's intermittency model

A typical distribution of the fluctuating pressure *p'* in the interaction region near separation is shown in Figure 19. The fluctuations increase rapidly after the onset of the interaction at *I* from the level experienced in the incoming unperturbed boundary layer, p_i', up to a peak value. It then decreases asymptotically towards the fluctuation level, p_p', in the plateau region.

The explanation of the obtained feature, first given by Kistler [69], is that the flow is intermittent. In the interaction region near separation the pressure jumps back and forth between the mean pressure levels p_i and p_p due to a fluctuation of the separation point, and at each pressure level the pressure oscillates with an amplitude characteristic of that level, i.e. p_i' and p_p' respectively, as illustrated in Figure 20.

According to Kistler, the wall pressure signal near the separation can be modeled as a step function representing the shock wave as it moves back and forth over a certain range, hereafter called the intermittency region length. By defining the "intermittency" factor ε as the fraction of time that the plateau pressure is acting over the point of interest, the mean pressure at a given axial position *x* can be expressed as follows.

$$p(x) = \varepsilon(x)\, p_p + \left[1 - \varepsilon(x)\right] p_i \tag{16}$$

Thus, ε can be determined from a mean pressure measurement at *x* as

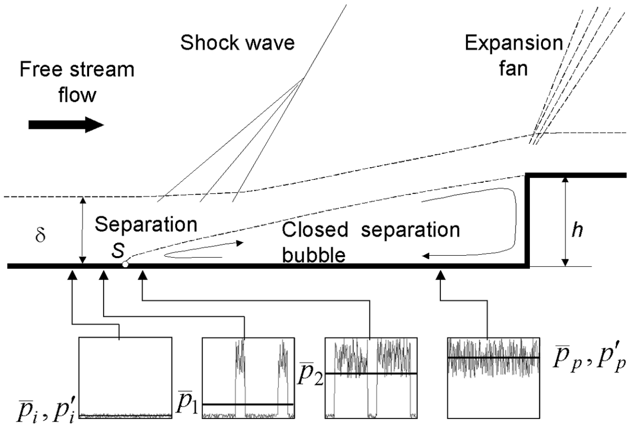

Figure 20. Sketch of the time variation of the pressure within the interaction domain according to Kistler [cf. 63,69]

$$\varepsilon(x) = \frac{p(x)/p_i - 1}{p_p/p_i - 1} \tag{17}$$

The rms fluctuation around the mean is then found to be

$$p'^2(x) = \underbrace{\overbrace{\varepsilon[1-\varepsilon](p_p - p_i)^2}^{Shock\ motion}}_{Low\ freq.\ part} + \underbrace{\overbrace{\varepsilon p'^2_p}^{Shear\ layer} + \overbrace{[1-\varepsilon]\, p'^2_i}^{Boundary\ layer}}_{High\ freq.\ part} \tag{18}$$

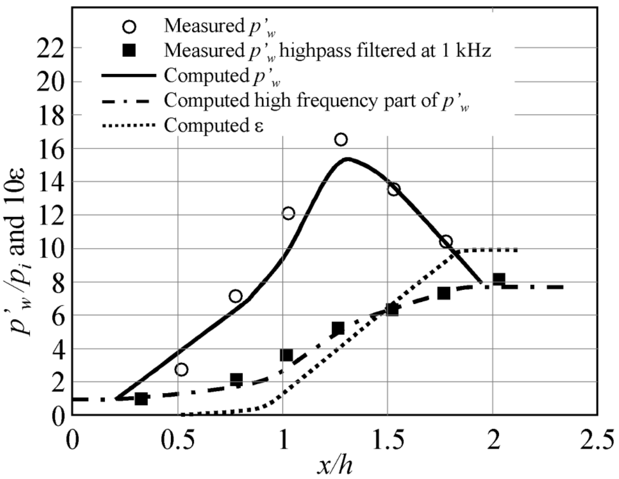

Figure 21. Fluctuating pressure in the intermittent region, computed according to Eq. (17-18). Symbols are test data of Kistler [69] from flow over a step with height *h*.

Here the first term contains only contributions from the intermittency of the shock wave movement, while the terms multiplying p'_i and p'_p can be interpreted as high frequency fluctuations generated by the boundary layer upstream of incipient separation (point *I*) and the shear layer downstream of the plateau point (*P*) respectively.

In Figure 21 the results from such a calculation are compared to test data by Kistler from step flow. First the distribution of ε was calculated from the measured values of the mean pressure, using Eq. (17), then the pressure fluctuations were computed from Eq. (18). The figure also shows that the terms labeled "high frequency part" in Eq. (18) correspond well to the high-pass filtered experimental data.

Erengil & Dolling [65] showed, on the basis of ramp flow data, that the error function gives an excellent fit to the distribution of ε over the intermittent region. This means that the position of the separation shock has a Gaussian distribution within this region. However, this can only be seen if ε is evaluated directly from the fluctuating pressure signal with the use of a conditional sampling method such as the two threshold method (TTM) [65].

3.3.2 Instantaneous pressure distribution

The mean pressure distribution over the interaction region, schematically shown in Figure 13, is in reality an average of instantaneous pressure profiles that have much steeper gradients. This was shown in an experiment by Erengil & Dolling [65] on a Mach 5 compression ramp, where the instantaneous profiles were obtained using a conditional sampling technique. Figure 22 shows the average wall pressure profile together with instantaneous profiles, obtained by picking out the pressure each time the shock front passes over a specific measurement position in the intermittent region (the various positions are denoted n=1 through 8 in Figure 22), and then ensemble-averaging for the selected values. The conditional ensemble average obtained in this manner is denoted $p_{E/A}$. The solid black line without symbols in the figure represents the mean pressure obtained by simply averaging the pressure over time at each position. The mean separation begins at s=1 and the flow reattaches downstream of the corner, which is located at s≈1.7.

Erengil & Dolling pointed out three characteristic features of the ensemble averaged

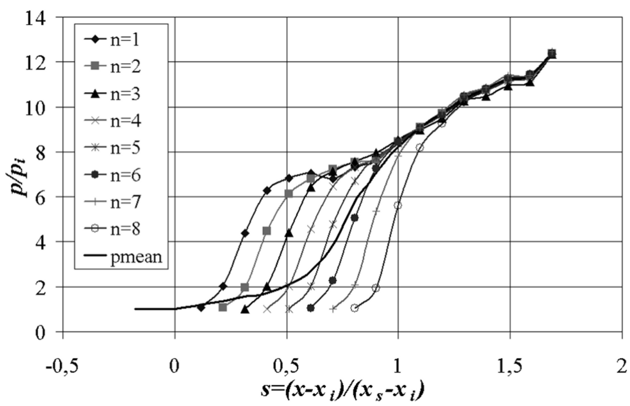

Figure 22. Conditional ensemble-average of the wall pressure upstream of a 28°, Mach 5 compression ramp (based on test data from Erengil & Dolling [65])

pressure distributions:

1. All $p_{E/A}$-curves converge in the separated flow region (s>1.2), i.e. the pressure there is independent of the shock position in the intermittent region.
2. For the "shock-upstream" case, i.e. n=1, a well-defined plateau region can be seen in $p_{E/A}$, consistent with a large-scale separated flow.
3. As the shock moves downstream from the n=1 position i.e. s>0.12, a progressive change in $p_{E/A}$ can be seen, to finally resemble that typical of a flow with a small separated region.

3.3.3 Universality of low frequency fluctuations

Power spectra of the fluctuating pressure in the intermittent region show that a large portion of the energy is concentrated at frequencies that are substantially below U_∞/δ_i, which is the frequency corresponding to the integral time scale of the incoming boundary layer. This has been observed in a variety of flow types. An example, adopted from Erengil & Dolling [65], is shown in Figure 23.

Here U_∞/δ_i is about 50 kHz, and this frequency is observed upstream and downstream of the intermittent region, $\varepsilon = 0$ and 1 (Figure 23c and f). It is interesting to note that the spectral distribution after separation – where the fluctuations are caused by the turbulent activity in the free shear layer near the dividing streamline – is quite similar to that of the incoming boundary layer. This is a general trend, which can be observed in all spectra presented in the literature. In the intermittent region, the pressure spectrum has a quite

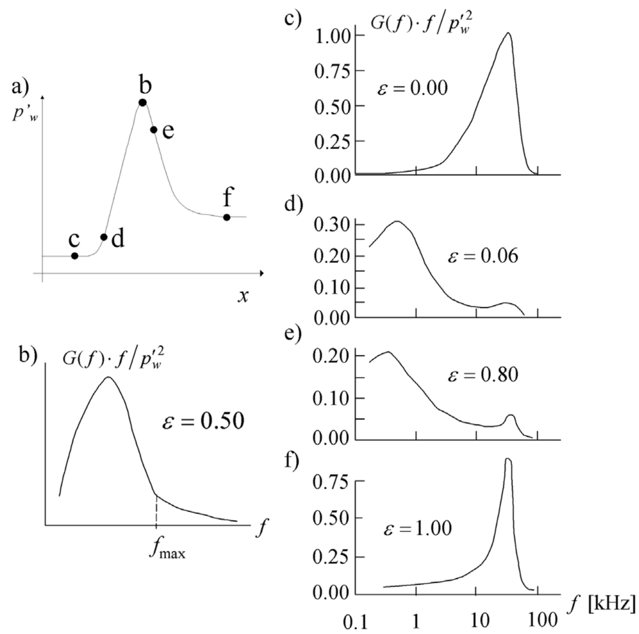

Figure 23. Normalized power spectra in the intermittent region in a 28°, Mach 5 compression ramp flow (adopted from Erengil & Dolling [65]). a) sketch of the streamwise evolution of the rms wall pressure and locations where the spectra have been evaluated, b) definition of f_{max}, c)-f) spectra at different streamwise locations.

Sr	**Test set-up**	**Ref.**	f_{max} **[kHz]**	U_i **[m/s]**	L_s **[mm]**	L_s/δ_i
0.072	45° ramp, *M*=2	[62]	1.0	1020	73.7	0.72
0.072	Step, *M*=3	[69]	1.0	635	45.7	1.20
0.068	28° ramp, *M*=5	[65]	2.0	$U_i/\delta_i \approx 50$ [kHz]		1.70
0.07	Cylinder, *D*=3/4", *M*=5	[70]	3.5	800	16.0	X
0.07	Cylinder, *D*=1/2", *M*=5	[70]	6.0	800	9.4	X
0.07	Cylinder, *D*=3/8", *M*=5	[70]	8.3	800	6.7	X
0.07	Cylinder, *D*=1/4", *M*=5	[70]	11.4	800	4.9	X

Table 1. Obtained Strouhal numbers for different flow configurations, when normalizing the maximum frequency value with L_s/U_i. (From Östlund [85])

different form, with a large fraction (~80-90%) of the energy concentrated at low frequencies, below $f_{max} \approx 2$ kHz, see Figure 23b. The figure shows the spectrum in the center of the intermittent region, $\varepsilon = 0.5$, with a spectral distribution which is representative for the entire intermittent region, except near the end points. At $\varepsilon = 0.06$ and $\varepsilon = 0.80$, Figure 23d-e, the spectra are bimodal, reflecting contributions both from the shock-induced low frequency fluctuations (about 0.2-2 kHz) and the high frequency fluctuations (about 50 kHz) outside the intermittent region.

Östlund [85] analyzed pressure spectra for a variety of different separated flows, and found that they are all similar to that described above. At maximum rms, i.e. at $\varepsilon = 0.5$, they have values of $f_{max} \approx 1$-10 kHz [62,65,69,70]. Östlund found that it is possible to define a Strouhal number for shock-induced movement, based on f_{max} as defined in Figure 23b, the separation length and the incoming flow velocity, $Sr = f_{\max} L_s / U_i$. The characteristics for these configurations, listed in Table 1, coincide on a Strouhal number near $Sr = 0.07$.

Analysis shows that the data are well correlated, when normalizing the maximum frequency value with L_s / U_i, corresponding to Strouhal numbers $Sr = f_{\max} L_s / U_i = 0.07$ for these configurations, see Table 1. This indicates, that with increasing separation length an increasing fraction of the energy will be located at low frequencies.

3.3.4 Causes of unsteadiness

There have been a number of studies focused on shedding light on the underlying cause, or causes, of the unsteadiness of SWBLI over the years. Where the most interesting studies are perhaps the ones by Erengil & Dolling [68], Ünalmis [79] and Beresh *et al.* [78].

Erengil & Dolling characterized the separation shock unsteadiness in terms of its position and velocity histories by using conditional sampling algorithms. These quantities were then correlated with conditionally extracted static pressure ratio histories, and with wall pressure measurements made upstream and downstream of the region of shock motion. Based on the test results they identified two different shock motions:

i) a small-scale or “jittery” motion caused by its response to the passage of turbulent fluctuations in the incoming boundary layer.

ii) a large-scale low frequency motion coupled with an expansion and contraction of the separation bubble.

Whereas Erengil & Dolling could explain the cause of the jittery motion they were not able to explain the cause of the low frequency motion.

To address this question Ünalmis investigated the structure of the supersonic turbulent boundary layer and its influence on unsteady separation. Ünalmis found evidence that meandering Görtler like vortices embedded in the incoming boundary layer were closely related with the low frequency behaviour.

However, the first experimental evidence of a direct relation between incoming boundary layer properties and the large-scale motion of the separation shock was provided by Beresh *et al*. They used particle image velocimetry (PIV) together with conditional sampling algorithms and found that near-wall negative velocity fluctuations were correlated with an upstream shock motion and positive velocity fluctuations were correlated with a downstream shock motion. Dolling *et al*. also concluded that these observations are consistent with the simple explanation that the unsteady shock behavior is due to changes of the shape of the instantaneous turbulent velocity profile. E.g. if the near-wall velocity fluctuations are negative, the instantaneous velocity profile loses fullness and tends to separate earlier, while positive fluctuations lead to the opposite.

3.3.5 3D effects

Another aspect to keep in mind is that shock wave boundary layer interactions are in fact 3D phenomena, even if the flow is nominally 2D. Since the velocity fluctuations are three-dimensional and occur randomly, they also cause a random distortion of the separation line in the spanwise direction. The 3D effect can be observed for instance in the oil flow visualization of Settles [46], where streamwise streaks of variable length and spacing can be seen projecting downstream from the separation line, giving evidence of spanwise motion. This also explains why Schlieren pictures taken normal to the flow near separation are blurred, since they give an averaged picture of the instantaneous spanwise separation line. One may hypothize that part of the pressure fluctuations, particularly in the low frequency band, may be caused by spanwise motion of streak like flow structures. However, as yet not much concrete work has been done to clarify this aspect.

4 SEPARATION AND SIDE-LOADS IN NOZZLE FLOW – TEST OBSERVATIONS

A flow exposed to an adverse pressure gradient of sufficient strength can cause the boundary layer to separate from the wall. In the previous section we examined the influence of such adverse pressure gradients generated by obstacles. A similar condition occurs when a nozzle is operating in an overexpanded condition, i.e. $n<1$ (cf. Eq. (5)). As soon as n is slightly reduced below one, an oblique shock system is formed from the trailing edge of the nozzle wall due to the induced adverse pressure gradient. When the ratio n is further reduced, to about 0.4-0.8, the viscous layer cannot sustain the adverse gradient imposed upon it by the inviscid flow and the boundary layer separates from the wall. This is the case e.g. when a rocket engine designed for altitude operation is tested at sea level. It also occurs during start transients, shut off transients, or engine throttling modes. In order to provide scientists and engineers with information on the turbulent shock wave boundary layer interaction in overexpanded nozzles, many experiments have been carried out both in the past and recently for full scale and subscale nozzles, see e.g. reference [2, 32-34,92-102]. Further support to the analysis of the flow separation behavior has been provided through numerical simulation [29,31,32,103-107].

Recent research has made it clear that two different separation patterns exist, the classical free shock separation, and the restricted shock separation, in the following denoted by their acronyms FSS and RSS respectively. Figure 24 shows schematic figures for the two separation patterns together with the definition of their characteristic points. In addition, Figure 25 compares measured and numerically calculated wall pressure distributions for the two flow patterns. Also shown is the numerically calculated Mach number distribution for FSS and RSS, respectively. In the following, these two regimes will be described in more detail.

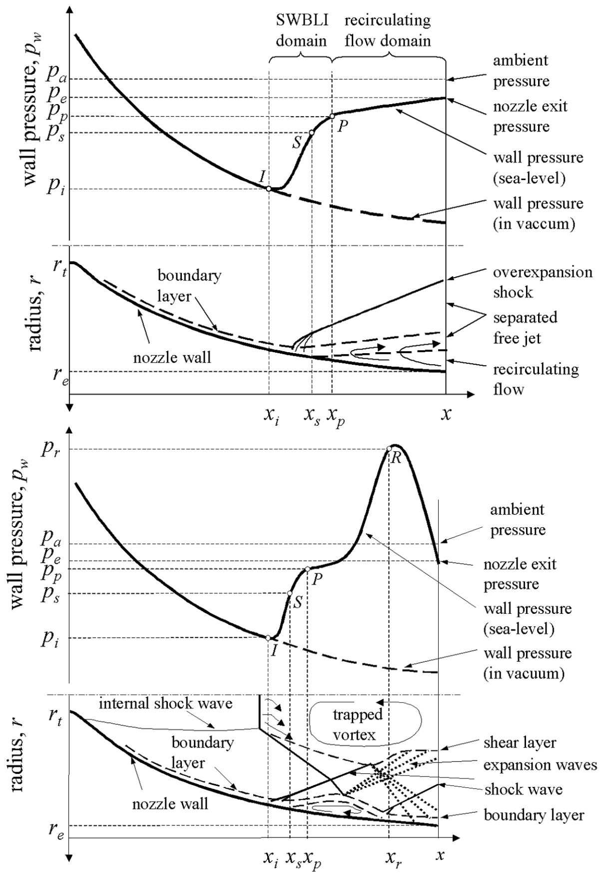

Figure 24. Phenomenological sketch of free shock separation (FSS, top), and restricted shock separation (RSS, bottom).

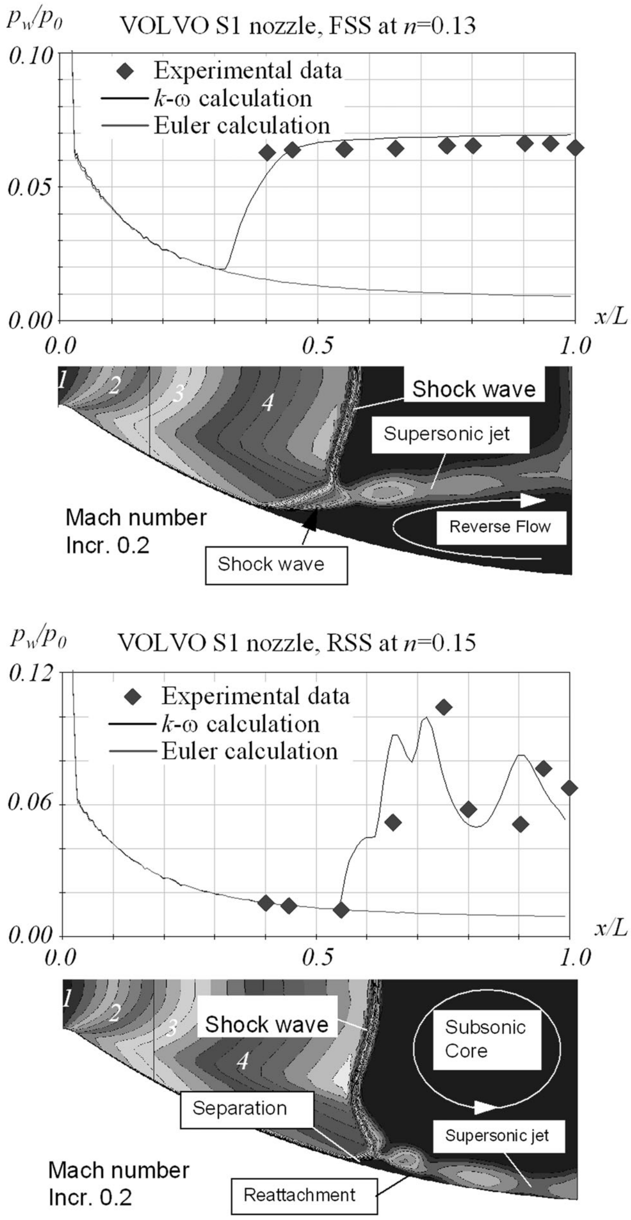

Figure 25. Free (top) and restricted shock separation (bottom) in the parabolic subscale nozzle VOLVO S1, comparison of measured and calculated wall pressures, and calculated Mach number distribution. Experimental data by FOI calculations performed by VOLVO (from Östlund [32]).

4.1 Free shock separation (FSS)

In the free shock separation case, the overexpanded nozzle flow fully separates from the wall. The resulting streamwise wall pressure evolution is mainly governed by the physics of shock wave boundary layer interactions occurring in any supersonic flow separation, cf. Sec. 3.1. However, in contrast to obstacle induced separation the separation location is not fixed by the geometrical properties of the test configuration, but results mainly from the degree of overexpansion.

As the degree of overexpansion is reduced, i.e. n is increased towards one, the separation shock moves out of the nozzle.

Based on the static wall pressure distribution, the flow can be divided into three regions, as sketched in Figure 24 (top): Upstream of the point of minimum static wall pressure (usually indexed "*i*"), the boundary layer is attached and its behavior is similar to that of a full-flowing nozzle. The following region of steep pressure rise, which is ended as soon as a certain "plateau" (often indexed "*p*") is reached, is usually referred to as separation zone. In the following, we will also refer to it as the interaction or the intermittent region. In this region, the whole separation process, i.e. thickening of boundary layer and actual separation (here indexed "*s*") at the zero wall friction point, $\tau_w=0$, takes place. The last portion of the nozzle, where the flow is fully separated and which is referred to as recirculation zone, shows a weak pressure increase until a wall pressure slightly below the ambient pressure, p_a, is reached at the nozzle exit. This gradual pressure rise, from p_p to p_e, is due to the inflow and upstream acceleration of gas from the ambience into the recirculation region.

4.1.1 Incipient separation at the nozzle exit

It was noticed already in the early 1950's [94-100], that the separation pressure ratio p_i/p_a decreases during the start-up of nozzle flows, as the separation point moves downstream and the degree of overexpansion decreases. This can be attributed to a Mach number influence, since wind tunnel experiments have shown that the separation pressure ratio decreases with increasing Mach number. However, an irregular behavior can be observed as the separation front approaches the nozzle exit [100-101]. At a location where the local area ratio of the nozzle has reached about 80% of its final value, the separation pressure ratio, p_i/p_a, reverses its previous trend and begins to increase as n is increased. An explanation for this behavior, given by Sunley & Ferriman [101], is that the plateau pressure increases to ambient pressure near the nozzle exit. For a constant pressure ratio, p_i/p_p, this causes an effective increase in separation pressure, p_i, in this last part of the nozzle, and thus an increase in p_i/p_a. Hence, as the pressure plateau p_p reaches the nozzle exit, the flow is actually attached all the way to the exit even though the sensors detect a clear pressure rise. This is usually referred to as incipient separation at the nozzle exit or the "end effect".

4.1.2 Pressure fluctuations and side-loads

Looking at the pressure fluctuations, we find distinct characteristics for the separation zone, as compared to the attached flow upstream of it, or the recirculation zone downstream of it.

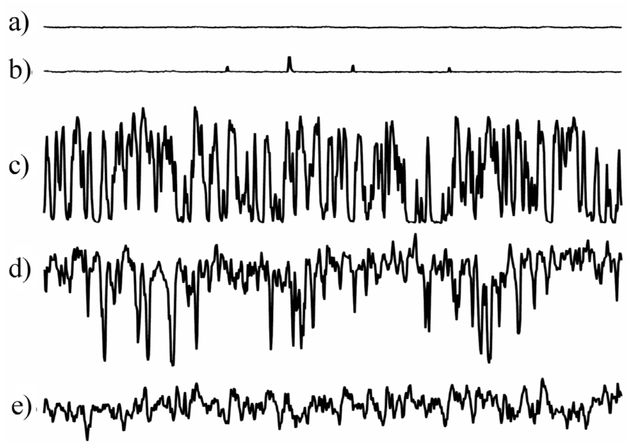

Figure 26. Pressure signals at different positions through the interaction region in the VOLVO S7 short nozzle. Measurements made during down ramping of p_0. (cf. [85, 108]). a): attached flow; b), c) and d): separation zone; e): recirculation zone downstream of separation.

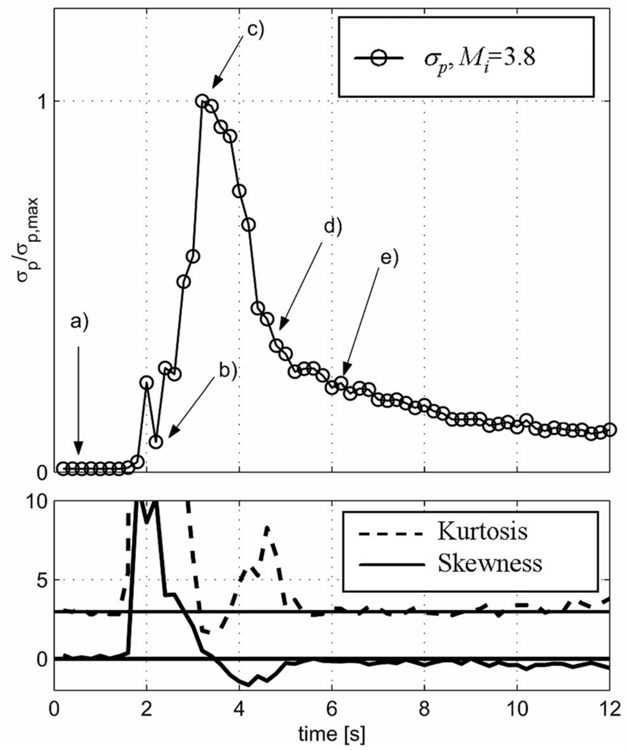

Figure 27. Statistical evaluation of pressure in the VOLVO S7 short nozzle during down ramping of p_0. The axial positions correspond to a wall Mach number of M=3.8 in the full flowing nozzle. Upper Figure: rms values, lower Figure: skewness and kurtosis. Each symbol is based on 800 samples collected during 0.2 [*s*]. (From Östlund et. al. [85,108]).

An example is given in Figure 26, which shows fluctuating wall pressure signals recorded at different positions through the interaction region in the truncated VOLVO S7 nozzle [85,108]. The statistical moments (rms, skewness and kurtosis) evaluated from such signals are shown in Figure 27. In the attached zones (signal a), the pressure fluctuations are quite small. They are due only to the turbulent fluctuations of the attached boundary layer upstream. Signals b-d is from the separation zone. The mean pressure rise is similar to that shown in Figure 25 (top), however, in analogy to the ramp flow case (see Figure 22), the instantaneous wall pressure rise may be expected to by much steeper. The large fluctuations are caused by the intermittent motion of the separation shock, causing an oscillation between the two levels p_i upstream of the separation shock, and p_p at the beginning of the recirculation zone – depending on the instantaneous position of the separation shock with respect to the pressure sensor. The interaction region is characterized by high intermittency – at the beginning with a positive skewness (see signal c) and towards the end with a negative skewness (signal d).

Signal e) shows the pressure fluctuations caused by the shear layer of the separated free jet in the recirculation downstream of separation. These fluctuations are low compared to the separation zone, yet substantially higher than in the attached flow.

Outside the interaction region (signals a and e), the pressure fluctuations are Gaussian, with skewness near zero and the kurtosis equal to 3. In fact the onset of high values of skewness and kurtosis could be used as an accurate criterion for detecting the beginning

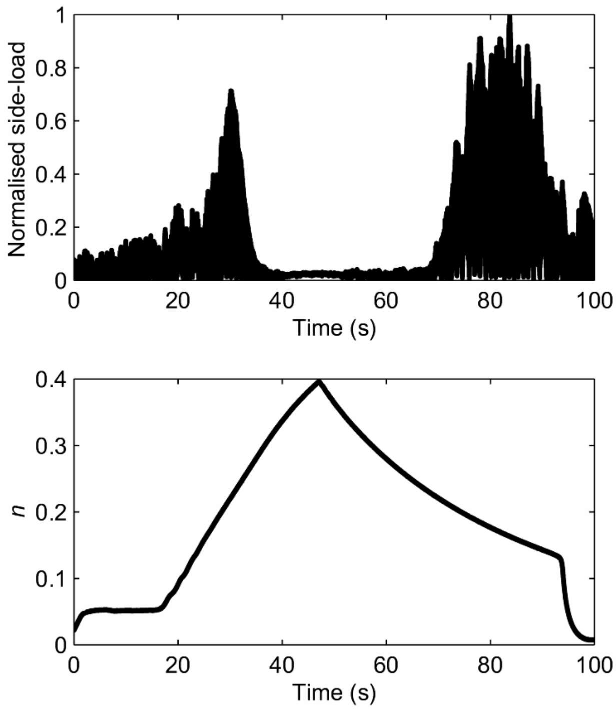

Figure 28. Side-loads in a truncated ideal nozzle (VOLVO S6) at free shock condition. (from Östlund *et al.* [109])

and end of the interaction region.

One should keep in mind that the oscillation of the separation front reflects a time-dependent motion of the nozzle jet, which occurs over a broadband low frequency spectrum, similar to that observed in basic interactions (see Sec. 3.3.3). It is not a local wall phenomenon, but affects the entire flow field downstream of separation. This is reflected in the relatively high fluctuation level in the recirculation zone as compared to the attached flow region (see Figure 26 e and a respectively). This is a feature particular to internal flow separation in nozzles, and it also explains why a correlation between the pressures at different circumferential positions has to exist.

This circumferential variation of the pressure is not necessarily axisymmetric, and may hence produce side forces perpendicular to the nozzle axis. Figure 28 shows side-loads measured in the VOLVO S6 short nozzle during a sequence of slow up- and down ramping of the chamber pressure (i.e. the different times correspond to different operational conditions). The side-load level is largest in the range of n=0.05 to n=0.25.

4.2 Restricted shock separation (RSS)

During cold-flow subscale tests for the J-2S engine development in the early 70s, a previously unknown flow separation pattern was observed at strongly overexpanded operating conditions [110]. In this flow regime, which only occurred at certain pressure ratios, the pressure downstream of the separation point showed an irregular behavior and partly reached values above the ambient pressure. This is due to a reattachment of the separated flow to the nozzle wall; inducing a pattern of alternating shocks and expansion waves along the wall, see Figure 24 and Figure 25. Due to the short separated region, this flow regime was called *restricted shock separation* (RSS) by Nave & Coffey [110]. The separation characteristics of RSS, as observed in the J-2S nozzle, and recently confirmed for subscale [32,33,34] and full-scale rocket nozzles [29-31], are described in the following.

4.2.1 FSS-RSS transition

Figure 29 shows CFD calculations visualizing the flow field (Mach number contours) during a start-up sequence of VOLVO S1.

During the start-up of the nozzle flow, featuring initially a pure free shock separation, transition from FSS to RSS occurs at a well-defined pressure ratio [31-32]. Figure 30 shows some typical measured steady-state wall pressure profiles in the VOLVO S1 nozzle during start up, as n is increased towards one. The wall pressure profiles indicate FSS for n<0.14 and RSS for n>0.14 (cf. Figure 24). The transition of the flow separation pattern from FSS to RSS takes places at n≈0.14. This can also be seen in Figure 29: at n<0.14, the exhaust jet is seen to occupy only a fraction of the nozzle exit whereas at n>0.14 the exhaust is attached to the nozzle wall.

The wall pressure distributions measured during shutdown are shown in Figure 31. Here, it can be seen that the transition between RSS and FSS occurs at a lower chamber pressure, n=0.11, indicating that there is a hysteresis effect. Figure 32 compares the wall pressure profiles at FSS and RSS condition at a pressure ratio of n=0.12. As can be seen the wall pressure distribution is quite different for the two cases. The main difference is that the RSS separation line is located much further downstream of the FSS separation line. The reason is that when the jet reattaches to the wall a closed recirculation zone is formed, with static pressures significantly below the ambient pressure level. Therefore, when an FSS-RSS or RSS-FSS transition takes place, the separation line jumps.

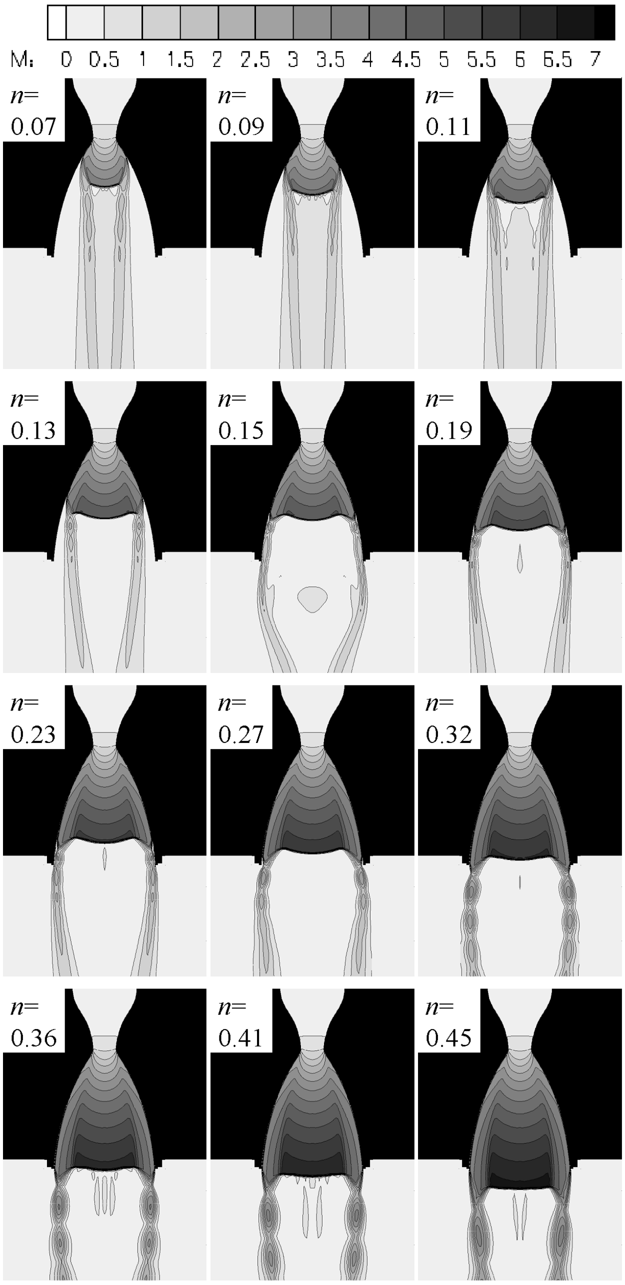

Figure 29. Calculated Mach number contours in the VOLVO S1 nozzle at different operational conditions, n=0.07-0.45, from Östlund [85].

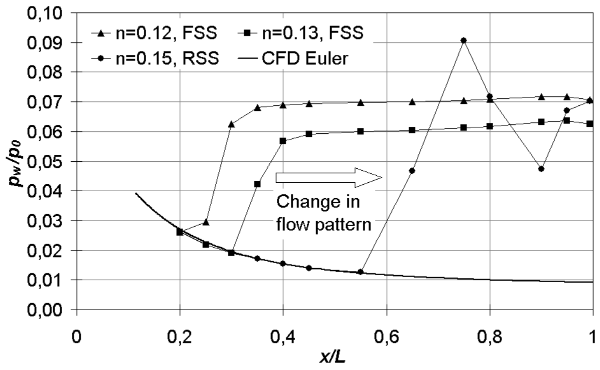

Figure 30. Wall pressure profiles in the VOLVO S1 nozzle during start-up, see also Östlund *et al* [32].

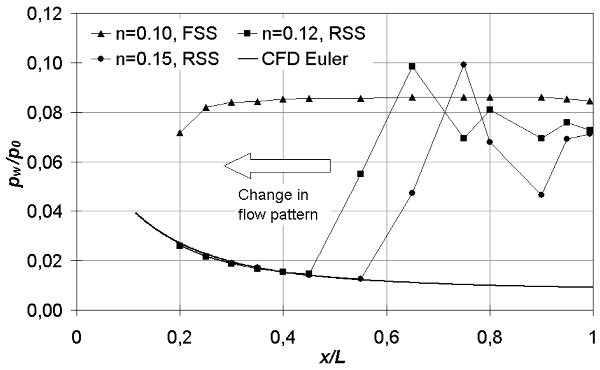

Figure 31. Wall pressure profiles in the VOLVO S1 nozzle during shut down, from Östlund [85].

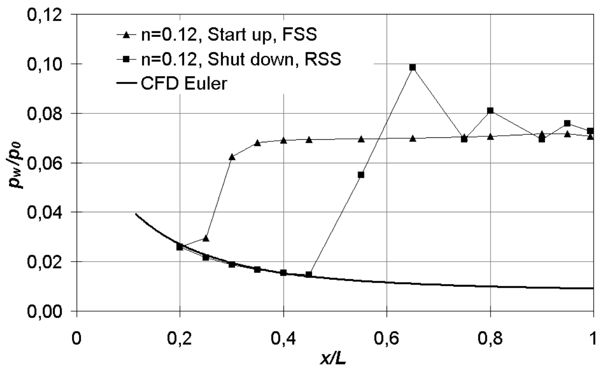

Figure 32. Comparison between wall pressure profile at FSS and RSS condition at n=0.12, from Östlund [85].

4.2.2 The "end effect"

Upon further increasing *n*, the closed recirculation zone is pushed towards the nozzle exit. Finally, the reattachment point reaches the nozzle exit, and the recirculation zone opens to the ambient flow. This is connected with a pressure increase in the recirculation zone behind the separation shock that pushes the separation point back upstream. The recirculation zone then closes again, connected with a drop in static pressure, which results again in a downstream movement of the separation point. A pulsating process is observed, connected with the opening and closing of the separation zone. This re-transition from RSS back to FSS is referred to in the literature as the "end effect" [31-32] and occurs in the VOLVO S1 nozzle at $n \approx 0.25$ [32]. The "end effect" is also observed during shutdown, at the same degree of overexpansion as during start-up, however in this case the transition is from FSS to RSS.

4.2.3 Side-loads generated by FSS-RSS transition

Östlund [32, 85] was the first to show, on the basis of analysis of the VOLVO S1 test, that these transitions between separation patterns are associated with distinct side-load peaks, which occur impulsively and are characterized by high amplitude. Figure 33 shows a time record of the measured side-load torque in the VOLVO S1 nozzle during a start-up and shutdown process. In each case, two distinct load peaks can be identified, one at n=0.14

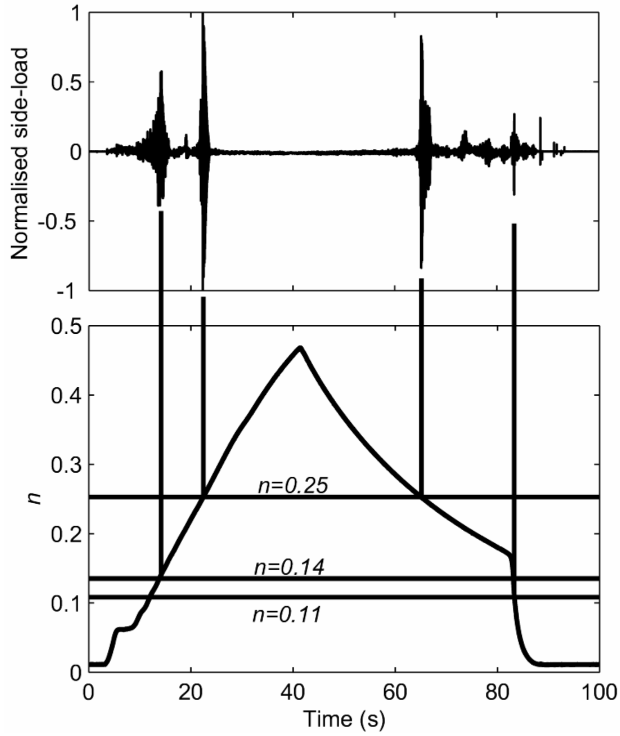

Figure 33. Side-loads due to transition in separation pattern in the VOLVO S1 nozzle, from Östlund *et a.l* [32].

and 0.11 for start-up and shutdown respectively, indicating FSS-RSS transition, and one at n=0.25, where the “end effect” takes place.

The above observations and conclusion by Östlund [32, 85], was followed up by intensive research both within and outside Europe. Further subscale experiments were performed within different FSCD test campaigns [2,33-34] as well as recent Japanese experiments [111], which confirmed this mechanism for TOP and CTIC nozzles (both of which have internal shocks). In addition, re-evaluation of test results of the Vulcain 1 engine confirmed this mechanism as key driver for side-loads during both start-up and shut-down [31].

4.2.4 Physical mechanisms driving the FSS-RSS transition

The theory of reattached flow in the J-2S sub-scale nozzle was first confirmed by numerical simulations of Chen *et al*. in 1994 [103]. In addition, their calculations revealed a trapped vortex behind the central normal shock, but they did not provide any explanation for the generation of such flow structure.

Later, Nasuti & Onofri [104-106] stressed the role played by the centerline vortex on the separation pattern and side-load generation. The centerline vortex acts as an obstruction for the exhausting jet, which is thereby pushed towards the wall. As a consequence a radial flow component is generated that tends to reattach the separated region, thus switching the flow from FSS to RSS.

Frey & Hagemann have given another explanation of the reattached flow based upon experimental observations and numerical simulation.[29-30]. According to their results, the key driver for the transition from FSS to RSS and vice versa is the specific cap-shock pattern. Thus, a transition from FSS to RSS can only occur in nozzles featuring an internal shock. According to their findings, the cap-shock pattern results from the interference of the separation shock with the inverse Mach reflection of the weak internal shock at the centerline [30]. A key feature of this inverse Mach reflection is the trapped vortex downstream of it, driven by the curved shock structure upstream of it, which generates a certain vorticity in the flow [30,112,113]. Thus, the vortex would be a result of the curved shock structure, which is partially in contrast to the explanation given by Nasuti & Onofri that includes also an effect of flow gradients upstream. Further experimental and numerical verification is planned to finally reach a conclusion with respect to this interesting vortex phenomenon.

An interesting point is that both the hypotheses of Nasuti & Onofri and Frey & Hagemann identify the curved cap-shock profile as driver for the transition from FSS to RSS, in agreement with what is experimentally proven in [2,31-34].

5 MODELLING AND PREDICTION OF SEPARATION AND SIDE-LOADS

It is clear from the previous section that side-loads are generated by different mechanisms, depending on the internal flow field and separation shock pattern, which in turn depend on the contour type. If the free shock separation (FSS) prevails, side-loads are generated by the movement of the separated jet and possibly by disturbances entering the separated region from the surroundings. For nozzles where the flow field is characterized by an internal shock, transition to restricted shock separation (RSS) is the main cause of side-loads. In the following we will outline the present status of knowledge and prediction models proposed for each of these cases.

5.1 Criteria for FSS

The theoretical prediction of free shock separation is the case, which has been most extensively studied in the past since almost all experiments have been performed in conical and truncated ideal nozzle contours, which only feature this separation pattern. Experimental data have been used to develop a number of empirical and semi-empirical criteria in order to give the nozzle designer a prediction tool for the separation point, bearing in mind that in reality there is no exact point of separation because it fluctuates between two extreme locations. But even today, an exact prediction cannot be guaranteed because of the wide spectrum of parameters involved in the boundary layer – shock interaction such as nozzle contour, gas properties, wall temperature, wall configuration and roughness.

5.1.1 Correlations based on p_i/p_a

The most classical and simple criteria for FSS purely derived from nozzle testing is that given by Summerfield *et al.* [96], which is based on extensive studies on the separation phenomenon in conical nozzles in the late 1940's

$$p_i / p_a \approx 0.4 \tag{19}$$

The first attempt to include the influence of Mach number was published by Arens & Spiegler [100] in the early 1960's. However, the major formula derived turned out to be too complex for engineering application.

Based on experiments with conical and truncated ideal nozzles, Schilling [98] derived in 1962 a simple expression accounting for the increase of separation pressure ratio p_i / p_a with increasing Mach number,

$$p_i / p_a = k_1 \left(p_0 / p_a \right)^{k_2} \tag{20}$$

with k_1 = 0.582, and k_2 = -0.195 for contoured nozzles, and k_1 = 0.541, and k_2 = -0.136 for conical nozzles. In 1965, based on Schilling's expression Kalt & Badal [99] chose k_1 = 2/3 and k_2 = -0.2 for a better agreement with their experimental results. NASA [114] adopted a correlation similar to the one of Schilling for truncated contoured nozzles as representing the state of the art in the mid 1970's.

Later investigations performed by Schmucker [115] led NASA to recommend the semi-empirical criterion of Crocco & Probstein [116], which is based on a simplified boundary layer integral approach. The criterion accounts for the properties of the boundary layer, the gas and the inviscid Mach number at the onset of separation. The NASA recommendation from 1976 was to use this criterion with an additional margin of 20% from the predicted separation occurrence [114]. Another inheritance from this time is the purely empirical criterion proposed by Schmucker [115]

$$p_i / p_a = \left(1.88 M_i - 1\right)^{-0.64} \tag{21}$$

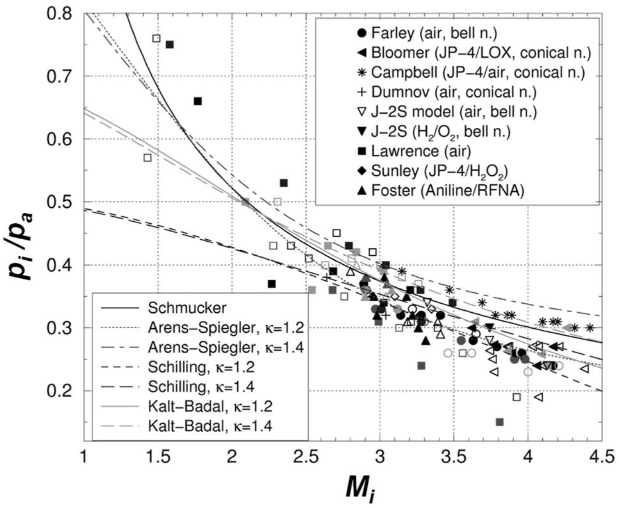

Figure 34. Comparison of simple separation prediction models for p_i/p_a with experimental results. The symbol shape in the legend indicates from which investigation the data is taken and the gray scale of the symbol correspond to different nozzle configurations tested, see Frey [28]. Also published in [27].

which has similar characteristics as the Crocco & Probstein criterion and is still widely used.

In Figure 34, these criteria are shown in comparison with test data. As indicated in the figure significant scatter can be observed. This explains why NASA advised a 20% margin and also points out the necessity of more reliable criteria.

5.1.2 Correlations based on p_i/p_p

A major reason for the rather poor agreement is that all the above criteria include in one single expression two separate mechanisms involved in the pressure rise of the flow. This fact was realized in the 1960's by Arens & Spiegler [100], Carrière [117, 118] and Lawrence [102]. The separation pressure ratio p_i/p_a includes the influence of both the pressure rise at the separation location itself and the gradual pressure rise in the recirculation region. Lawrence [102] therefore suggested that the pressure recovery p_i/p_a should be subdivided into two factors, $p_i/p_p \cdot p_p/p_a$, each describing a separate physical phenomenon: p_i/p_p for the separation itself, and p_p/p_a for the subsequent open recirculation and inflow of ambient gas.

The pressure rise p_i to p_p is caused by shock-wave boundary layer interaction, as described in Sec. 3. This is a general mechanism, not restricted to nozzle flow separation, which has been extensively studied. As an example, Zukoski [49] found the following simple relation to be in good agreement with experimental results for high Reynolds number (cf. Eq. (15))

$$p_i/p_p = (1 + 0.5M_i)^{-1} \tag{22}$$

for the Mach number range of M_i = 1.4-6.0 and $Re_{\delta i} \geq 10^5$. According to the author, this correlation also agrees with the plateau pressure values measured in overexpanded conical nozzles in the Mach number range M_i=2.0-5.5.

The drawback of the Zukoski criterion is that it does not include the dependency of the specific heat ratio observed in experimental data and should thus only be used for gas flow with γ=1.4, since the experiments were performed with air. A first attempt to account for the specific heat ratio dependency by using oblique shock relations was proposed by Summerfield *et al*. 1954 [96]. From experimental data they found that the flow deflection angle θ of the separated flow was nearly constant at 15° for the nozzles tested. With this value and the use of oblique shock theory the pressure rise for different gas mixtures can thus be calculated. This observation has also been confirmed in later synthesis of nozzle flow separation data, from a number of experiments performed with both hot and cold gas flows [29]. However, the data also indicate that the Summerfield criterion with a constant θ value is too simple. In fact the data indicate a linear dependence of the Mach number on both the deflection angle θ and the shock angle β itself. Based on this and data from the VOLVO subscale tests [2] Östlund [85,119] proposed an empirical criterion based on oblique shock relations

$$\frac{p_i}{p_p} = \left\{1+\gamma M_i^2 \sin^2(\beta) \cdot \left[1-\frac{\tan(\beta-\theta)}{\tan(\beta)}\right]\right\}^{-1} \tag{23}$$

with β =-3.764M_i+42.878 [°] and θ =1.678M_i +9.347 [°] for the Mach number range 2.5≤ M_i ≤ 4.5. Östlund used linear expressions for both θ and β in the correlation since he found that a criterion only based on the shock angle β (and θ calculated with the θ-β-M relation) experiences a minimum already for a modest extrapolation above M_i=4.5. Frey [28] has proposed a similar criterion based only on the shock angle β as

$$\frac{p_i}{p_p} = \left[1+\frac{2\gamma}{\gamma+1}\left(M_i^2 \sin^2(\beta)-1\right)\right]^{-1} \tag{24}$$

with β =-4.7M_i+44.5 [°] for the Mach number range 2.5≤ M_i ≤ 4.5, which produces a similar result as the criterion by Östlund (Eq. (23) reduces to Eq. (24) with the use of the θ-β-M relation). However, it does not give the correct trend of p_i/p_p for higher Mach numbers. At M≈4.8 the function has a minimum and p_i/p_p suddenly increases with the Mach number.

5.1.3 *Modeling p_i/p_p with generalized free interaction theory*

Although these criteria give a significant improvement, they are still purely empirical and it is in general preferable to base a criterion on a physical model in order to include the influence of governing parameters correctly. A promising theory to build such a criterion on seems to be the generalized free interaction theory by Carrière *et al*. [118], which has received new attention within the European FSCD group [85,120,121].

5.1.3.1 Theory of Carrière

Carrière *et al*. generalized the free interaction theory by Chapman (described in Sec. 3.2), by taking into account the non-uniformity in the incoming outer flow as well as the wall curvature in the interaction region. They found that, for the most generalized case, the universal wall pressure correlation function for non-uniform flow takes the form (cf. Eq. 7-11)

$$F\left(\frac{x-x_i}{x_s-x_i}, p'\right) = \sqrt{\frac{p(x)-p_i}{q_i}\frac{\bar{\nu}(x)-\nu(x)}{C_{fi}}}$$

$$p' = \frac{\delta_i^*}{q_i}\frac{dp}{dx} \qquad (25)$$

where ν is the Prandtl-Meyer function for the actual pressure at x and $\bar{\nu}$ the value ν would take at the same location in absence of flow separation, and p' is the normalized pressure gradient characterizing the non-uniformity of the flow. The function F is to be determined from experiment for each specific value of p'. Note that F according to this correlation is independent of Mach and Reynolds numbers. Figure 35 shows the generalized wall pressure correlation function, F, and the separation length, l_s, obtained by Carrière *et al*. The correlation function for uniform flow is also included in the figure so the influence of p' on F can be seen. Carrière *et al*. based their correlation on axisymmetrical experimental data from one ideal nozzle with design Mach number M_D=3 and three conical nozzles with half-angles of 5º, 10º and 17.5º respectively. The experiments spanned the Mach numbers $2.06 \le M_i \le 2.78$ and $4.12 \le M_i \le 5.04$ for pressure gradient in the range $-1.2 \le p' \bullet 10^3 \le -0.8$, a range that is quite typical for adiabatic nozzle flow.

It can be seen in Figure 35 that $F(s)$ is qualitatively similar for the uniform and non-uniform flow cases, while the dependence of l_s on $F_s/(\bar{\nu}_s-\nu_s)$ shown in Figure 35b has the opposite tendency compared to the uniform flow case of Chapman *et al.* [39] and Erdos & Pallone [84] (*cf.* Eq. (10), where l_s is assumed to be proportional to $F_s/(\bar{\nu}_s-\nu_s)$ by a positive constant k). In other words, $F(s)$ appears to be a fairly universal function, while the suggested form for l_s is not universally valid.

5.1.3.2 Separation criteria

In the context of nozzle flow separation, the length over which the separation front moves back and forth can be roughly identified with the distance between the point of incipient separation (I) and the plateau point (P).

In the case of obstacle-induced separation in uniform flow, P is well defined by the wall pressure distribution (see Figure 13), however this is not the case in overexpanded nozzle flows, as sketched in Figure 24. A common approach is to define the plateau pressure as the pressure value at the intersection between two straight lines, one line being tangent to the steep pressure rise obtained in the interaction region, and the other one tangent to the pressure rise in the recirculating flow region. Since the determination of the plateau point is rather arbitrary with this method, Östlund [85] defined the plateau point as the position where the function F has the value F_p=6.0, which is analogous to Erdos & Pallone's [84] definition of the plateau point in uniform flow, cf. Figure 35. Östlund then reformulated

Carrière's generalized free interaction theory so as to obtain a separation criterion based on p_i/p_p. By rewriting Eq. (25) at the plateau point (P) the following implicit equation set is obtained

$$\frac{F_p}{\overline{\nu}\left(x_i + \frac{l_p}{\delta_i^*}\left(f_i\right)\cdot\delta_i^*\left(x_i\right)\right) - \nu_p\left(p_p\right)} = f_i \qquad (26)$$

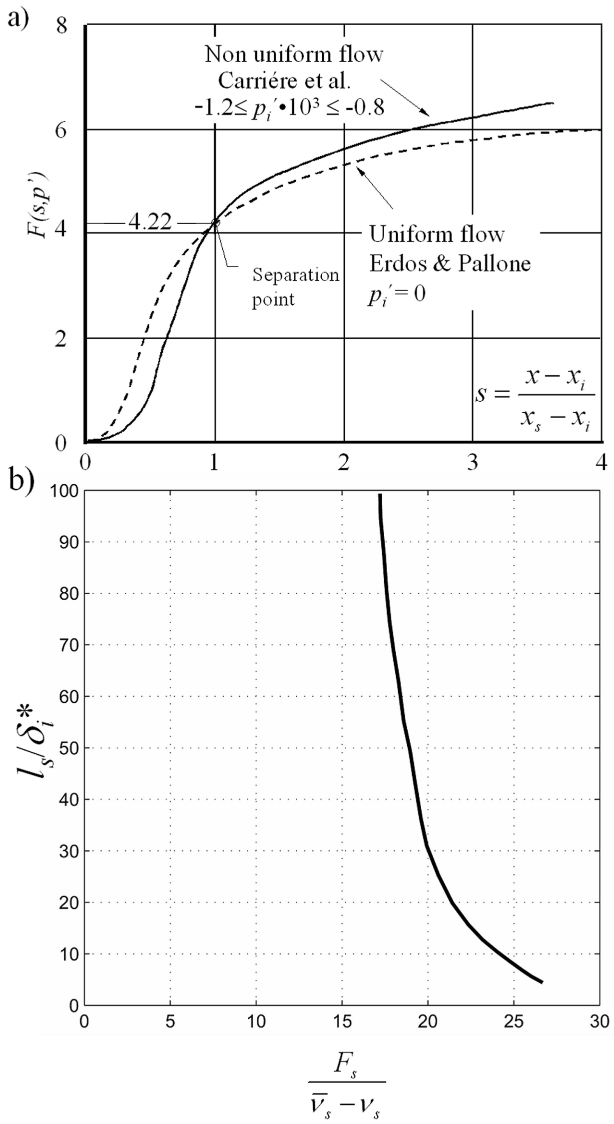

Figure 35. a) Wall pressure correlation, and (b) separation length for F_s=4.22, according to the generalized free interaction theory for non-uniform flow by Carrière *et al.* [118].

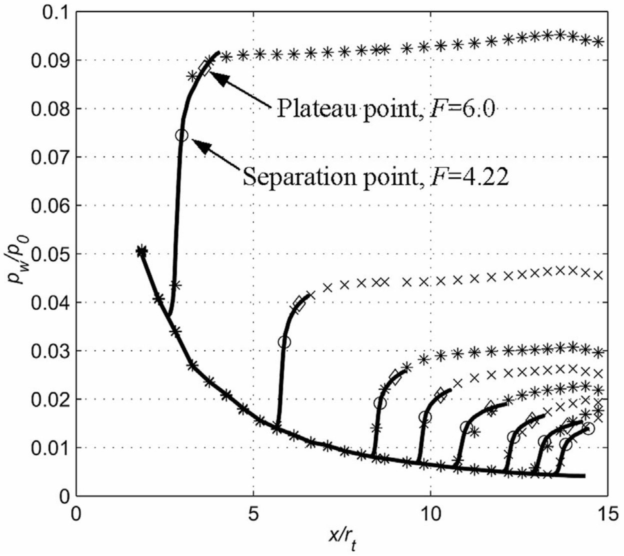

Figure 36. Fit of generalized pressure correlation curve by Carrière *et al*. to VOLVO S6 data, x_i and l_s varied, $2.82 \le M_i \le 3.25$, $-0.9 \le p' \bullet 10^3 \le -0.5$, n=0.04-0.24, from Östlund [85]

with

$$f_i\left(x_i, p_p\right) = \frac{p_p / p_i - 1}{\frac{1}{2}\gamma M_i^2 C_{fi} F_p}$$

where F_p is the value of F at the plateau point and

$$l_p \Big/ \delta_i^* = f\left(F_p \Big/ \left(\bar{\nu}_p - \nu_p\right)\right)$$

is a correlation function for the interaction length. By iteratively solving Eq.(26), the location of the start of the interaction process (x_i) can be determined in a nozzle at a given operation condition and plateau pressure value. With this approach, a correlation function for the interaction length l_p, i.e. from the start of the shock boundary layer interaction to the plateau point, is needed rather than the separation length l_s itself as given by Carrière *et al.*

To find an interaction length law, Östlund [85] used a least squares method to fit the pressure correlation function to experimental data from different VOLVO subscale test campaigns [2]. Results from such a procedure, applied to data obtained from VOLVO S6, are shown in Figure 36, which shows that Carrière's theory fits the experimental data quite well. The corresponding values of l_s and l_p are plotted in Figure 37, together with those given by Carrière *et al*. for the separation length l_s (F=4.22). As a next step, Östlund [85] determined a correlation for the plateau length by least squares fit to the experimentally determined values of l_p (dashed in Figure 37).

In order to check the validity of the obtained separation criterion, Östlund applied it to the VOLVO S7 short nozzle. For each flow condition a plateau pressure value was specified based on test data experience. As can be seen in Figure 38, the predicted pressure profiles in the interaction zone show a good agreement with the test data for all cases.

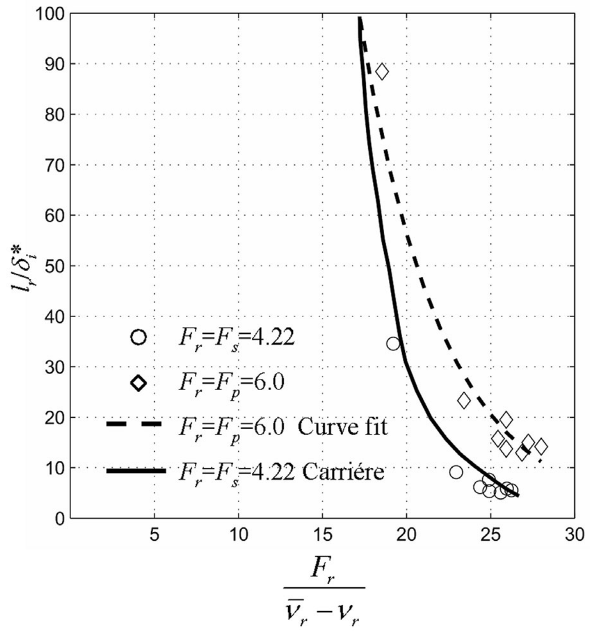

Figure 37. Interaction length correlation, to separation point (l_s) and plateau point (l_p) respectively. Symbols indicate calculated values based on VOLVO S6 nozzle test data, from Östlund [85].

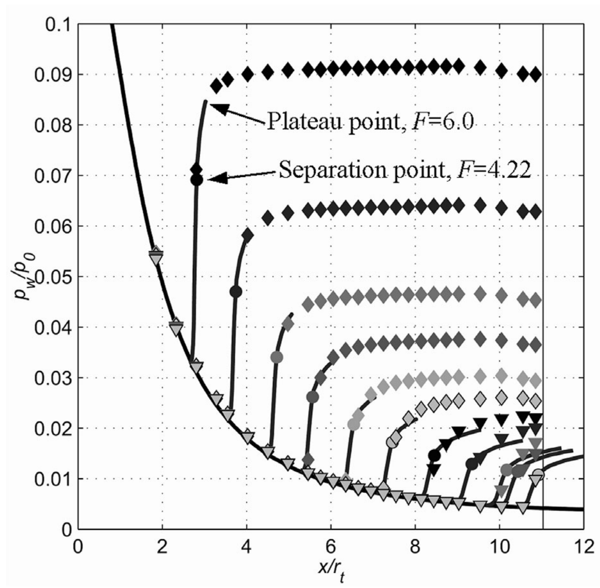

Figure 38. Predicted and measured wall pressure profile in the VOLVO S7 short nozzle, from Östlund [85].

5.1.3.3 Open ends

Although these first results look promising, Östlund [85] points out that more efforts are needed before a reliable and accurate criterion can be established. It is necessary to evaluate further experimental data, in order to increase the accuracy of the correlation functions. The applicability to chemically reacting flows, where the value of the specific heat ratio is different from that of air, must also be validated. The influence of wall cooling needs to be examined, especially the effect of wall temperature on the interaction length. Östlund [85] suggested a simple way to account for this influence, by applying a correction function $l_{r,cooled}/l_{r,adiabatic}=f(M_i,T_w/T_r)$. This is similar to the approach used by Lewis *et al*. [122] for laminar flow, see also the results obtained by Spaid & Frishett [58] for turbulent ramp flow in Figure 18. The scaling of the interaction length with the displacement thickness, δ_i*, must also be revised since δ_i* may become negative in strongly cooled nozzle flows. The boundary layer thickness, δ_i, or the momentum thickness, θ_i, may be a better choice for scaling in such cases. In order to shed light on these open ends, test are presently being prepared at VOLVO, ASTRIUM and DLR with some test objectives specially focused on the wall temperature effects on nozzle flow separation [123].

In contrast to the free interaction theory for uniform flow (see Sec. 3.2) the interaction length for non-uniform flow (such as overexpanded nozzle flow) also depends on the downstream conditions. The influence of e.g. the plateau pressure value on interaction length can be found by rewriting Eq. (25) at the plateau point as

$$\frac{F_p}{\bar{\nu}_p - \nu_p} = \frac{p_p / p_i - 1}{\frac{1}{2}\gamma M_i^2 C_{fi} F_p} \tag{27}$$

Inspection of Eq. (27) together with Figure 37 shows that l_p/δ_i* increases as the plateau pressure is reduced, which has also been verified in experiments [118]. This influence is not accounted for in empirical relations given by some earlier researchers, e.g. Dumnov *et al*. [124] suggested $l_r/\theta_i=f(M_i,T_{wi})$, (where θ is the momentum thickness, and the correlation applies to separated nozzle flows), which depends only on quantities at the start of the interaction.

5.1.4 Prediction of the plateau pressure

As seen above, the streamwise length of the interaction zone cannot be predicted with the generalized free interaction theory alone, since it depends on the flow downstream of the shock-wave boundary layer interaction region. It needs to be coupled with a model describing the flow in the downstream separated region, where the pressure recovery p_p / p_a takes place. Such a model is currently not available for contoured nozzles. The only reported models for the recirculating flow in the literature are the ones by Kudryavtsev [125] and the one by Malik & Tagirov [126], both for conical nozzles operated with air. The model by Kudryavtsev is purely empirical. He found that in conical nozzles with a half angle α<15° the pressure rise in the recirculating zone could be approximated as

$$\frac{p_p}{p_a} = \left[1 + \left(\frac{0.192}{\sin\alpha} - 0.7\right)\left(1 - \frac{M_i}{M_a}\right)\right]^{-1} \tag{28}$$

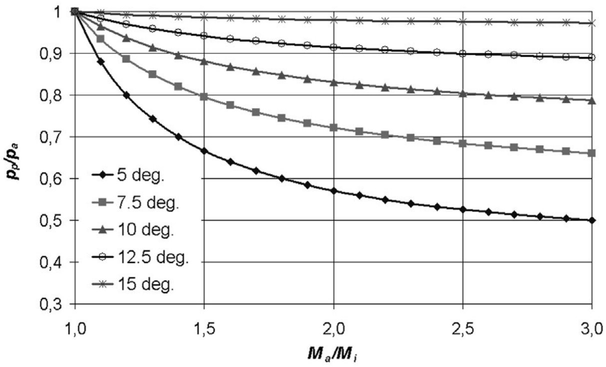

Figure 39. Pressure rise in the recirculating zone in conical nozzles with half angles α<15° according to the model by Kudryavtsev [125]

where M_a is the average exit Mach number defined by the nozzle expansion area ratio ε. (In contrast, in conical nozzles with a half angle α>15°, he found that the pressure rise $p_p/p_a \approx 1$, i.e. independent of the Mach number.) The pressure rise calculated with Eq. (28) is shown in Figure 39 for conical nozzles with half angles 5°≤α≤15°.

The model by Malik & Tagirov on the other hand is semi-empirical and is based on Abramovich's theory for the mixing of counter flowing turbulent jets [127]. This model shows good agreement with test data and if it is generalized it could be a promising model for contoured nozzles operated with hot propellants. A model for recirculating flow in contoured nozzles, whether empirical or semi-empirical, must take into account a number of parameters. Experimental data indicate e.g. that the wall contour downstream the separation point has a significant influence on the pressure increase in the recirculation zone [102]. As reported in reference [29], the length of the separated region, the curvature of the wall downstream of the separation and the radial size of the recirculating zone between the wall and the jet are further parameters influencing the pressure rise p_p/p_a. A clear indication of this can be found in Figure 40, where p_p/p_a is plotted versus ε-ε_i, which is a measure of the radial size of the recirculation zone. For large values of ε-ε_i, the downstream contour has a negligible influence on the pressure rise, whereas for the case when the separated jet is close to the wall (small ε-ε_i) there is a large variation in p_p/p_a. Besides that, the sudden increase of p_p/p_a as the incipient separation point enters the nozzle exit region must also be included. This increase of p_p/p_a is a general feature for all nozzle flows, illustrated in Figure 41 by results from the short VOLVO S7 nozzle.

Thus, it is obvious that in order to predict the location of separation successfully, a separation criterion must consist of two parts: First of all a model where the shock-boundary layer interaction is adequately described, and secondly a model where the pressure rise in the recirculating zone is included, accounting for downstream conditions and nozzle geometry. Development and validation of such models is currently ongoing at the different partners of the FSCD group, see e.g. the recent work by Reijasse & Birkemeyer [121].

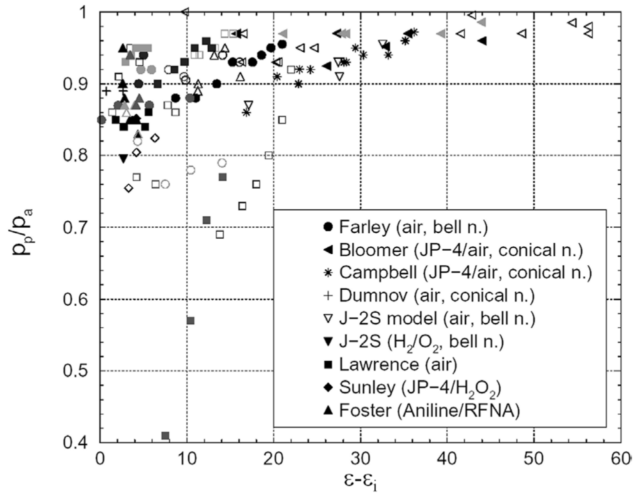

Figure 40. Experimental results for the pressure rise p_p/p_a as function of separation location. The symbol shape in the legend indicates from which investigation the data is taken and the gray scale of the symbol correspond to different nozzle configurations tested, see Frey [28]. Also published in [27].

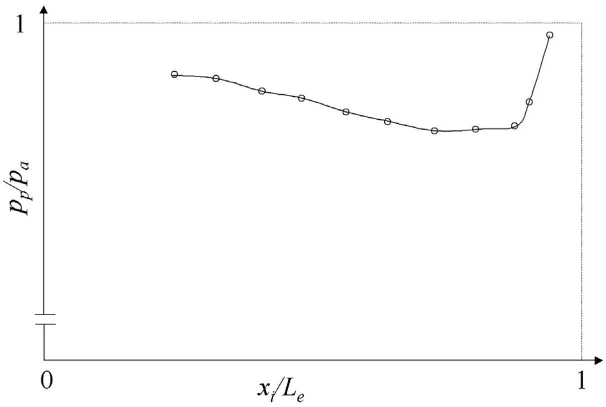

Figure 41. Illustration of p_p/p_a vs. x_i/L_e with the use of test data from the short VOLVO S7 nozzle, from Östlund [85].

5.2 Prediction of side-loads due to pressure fluctuations

5.2.1 The Schmucker model

A simple model for side-load prediction under pure free shock conditions is obtained by using the assumption of a tilted separation, as illustrated in Figure 42. This is the basis of several side-load models, e.g. of Pratt and Whitney, Rocketdyne, Aerojet and Schmucker [115].

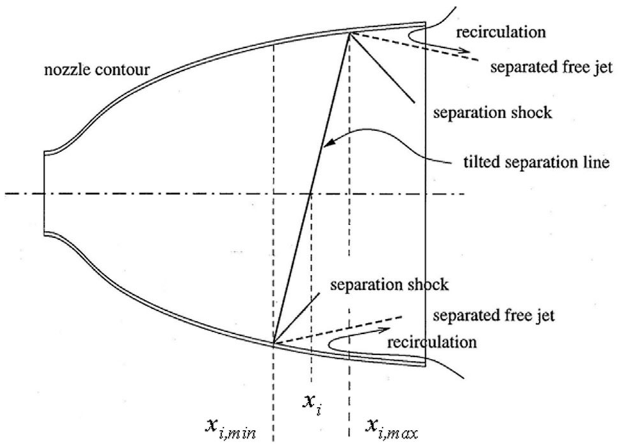

Figure 42. Principle idea of a tilted separation line.

If the wall pressure distribution is asymmetric, the integrated force acting over the nozzle wall yields a non-zero side force

$$F_{sl} = \int_0^L \int_0^{2\pi} \left(p_a - p_w \right) \cos \tau \, d\vec{A} \qquad (28)$$

where $d\vec{A}$ is a nozzle surface element, τ is the local contour angle, $x_{i,min}$ and $x_{i,max}$ are the axial distances at which the asymmetric flow separation begins and ends. This equation can be written in a simplified form as

$$F_{sl} = \int_{x_{i,\min}}^{x_{i,\max}} \int_0^{2\pi} \left(p_a - p_w \right) \cos \tau \, d\vec{A} \approx \left(p_a - p_i \right) A_{sl} \qquad (29)$$

A_{sl} , the effective area over which the pressure difference acts, is obtained in the Schmucker model by considering the variation of the position of separation caused by pressure fluctuations. The latter are assumed to be proportional to the nominal wall pressure p_w (this is empirically valid in the attached flow region).

The model depends on several empirical constants, which need to be determined for each new nozzle. It does not take into account how the separated region depends upon the incoming boundary layer or the characteristics of the downstream flow. More important may be, the approach is a quasi-static one, which does not model the time dependence (frequency spectra) of the pressure forces.

5.2.2 The Dumnov model

A more elaborate method, which takes into account the frequency content of the pressure fluctuations, was presented by Dumnov [128]. Inspired by findings of Coe *et al.* [62] on interactions in ramp and step flow, Dumnov constructed a generalized pressure fluctuation function for internal nozzle flow, which can be coupled to a transfer function to assess the mechanical load.

Starting from Eq. (30), the instantaneous side force acting on the nozzle wall is obtained by integrating instantaneous wall pressure $p'_w\left(x,\varphi,t\right)$ over the nozzle wall

$$F'_{sl} = \int_0^L \int_0^{2\pi} p'_w r(x) \cos\varphi \, dx \, d\varphi \tag{30}$$

where, $r(x)$ is the local nozzle radius, φ is the circumferential angle. The pressure distribution $p'_w(x,\varphi,t)$ was extracted from test data for various operating modes of a selected TIC nozzle and a conical nozzle in sub-scale cold-gas tests. From the experimental data, Dumnov constructed a spectral correlation function $W_p(x, f, \Delta x, \Delta\varphi)$, the autocorrelation of $p'_w(x,\varphi,t)$ in time and space, Fourier transformed with respect to time, i.e.

$$W_p = \mathcal{F}\left\{\frac{1}{T}\int_0^T p'_w(x,\varphi,t)\cdot p'_w(x-\Delta x,\varphi-\Delta\varphi,t+\tau)\,dt\right\} \tag{31}$$

This function is claimed to be generally applicable, if normalized in the following manner

$$\bar{W}_p = W_p \cdot \frac{U}{\sigma_p^2 \theta_i} \tag{32}$$

Here U is the velocity of the separated jet, σ_p is the rms level of the pressure pulsations, θ_i is the momentum thickness at the start of the interaction, x_i. No information is given concerning frequency scaling.

Dumnov [128] suggests formulas for the determination of σ_p in the vicinity of the separation point, $x_i \le x \le x_p$, and in the recirculating flow region, $x_p<x<L$, cf. Figure 19, while the pressure fluctuations in the boundary layer of the attached flow are neglected, since they are substantially smaller. The rms pressure fluctuation in the separation point region, σ_{sh}, given by Dumnov is

$$\sigma_{sh} = \frac{p_p - p_i}{2\sqrt{2}} \tag{33}$$

This is equivalent to that obtained by assuming a sinusoidal fluctuation between the two pressure levels p_i and p_p. Similarly, the formula given by Dumnov for the pressure variation in the recirculating zone, σ_{rec}, can be shown to be equivalent to

$$\sigma_{rec} = \frac{d\,p_p}{dx}\frac{l_p}{2\sqrt{2}} \tag{34}$$

The interaction length l_p, defined as $l_p = x_p - x_i$, is hence a key element in determining σ_{rec}, as well as in defining the limits of integration over the respective zones, and a correct prediction of its value of is therefore essential. Dumnov [128] gives no information about the interaction length in his paper. However, he probably used experimentally determined values of the interaction length when calibrating the model. When applying it to other nozzles, Dumnov *et al.* [124] use a semi-empirical correlation function for the interaction length similar to that derived from the free interaction theory, see Figure 37, where the interaction length is coupled to the incoming boundary layer properties. However, this correlation is not explicitly stated, and its validity can therefore not be assessed.

The application of the Dumnov-model to the Russian rocket nozzle RD-0120 gives reasonable agreement between measured and predicted side-load [128]. According to the author, the accuracy of the model is within 20%.

However, several key elements are missing to make the method generally applicable. This together with the lack of experimental data in the paper by Dumnov makes it impossible to reproduce the model or estimate how general the obtained spectrum actually is.

Nevertheless, the approach appears to be superior to the Schmucker model, where the interaction length has no coupling to the boundary layer properties at all.

Since the Dumnov model is based on the pressure fluctuation spectrum rather than just a single rms value, it is also able to give a more accurate description of the resulting mechanical side-load acting on the support structure. In reference [128], the obtained aerodynamic side force was translated into a mechanical load on the test stand with the RD-0120 nozzle by use of a transfer function, *H(f)*, which characterized the mechanical system, which was described as a simple harmonic oscillator. At the time it was published, this is an significant improvement compared to the common practice of using a just a constant dynamic response factor, and it gave the engineer a valuable tool to estimate expected side-loads on the thrust chamber and gimbaling system of the actual rocket engine.

In general it can be said that appropriate parameters for normalizing power spectra in the intermittent region still requires more work, and reliable quantitative data on the structures and pressure fluctuations in the transverse direction are still lacking. This may be a fruitful area of future work.

5.2.3 The Kistler approach

An accurate and physically more correct method is proposed by [85], on the basis of the intermittency model of Kistler [69]. In contrast to the Dumnov model, which uses a constant value of the rms pressure fluctuations, σ_p, throughout the interaction region, this approach makes it possible to render the streamwise evolution of σ_p, by defining an intermittency factor, ε, for the fraction of time that the plateau pressure is acting over the point of interest, see Sec. 3.3.

Östlund [85,108] applied this method to test data from VOLVO S7 nozzle, and to the LEA TIC data of Girard & Alziary [129], and showed that the intermittency model also gives good results in free shock separation in nozzle flow.

Figure 43 shows the pressure distribution in the VOLVO S7 short nozzle for two different cases. The measurements were made during transient operation, ramping down the chamber pressure, such that the interaction zone moves over the transducer during the time t_p-t_i, where subscript *i* and *p* refer to the start of the interaction and the plateau point respectively. Since the ramping is slow compared to the typical time scale of the pressure fluctuations, the variation of σ_p over time can be interpreted as the streamwise evolution by defining a non-dimensional coordinate $s=(t-t_i)/(t_i-t_p)$. Figure 43 shows this behavior for two pressure transducers located at different axial positions. As can be seen, the two pressure curves in Figure 43 coincide, which proves that the quasi-steady approach is valid. Normalized in this way, the pressure curves are seen to coincide with the pressure distribution obtained with the intermittency model of Kistler, confirming that the model is applicable to nozzle flow.

Östlund [85] also applied the Kistler model to data obtained by Girard & Alziary [129] for the LEA TIC nozzle. This is reproduced in Figure 44. In this case, the pressure distribution (σ_p) is normalized with the pressure rms at the start of the interaction zone

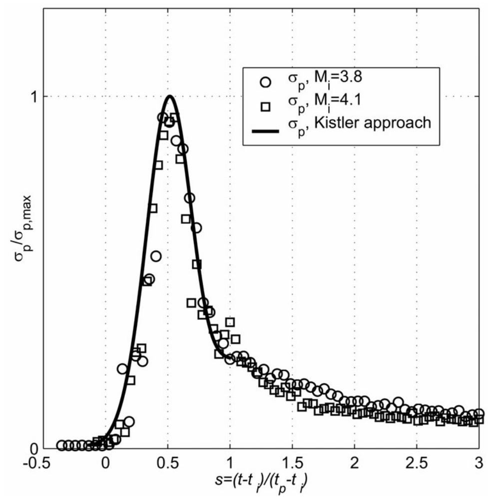

Figure 43. Distribution of the rms pressure fluctuations at two different axial locations in the VOLVO S7 short nozzle during down ramping of p_0. The axial positions correspond to M=3.8 and M=4.1 in the full flowing nozzle. Each symbol is based on 800 samples collected during 0.2 [*s*]. (From Östlund et. al. [85,108]).

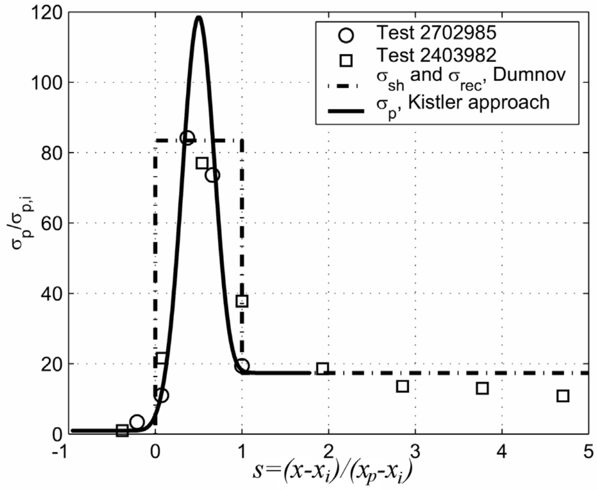

Figure 44. Rms pressure fluctuations in the LEA TIC nozzle, comparison between measured and values calculated with the Kistler approach, (Test data taken from Girard & Alziary [129], Figure from Östlund [85])

($\sigma_{p,i}$), in order to compare the actual level or σ_p. The figure also shows σ_p as obtained from the Dumnov model. As seen in Figure 43 and Figure 44, the level of σ_p is quite low at the end points of the interaction zone. Hence a reasonable approximation of the Kistler expression is obtained by leaving out the two last terms in Eq. (18), which gives

$$\sigma_p^2 \approx \varepsilon(1-\varepsilon)\left(p_p - p_i\right)^2 \tag{35}$$

According to this expression, the maximum rms, $\sigma_{p,max}$, occurs at ε=0.5 (i.e., the mid-point of the intermittent region) and has a value of $\sigma_{p,max}$=0.5(p_p-p_i). Eq. (35) then gives the corresponding average rms value in the intermittent region $\bar{\sigma}_p = 0.2420\left(p_p - p_i\right)$. This is close to the averaged value $\bar{\sigma}_p = 0.2514\left(p_p - p_i\right)$ obtained by inserting $\sigma_{p,i}$ and $\sigma_{p,p}$ from the LEA TIC test.

However, the averaged rms level obtained with the Dumnov approach is significantly higher. Eq. (33) gives $\sigma_{sh}/\sigma_{p,i}$ = 83; this is included in Figure 44 for comparison. In fact, the difference in σ_p between the two approaches is $\sigma_{sh} / \bar{\sigma}_p \approx \sqrt{2}$. This implies that Dumnov's assumption of a sinusoidal fluctuation between the two-pressure levels p_i and p_p is an over-simplification that over-predicts the averaged fluctuation level in the intermittent region. .

5.2.4 3D structure of the pressure fluctuations

The drawback of the methods described above is that they are purely statistical, and do not account for the physical process generating the pressure fluctuations. Observations in tests as well as on real engine nozzles give at hand that the separated region is characterized 3D a regular motion, which can be seen as a regular periodic pattern. A striking example is the so-called "tepee" pattern observed in the separated region during start-up of the SSME nozzle, see Figure 45. The regular zigzag pattern moves around the circumferential direction, and the distinct periodicity of the pattern indicates that it may caused by an instability mechanism with a clear wavelength selection. If it could be proven that such a mechanism is operative in nozzle flows, it would provide a physical basis for determining the universal pressure fluctuation function postulated by Dumnov [128].

To the authors' knowledge, the only attempt so far to analyze the problem from this point of view is a paper by Sergienko & Kirillov published in a Russian journal [130]. They consider the separated region at the nozzle exit as an annular volume bounded by the fixed nozzle wall on the outer side, and the movable separation shock and free jet on the inner side, while open to the ambient on the downstream end. This system is subject to a

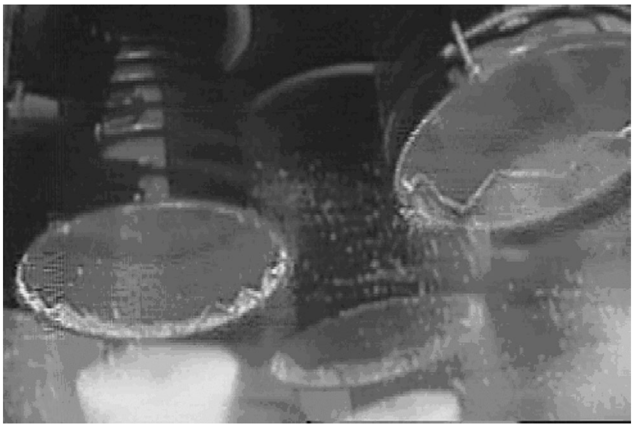

Figure 45. The three Space Shuttle Main Engines SSME at transient start-up process (courtesy of NASA).

spectrum of acoustic instability modes, with specific frequencies and circumferential wavelengths, which the authors attempt to relate to the RD-0120, SSME and Vulcain engine nozzles. In particular, modes with Strouhal numbers around 1.6-1.9 (based on local nozzle radius and sound speed in the separated region), corresponding to a frequency of about 300 Hz on the SSME nozzle, seem to correlate well with observations made during start-up of this engine. Higher modes of this type (although not considered in this analysis in ref. [130]) may provide an explanation of the observed "tepee" pattern.

It remains to be seen if this type of analysis can give a general explanation of the pressure fluctuations in free shock separation, and to what extent the observed spectra depend on boundary conditions. This is only possible by obtaining reliable quantitative data on the structure of pressure fluctuations in the transverse direction in model and real engine tests.

5.3 RSS criteria

The prediction of restricted shock separation has only been addressed in the last years, see Ref. [2,30]. The key point for the prediction of RSS is to predict the location where the transition from FSS to RSS takes place. The separated jet provides a driving force for reattachment when it contains a component of radial momentum directed towards the wall. This can occur with a cap-shock pattern, whereas, with a Mach disc pattern, no reattachment is possible, since the radial momentum is directed towards the centerline. Thus, by quantifying the momentum balance of the jet, the transition point can be determined. On this basis Östlund & Bigert [2] proposed a simple empirical criterion for the prediction of transition from FSS to RSS, which relates the FSS-RSS transition to the axial position where the small normal shock at the centerline coincides with the RSS separation front, see Figure 46. As indicated in Figure 46 and Table 2 this model shows very good results considering its simplicity.

Frey & Hagemann [30] developed the model further by introducing a physically more precise prediction of the shock pattern. First, numerical flow field is computed with the FSS shock system, which always prevails before a possible reattachment. From this flow field, the corresponding cap shock pattern is then constructed using a shock-fitting

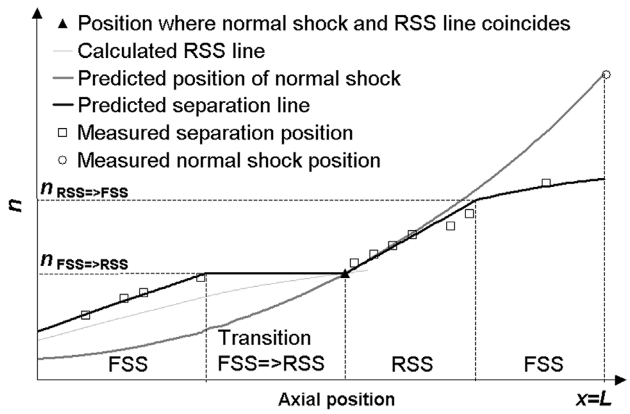

Figure 46. FSS-RSS transition model, principle of model together with comparison of predicted and measured values for the VOLVO S3 nozzle, from Östlund [85].

technique. The driving force for reattachment (i.e. the direction of the radial momentum) can then be evaluated from a momentum balance over the cap shock, and the location where the transition takes place can thus determined from the direction of the jet downstream of cap shock.

Both models account for the sudden pressure drop of the plateau pressure and the subsequent jump of the separation point when the flow reattaches and the separated region becomes enclosed by supersonic flow. Due to the complexity of the flow downstream of the reattachment point, which is characterized by subsequent compression and expansion waves, no models for this pressure recovery process exist so far. Instead a constant value of the plateau pressure based on test data experience is often used. This value is kept until the RSS is transformed back into FSS and FSS criteria are applicable again. This transformation occurs either when the cap-shock is converted into the Mach disc or when the enclosed separation zone is opened up at the nozzle exit, as shown in Figure 46.

Based on numerical simulations of the cap shock pattern with the trapped vortex, Reijasse [33] has proposed a further transition prediction model based on an effective area ratio for the RSS condition, estimated with the effective nozzle exit area occupied by the re-attached annular jet, and the throat area. Thus, the remaining exit area filled with the re-circulating flow of the trapped vortex is ignored in this approach.

5.4 Side-loads due to FSS to RSS transition

Side-load models based on the separation criteria described above have been developed simultaneously at ASTRIUM/DLR [31] and VOLVO [2]. The basic idea is that during the phase of transition from FSS to RSS (or vice versa), one side of the nozzle experiences a free shock separation while at the other side the flow reattaches. This will generate side-loads due to the asymmetry in the separation position and pressure distribution between the two sides.

The side-load is then simply calculated from the momentum balance over the entire nozzle surface area.

The “worst case” – i.e. the maximum side-load – occurs if one half of the nozzle experiences FSS, while the other half has RSS, as illustrated in Figure 47.

With this model the aerodynamic side-load is obtained. Since the duration of these loads is very short, the corresponding mechanical load can be obtained using pulse excitation theory. For a single pulse excitation, the dynamic response factor (i.e. the amplification of the applied load due to the dynamic system) is always less than 2. Figure 48 shows the shock response spectrum (SRS) for a system excited with different pulse types. The most critical pulse is the single square wave, since it contains the highest energy that any single pulse can have. Figure 48 shows the Shock Response Spectrum (SRS) for a single square wave together with the SRS for the half-sine wave and the triangular pulse. The half-sine and the triangular pulse are often good approximations to actual pulse shapes, e.g. the pulse creating the side-load when the separation pattern is changed from FSS to RSS. If the transition time, t_1, and the natural period of the mechanical eigenmode, τ, are known, the dynamic response factor can be obtained from Figure 48.

The recent advances in the understanding of separation and side-loads are based on model tests, which first revealed the transition between the different separation patterns as a basic mechanism for side-load generation. Stimulated by this finding, the prediction methods described above were developed within the European space community and validated against the experiments. A high accuracy was achieved in matching model and experimental results. In Table 2, values with the side-load model of basis Östlund & Bigert [2] are compared with the maximum measured values in VOLVO subscale and full-scale experiments showing that the accuracy is within 6%.

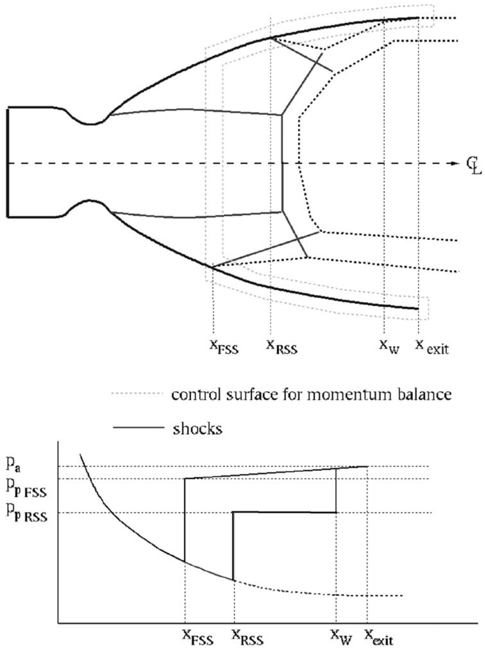

Figure 47. Asymmetric flow field inside nozzle at instant of FSS-RSS transition for worst-case side-load prediction. Control surface for momentum balance included. Momentum of impinging jet on wall taken into account at x_w, from Hagemann *et al*.[27].

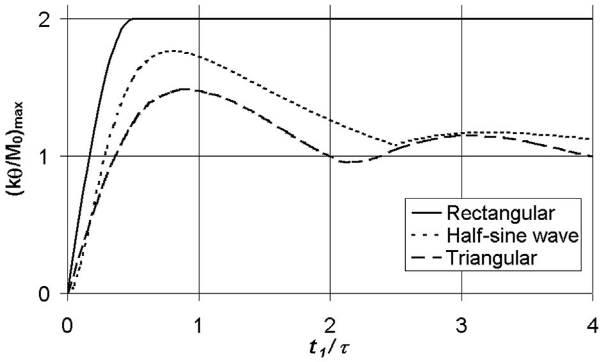

Figure 48. Shock response spectrum for different pulse shapes, from Östlund *et al*. [109]

Nozzle	n_m/n_c	M_m/M_c
VOLVO S1	0.94	1.01
VOLVO S3	1.0	1.02
Vulcain	1.05	1.05

Table 2. Comparison between VAC calculated (subscript c) and measured (subscript m) transition operational condition (n) and aerodynamic torque (M) , from Östlund *et al.* [109].

6 AEROESLASTIC COUPLING

A mechanism that may potentially generate high structural loads is the aeroelastic interaction between flow-induced wall-pressure fluctuations and the mechanical eigenmodes of the nozzle and thrust chamber. A non-uniform distribution of the wall pressure in the circumferential direction will cause an elastic deformation of the contour, which in turn results in a further deviation in wall pressure. This process forms a closed loop, which can result in a significant amplification of the side-load.

6.1 Experimental evidence of aeroelastic effects

Experimental investigations of such closed-loop effects in separated nozzle flows were performed by Tuovila & Land [131], Östlund *et al.* [32,109] and by Brown [132].

The mechanical structure of the nozzle has a spectrum of discrete eigenmodes, see Figure 49, of which the two lowest asymmetric modes may generate side-loads: a) the pendulum mode where the nozzle oscillates around the cardan and b) the bending mode where the nozzle oscillates around the throat. In addition, there are a series of buckling modes and higher circumferential deformation modes, which were first visualized in nozzle tests of Tuovila & Land. The experiments of Östlund *et al.* have shown that when the bending mode is excited in weak nozzle structures, aeroelastic effects cannot be neglected.

A system which is aeroelastically stable will behave almost like a regular forced response system, i.e. the closer the mechanical eigenfreqencies are to the frequencies of the aerodynamic load the higher the generated loads. The only aeroelastic effect is that a small shift of the system eigenfreqency and a corresponding small amplification of the forced response load will occur. The frequency shift and the aeroelastic side-load amplification depend on the degree of coupling. This is illustrated in Figure 50, which shows how the eigenfrequency of the bending mode depends on operational condition in the VOLVO S6 nozzle [109]. When there is no flow in the nozzle, the eigenfrequency Ω of the coupled system (including mechanical and aerodynamically forces), is equal to the mechanical eigenfrequency ω. However, as soon as there is a flow through the nozzle (n>0), aeroelastic coupling is present and manifests itself as a shift in the eigenfrequency. As the separation line moves down through the nozzle with increasing n (cf. Figure 36 and Figure 76 for the VOLVO S6 nozzle), Figure 50 shows that there is a gradual decrease in eigenfrequency. This means that the induced aeroelastic pressure force acts in the same direction as the displacement of the nozzle wall, i.e. the system becomes weaker than the

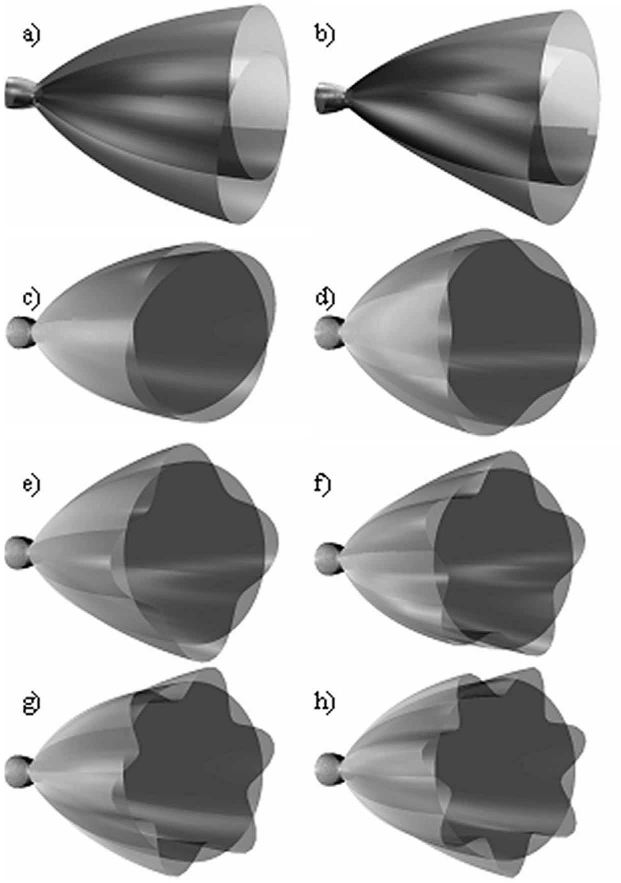

Figure 49. Schematic representation of the 8 first nozzle mode shapes. a) Pendulum- b) Bending- c) Ovalisation- d) Triangular- e) Square- f) Penta- g) Hexa- and h) Hepta-mode.

mechanical structure in itself, and the side-load becomes higher than for mere forced response. When the separation line comes close to the exit (n > 0.18, cf. Figure 36 and Figure 76), the eigenfrequency reverses its trend and begins to increase, finally reaching a higher frequency than that of the mechanical system alone. Now the induced pressure force acts in the direction opposite to the nozzle movement, i.e. as a restoring force, and the system is thus stiffer than the mechanical structure itself.

Under certain conditions, the eigenfrequency Ω of the coupled system may become imaginary, which means that the system is aeroelastically unstable In this case the eigenmode is aeroelastically unstable, since the oscillation amplitude (which is proportional to $\sim e^{i\Omega t}$) will grow exponentially. Eventually, when the displacement becomes sufficiently large, there will be a saturation of the amplitude growth, as parts of the separation line move out of the nozzle. The experiments of Östlund [32] have verified that this occurs in nozzles with weak throat areas, and that the aeroelastic coupling mechanism can give a significant amplification of the side-loads.

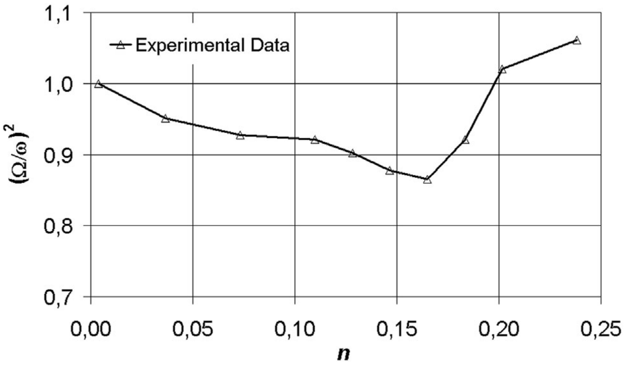

Figure 50. VOLVO S6 nozzle bending mode eigenfrequency versus operational condition, (from Östlund *et al*. [109])

6.2 Aeroelastic stability of the bending mode

The study of aeroelastic effects in separated nozzle flows is rather complex, requiring dynamic models of the mechanical nozzle-engine support system, the flow separation, as well as the coupling between these two. A technique for handling these difficult coupling problems was proposed by Pekkari [133,134] in the early 1990's. The model consists of two main parts, the first dealing with the equation of motions of the thrust chamber as aerodynamic loads are applied, and a second part modeling the change of the aerodynamic loads due to the elastic deformation of the wall contour. This model was later improved by Östlund [109], who showed that it is necessary to take into account the non-linear modification of the flow field in order to correctly predict the aeroelastic behavior. In the following we will present the basic ideas of aeroelastic analysis of Pekkari and Östlund, applied specifically to the bending mode.

Consider the flow through a nozzle as indicated in Figure 51. For simplicity, the bending resistance of the nozzle is modeled as a spring with stiffness *k* (this corresponds to the experimental setup in [32], where the nozzle was mounted on a flexible joint or cardan with springs of variable stiffness). θ is the tilt angle between the nozzle centerline and the combustion chamber centerline. *L* is the length (from the throat to the exit), *m* is the mass, J_y is the mass of inertia around the y-axis, τ is the local contour angle, and *r* is the local radius of the nozzle. $\vec{w}$ is the displacement of the nozzle wall. The azimuthally position is denoted by φ and *p, M, u* and ρ are the properties of the free stream flow along the wall.

Following the analysis of Pekkari [133,134], the system is considered as quasi-static with respect to the flow, i.e. the characteristic time scales of the flow are considered to be much larger than the characteristic time scales of the mechanical system. The equation of motion in the *y*-direction for the bending of the nozzle by an angle θ is

$$J_y\ddot{\theta} = M_m(\theta) + M_a(\theta) \tag{36}$$

Here M_m is the mechanical torque, i.e. the restoring torque of the spring in the nozzle suspension

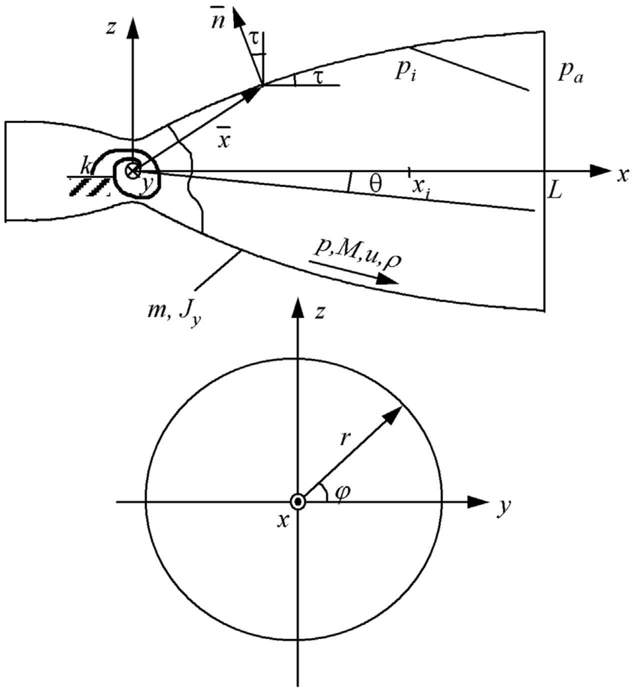

Figure 51. Nozzle and flow separation geometry.

$$M_m = -k\theta \tag{37}$$

and M_a is the y-component of the aerodynamic torque induced by the pressure load onto the nozzle wall, i.e.

$$\vec{M}_a(\theta) = \oint\!\!\!\oint \vec{x} \times \left[p\left(\vec{w}(\theta), x\right) - p_a \right] \cdot \vec{n}\, dS \tag{38}$$

where $\vec{n}$ is the wall surface normal vector and $\vec{x}$ is the corresponding vector of location.

The eigenfrequency for the mechanical system alone is formed by inserting a harmonic amplitude ansatz

$$\theta \sim e^{i\omega t} \tag{39}$$

into Eq. (36) and leaving out the aerodynamic torque M_a.
This gives

$$\omega^2 = \frac{k}{J_y} \tag{40}$$

Now, consider the nozzle displaced when subjected to mechanical and aerodynamic loads and again assume the motion to be purely harmonic, i.e.

$$\theta \sim e^{i\Omega t} \tag{41}$$

Introducing Eqs. (40-41) into Eq. (36) and rearranging gives

$$\left(\frac{\Omega}{\omega}\right)^2 = 1 - \frac{M_a(\theta)}{k\theta} \tag{42}$$

Inspection of Eq. (42) shows that:

1. When M_a / $k\theta$ <0, the aeroelastic torque acts to restore the nozzle to its nominal position, i.e. the system becomes stiffer than the mechanical structure itself and the frequency of the eigenmode is shifted to a higher value, i.e. $(\Omega/\omega)^2 > 1$.
2. When M_a / $k\theta \in$ [0, $k\theta$], the aeroelastic torque acts in the same direction as the displacement of the nozzle wall, i.e. the system becomes weaker than the mechanical structure itself and the frequency of the eigenmode is shifted to a lower value, i.e. $(\Omega/\omega)^2 \in [0, 1]$.
3. When M_a / $k\theta$ > 1, the unconditionally stable eigenmode becomes aeroelastically unstable, i.e. $(\Omega/\omega)^2 < 0$, and the displacement of the nozzle will thus start to grow exponentially.

By linearizing the expression for aerodynamically induced torque, Eq. (38), around the initial location of the separation line, the aerodynamic torque can be approximated as (cf. Östlund *et al*. [109])

$$\begin{aligned} \vec{M}_a(\theta) &\approx \{0, M_a, 0\} \\ M_a(\theta) &= (p_a - p_i) C r\pi (x\cos\tau + r\sin\tau)\theta\Big|_{x=x_{i0}} \end{aligned} \tag{43}$$

where C gives the change of the separation location due to the shift of the nozzle wall slope.

Inserted into Eq. (42), this gives a linearized expression of the frequency shift, which is independent of the defection angle θ

$$\left(\frac{\Omega}{\omega}\right)^2 = 1 - \frac{(p_a - p_i) C r\pi (x\cos\tau + r\sin\tau)}{k}\Bigg|_{x=x_{i0}} \tag{44}$$

This gives a significant saving in computational effort, and is therefore useful as a first approximation, however it cannot account for the transition between attached and separated flow and conclusions must therefore be verified with fully non-linear calculations.

6.2.1 Modeling the wall pressure perturbation

In order to calculate the aerodynamic torque M_a and the frequency shift Ω/ω, the perturbed wall pressure distribution must be known. In the original work by Pekkari [133,134], this pressure shift is determined using linearized supersonic flow theory (SPT, see e.g. Shapiro [6] p. 436). However, this assumption, when applied to internal nozzle flow, gives a significant overprediction of the pressure shift, which may result in an overestimate of Ω/ω and M_a by an order of magnitude of 100% or more. Östlund [109] therefore proposed a modified approach where the pressure shift is extracted from 3D Euler simulations. The position of the separation line is assessed with a simple separation criterion and downstream of separation the wall pressure is assumed to be equal to the ambient pressure. With this model it is possible to predict the aeroelastic stability, the modification of eigenfrequencies due to aeroelastic effects, and the transient behavior during start up and shutdown of the nozzle.

As emphasized by Östlund [109], the pressure perturbation caused by the elastic wall deflection is highly dependent on the nozzle contour. In some cases, the induced compression/expansion waves inside the nozzle may interact such that the pressure perturbation trend is actually reversed. E.g. the observations in Ref. [28,109,135] in a bent 15° conical nozzle showed that on the side that was deflected away from the flow, where more expansion would be expected, the wall pressure was in some portions of the nozzle even higher than on the opposite side, which was deflected into the flow. This underlines the necessity of case-sensitive methods.

6.3 Implementation on test models and comparison with test results

The above analysis can be illustrated by applying it to the VOLVO S1 and S6 nozzle test setups and comparing the results of the analysis with the test results. The setup is described in Ref. [32] (the setup is shown in Figure 71 and Figure 72 in Sec.8.4). The model is flexibly hinged on torsion springs at the nozzle throat.

6.3.1 The stable case (VOLVO S6)

The VOLVO S6 nozzle does not display aeroelastic instability, however aeroelastic effects can be observed in terms of a change in frequency depending on operation conditions. In Figure 52 the predicted aeroelastic frequency shift for the S6 nozzle is compared with experimental data, where the frequency shift of the eigenmode was evaluated from the strain signal, and the predictions based on Eq. (42), using a tilt angle θ=0.1°. The pressure shift was extracted from an Euler calculation according to the method of Östlund. Also shown is the result obtained when linearizing around the separation point, Eq. (44).

The linearised frequency shift obtained with the Pekkari [133,134] approach is also

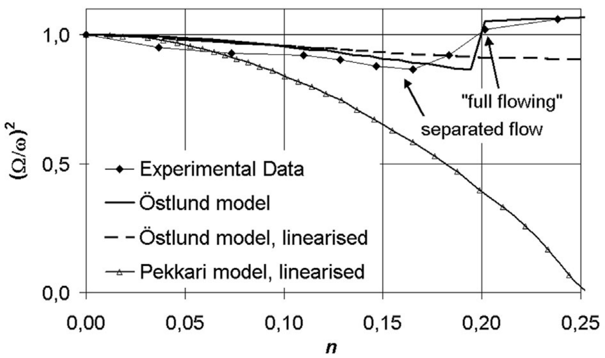

Figure 52. Comparison between measured and calculated frequency shift for the S6 nozzle, from Östlund *et al*. [109].

included in Figure 52 in order to visualize how the frequency shift is overpredicted when determining the pressure shift with SPT.

As n is gradually increased during the start-up process, the frequency decreases up to the point where the nozzle becomes full flowing. In the separated flow region, the theory predicts almost the same frequency shift as observed in experiments. The discrepancy is mainly due to the fact that both structure and gasdynamic damping are neglected in the model [109]. However, the effect of the damping is only significant during steady state operation whereas during short transient phases, such as a rocket engine start up, the damping plays a minor role and the model assumptions will thus come closer to reality.

When the nozzle becomes full flowing, a step-like increase occurs, and the system frequency becomes higher than the mechanical eigenfrequency. This process is clearly captured by Östlund's model, however the linearized model is unable to account for the transition between attached and separated flow, and therefore cannot predict the frequency step.

6.3.2 The unstable case (VOLVO S1)

In the VOLVO S1 tests, the bending resistance was varied by varying the spring stiffness, thus producing different mechanical eigenfrequencies in the range between 25 and 120 Hz. The different spring setups were labeled “rigid”, “stiff”, “medium”, “weak”, and “super weak” in order of decreasing eigenfrequency, and for each set-up, the aeroelastic stability characteristics of the nozzles were calculated using linearization around the separation point, Eq. (44). The result is shown in Figure 53. It can be seen that, for all setups from “rigid” to “weak”, the coupling is insignificant in the sense that the only aeroelastic effect is a modification of the system eigenfreqency, leading to a minor enhancement of the side-load response.

Only the “super weak” spring set-up displays aeroelastic instability, namely $(\Omega/\omega)^2 < 0$ when $x/L > 0.83$. When the separation front enters the section of the nozzle that is unstable, the displacement of the nozzle wall will begin to grow exponentially, and the separation line will be displaced accordingly. When the displacement is sufficiently large, parts of the separation line will reach the nozzle exit, and this will check the growth of displacement.

This is described by the non-linear stability relation, Eq. (42), which is displayed in

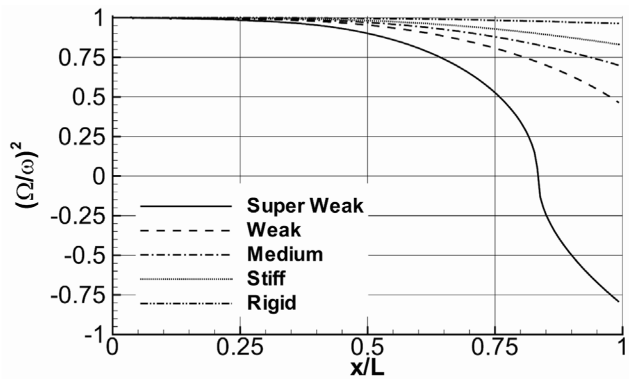

Figure 53. Aeroelastic stability of the S1 nozzle for the different spring set-ups, from Östlund *et al*. [2,109].

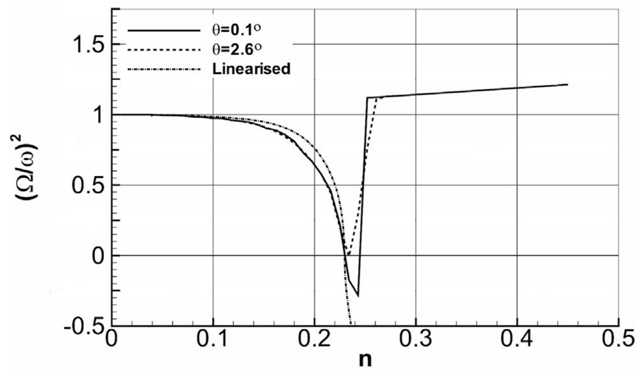

Figure 54. Aeroelastic stability relation for the S1 nozzle, flexible hinged with the super weak spring, from Östlund *et al*. [109].

Figure 54 for the S1 nozzle with tilt angles θ=0.1^o and θ=2.6^o. It can be seen that the aeroelastic instability occurs at n=0.25. Upon further increase of n, the nozzle will becomes full-flowing, and for n≈0.27 the system becomes stiffer than the mechanical structure itself, i.e. $(\Omega/\omega)^2$ >1, since the aerodynamic torque now acts to stabilize the nozzle.

For comparison, the linearised expression Eq. (44) is also included in the in Figure 54. It can be seen that the linear expression describes the process well up to the point where aeroelastic instability sets in, but is not able to account for the subsequent stabilization at n>0.25.

The nozzle experiences significant side-loads at n=0.25, due to the transition from RSS to FSS at the nozzle exit (cf. Sec. 3), which generates a pulsating aerodynamic load with a frequency of about f_a =100 Hz [85]. Table 3 displays the measured amplitude of this side-load (M/M_{max}) for each of the test set-ups analyzed above, together with the ratio between the frequencies of the aerodynamically force (ω_a=2πf_a) and the mechanical systems (ω_m). It can be seen that the trend in the measured side-loads is in accordance with predictions displayed in Figure 53 and Figure 54. The side-load level decreases with decreasing spring stiffness for the “rigid” to the “weak” spring setups, a trend which is in accordance with forced response theory.

This trend is interrupted only by the “super weak” case, which is aeroelastically unstable, and gives the highest side-load of all the cases.

Spring	ω_a/ω_m	$M/M_{\max}$
Rigid	0.8	0.66
Stiff	1.7	0.63
Medium	2.2	0.48
Weak	2.8	0.45
Super Weak	3.9	1

Table 3. Measured side-load magnitude versus frequency ratio between the exiting load (ω_a) and the mechanical system (ω_m), at n=0.25, from Östlund *et al*. [109].

6.4 Other modes

The above observations prove that the aeroelastic instability is present in weak nozzle structures, and can be correctly predicted using the analysis by Östlund [109]. The test setup used in the experiments is unique in that it focuses on a pure bending mode. This greatly simplifies the description of the mechanical system and makes it possible to handle the problem with simple analytic tools. In order to analyze the full spectrum of eigenmodes, it is necessary to perform a FEM analysis of the nozzle structure, as first suggested by Pekkari [133,134].

Compared to the bending mode, the pendulum mode does not generate a phase lag between the jet motion and the response of the nozzle wall. This probably explains why no evidence of aeroelastic coupling is found in set-ups simulating the pendulum mode (examples of such setups are shown in Figure 74 and Figure 57 in Sec.8.4).

The existence of aeroelastic effects on the ovalisation mode has been subject to discussion in the literature. The study of Tuovila & Land was performed in 1968 and focused on possible aeroelastic instability of nozzle shell buckling modes. From tests on different lightweight nozzle extensions mounted on a rigid 22.5° half-angle conical nozzle with ε=16, they concluded that the instability of the tested nozzle shells was a static phenomenon, not caused by any self-exciting mechanism. However, in recent tests of a flexible ideal nozzle, Brown [132] found indications of a self-excited vibration loop coupling the ovalisation mode to the flow separation. So far, the mechanism for the observed response has not been clarified, and the author suggests that the lines laid down by Pekkari should be followed.

7 TEST METHODOLOGY

The positive results obtained during recent years concerning separation and side-load behavior are the fruit of combined analytical, numerical and experimental efforts, where CFD has been employed to support the design of test models, and tests have furnished input for refinement of CFD-methods, thus achieving a physical understanding of the flow processes that would not have been possible only a generation ago.

A schematic of the development loop is shown in Figure 55. A design loop usually begins with a contour layout, where MOC and/or other CFD methods are used to optimize the aerodynamic performance (as described in Sec. 2) for a given design specifications (e.g. length, area ratio, weight etc). The next step is to verify, and if necessary modify, the design so as to meet specified load requirements. For this it is necessary to know pressure and temperature loads acting on the wall, but it is also necessary to assess the internal flow field, in order to predict the flow regime at each given operational conditions (cf. Sec. 4). This is done using a combination of numerical and experimental methods, which will be described in more detail in the following sections. CFD methods are usually calibrated and validated in a specific flow regime, and hence may only give reliable results as long as the flow remains within the same regime. It is therefore imperative to perform hardware tests in order to verify that the nozzle flow actually lies within this regime. Most test methods, on the other hand, can only access wall properties and hence experimental results on the internal nozzle flow field are usually not available. Flow measurements and visualization therefore need to be used interactively with CFD in order to draw conclusions concerning the physical mechanisms at work. In this process, the engineer will arrive at generalized correlations, which serve to evaluate a given design. A last step will be to apply these to

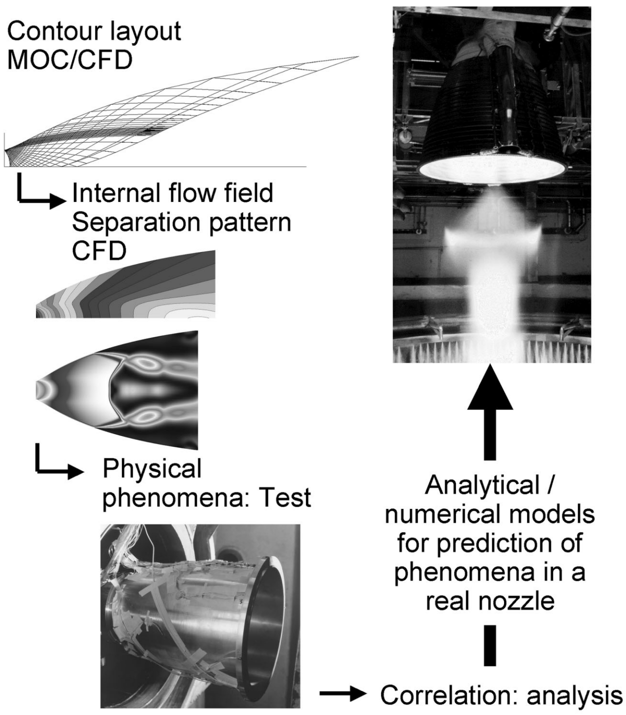

Figure 55. Logic of nozzle development.

the full-scale nozzle operating with real combustion gases on the rocket engine, which may require yet another loop of interaction between test, CFD and analysis.

7.1 Scaling with respect to γ: general considerations

Figure 56 shows some typical test configurations and how they relate to the full-scale engine nozzle in terms of complexity of the setup versus representatively of the obtained results. Which type of test to perform will depend on the stage of development, i.e. whether one is interested in general results of a fundamental character or data for a specific design.

Subscale model experiments are basically of two kinds:

(i) Hot gas tests, using gases with the same physical properties as a full-scale propellant gas. This allows for a simple geometric scale-down, leaving dynamical parameters unchanged. This type of sub-scale tests was performed e.g. during the development of the Vulcain engine [136] and also recently in a demonstrator test of a radiation cooled C/SiC nozzle extension [137]. In both of these cases, the test model was a complete scale-down of the Vulcain nozzle. As expected, the separation characteristics in the scaled nozzles [136, 137] showed close agreement with the Vulcain nozzle [30-31]. For instance, the transition of the separation pattern inside the nozzle from FSS to RSS and the transition from RSS to FSS at the exit of the nozzle occurred at the same conditions as in the Vulcain nozzle.

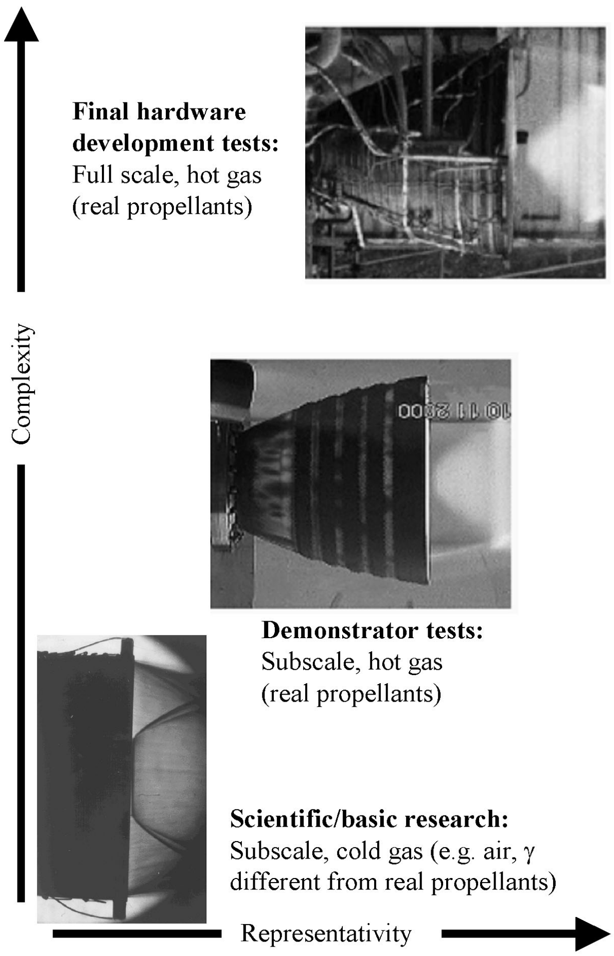

Figure 56. Subscale model testing.

However, the test and instrumentation cost for this kind of test is high, and the high temperature imposes severe limitations on the measurement equipment that can be used. The information that can be obtained is further restricted by the test duration time, which is usually short due to test rig limitations. It is therefore necessary to complement with wind tunnel testing, where the test duration can be significantly increased.

(ii) Cold gas tests, using e.g. air (γ= 1.4) instead of hot gas propellants (e.g. $\gamma \approx$ 1.2 for engines operated with H_2-O_2), are a relatively inexpensive alternative, allowing for more extensive testing, and parameter variation. The draw-back is that it is no longer possible to separate geometrical and dynamical parameters, since all gasdynamical quantities are functions of both Mach number and γ. In this case CFD is indispensable as a tool to define appropriate test models as well as making meaningful test evaluations. The main challenge in such tests is to reproduce the actual behavior of a nozzle run with hot propellants.

In the present context, the main scaling requirement is that the model nozzle should have similar separation and side-load characteristics as the original. This means that the essential features of the interior flow field must be reproduced, while maintaining a similar wall pressure distribution. As we will see, these requirements cannot be simultaneously fulfilled, if the gas used to operate the model does not have the same γ as in the real nozzle.

7.1.1 Reproducing separation and side-load behavior in subscale tests with different γ

According to the Schmucker criteria [115] the separation position is a function of the wall Mach number, M_w, and the wall pressure p_w/p_0, thus it is necessary to achieve similarity of their distributions in order to model the separation behavior. In particular, the side-load magnitude depends on the local pressure gradient along the wall, $\mathrm{d}p_w/\mathrm{d}x$, scaled for instance with L_{ref}/p_0. Apart from the flow properties along the wall, the internal flow field has a strong influence on the separation and side-load characteristics in the nozzle, since the shape and strength of the internal shock emanating from the inflection point of the contour affects FSS to RSS transition. Therefore the entire flow field needs to be correctly modeled, in particular the Mach number distribution $M(x/L_{ref}, r/L_{ref})$.

The choice of a characteristic length, L_{ref}, is not obvious. If we assume a model nozzle designed such that the Mach number distribution is identical to the original, but operated with gases with a different specific heat ratio γ, the area ratio ε, and hence the nozzle shape, will be quite different. In Figure 57, 1D isentropic relations (stream tube relations for calorically perfect gases) have been used to show how the area ratio varies with Mach number, assuming γ=1.2 in the original nozzle and γ=1.4 in the scaled nozzle (in reality, the relation is actually more complex, since γ is not constant throughout the nozzle, e.g. for Vulcain it varies in the range γ=1.14-1.24). It can be seen that the subscale nozzle needs to be substantially less expanded to achieve a given Mach number. Hence, the scale nozzle is more slender than the original.

As a consequence, even if $M(\varepsilon)$ could be reproduced in the model, there is no single length scale that will give similarity in the wall distribution $M_w(x/L_{ref})$. Furthermore, it is impossible to simultaneously reproduce $M_w(x/L_{ref})$, $p_w(x/L_{ref})$ and $\mathrm{d}p_w/\mathrm{d}x\ L_{ref}/p_0$, since their variation with ε is not the same. In fact, it is impossible to reproduce even $M(\varepsilon)$ in a 3D flow, since the change of contour proportions invariably affects the internal flow field

At best, it may be possible to design a nozzle belonging to the same family of contours.

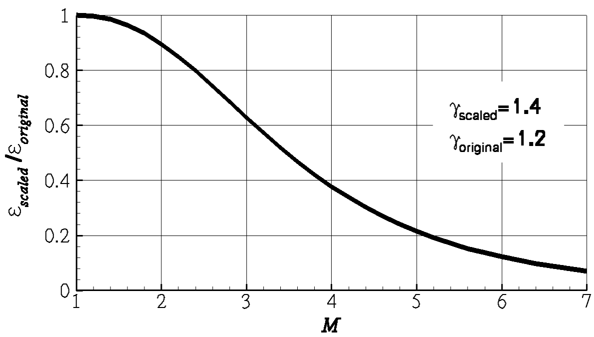

Figure 57. Ratio between scaled and original expansion ratio to keep identical Mach number distribution.

As described in Sec. 2, the initial expansion region determines the length of the kernel as well as the internal shock and compressing wave system. It can be seen from the Prandtl-Meyer function that with increasing γ, a smaller expansion angle is required to reach a specified Mach number. The design of the throat contour is hence an important parameter for achieving similarity in the internal flow field For an ideal nozzle a subscale nozzle could be designed with an exit area ratio corresponding to the required exit Mach number, and this would give a qualitative coincidence in M-distribution, e.g. the flow would by definition be shock free and it is likely that the separation behavior would be quite similar. However, for other types of nozzles, e.g. a parabolic contour such as Vulcain, there is no analytical way of producing a similar internal flow field. In this case a best choice has to be made by optimizing the design with respect to different flow field characteristics. Sec. 7.3 describes how this was tackled by the European FSCD group in the various Vulcain sub-scale test campaigns.

7.2 Scaling with respect to viscosity

In general, the viscous length scale is different from the inertial one, and hence it is not possible to simultaneously obtain similarity with respect to both inviscid and viscous quantities.

The local Reynolds number, based on a characteristic length y, e.g. axial distance or local nozzle diameter, can be written as

$$\mathrm{Re}_{y1} = \frac{\rho_1 V_1 y}{\mu(T_1)} \tag{45}$$

The dynamic viscosity at T_1, $\mu(T_1)$, can be related to $\mu(T_0)$ by a viscosity law, e.g. the law of Sutherland or an exponential law. The local Reynolds number is thus related to the stagnation condition Reynolds number based on throat diameter,

$$\mathrm{Re}_{0d_t} = \frac{\rho_0 a_0 d_t}{\mu(T_0)} = \frac{p_0 d_t}{\sqrt{R_0 T_0}} \frac{\sqrt{\gamma_0}}{\mu(T_0)} \tag{46}$$

by

$$\mathrm{Re}_{y1} = \mathrm{Re}_{0d_t} \frac{y}{d_t} f(M_1 \text{ and gas properties}) \tag{47}$$

The function f is independent of nozzle size and gives the distribution of the local Reynolds number in the nozzle as a function of Mach number and gas properties. Even if an identical Mach number distribution could be achieved, the difference in gas properties, in particular γ, makes it impossible to reproduce the Reynolds number distribution in the scaled nozzle. At best, a Reynolds number of similar order of magnitude can be achieved by matching Re at stagnation. (A similar argument can be made concerning the similarity of Reynolds number based on boundary layer thickness.)

Flow separation is rather insensitive to Reynolds number as long as $Re_{\delta i} > 10^5$ (see Sec. 3.2 and 5.1 above) and it may therefore be sufficient to require $Re_{\delta i}$ being in the same range as for the full-scale nozzle. For instance, according to experiments by Spaid & Frishett [58] (see Figure 17a) a variation of $Re_{\delta i}$ by a factor of 2 results in an increase of

L_s/δ_i less than 10% at a shock angle of 14^0 and $Re_{\delta i}$ ~10^4. At $Re_{\delta i} > 10^5$ L_s/δ_i is almost constant according to the experiments by Settles [44] (see Figure 17b).

7.3 Two attempts of physical scale down of the Vulcain nozzle

The most serious attempt so far to apply the foregoing considerations in nozzle development tests is probably the preparation of the VOLVO S campaigns for cold sub-scale testing of the Vulcain nozzle with air – in particular VOLVO S1 and S3 (see Ref. [2,32]), which address the side-load problem. We will here briefly describe the scaling procedure, and assess the degree of success of the scaling in terms of agreement with full scale test results regarding separation and side-loads.

Vulcain being a parabolic nozzle, a parametric study of different TOP contours was first performed, were the values of the contour variables r_{td}, θ_N, L, r_e, and θ_E where varied in order to reach a final test nozzle contour that fulfilled specified similarities. S1 was designed with the primary aim of verifying the aeroelastic behavior. Great care was therefore taken to reproduce the wall pressure gradient. S3, on the other hand, was designed to give as close an agreement as possible with Vulcain with respect to the general flow field characteristics. The resulting dimensions of the model nozzles are given in Table 4 together with the Vulcain dimensions. The characteristic length, L_{ref}, was the nozzle exit radius, r_e, in S1and the nozzle throat radius, r_t, in sub-scale nozzle S3. Using $L_{ref}=r_e$ the geometrical contour comes closer to the original nozzle contour at the nozzle exit, whereas $L_{ref}=r_t$ results in a longer and thus a more slender contour, and the geometrical similarity will be restricted to the throat region.

The internal Mach number distributions are shown in Figure 58, and Figure 59 compares the distribution of different flow quantities along the wall.

Nozzle	*Vulcain*	*S1*	*S3*	
Area ratio	*45*	*20*	*18.2*	-
Nozzle length	*2065.5*	*350*	*528.2*	mm
Throat diameter	*262.4*	*67.08*	*67.08*	mm
Normalised inlet wall radius (r_{td}/r_t)	*0.5*	*0.5*	*3.0*	-
Throat wall angle	*35.025*	*35.025*	*27*	°
Nozzle exit angle	*6.5*	*4.0*	*0.0*	°
Nozzle exit diameter	*1760.2*	*300*	*286.5*	mm
Design feeding pressure (p_0)	*11.0*	*5.0*	5.0	Mpa
Design feeding temperature (T_0)	*3500*	*450*	450	K
Feeding gas	*LOX/LH2*	*Air*	Air	-

Table 4. Main characteristics of the different nozzles

In Figure 58 and Figure 59, one can clearly see the effect of the throat region on the initial expansion. In S1, the same values of θ_N and r_{td}/r_t were used as in Vulcain. Because of the different values of γ, this results in a more rapid initial expansion and hence a higher Mach number at the contour inflection point, which in turn gives a more intense internal shock compared to Vulcain. In S3, θ_N was reduced and a kernel more similar to Vulcain was achieved. The radial extension of the kernel is gradually reduced from about 70-80% of local nozzle radius near the throat region to about 30% at the nozzle exit. Note also that the curvature of the Mach number contours of S3 is more similar to Vulcain, affecting the shock and separation pattern.

Figure 60 shows the Reynolds number based on displacement thickness, Re_{δ^*}, in the Vulcain, S1 and S3 nozzles. In Vulcain, Re_{δ} is of order 10^5, which is high enough to have fully turbulent flow. Comparing the sub-scale nozzles, Re_{δ^*} is higher in S3 than in S1, because of the thicker boundary layer obtained in the much longer S3 nozzle. However, both sub-scale nozzles have a much larger Reynolds number than Vulcain, despite their small size. This is due to the difference in stagnation density, which is much higher in the wind tunnel (air at 500 K) than for hot propellant gases. For a complete matching of the stagnation Reynolds number, the throat radius of the model nozzles would have to be about 0.01 m, however for instrumentation purposes a larger scale size was chosen. As argued in Sec. 7.2 above, this difference in *Re* may be considered small.

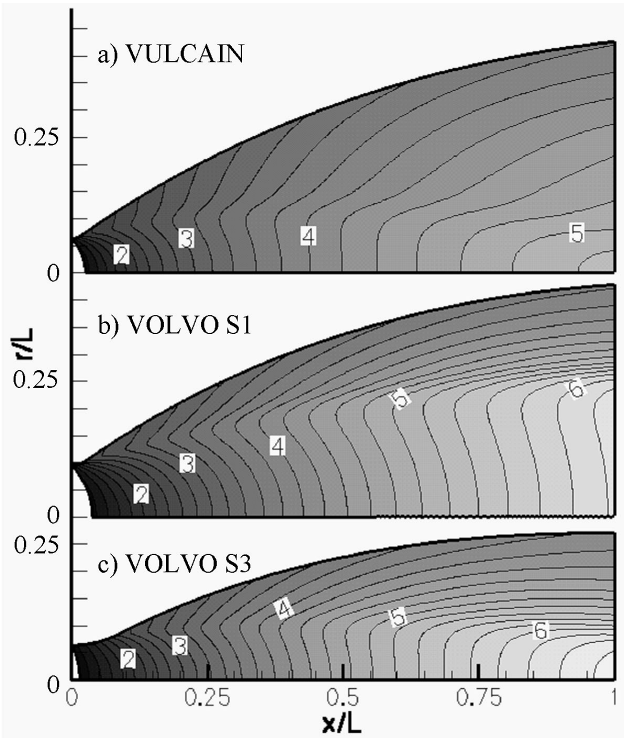

Figure 58. Mach number distribution in the: a) Vulcain , b) VOLVO S1 and c) VOLVO S3 nozzle, from Östlund *et al*. [2].

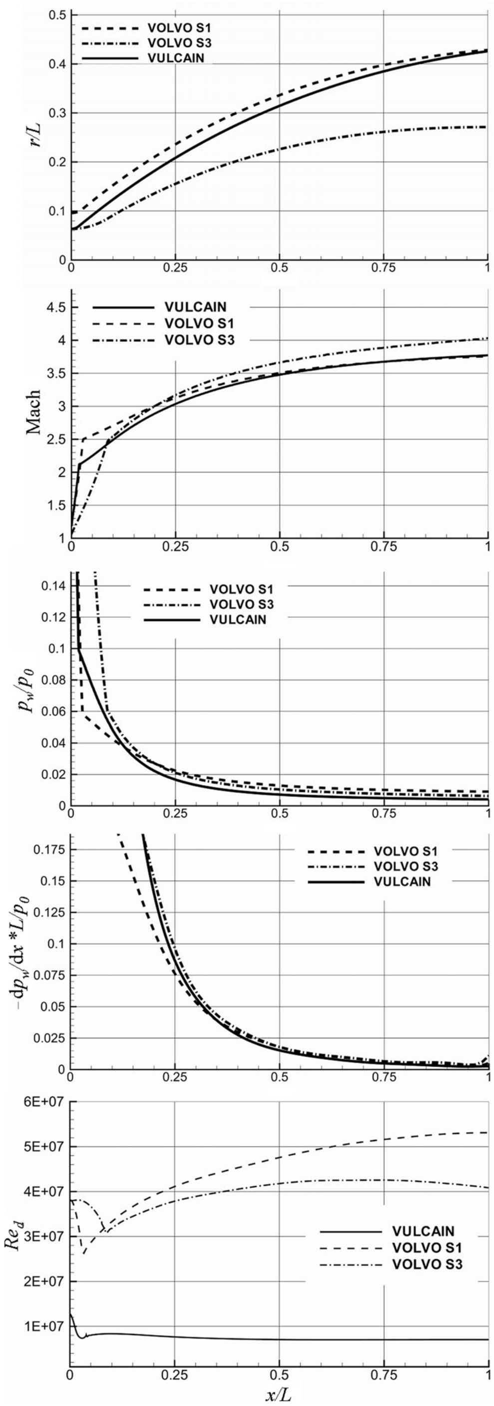

Figure 59. Comparison of wall properties between Vulcain and model nozzle S1 and S3, from Östlund [85].

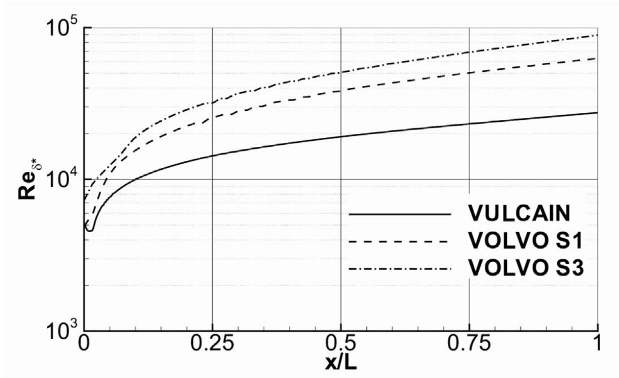

Figure 60. Reynolds number based on displacement thickness in the Vulcain, S1 and S3 nozzles, from Östlund [85].

7.3.1 *Experimental verification of the scaling*

Table 5 gives a comparison between the model nozzles and Vulcain regarding separation, side-loads and transition behavior. Both S1 and S3 have the same type of transition phenomenon as Vulcain, first from FSS to RSS inside the nozzle and, second, from RSS to FSS at the nozzle exit. These transitions occur almost at the same thrust levels (n) in the model nozzles as in Vulcain. However, when it comes to the location of the incipient separation, x_i, which occurs at FSS before the transition, a large difference between the sub-scale models and Vulcain can be seen. The table shows that in both model nozzles x_i is located about 30% upstream of corresponding location in Vulcain, however the reason for this is different in the two cases. In S3, the main reason is that the pressure recovery in the recirculating zone at FSS is sensitive to the downstream contour geometry (cf. Figure 40), which for S3 is quite different from that of Vulcain. In the S1 nozzle, on the other hand, the earlier separation is due to the dissimilarity of the internal flow field,

Case	$\dfrac{x_i/L_{ref}\big\|_{Model}}{x_i/L_{ref}\big\|_{Vulcain}}$		$\dfrac{n_{trans}/n_{nom}\big\|_{Model}}{n_{trans}/n_{nom}\big\|_{Vulcain}}$		$\dfrac{\left.\frac{M_{SL}}{r_t^2 r_e}\right\|_{Model}}{\left.\frac{M_{SL}}{r_t^2 r_e}\right\|_{Vulcain}}$
	FSS	RSS	FSS to RSS	RSS to FSS	
S1	0.67	0.99	0.84	0.92	0.65
S3	0.72	0.88	0.94	1.03	1.01
Vulc	1*	1*	1	1	1

Table 5. Comparison of measured quantities between model nozzles and Vulcain. (*=from CFD calculations, *nom*=design condition see Table 4), from Östlund [85]

which causes FSS-RSS transition to occur earlier in S1 than in Vulcain, while the pressure recovery after RSS is probably less geometry-dependent due to the reattachment and subsequent shock/expansion system.

Östlund [85] showed that a correct scaling of the side-load moment (M_{SL}) involves two different length scales, namely r_t and r_e, the throat and exit radii respectively. Table 5 shows that in S3, the side-load moment is accurately reproduced by combining the two length scales as $r_t^2 r_e$. With this scaling, side-load moment due to FSS-RSS transition is predicted with high accuracy, within a few percent.

The sensitivity of M_{SL} to different length scales can be understood by considering the following expression of the FSS to RSS transition side-load (cf. Sec. 5.4)

$$\begin{aligned}\vec{M}_{SL} &= \int_0^{L_e}\int_0^{2\pi} x\cdot\left(p_w - p_a\right)\vec{n}_\perp r\, d\varphi\, dx = \\ &= \int_{x_{i,FSS}}^{x_{i;RSS}}\int_0^{2\pi} x\cdot\left(p_w - p_a\right)\vec{n}_\perp r\, d\varphi\, dx + \\ &+ \int_{x_{i,RSS}}^{L_e}\int_0^{2\pi} x\cdot\left(p_w - p_a\right)\vec{n}_\perp r\, d\varphi\, dx\end{aligned} \tag{48}$$

The first term is associated with the sudden downstream shift of the separation line during the FSS to RSS transition. The second term is the side-load contribution due to the difference in the wall pressure distribution between the separation patterns downstream of x=$x_{i,RSS}$. Neglecting the second term and approximating the first integral, we obtain

$$M_{SL} \propto \left(x_{i,RSS}^2 - x_{i,FSS}^2\right)\left(r_{i,FSS} - r_{i,RSS}\right)\Delta p \tag{49}$$

This gives

$$\frac{M_{SL}/r_t^2 r_e\big|_{Model}}{M_{SL}/r_t^2 r_e\big|_{Vulcain}} \approx C_1 \cdot C2 \tag{50}$$

where

$$C_1 = \frac{\left(\dfrac{x_{i,RSS}^2 - x_{i,FSS}^2}{r_t^2}\right)_{Model}}{\left(\dfrac{x_{i,RSS}^2 - x_{i,FSS}^2}{r_t^2}\right)_{Vulcain}} \quad ; \quad C_2 = \frac{\left(\dfrac{r_{i,FSS} - r_{i,RSS}}{r_e}\right)_{Model}}{\left(\dfrac{r_{i,FSS} - r_{i,RSS}}{r_e}\right)_{Vulcain}}$$

Inserting the values for the shock jumps, and scaling axial coordinates with r_t and radius with r_e we obtain

$$\frac{M_{SL}/r_t^2 r_e\big|_{Model}}{M_{SL}/r_t^2 r_e\big|_{Vulcain}} \approx \begin{cases} 0.69\cdot 0.95 = 0.64 & for\ S1 \\ 1.04\cdot 0.89 = 0.92 & for\ S3\end{cases}$$

And applying the same scaling to the measured side-load

$$\frac{M_{SL}/r_t^2 r_e\big|_{Model}}{M_{SL}/r_t^2 r_e\big|_{Vulcain}} = \begin{cases} 0.65 & for\ S1 \\ 1.01 & for\ S3 \end{cases}$$

in other words, an excellent agreement between S3 and Vulcain is obtained, whereas the lack of agreement in the case of S1 may be attributed to deficiencies in the scaling of the internal flow field.

The results and analysis shown above verify that the applied methodology for designing a scale model operated with air is successful. Both S1 and S3 have captured the relevant physical phenomenon found in Vulcain. These model tests have given detailed information of the different phenomena, and have made it possible to develop generalized mathematical descriptions of the processes, which allow accurate prediction of separation positions and side-load magnitudes in rocket engine nozzles.

8 EXPERIMENTAL TECHNIQUES

The results described in the foregoing are based on a large amount of test data, used for constructing analytical models, verification of CFD results, as well as for direct design verification at different development stages. The specific objectives set for each specific test campaign will determine the type of test to perform (e.g. cold or hot, full scale or subscale), the kind of data to be acquired, instrumentation and measurement techniques. Experiments in supersonic nozzle flows impose certain requirements and limitations in terms of optical access, spatial resolution and frequency response. In hot gas tests, the sensors as well as their mountings must be able to resist very high temperatures, while special problems arise e.g. in connection with pressure measurements in low density gases. Some of these problems will be addressed in the following, where we will give an overview of common techniques used in supersonic nozzle flow testing.

8.1 External flow visualization

The simplest method to visualize the flow direction in an exhaust plume is to insert a wire with threads (tufts) into the flow. Figure 61 shows typical experimental results obtained by Stark *et al.* [138] in the exhaust flow of a TOP nozzle. The photo shows the movement of the tufts together with a numerical calculation superimposed, indicating the presence of a stable recirculating flow region in the plume by the threads, which are directed upwards. The indicator shows strong fluctuations in the recirculating zone downstream of the nozzle as well as in some outer regions. The movement of the threads is in good agreement with the calculated flow vector field, especially the location of the recirculating flow region at the centerline. The trapped vortex behind the cap shock pattern has been found in several CFD calculations, however, it has been questioned whether the trapped vortex is a numerical artifact or if it really exists in this type of flow. The experiment by Stark *et al.* (Figure 61) is important, as it is the first to validate the existence of a recirculation region behind the cap shock. Based on recent Laser Doppler Velocimetry measurements, Reijasse *et al.* [139] have also been able to produce a quantitative confirmation of the back flow.

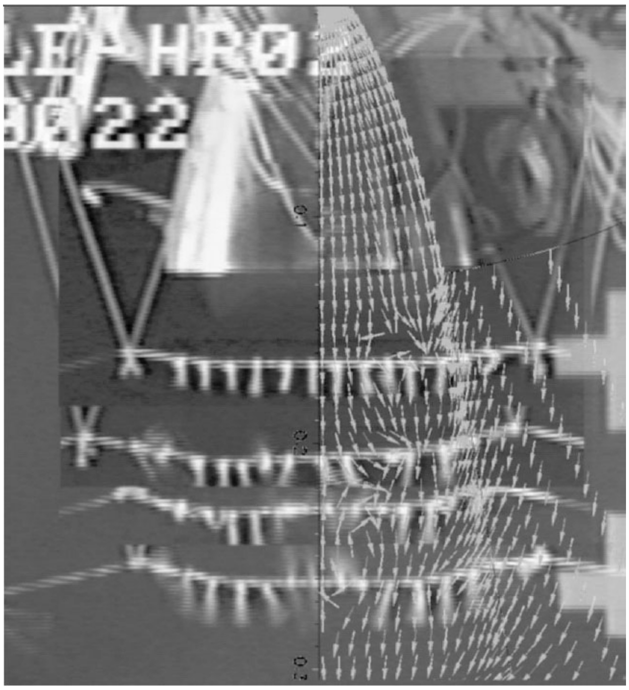

Figure 61. Visualization of flow field in the plume of the DLR TOP nozzle by using threads, experiment by Stark *et al*. [138]. (Courtesy of DLR and ASTRIUM)

8.1.1 Shock visualization

Compressible gas flows lend themselves particularly well to optical methods of investigation based on density variations (which are related to variations in index of refraction). Among these methods are Schlieren imaging and shadowgraphs. The former visualizes density variations, while the latter is sensitive to the second derivative of the density and therefore makes visible only those parts of the flow where the density gradients change very rapidly. For axially symmetric nozzle flows, these methods are only practically applicable to the exhaust flow. Typical results obtained with the Schlieren method and with the shadowgraph method are shown in Figure 10 and Figure 62 respectively for different sub-scale nozzles. To exemplify the usefulness of these methods it can be mentioned that Schlieren photos as the ones shown in Figure 10 have been an important source for the understanding of the physics behind the cap shock pattern. High-speed video recording of the Schlieren pattern during transient operation was used extensively in the VOLVO S1-S8 campaigns, and has given valuable information of e.g. the transition from FSS to RSS and vice versa, while Schlieren photos at stationary conditions have been used to validate CFD results, see Figure 78.

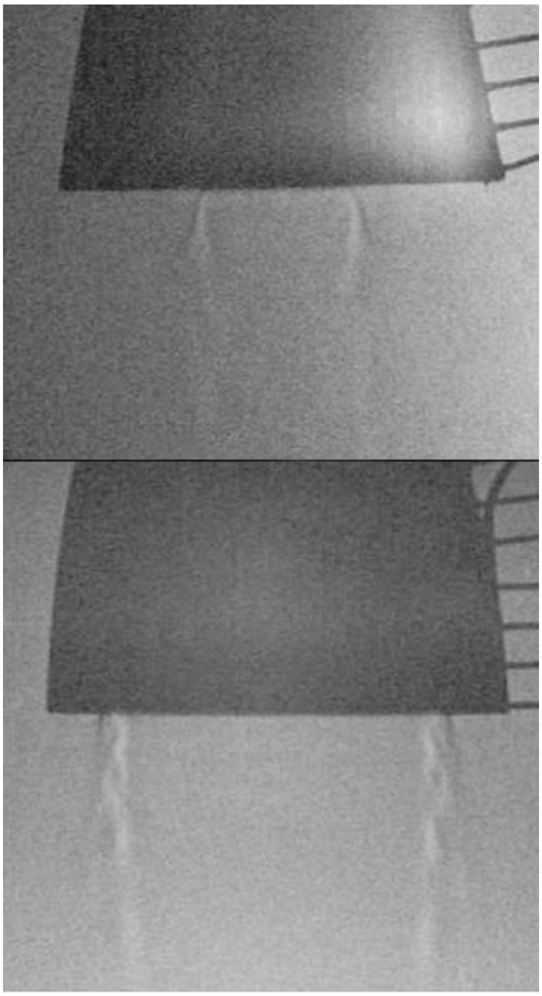

Figure 62. Shadowgraph photos of shock structure in the CTP86L (top) and CTP50-R5-L (bottom) nozzles by Tomita *et al* [111]. (Courtesy of NAL)

8.2 Visualization of the separated region

8.2.1 Oil flow visualization

Oil flow visualization is a common method for detection of the separation line. Figure 63 shows typical results obtained with this method from an experimental study of a TOP nozzle by Girard & Alziary [140]. They used a mixture of oil and carbon black to visualize the separation line, while the reattachment line was visualized with a much more viscous mixture of oil and grease. Before each run, the two mixtures were painted on the wall downstream of the estimated separation position and in a band over the estimated reattachment line respectively. During the run the oil and carbon black mixture would

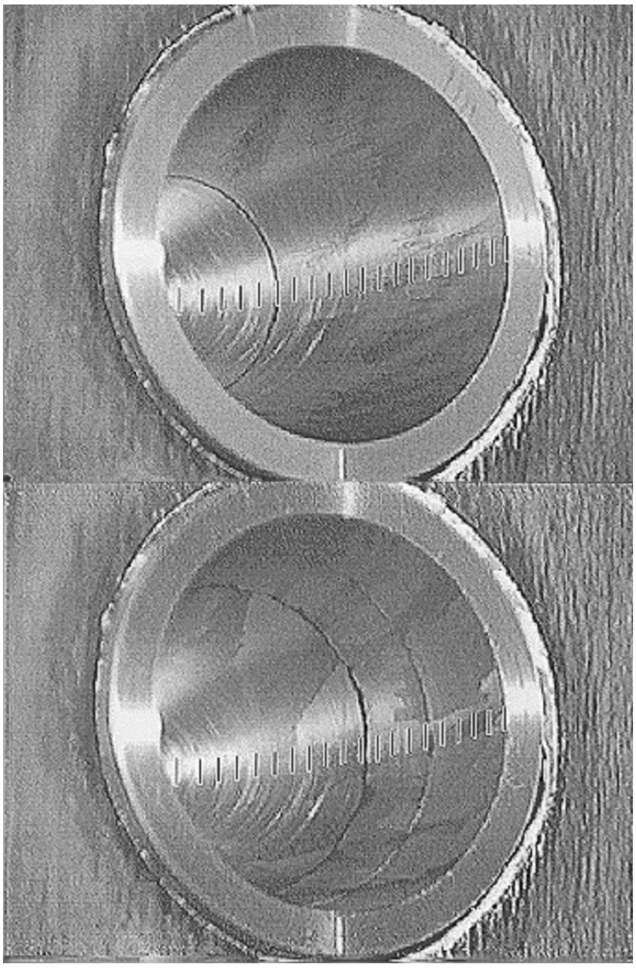

Figure 63. Oil film visualisation of separation line in a TOP nozzle, experiment by Girard & Alziary [140]. FSS line (top) and separation and reattachment line (bottom). (Courtesy of LEA Poitiers)

move upstream towards the separation line allowing a precise determination of its location. At the same time some of the oil and grease mixture would move downstream of the stagnation point and some would move upstream in the recirculation zone. Due to the low shear stress in the vicinity of the reattachment line, an amount of the mixture will remain around the reattachment line for several seconds.

Since surface oil flows are widely used to draw “conclusions” about a flow field as well as for comparisons with separation predictions from CFD, it is important to understand what the well-defined lines represent, especially as we have seen that the instantaneous separation line keeps moving upstream and downstream in this type of flow (see Sec. 3.3). This question has been addressed in a study by Gramann & Dolling [141]. Based on cross-correlations of the fluctuating wall pressure field measured down-stream of the instantaneous shock wave in different SWBLI configurations at Mach 5, they showed that

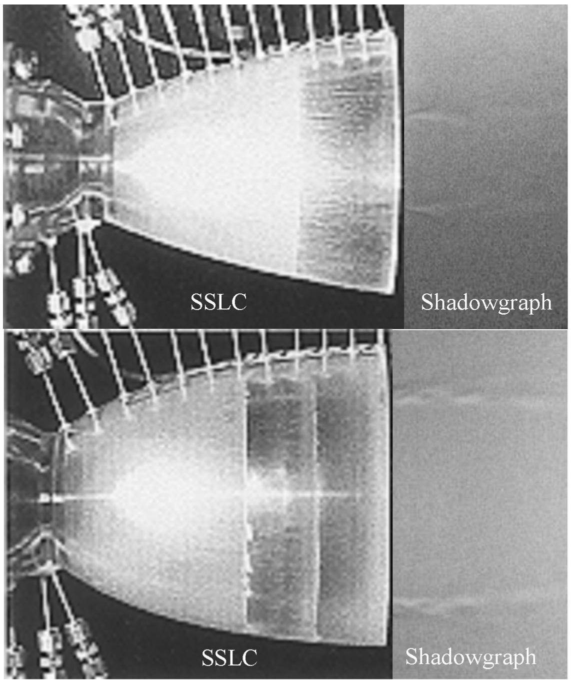

Figure 64. Visualization of separation line with Shear Sensitive Liquid Crystals (SSLC) and shock visualization with shadowgraph in the CTP86L (top) and CTP50R5L (bottom) nozzle by Tomita *et al*. [111] (Courtesy of NAL)

the separation occurs at, or just downstream of, the instantaneous shock position, and undergoes the same large-scale motion as the separation shock wave. Thus the separation line indicated by surface tracers falls into a region of intermittent separation, corresponding to the position where the time averaged wall shear stress becomes zero. Gramann & Dolling showed that this position is located well inside the intermittent region. Erengil & Dolling [67] later showed that its exact location depends on the sweep of the separation line, see also Ref. [71].

8.2.2 The use of Shear Sensitive Liquid Crystals (SSLC).

SSLC is a novel method for separation line visualization in internal flow [111,142]. The method consists of applying SSLC on the inner wall surface of a transparent specimen. As the color of the crystals is a function of the shear stress, the separation line corresponding to τ_w=0 is visualized. This technique has recently been applied to highly overexpanded nozzle flows by Tomita *et al*. [111], see Figure 64-Figure 65. Figure 64 shows the SSLC pattern and the corresponding shadowgraph image, also shown in Figure 62, for two different compressed truncated ideal nozzle contours at free shock separation conditions. As can bee seen in the figure a sharp and symmetric separation line is visible in both nozzles. The asymmetric movement of the separation line and the sudden downstream shift of the separation position during transition from FSS to RSS are clearly visible in Figure 65.

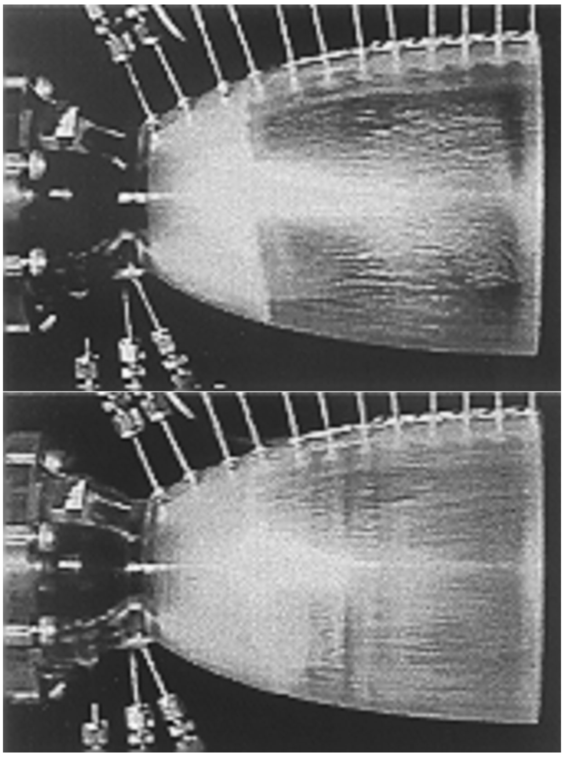

Figure 65. Two instant pictures of the wall shear stress field before (top) and after (bottom) transition from FSS to RSS in the CTP50R5L nozzle [111]. (Courtesy of NAL).

8.2.3 Infrared radiometry (IR)

IR is another experimental technique which can contribute to the insight in the separation behavior of nozzle flows. In recent experiments performed at DLR, IR has been used to visualize the wall temperature inside a sub-scale TOP nozzle operated at separated flow conditions [138]. Typical results from this test campaign are shown in Figure 66-Figure 68 at FSS and RSS conditions respectively. It is clearly seen that a wall temperature increase is induced in the incipient flow region, where the flow is still physically attached to the wall (see Figure 66 and Figure 67). In the case of reattachment of the jet to the wall, Figure 67, the wall temperature reaches a plateau value after this first temperature increase and then begins to decrease towards a constant value at the point where the flow reattaches the wall. In between the incipient separation line and the reattachment line a closed recirculating zone is established. Further downstream a second temperature peak can be observed, which is believed to be the affect of a second recirculation zone. IR-images have also made it possible to detect axial lines along the wall, which originate in the upper part of the nozzle, which are likely to have an influence on the separation and wall heat transfer behavior. Figure 68 shows an image where such lines are clearly visible downstream of the throat. As seen in Figure 67, traces of such vortices can also be observed downstream of the flow separation line.

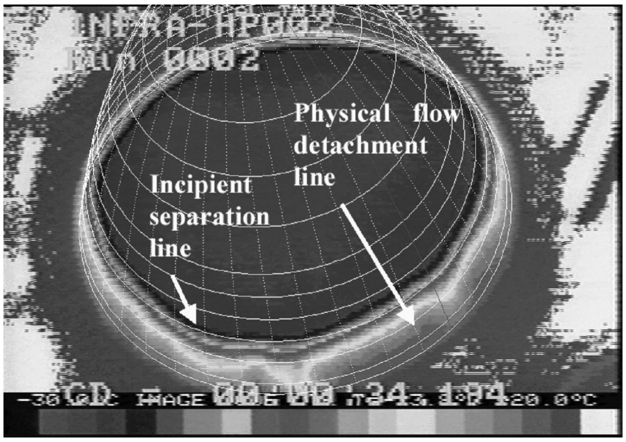

Figure 66. IR image: DLR TOP nozzle, during start-up, from Stark *et al.* [138]. (Courtesy of DLR and ASTRIUM)

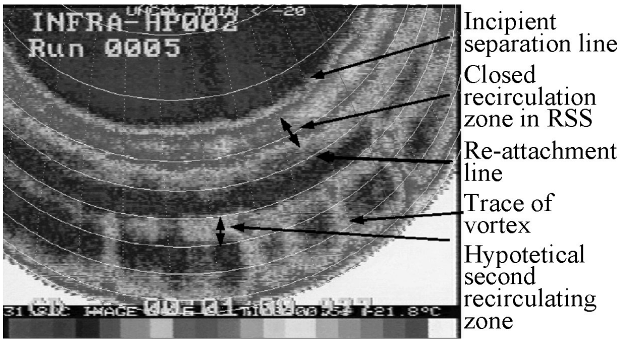

Figure 67. IR image: DLR TOP nozzle, during shut down, from Stark *et al.* [138]. (Courtesy of DLR and ASTRIUM)

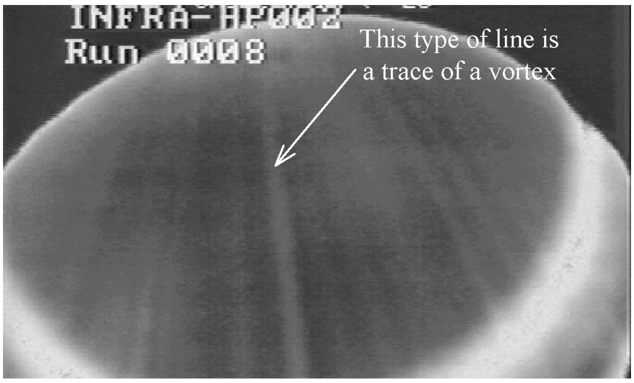

Figure 68. IR image: DLR TOP nozzle, vortex origin shortly after nozzle throat, from Stark *et al* [138]. (Courtesy of DLR and ASTRIUM)

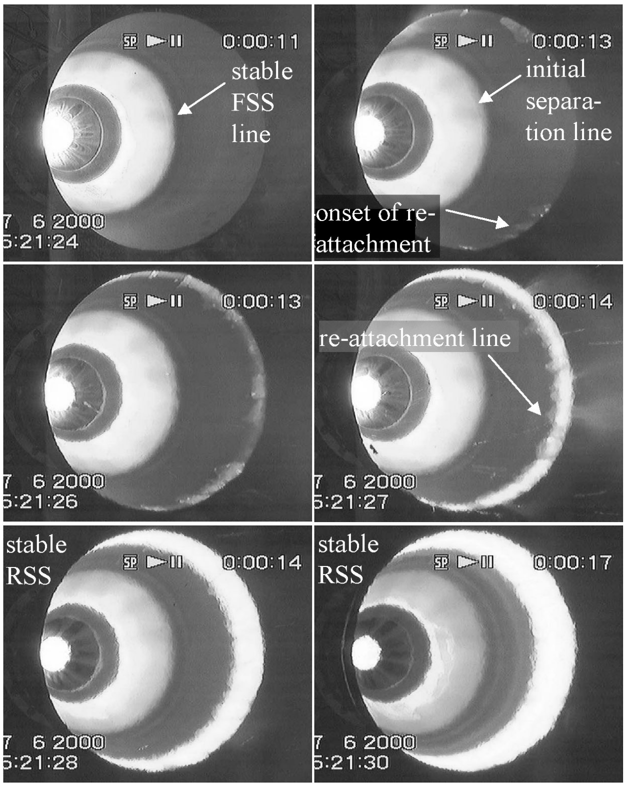

Figure 69. Details of the transition process from FSS to RSS in the long Vulcain C/SiC sub-scale, from Hagemann *et al.* [137]. (Courtesy of ASTRIUM)

In hot-gas tests, heat radiation in the visible band can also be used to observe separation phenomena. In a paper by Hagemann *et al.* [137] the transition process from FSS to RSS is illustrated by pictures obtained by a regular Video recording of the nozzle wall, see Figure 69. Here the separation and reattachment line can be identified from the onset of intensive radiation from the wall as the attached jet heats up the nozzle wall.

8.3 Pressure measurement of separating nozzle flows

Pressure measurements can give valuable information of the flow process if the instrumentation is carefully placed and correct interpretations of the measurements are made.

8.3.1 Static wall pressure measurements.

Static pressure taps are standard instrumentation used to monitor the flow response to variations in supply pressure and to locate the separation position. Figure 70 shows a typical wall pressure profile for a highly overexpanded nozzle flow.
The location where the static wall pressure starts to rise, x_i, is the origin of the shock wave boundary layer interaction, and a correct determination of this position is essential for constructing flow separation models. In order to experimentally locate this position, an

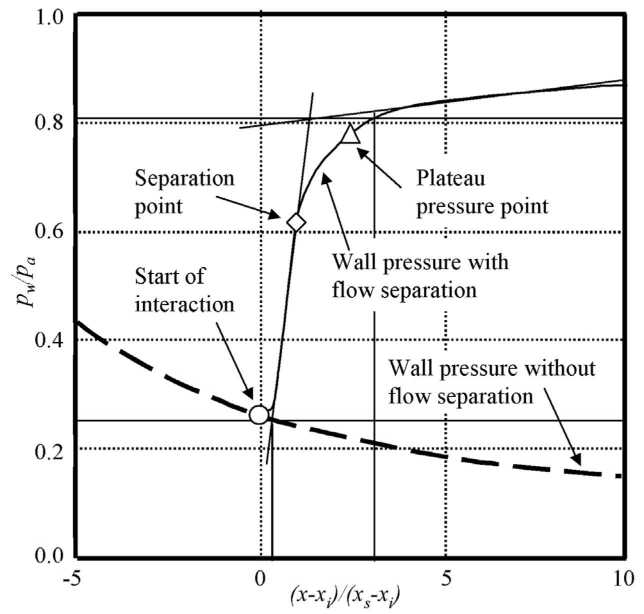

Figure 70. Typical wall pressure profile obtained in a highly overexpanded nozzle.

extremely narrow spacing of the pressure transducers is required. The separation length, $l_s=x_s$ $-x_i$ (cf. Figure 13 and Figure 24), where most part of the pressure rise takes places ranges from 1 to 100δ^*, depending on operational condition, degree of overexpansion, nozzle contour etc., see Figure 37. A rough estimate, which should only be considered as a rule of thumb to get the order of magnitude, is $l_s < 0.5r_t$, based on "cold" sub-scale test data see e.g. Figure 36 and Figure 38. As indicated in the schematic in Figure 70, a modest increase in the wall pressure takes place before a steep and almost linear pressure rise. To resolve this initial gradual increase and locate the first deviation from the vacuum pressure profile would require a transducer spacing of about $\Delta x=l_s/10\approx 0.05r_t$. In the VOLVO sub scale nozzles, which are considered to be of large scale in the context of cold flow model nozzles, the throat radius is r_t =33.54 mm. Thus the order of magnitude of the separation length in these nozzles are about l_s < 0.5*33.54≈17 mm, and to resolve the first deviation from the vacuum pressure profile would require a transducer spacing of $\Delta x\approx 0.05r_t$ =1.7 mm in this case. Such resolution can be realized, i.e. transducer spacing of 0.5 mm have been used at FOI, however the instrumentation cost will become high and the transducers may influence the flow. However, despite the practical resolution problems, some investigators, e.g. Carrière *et al.* [118], have used static pressure taps to determine the origin of the interaction.

8.3.2 Fluctuating wall pressure measurements.

In order to resolve the streamwise distribution of the rms pressure fluctuations in this region an extremely narrow spacing of the pressure transducers is required, as indicated in Figure 27 and Figure 44 we can see that an array of at least 5-10 pressure sensors along the interaction region would be needed in order to resolve the pressure rms distribution. The most important points to capture in this region are the point of maximum pressure rms and the locations of the origin and the end of the shock wave boundary layer interaction. In practice however, the spatial resolution is limited and the sensors are placed where they can capture the most important events. A simple way to capture the peak value is to find the operational condition when the peak is locked on a pressure transducer. This operational condition can be found by changing the operational condition *n* with small stepwise increments or with a slow continuous ramp, as in Figure 27.

In the separated region, the gradients are small, and hence it is less important to have a fine streamwise resolution. 5-10 evenly spaced pressure sensors would be sufficient to capture the most significant features of the recirculating flow zone.

In order to quantify the instantaneous asymmetry of the pressure load, pressure sensors must also be installed in the transversal direction in the separation and the separated zone respectively. It is difficult to specify a minimum number of pressure sensors required in the transversal direction. In general reliable quantitative data on the structures and pressure fluctuations in the transverse direction are lacking and is fruitful area of future work. However, as an indication Dumnov [128] used 8 fast pressure transducers in the transversal direction in order to obtain the pressure correlation function, on which he based his side-load model. For a more general survey of fluctuating wall pressure measurements for this type of flow, the work by Dolling & Dussauge [144] is recommended, where method of measurement, common sources of error and calibration methods are discussed.

8.3.3 Pressure sensitive paint.

The problem of spatial resolution can be overcome by using modern field measurement techniques such as Pressure Sensitive Paint (PSP). PSP is commonly used for external high-speed flow situations [145], whereas there are only a few studies in the literature, where PSP has been applied to internal supersonic flow, see e.g. Ref. [146-148]. The main problem with PSP is that the paint has a strong temperature dependency. It must therefore be used together with IR-techniques or Temperature Sensitive Paint (TSP). In the case of internal flow, the visual access further complicates the situation. PSP is not as accurate as static pressure taps, the accuracy being only about 5%. That is why a combination of PSP and regular pressure taps is often used.

The development of fast pressure sensitive paint (FPSP) has evolved rapidly in recent years, see e.g. Ref. [149]. FPSP has response times in the range 3-12 kHz. It may hence be possible in the near future to resolve the global unsteady pressure field in separated nozzle flows with this method.

8.4 Side-load measurements

Direct measurement of the global asymmetric fluctuating pressure load obtained during nozzle operation with flow separation would require a fast and global surface field measuring method, i.e. either the use of an enormous number of fast pressure transducers or the use of fast pressure sensitive paint, non of which is feasible today. Instead, the commonly used method is to measure the system response to the aerodynamic side-load as it acts on the structure. If the structural dynamic transfer function is known, the aerodynamic side-load can then be calculated.

In a rocket engine the aerodynamic side-load can excite two different modes of the rocket engine structure. These modes are 1) the pendulum mode where the nozzle oscillates around the cardan and 2) the bending mode where the nozzle oscillates around the throat. An experimental set-up must simulate the most significant of these modes. In Figure 71-Figure 74 the experimental test set-ups used by VOLVO [2,32], ONERA [150] and DLR [28] are shown respectively (the test set-ups used at Keldysh [128] and NAL [111] are similar to the one used at DLR). The VOLVO test set-up simulates the bending mode, whereas the set-ups of ONERA and DLR simulate the pendulum mode.

The device for measuring dynamic unsteady side-loads at ONERA [150] consists of a support-tube equipped with semi-conductor strain gauges in order to measure the bending moment in two planes, i.e. the two perpendicular components of the general side-load moment. The reference point for these torque measurements is labeled CRB Tube in Figure 73.

The side-load measuring system in the DLR test facility P6.2 consists of one thin walled Aluminum pipe which connects the rigid test nozzle to the rigid gas feeding system [28], see Figure 74. As side-loads are produced in the nozzle, the thin walled pipe will bend and with the use of strain gauges the two perpendicular components of the resulting side-load response are measured. By changing the length of the strain-measuring pipe different system eigenfrequencies can be obtained.

In the test set-up used by VOLVO [2,32], the nozzle consist mainly of two parts, one fixed part mounted to the downstream flange of the wind tunnel and one flexible hinged part, see Figure 71. The flexible part is suspended with a universal joint/cardan, Figure 72, permitting motion in all directions around the throat and the motion simulates the throat-bending mode of a real rocket nozzle. The bending resistance is simulated with torsion springs, which are exchangeable, that the influence of the structure stiffness on the side-load response and aeroelastic coupling can be studied. The side-load response components are measured with strain gauges mounted on the torsion springs. Typical results from the latter can be seen in Figure 28.

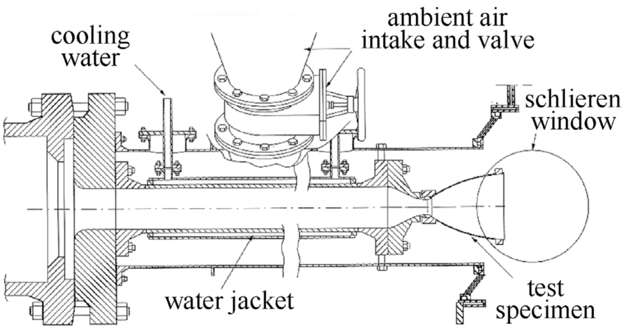

Figure 71. Schematic side view of the experimental test set-up in FFA wind tunnel HYP 500, from Östlund *et al.* [2,32].

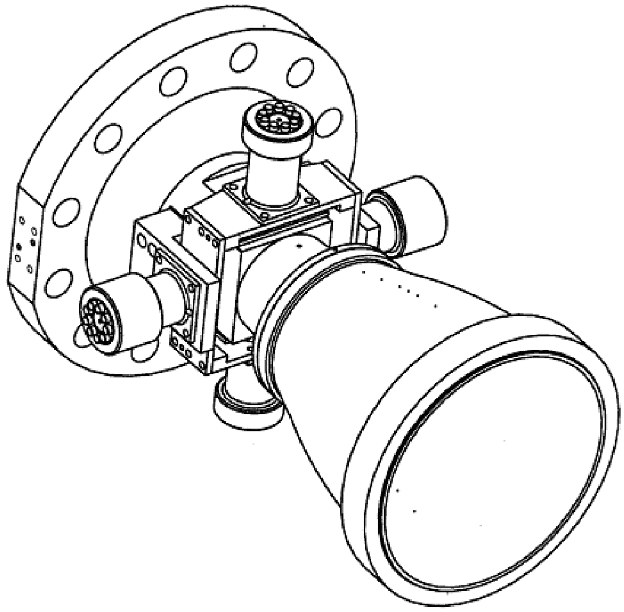

Figure 72. Schematic side view of the cardan hinged test nozzle in FFA wind tunnel HYP 500, from Östlund *et al.* [2,32].

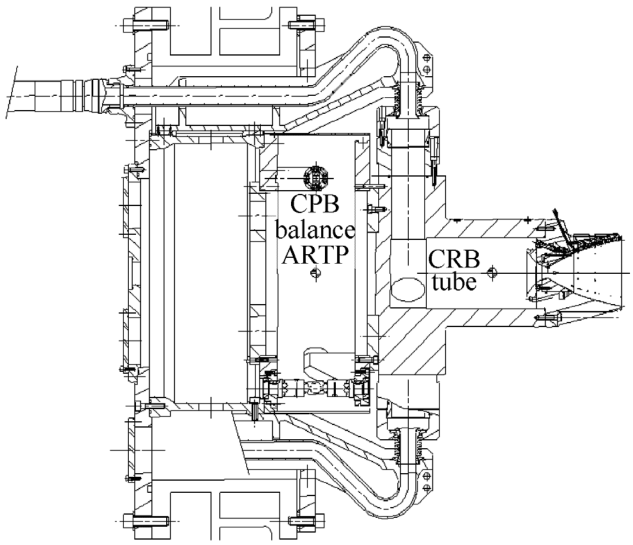

Figure 73. Sketch of the experimental set-up in the ONERA R2Ch blow down wind tunnel, from Reijasse *et al.* [150].

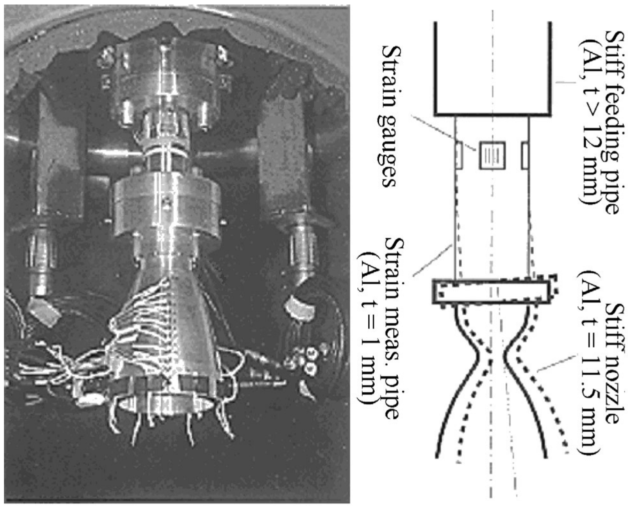

Figure 74. Experimental test set-up and principles of the side-load measuring system in the DLR test facility P6.2, from Frey [28].

8.4.1 Determination of the system response function

In the test set-ups described above, the side-load response of the mechanical system is measured, not the side-loads as such. Hence a method is needed for calculating the aerodynamic side-load that occurs on the nozzle wall.

During a test run, the strain gauges measure the strains, $\vec{S}(t)$, resulting from the dynamical response of the system to the aerodynamic side-load torque $\vec{M}_a(t)$. $\vec{S}(t)$ and $\vec{M}_a(t)$ are vectors with two components representing motion in two directions around the main axis. These are usually different due to the asymmetry introduced by the instrumentation and the test set-up.

After Fourier transform of $\vec{S}(t)$ and $\vec{M}_a(t)$ and introducing the transfer function *H(f)* (system frequency response function) we get

$$\hat{\vec{S}}(f) = H(f)\hat{\vec{M}}_a(f) \tag{51}$$

Once *H(f)* is known, the aerodynamic load components M_{a1} and M_{a2} can be reconstructed from the strain-gauge signals after computing the inverse of Eq. (51).

Here *H(f)* is generally a complex 2x2 matrix, which can only be determined with the use of advanced structural testing methods such as described in e.g. Ref. [151-152]. However, if the experimental set-up is carefully designed it may be approximated by a dynamic system with one degree of freedom (1-DOF), which greatly simplifies the determination and description of the transfer function. Such an approximation is only valid if the system is isotropic, i.e. the transfer function matrix is diagonal with $H_{11}=H_{22}=H$, and the eigenfrequencies of any higher order modes are far from the fundamental eigenfrequency f_0. If this is the case, one can reconstruct the aerodynamic load components from the strain-gauge signals as

$$\hat{M}_{a1,2}(f) = H^{-1}(f) \cdot \hat{S}_{1,2}(f) \tag{52}$$

An expression for the transfer function can be obtained from the characteristic differential equation for a system with 1-DOF. Further, the parameters to be experimentally determined have been reduced to the fundamental eigenfrequency (f_0), the system stiffness (k) and the damping coefficient (ζ).

However, even in a perfectly symmetrical setup, there will be an overlaid tangential component, which will have a parasitic effect on the side load measurement. This effect, which is present whether a bending tube or a cardan construction is used, can be minimized by minimizing the bending amplitude, i.e. by using a stiff construction.

9 PREDICTION BASED ON RANS METHODS

The most common approach for predicting turbulent shock wave boundary layer interactions, including those involving separation, is to solve the Reynolds-averaged Navier-Stokes (RANS) equations. In the following a few problems specific to shock boundary layer interactions and flow separation will be addressed, and the need for more advanced CFD methods will be discussed.

9.1 Interactions in basic configurations

A critical survey of current numerical prediction capabilities for simulation of laminar and turbulent interactions in basic configurations, such as the single fin, double fin and hollow cylinder flare, were presented by Knight & Degrez [87] in 1998. The objective of their study was to determine how well current codes could predict quantities needed in the design of high speed vehicles, including flow field structure, and mean and fluctuating aerodynamic and thermal loads. They concluded that for laminar flows existing codes accurately predict both aerodynamic and thermal loads. However, the situation for turbulent flows is not as satisfactory. They concluded that mean pressure distribution in 3-D interactions can be computed quite well, with little variation between computations using different turbulence models. On the other hand, skin friction and heat transfer distributions are generally poor, except for weak interactions (no separation), with different turbulence models producing different results. The differences between measured and predicted heat transfer are substantial. Knight & Degrez note differences up to 100% for strong interactions (separated flow). In 2-D interactions, especially strong ones, the situation is somewhat bleaker. Mean surface pressure distributions are satisfactory only for weak interactions. In strong interactions, the models generally predict too little upstream influence, i.e. the calculated separation length is shorter compared with the one observed in experimental data.

9.2 RANS corrections

Much effort has been spent by different researchers on corrections that cure some of the apparent anomalies in RANS simulations of strong interactions. The most common corrections for compressible boundary layers are the compressibility correction, the turbulent length scale limit and the realizability correction. A brief description of these concepts is given below.

9.2.1 Compressibility corrections

For high-Mach-number flows, compressibility affects turbulence through so-called dilatation dissipation ε_d , which is normally neglected in the modeling of incompressible flows. Neglecting the dilatation dissipation fails to predict the observed decrease in spreading rate with increasing Mach number for compressible mixing and other free shear layers (see e.g. Ref. [154]). To account for these effects dilatation dissipation terms must be included in the turbulent kinetic energy and dissipation equations. Common for all proposed models is that the dilatation dissipation is a function of the turbulent Mach number defined by

$$M_t = \sqrt{2k} / a \tag{53}$$

where a is the speed of sound.

The most popular corrections are due to Sarkar *et al.* [155] and Zeman [156] primary derived for compressible mixing layers. However, since they gives undesirably lowered skin-friction in turbulent boundary layers [157-159], neither of these corrections are completely satisfactory for both the mixing layer and boundary layers. The model by Wilcox [159] resolve this dilemma by activating the compressibility correction first when a threshold value of the turbulent Mach number $M_{t0} = 0.25$ is reached.

This type of compressibility corrections generally improves the prediction capability of flow fields involving compressible mixing and other free shear layers. Further, Wilcox [159] showed that including the compressibility correction in the simulation of a Mach 3 flow into a 24° compression corner yield a much closer agreement to measurements compared with the case with no correction.

However, these corrections should be regarded as completely empirical rather than true models of dilatation dissipation.

9.2.2 The turbulent length scale limit

The concept of the turbulent length scale limit, introduced by Coakley & Hung [157], is as follows. First, the so-called von Karman length scale, l_μ , is calculated as

$$l_\mu = \begin{cases} \min\left(2.5y, k^{1/2}/\omega\right), \ k-\omega \text{ model} \\ \min\left(2.5y, k^{3/2}/\varepsilon\right), \ k-\varepsilon \text{ model} \end{cases} \tag{54}$$

where y is the distance to the wall. Then, the value of ε or ω is recomputed according to

$$\omega = k^{1/2}/l_\mu , \quad \varepsilon = k^{3/2}/l_\mu \tag{55}$$

This correction has shown to be very effective in reducing predicted heating rates at the reattachment point for shock-separated flows to realistic values [157]. However, as pointed out by Thivet *et al*. [160] a similar effect may be achieved in a more natural way with a realizability correction.

9.2.3 Realizability constraints

The mathematical concept of realizability [161,162] is that the variance of the fluctuating velocity components must be positive and the cross-correlations bounded by the Schwartz inequality. Solutions obtained for strong interactions with common two-equation turbulence models violate this realizability constraint in the outer part of the boundary layer and outside [163]. The size of the unrealizable zones increases with the interaction strength and they are clearly related to the largest values of the dimensionless strain rate invariant in the flow, especially across the shocks.

A recent review of realizability correction of two-equation turbulence models by Moore & Moore [164] recalls that the idea is to enforce the realizability constraints by limiting the value of the constant in the definition of the eddy-viscosity $\mu_t = \alpha_v C_\mu \rho k/\omega$ (where $\omega = \varepsilon/k$) as follows

$$\alpha_v = \min\left(1, \bar{\alpha}_v\right) \tag{56}$$

where $\bar{\alpha}_v$ is defined by

$$\frac{1}{\bar{\alpha}_v C_\mu} A_0 + A_s \sqrt{s^2 + A_r \bar{\varpi}^2} \tag{57}$$

C_μ is the usual constant 0.09, s is the dimensionless mean strain rate S/ω with $S^2 = 2S_{ij}S_{ji} - 2/3 S_{kk}^2$, and $\bar{\varpi}$ is the dimensionless vorticity invariant $\sqrt{2\Omega_{ij}\Omega_{ij}}\big/\omega$ where

$$S_{ij} = \frac{1}{2}\left(\frac{\partial U_i}{\partial x_j} + \frac{\partial U_j}{\partial xi}\right) \;\; ; \;\; \Omega_{ij} = \frac{1}{2}\left(\frac{\partial U_i}{\partial x_j} - \frac{\partial U_j}{\partial xi}\right) \tag{58}$$

Moore & Moore [164] propose a set of constants (i.e. A_0, A_s and A_r) derived from an Algebraic Reynolds Stress Model (A_0=2.85, A_s=1.77) and assumed, in a first approximation, that the strain rate and rotation have symmetrical effects (A_r=0). They show that, in the case of flows near leading edges, where the inviscid strain rate is very large (s=100-400), the modifications ends up with a much better prediction of the level of the turbulent kinetic energy (k_t). Other researchers have proposed other values of the constants, e.g. Durbin *et al*. [165,166] proposed a similar correction with A_0=A_r=0 and 1/A_s=0.29. This gives smaller values of α_v then those obtained by Moore & Moore, but and is virtually identical to those by Coakley [157,167] or by Menter [169] using the SST model, where 1/A_s=0.3.

The effect of this type of correction is illustrated in Figure 75, showing the pressure, Mach number, turbulent kinetic energy *(k_t)* and dissipation *(ω)* distribution in a quasi one-dimensional nozzle, which adapts to the exit condition through a normal shock. The turbulence model used is the Wilcox standard k-ω model, with and without a realizability correction similar to the one proposed by Moore and Moore. Here we label the standard model without correction as *WS* and the one with correction as *WM* respectively. The pressure and Mach number distribution obtained with the Euler equations are also included in the figure for comparison. As can be seen in the figure, the *WS* model gives an unphysical increase of k_t and ω already in the convergent part of the nozzle, where the flow is accelerated to sonic conditions.

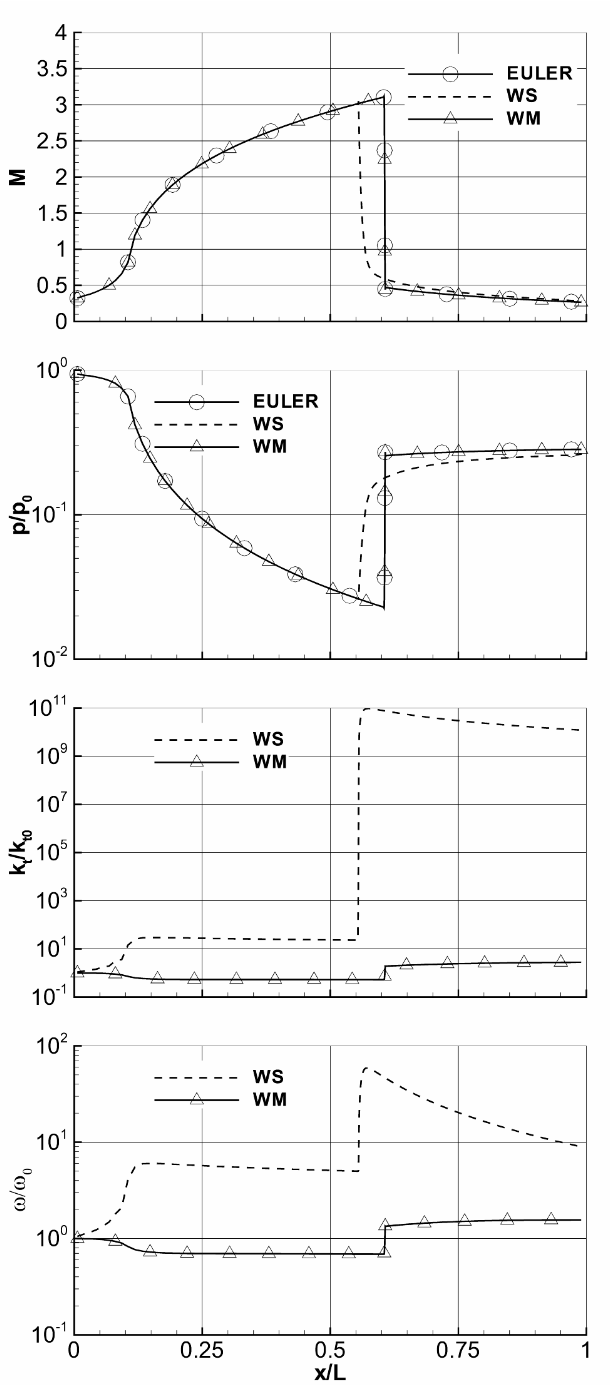

Figure 75. Influence of realizability corrections on a normal shock in a quasi one-dimensional nozzle, from Östlund [85].

In a real case, strong acceleration can lead to relaminarisation of the flow and this trend is captured with the *WM* model. With the *WS* model the production of k_t explodes over the shock, which smears out the shock and affects its predicted position. The *WM* model cures this stagnation point anomaly at the normal shock and therefore virtually duplicates the Euler solution. With this type of correction the results are generally improved, however, the results are still not satisfactory as will be illustrated in the following example of a nozzle at overexpanded flow conditions.

9.3 Overexpanded nozzle flow

The nozzle studied is the VOLVO S6 nozzle tested in the HYP 500 wind tunnel at FOI. The nozzle is an ideal truncated nozzle with design Mach number M_D=5.15 truncated at ε=20.6 [85].

In Figure 76 calculated and measured wall pressure profiles are shown for three different operational conditions, *n*=0.04, 0.08 and 0.28 respectively. As can be seen, the predicted incipient separation point, i.e. the first deviation from the pressure profile obtained with attached flow condition, occurs upstream of the measured one for all operational conditions. The incipient separation position predicted for the *n*=0.04 case is closest to the experimental data and as *n* increases the discrepancy increases, to finally become significant for the *n*=0.28 case. In all cases the predicted separation length is shorter than observed in the test data, which gives a steeper pressure rise in the separation region compared with experimental values.

The misprediction of the location of incipient separation point at moderate overexpansion also influences the predicted position of the Mach disc. Figure 77 shows the calculated Mach number distribution at *n*=0.20 and in Figure 78 the predicted shock system is compared with a Schlieren image obtained for VOLVO S6 at the same operational condition. It can be seen that the Mach disc obtained in the simulation is located too far upstream compared with the test data. It is not clear if it is only the separation line that drives the location of the Mach disc or if other factors are involved.

The coefficients in the realizability constraint used in the Menter SST model are A_0=A_r=0 and A_s=10/3. Since researchers have proposed different values, it was necessary

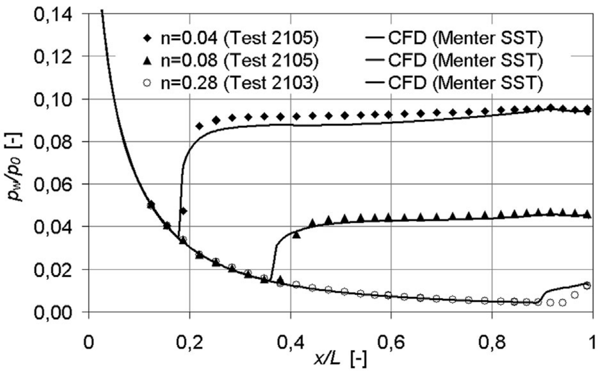

Figure 76. Wall pressure in the VOLVO S6 nozzle, comparison between Menter SST and test data, from Östlund [85].

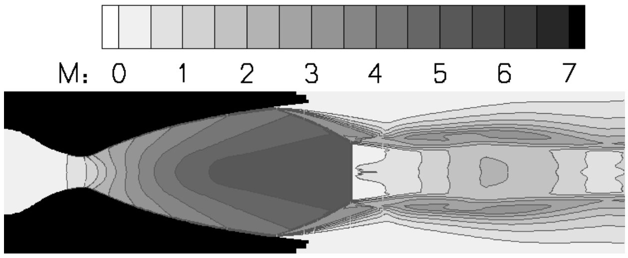

Figure 77. Mach number distribution in the VOLVO S6 nozzle at n=0.20, from Östlund [85].

to assess the influence of A_s on the computed flow field. Such a study was performed, see Östlund [85], where A_s was varied within the range 1/3-10/3, and lead to the conclusions that when A_s is reduced the incipient separation point and corresponding shock system are moved further downstream and the opposite happens if it is increased. Thus by adjusting A_s, a better prediction can be obtained at moderate overexpansion, however, this will instead cause increased discrepancies at highly overexpanded conditions. On the whole, the procedure of adjusting turbulence model parameters "on hand" is not satisfying, since it is somewhat arbitrary and does not guarantee adequate results for new types of flow fields.

9.4 Advanced CFD methods

It is clear from the above that the current capability to predict critical quantities for design of applications featuring strong shock wave boundary layer interactions is not satisfactory. One of the drawbacks is that the eddy-viscosity models use a single length scale to represent the turbulence, which is insufficient in separated flow. Secondly RANS calculations do not model coherent flow field unsteadiness. As noted earlier (see Sec. 3.3 and especially Figure 22) the global flow field unsteadiness is such a dominant feature in this type of flow, and that without modeling it, not even mean quantities can be computed accurately.

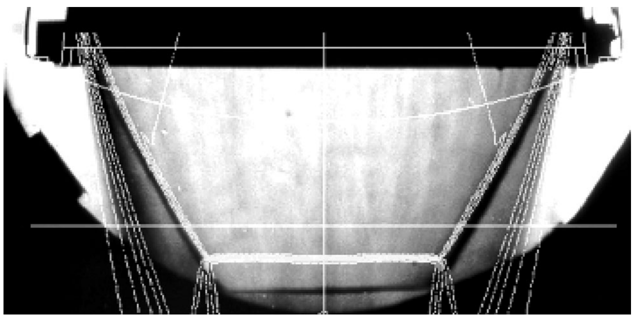

Figure 78 Comparison of shock system position at n=0.20. The simulated value is compared to a Schlieren photo from the test, from Östlund [85].

9.4.1 Unsteady RANS

In recent studies, see e.g. Deck *et al.* [170-171] and Yonezawa *et al.* [172], three-dimensional unsteady RANS (URANS) simulations have been used in an attempt to capture the unsteadiness of separated nozzle flows and thereby improve the prediction capability. The obtained results show generally a qualitative agreement with the characteristics found in experiments, i.e. low frequency pressure fluctuations in the separation region, 3D flow structures and the generation of side-loads. In that sense URANS calculations show a dramatic improvement compared with steady 2D RANS simulations. Nevertheless, it should be said that not even URANS methods can simulate the causes of the unsteadiness correctly.

Consider e.g. the hypothesis by Sergienko *et al.* [130] (see Sec. 5.2.4), which states that the pressure pulsations (acoustic field) generated by the mixing layer of the jet and the ambient gas are transferred to the separation zone, where they are reinforced on the resonant frequencies of gas free oscillations of the separation zone. This amplifies the oscillation amplitude of the separation line position, and as a consequence, a pressure redistribution along the inner nozzle surface takes place and the appearance of fluctuating loads. In such a scenario, URANS can at best model the dynamic characteristics of the separated zone to some extent. But it is incapable of accurately simulating the main source, i.e. the acoustic field of the jet caused by the shear layer and shocks. Furthermore, the incoming boundary layer upstream the SWBLI in a URANS simulation does not contain any turbulent structures or vortices, which has been pointed out as the possible source for the low frequency shock motion found in the generic SWBLI test cases presented in Sec. 3.

To address these deficiencies of RANS methods, it appears necessary to move towards large eddy simulations (LES). This perspective is not unique for separated nozzle flow; Knight & Degrez [87] reached the same conclusion in their review of generic SWBLI test cases.

9.4.2 LES and DNS

The development of compressible LES or variants of LES for application to SWBLI is still very much in its infancy. However, since the first LES of a SWBLI by David in 1993 [173] much progress has been done in this field, see e.g. Ref. [88,179].

Knight *et al.* [88] reviewed recent DNS, LES and RANS simulations of turbulent SWBLI, and found that a comprehensive assessment of the capability of DNS and LES was not possible for two reasons. First, the DNS and LES simulations have been performed at lower Reynolds number than the experiment for all cases except one. Second, the DNS and LES have been performed for nominally 2D flows. Both reasons are attributed to the computational cost of DNS and LES.

Although the set of comparisons between DNS and LES with experiment was limited, they found that good agreement with experimental data were achieved in those cases where the computations were performed at Reynolds numbers close to the experiment. The general conclusion is that significant progress has been achieved in the prediction of SWBLI using DNS and LES. It is therefore likely that this type of CFD methods will be more extensively used in the future for the modeling and prediction of the unsteady thermal and pressure loads in SWBLI and separated nozzle flows in particular.

10 IDEAS AND CONCENCEPTS FOR FLOW SEPARATION CONTROL

As discussed in the introduction (see Figure 2), much would be gained in terms of performance, if a rocket engine nozzle could adapt to the changes of ambient pressure during ascent, to give ideally expanded flow at all altitudes. The closest one can get to realizing this objective is the external expansion nozzle (also called aerospike or plug nozzle), where the flow expands on the outside of the nozzle, thereby automatically adapting to the ambient. This concept – altogether different from the traditional bell nozzle concept – may hold a potential for the future, however many technical problems remain to be resolved before it can be applied in a rocket engine.

At present, the rocket community still favors internal flow nozzles, where the main development objective is to extend the operational margin by controlling the separation position and/or the unsteady movement of the separation line so as to reduce side-loads. Figure 79 shows some of the concepts that are presently being considered, where the idea is either control (Figure 79a-d,f), avoid (Figure 79e, g-h), inhibit (Figure 79i) or reduce the effect of flow separation (Figure 79j).

Some of the factors to be considered to assess the realizability of a concept are:

- Reliability
- Functionality
- Lifetime
- Aerodynamic performance
- Weight
- Mechanical complexity
- Cooling requirements
- Required manufacturing techniques
- Cost (including development cost)

The demand for reduced development cycles also raises the question of technological uncertainty, i.e. the risk to fail to realize a concept within a given time.

In the following a short description together with the potential and drawbacks of each concept will be given.

10.1 Abrupt contour changes

10.1.1 Dual-bell

The dual-bell nozzle, as sketched in Figure 79a, was first studied at the Jet Propulsion Laboratory in 1949 by Forster & Cowles [94]. This nozzle concept, which was patented in the late 1960’s by Rocketdyne, has received new interest in recent years within the space propulsion community, see e.g. Refs. [181-187]. The reason for this interest is the one-step altitude adaptation, achieved only by a wall inflection and, thus, without any moving parts. At low altitude (sea-level mode, SM) a controlled and symmetrical flow separation occurs at the wall slope discontinuity, resulting in a nozzle with a lower effective expansion ratio. At high altitudes (altitude mode, AM) where the ambient pressure is low, the flow expands and attaches to the nozzle wall, and the full geometrical expansion ratio is used. Because of the higher expansion ratio, an increase in vacuum performance is achieved.

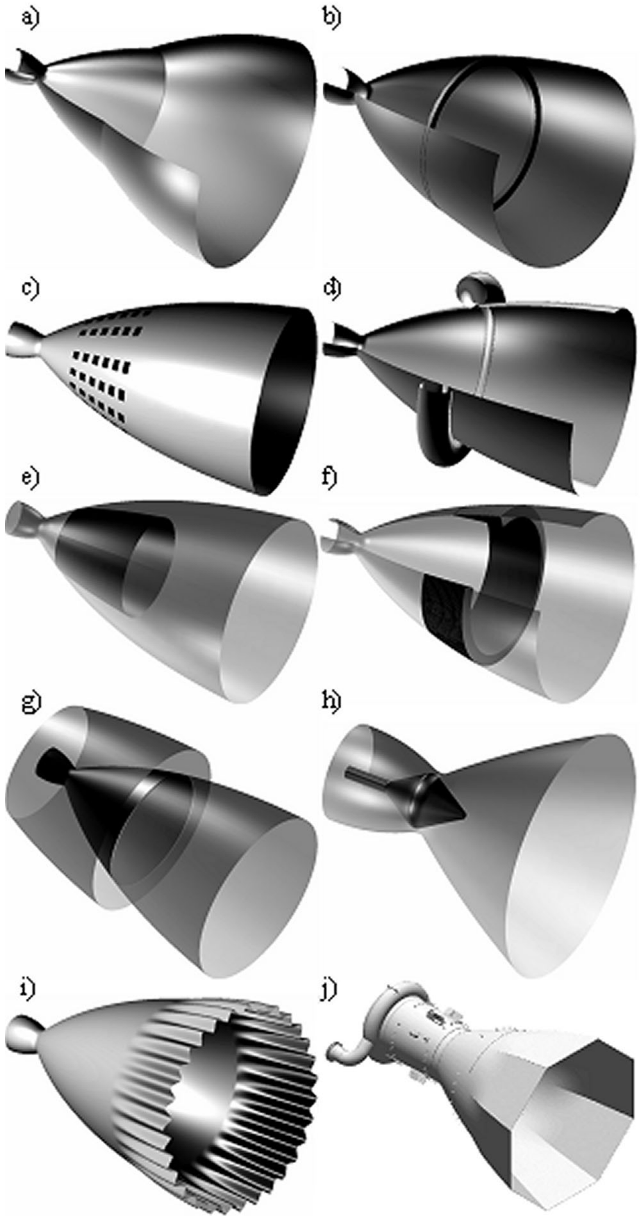

Figure 79. Schematic representation of different concepts for flow separation control. a) Dual-bell. b) Trip-rings. c) Vented nozzle. d) Secondary gas injection. e) Ejectible insert. f) Ablative insert. g) Two-position nozzle. h) Nozzle with pintle. i) Convoluted nozzle. j) Polygon nozzle.

However, additional performance losses are induced in the dual-bell nozzle, when compared with two baseline nozzles having the same expansion ratio as the dual-bell nozzle at its wall inflection, and at its nozzle exit, respectively [181]. The main uncertainty of the duel-bell concept is the aerodynamic behavior at the transition of the flow from SM to AM during the launcher ascent. Several studies, see e.g. Refs. [185-187], have been performed in order to investigate:

- how and when (e.g. at which altitude) the SM to AM transition occurs, depending on the dual-bell design
- the time needed for the transition
- the separation characteristics after transition
- the side-loads generated due to the transition
- the heat loads on the nozzle extension before, during, and after transition

which are the essential factors when designing a dual-bell nozzle.

10.1.2 Trip rings

Figure 79b shows a trip ring attached to the inner nozzle wall. The trip ring disturbs the turbulent boundary layer, and promotes a controlled and symmetrical flow separation when the nozzle operates at a highly overexpanded condition in the SM. At higher altitudes with lower ambient pressure, the flow re-attaches to the wall behind the trip ring, and a full flowing nozzle is achieved. The transition from SM to AM depends on the wall pressure near the trip ring location and on the disturbance induced by the trip ring. The size of the trip ring is a compromise between stable flow separation at SM and the induced performance losses in the AM. According to Schmucker [188], a trip ring size of 10% of the local boundary layer thickness is sufficient to ensure stable flow separation. This concept is in principle similar to the dual-bell concept with regard to performance characteristics.

By the use of several trip rings, mounted one behind the other, several altitude adaptations can be achieved with the nozzle. However, this results in increasing vacuum performance losses. The trip rings can also be attached to existing nozzles and therefore represent an economical concept, at least for test purposes, with low technological risk. The rings have been demonstrated to be effective for side-load reduction during transient start-up of rocket engines [189].

The main problems of this concept with trip rings are not only the performance losses, but also the ring resistance in high temperature boundary layers, the exact circumferential fixing and the uncertainties in the SM to AM transition behavior. These uncertainties might be the reason that the active interest in the concept in the 1970’s [188-191] has dwindled over the past years.

10.2 Secondary flow injection

10.2.1 Vented nozzle

In the vented nozzle, Figure 79c, a section of the nozzle wall has slots or holes opened to the outside atmospheric pressure. At low altitude, the slots or holes are opened to allow adequate passive inflow to sustain a stable and symmetrical separation of the flow. By closing the holes at high altitude a full flowing nozzle is achieved. It is also feasible to provide multiple steps of altitude compensation.

This concept attracted attention by Parsley & Van Stelle in 1992 [192] as a possible candidate for reusable launch vehicle applications. They conducted hot-fired tests to characterize the performance of this concept. Test results showed that the nozzle operated as a nozzle truncated at the start of the perforation in the SM. However, no investigation of the flow behavior at the SM to AM transition was performed.

The number and position of the holes limit the altitude range of this concept, since the pressure within the nozzle must be lower than the ambient pressure. Furthermore, as the rocket aft-body base pressure is lower than the atmospheric pressure in case of surrounding ambient flows, the nozzle transition occurs at a lower altitude, and thus the range of compensation is further reduced.

Another disadvantage of this concept is that a mechanism is required to close the holes, with increased rocket engine mass and reduced reliability as a result. Further, a more complex cooling technique must be used if active cooling of the nozzle wall at and downstream of the perforation is required.

10.2.2 Active fluid injection

By injecting a second fluid into the nozzle gas stream, normal to or at an angle from the nozzle wall, an overexpanded nozzle flow can be forced to separate at a desired location. Figure 79d shows an example of such a concept, where a gas is injected from the side through an annular slot.

Experience on forced secondary flow injection [193] shows, that a large amount of fluid injection is required to induce a significant flow separation. Furthermore, no net performance increase is realized when considering the additional fluid flow rate.

10.3 Variable expansion area

10.3.1 Nozzles with temporary inserts

Another concept for controlled flow separation is temporary inserts, which are removed for vacuum operation. These inserts can be either consumable or ejectable. The inserts can be a complete secondary nozzle or be a partial insert attached to the inside of the nozzle wall as shown in Figure 79e-f.

The nozzle operation with inserts at SM results only in a slight performance loss compared to a bell nozzle with the same reduced area [194-195].

Hot-firing tests performed with an ejectiale secondary nozzle insert [194] have demonstrated the durability of used materials, sealings and the release mechanism, and thus the feasibility of this concept. However, it should be stressed that an ejectable concept is highly dependent on a reliable mechanism that provides a sudden and symmetrical detachment of the insert. During the transient ejection shocks are induced, since the insert act as an obstacle in the supersonic exhaust flow. These shocks also interact with the nozzle walls, and increase the pressure loads and the local heat fluxes on the walls. A non-symmetrical ejection would then result in generation of side-loads. Furthermore, the danger of collision further downstream with the nozzle wall arises, since the inserts might also experience a transversal movement towards the wall.

Another method to remove the inserts is to use combustible or ablative elements [188,195,196]. During the ascent of the launcher, the size of the insert is continuously reduced until its complete consumption. This will finally result in a full flowing bell nozzle with a clean contour for best vacuum performance. However, the main uncertainties of this nozzle concept are the stability and surface regression rates of the used inserts. Furthermore, a homogeneous, symmetrical and timely defined consumption must be guaranteed, despite possible local fluctuations of pressure and temperature near the nozzle walls. With current technology attainment of this goal is very uncertain.

10.3.2 Two-position or extendable nozzle

The main idea of a nozzle with an extendable extension, as illustrated in Figure 79g, is to use a truncated nozzle with low expansion in the SM. At AM the extension is deployed, which results in a larger expansion ratio and thereby increased performance. Its capability for altitude compensation is indisputable, and the nozzle performance is predictable. The whole nozzle contour (including the extendable extension) is contoured for maximum vacuum performance. The contour is then divided into two parts, the fixed nozzle part, and the extendable part. Where to split the nozzle is a trade-off between stable operation in SM, overall trajectory performance and geometrical limitations, which restricts the size of the extension, when it is initially retracted. The SM operation of the fixed nozzle part is connected with a minor performance loss, since it has a non-optimal contour for this interim exit area ratio. However, the concept has a good overall trajectory performance, which is very similar to a nozzle with an ejectable insert [197].
The main drawbacks are the mechanical devices needed for the deployment of the extension, which reduces the engine reliability and increases the total engine mass. The necessity of active cooling of the extendable part requires flexible or movable elements in the cooling system, which also reduces the system reliability. When the extension is in its initial retracted position, during the first phase of the flight, the external flow causes both steady and unsteady pressure loads on the extension, and the engine jet noise causes strong vibrations of the nozzle extension. This, together with the large heat fluxes induced when the flow reattaches to the extension during the deployment, are key areas that have not been fully investigated until now [187,197].

10.3.3 Nozzle with variable throat area

This nozzle concept utilizes a conventional bell nozzle with a fixed area and a mechanical pintle in the combustion chamber and throat region to vary the throat area, and hence, the expansion ratio, see Figure 79h. By moving the pintle axially, the nozzle throat area – an annulus between the pintle and the shroud – is varied. The pintle concept has so far only been used as a mean to provide variable thrust, see e.g. Ref. [198]. In principle, the concept allows a continuous variation of the throat area and thus optimum expansion ratio can be utilized throughout a flight. However, it requires an actuator and a sophisticated control system. The concept raises issues of reliability, design weight, design complexity, cooling of pintle as well as nozzle throat.

The aerodynamic performances of nozzles with five different pintle geometries were calculated and compared with a reference bell nozzle by Smith-Kent *et al.* [199]. The performance losses of these pintle nozzles when compared with the reference nozzle are in the range between 1-2.5%. Performances of fixed pintle geometry at three different locations were also calculated. The results show that the performance loss varies with the pintle location.

10.4 Vortex generators

10.4.1 Convoluted nozzle

The basic idea behind this concept is to increase the margin against flow separation by using a convoluted contour at the exit of the nozzle, as depicted in Figure 79i. This will presumably delay the separation onset and inhibit the lateral movement of the separation line by (i) increasing the drag in the critical region, (ii) inducing streamwise vortices which fix the circumferential flow structure.

Cold sub-scale test [200] has showed that convoluted configurations significantly reduce, and in some cases totally eliminate, shock-induced boundary layer separation in overexpanded flow. However, due to the large skin friction of the convoluted surface and increased overexpansion losses, separation control is achieved at the cost of significant performance penalties, ranging from 3.6%-6.4% compared to the fully separated case. At full flowing conditions, the performance losses ranged from 1%-2.9% compared to the base line configuration.

Another disadvantage when considering the trade-off between separation control and nozzle performance is that the convolution only affects the flow separation behavior in the nozzle exit region. The control effect is therefore less dramatic than for other concepts described above.

Further, the design and manufacturing complexity increases significantly when changing from an axisymmetric to a three-dimensional geometry. An additional issue is the increased heat-load due to the convoluted wall.

10.4.2 Polygon nozzle

The polygon shaped nozzle, Figure 79j, is a relative new concept (patented by VOLVO in the early 1990’s). Conceptually it works as the convoluted nozzle, i.e. a non-axisymmetric geometry generating multi-dimensional flows that influences the flow separation process. The main difference between these two concepts is the periodicity or scale of the vortex generators. In the polygon nozzle the number of sides is envisaged to be 7-11, whereas the number of periodic elements is significantly larger in the convoluted nozzle. While the main purpose of the convolutions where alleviation of the flow separation, the aim of the polygon nozzle is more a design with a side-load reduction relative to an axisymmetric nozzle. The polygonization can be done in several ways, depending on which axial position the effect is desired. Of high interest is also the transition from the circular to the polygon cross-section.

An evaluation of this concept has been performed by Östlund & Bigert [2]. They conducted cold sub-scale tests of two different polygonized Vulcain nozzles. The result showed that the side-load steaming from the RSS to FSS transition at the nozzle exit was reduced by 20% compared with an axisymmetric baseline contour, when putting the major part of the polygonization at the nozzle exit region. When the polygonization was focused at the region where the FSS to RSS transition take place, the side-load reduction was recorded to be 30%. In both cases, only a very small performance loss due to the polygonization was found.

The drawbacks of this concept are the same as for the convoluted nozzle, i.e. the increased complexity when designing and manufacturing an effective three-dimensional contour.

10.5 Concluding remarks

As shown above, each concept has its specific strengths and weaknesses, and there is no concept that stands out as clearly superior compared to the others. Rather, the choice of concept results from a careful trade-off between different factors such as reliability, mechanical complexity etc. presented in the introduction to this chapter. The “winning” concept from such a trade-off is further highly influenced on how these factors are ranked in order of importance. Based on the results presented in this short review and a look on which concepts that have received greatest attention in the recent literature, it is concluded that the dual-bell and two-position nozzle are the two most attractive candidates; the dual-bell nozzle for its simplicity and the two-positional nozzle for its indisputable capability for altitude compensation. Alternatively, inserts such as trip rings, although less efficient, may be a low risk and cost-effective way of upgrading existing nozzle configurations.

11 PRESENT STATUS AND OUTLOOK

The research reviewed in the present paper is to a large extent concerned with basic physical phenomena that are common to all supersonic nozzle flows, regardless of application. The past decade has seen a great advancement in this field, motivated by the increasing demand for satellite launchers, which has pushed forward the development of high performance engines. As we have seen, the aerodynamic characteristics of the first stage exhaust nozzle play an essential part in the performance. The present discussion has been strictly confined to these aerodynamic aspects, leaving out related subjects such as heat loads in separated flow, the influence of “buffeting” (i.e. external pressure loads which interact with the nozzle flow at launch), or the influence of different types of wall cooling on the boundary layer. The latter includes the idea of film cooling, which would completely alter the boundary layer and flow separation characteristics.

The present discussion revolves around the issue of side-loads, which can be grossly sorted into three categories: Side-loads due to aeroelastic effects, side-loads in the free shock separation (FSS) and in restricted shock separation (RSS).

Aeroelastic effects differ depending on which modes are excited. The lowest aeroelastic nozzle shell mode is the ovalisation mode, which is symmetric and may induce buckling. With regard to side-loads, however, the most relevant mode is the bending mode, where the nozzle bends around the weakest section, i.e. the throat. This mode is asymmetric and may interact with aerodynamic modes in such a way as to cause super-resonant instability. One decade ago, aeroelastic instability of the bending mode was believed to be a major source of side-loads. After several test campaigns, designed for this specific purpose, it has become clear that this is not the case in current rocket engine nozzles, however the effect needs to be taken into account if designs with low structural stiffness are considered.

The most significant result obtained in the recent research is probably the clarification of the origin and effects of different separation shock patterns. The restricted shock pattern was first observed the early 70’s [110], and it was then assumed to be an artifact of the subscale test conditions. Recent research has firmly established the fact that RSS occurs in nozzles with non-ideal contours as a result of internal shocks, and shown its relation to the so-called cap-shock pattern in full flowing nozzles [2-3,27-34,109,111]. In the past, internal shocks were purposely used in the design of overexpanded nozzles as a means of increasing the wall pressure and thereby the separation margin at ground level. With the present day's awareness of the undesirable effects of RSS in terms of increased side-loads and thermal loads, it is likely that designs featuring RSS will rather be avoided.

The third scenario discussed in the present paper is the free shock separation (FSS), which always prevails during the beginning of the start-up process, regardless of nozzle contour type. So far, no complete model has been put forward which accounts for these pressure fluctuations in FSS. Different statistical approaches have been proposed in recent years, the most relevant of which is probably that of Dumnov [128], however important elements are still missing for such models to be applied in practice. Most importantly, the core of the problem has not been clarified, namely the question: what is the physical source of the observed pressure pulsations in the free shock condition?

Disturbances may emanate either from the upstream (attached) boundary layer, from the motion of the free jet, or from outside disturbances propagating into the nozzle via the subsonic near wall region. The spectrum of possible side-load mechanisms are considerably more complex in FSS than in the simpler cases of obstacle induced separation or RSS. To mention just a few factors that may be relevant:

- The wall curvature may generate Görtler-like streak structures that form part of the incoming fluctuation field. Such structures have been observed e.g. in flow visualizations.
- The pressure gradient has a major effect on the interaction length L_s in FSS. For instance, as seen in Sec. 5.1.3, L_s varies with the local pressure rise in a manner that is completely different from the trend seen in obstacle-induced separation.
- Compared to RSS, where the flow reattaches, the separated zone in FSS extends down to the nozzle exit, and hence the separated jet has a much larger degree of freedom of movement.
- The internal free jet with its shock structure constitutes a complex boundary condition as compared to the basic SWBLI cases with a uniform free stream.

Most efforts in the past have been directed towards the measurement and modeling the mean wall pressure, while measurements of flow field unsteadiness have been few, and there is still a lack of basic understanding of the causes of large scale, low frequency pulsations in separated flow. Another factor that deserves careful attention is the 3D structure of the fluctuations. Experiments have shown clear evidence of a periodic pattern in the separation region, which may indicate some type of generic instability. This is supported by the observation of preferred frequency bands in the near wall pressure spectrum in separated flow. On the other hand, it is possible that the separated flow is susceptible to outside acoustic or other ambient conditions (e.g. "buffeting"), which brings up the delicate issue of receptivity, and also raises questions concerning the relevance and validity of wind tunnel testing. If the pressure fluctuations are ultimately determined by the surrounding conditions on the launch pad, wind tunnel testing will be of little avail, unless the specific conditions can be mimicked in the laboratory.

It is likely that CFD methods such as LES and variants thereof, will become more available in the future for the modeling and prediction of the unsteady thermal and pressure load in separated nozzle flow. This will certainly increase our understanding of the flow separation phenomena and its corresponding loads, but it is doubtful if these highly time consuming methods will ever become routinely used design tools. But as pointed out by Jameson [201] it is possible that LES may provide "an improved insight into the physics of turbulent flow, which may in turn lead to the development of more comprehensive and reliable turbulence models", which in turn would improve RANS based modeling for engineering purpose.

From an engineering point of view, more easy-to-use prediction methods are preferred. However, simple tools such as correlation functions and prediction schemes will not be reliable unless they are based on a thorough understanding of the underlying physics, which can only be reached using a combination of the most advanced experimental and numerical methods. It is only during the past decade that studies in this direction were undertaken, and not all of the obtained results are publicly available.

In summary, it is crucial at the present stage of development to closely investigate more the 3D fluctuating flow field in order to identify the factors involved in side-loads generation under FSS, which is the basic operating condition in overexpanded nozzle flow. For this, more experimental data on the unsteady wall pressure field is needed, which involves the development and application of advanced techniques for measurement and evaluation of high frequency pressure fluctuation, while field measurement techniques need to be applied in order to obtain more information on the 3D structure of the flow field. Experimental campaigns need to be matched by numerical studies of the unsteady 3D flow field, employing methods capable of accurately reproducing the internal shock system as well as the boundary layer separation, and to resolve fluctuations on a broad band of temporal and spatial scales. If efforts in the analytical, experimental and computation fields are efficiently coordinated, it should be possible to reach the goal within a foreseeable future.

12 ACKNOWLEDGEMENT

This work has been carried out within the GSTP program in the framework of the European FSCD working group. The authors would like to acknowledge all FSCD members, especially Dr. G. Hagemann, Dr. M. Terhardt (ASTRIUM), Dr. M. Pons, Dr. P. Vuillermoz (CNES), R. Stark (DLR), Dr. R. Schwane, L. Torngren (FOI), Dr. Ph. Reijasse (ONERA) , Dr. Ph. James (SNECMA) and Dr. Alziary de Roquefort (University of Poitiers), for their fruitful cooperation. Valuable help and suggestions from many people at Volvo Aero Corporation are appreciated, with special thanks to those working at the Business Unit Nozzles.

Special thanks are due to Dr. Lars Ljungkrona, Dr. Manuel Frey, Dr. Lars-Erik Eriksson and Dr. Ardeshir Hanifi for their suggestions, remarks and inspiring discussions. The authors also wish to thank the AMR reviewers for their careful revision of the paper and useful comments.

This work has been supported through grants from Volvo Aero Corporation and the Swedish Research Council for Engineering Sciences (TFR contract 285-98-717). These sources of support are gratefully acknowledged.

13 REFERENCES

[1] Wade M (1999), Encyclopedia Astronautica, http://www.friends-partners.ru/partners/mwade/spaceflt.htm

[2] Östlund J and Bigert M (1999), A subscale investigation on side-loads in sea level rocket nozzles, *35th Joint Propulsion Conference and Exhibit,* AIAA Paper 99-2759.

[3] Frey M, Ryden R, Aziary de Roquefort T, Hagemann G, James P, Kachler T, Reijasse P, Schwane R and Stark R (2002), European cooperation on flow separation control, *4th International Conference on Launcher Technology "Space Liquid Propulsion", Lige, Belgium*.

[4] Malina F J (1940), *Characteristics of the rocket motor based on the theory of perfect gases, Volume 230*, J. Frankling Inst., 433-454.

[5] Beneche T and Quick W W (1957), *History of German guided missile development,*AGARDograph 20, Verlag E. Appelhos & Co, Brunswick

[6] Shapiro A H (1953), *The dynamics and thermodynamics of compressible fluid flow Volume I*, The Ronald Press Co., New York.

[7] Ahlberg J H, Hamilton S, Migdal D and Nilson E N (1961), Truncated perfect nozzles in optimum nozzle design, *ARS Journal*, **31(**5), 614-620.

[8] Guderley G , Hantsch E (1955), Beste formen für achsensymmetrische Überschallschubdüsen, *Zeitschrift für Flugwissenschaften*, **3**, 305-313.

[9] Guderley G (1959), On Rao's method for the computation of exhaust nozzles, *Zeitschrift für Flugwissenschaften*, **12**, 345-350.

[10] Rao G V R (1958), Exhaust nozzle contour for optimum thrust, *Jet Propulsion*, **28**(6), 377-382.

[11] Shmyglevsky Yu D (1957), Some variational problems in the gas dynamics of axially symmetric supersonic flows (In Russian), *Prikladnaya Matematika i Mekhanika*, **21(**2), 195-206.

[12] Shmyglevsky Yu D (1957), A variational problem in the gas dynamics of axially symmetric supersonic flow (In Russian), *Dokl. Akad. Nauk SSR* **113**(3).

[13] Shmyglevsky Yu D (1958), Supersonic profiles with minimum drag (In Russian), *Prikladnaya Matematika i Mekhanika*, **22**(2), 269-273.

[14] Shmyglevsky Yu D (1963), Some gas dynamic variation problems (In Russian), M.: VTs AN USSR.

[15] Huzel D K and Huang D H (1992), *Modern engineering for design of liquid propellant rocket engines, AIAA Progress in Astronautics and Aeronautics, Vol. 147*, AIAA, Washington DC.

[16] Rao G V R (1960), Approximation of optimum thrust nozzle contour, *ARS Journal*, **30**(6), 561.

[17] Rao G V R and Dang A L (1992), Thrust optimization of nozzle contour including finite rate chemical kinetics, *28th Joint Propulsion Conference and Exhibit*, AIAA Paper 92-3729.

[18] Gogish L V (1966), Investigation of short supersonic nozzles (In Russian), *AN SSSR, Izvestiya, Mechanica Zidkosti i Gaza*, 1966, 2, 175-180.

[19] Hoffman J D (1985), Design of compressed truncated perfect nozzles, *21st Joint Propulsion Conference and Exhibit*, AIAA Paper 85-1172.

[20] Nickerson G R, Berker D R, Coats D E and Dunn S S (1993), Two-dimensional kinetics (TDK) nozzle performance computer program Volume II, Users Manual, prepared by Sofware and Engineering Associates, Inc. for George C. Marshall Space Flight Centre under contract NAS8-39048, SEA Inc., Carson City NV.

[21] Ponomarev N V (1992), Direct optimisation of rocket engine nozzle contours (In Russian), *Raketno-Kosmicheskaya Tekhnika: Raketney Dvigateli I Energeticheskie Ustanovki*, **2**(135).

[22] Dumnov G E, Nikulin G Z and Ponomarev N B (1995), A study of promising rocket nozzles (In Russian), NITTP Report YDK 533.697.4, Moscow.

[23] Dritov G V and Tishin A P (1971), On the contouring of nozzles operating with condensate particles (In Russian), *Izv.AN.USSR.MZhg*, **1**.

[24] Davis D K (1982), Investigation of optimisation techniques for solid rocket motor nozzle contour, *18th Joint Propulsion Conference*, AIAA Paper 82-1188.

[25] Hussaini M M and Korte J J (1996), Investigation of low-Reynolds-number rocket nozzle design using PNS-based optimization procedure, NASA Technical Memorandum 110295, Langley Research Center, Hampton VA.

[26] Moelder A, Gluamhussein A, Timofeev E, and Voinovich P (1997), Focusing of conical shocks at the centreline of symmetry, *Proceedings of the 21st International Symposium on Shock Waves*, Paper 5601.

[27] Hagemman G, Terhardt M, Frey M, Reijasse P, Onofri M, Nasuti F and Östlund J (2000), Flow separation and side-loads in rocket nozzles, *4th International Symposium on Liquid Space Propulsion. DLR, Lampholdshausen, Germany*.

[28] Frey M (2001), Behandlung von Strömungsproblemen in Raketendüsen bei Überexpansion, Ph.D. dissertation, Insitut für Aerodynamik und Gasdynamik Univesität Stuttgart, Stuttgart.

[29] Frey M and Hagemann G (1998), Status of flow separation prediction in rocket nozzles, *34th Joint Propulsion Conference and Exhibit*, AIAA Paper 98-3619.

[30] Frey M and Hagemann G (1999), Flow separation and side-loads in rocket nozzles, *35th Joint Propulsion Conference and Exhibit*, AIAA Paper 99-2815.

[31] Terhardt M, Hagemann G and Frey M (1999), Flow separation and side-load behaviour of the Vulcain engine, *35th Joint Propulsion Conference and Exhibit*, AIAA Paper 99-2762.

[32] Mattsson J (changed name to Östlund 1999), Högman U and Torngren L (1998), A sub-scale test programme on investigation of flow separation and side-loads in rocket nozzles, *Proceedings of the 3rd European Symposium on Aerothermodynamics of Space Vehicles*, ESA SP-426, 373-378.

[33] Reijasse P, Servel P and Hallard R (1999), Synthesis of the 1998-1999 ONERA works in the FSCD working group, ONERA Rept. RTS 49/4361 DAFE/Y, ONERA, Châtillon-sous-Bagneux.

[34] Frey M, Stark, R, Cieaki H K, Quessard F and Kwan W (2000), Subscale nozzle testing at the P6.2 test stand, *36th Joint Propulsion Conference and Exhibit*, AIAA Paper 2000-3777.

[35] Donaldson C and Lange R (1952), Study of the pressure rise across shock waves required to separate laminar and turbulent boundary layer, NACA Technical Note 2770, Langley Aeronautical Laboratory, Langley Field.

[36] Green J E (1970), Interactions between shock waves and turbulent boundary layers, *Progress in Aerospace Sciences*, **11,** 234-341.

[37] Adamson T C and Messiter A F (1980), Analysis of two-dimensional interactions between shock waves and boundary layers, *Ann. Rev. Fluid Mech.* **12**, 103-138.

[38] Elfstrom G (1972), Turbulent hypersonic flow at a wedge-compression corner, *Journal of Fluid Mechanics*, **53**(1), 113-127.

[39] Chapman D, Kuehn D and Larson H (1958), Investigation of separated flows in supersonic and subsonic streams with emphasis on the effect of transition, NACA Report 1536, Ames Aeronautical Laboratory, Moffet Field.

[40] Hamed A and Kumar A (1992), Hypersonic flow separation in shock wave boundary layer interactions, *37th International Gas Turbine and Aeroengine Congress and Exposition*, ASME Paper 92-GT-205.

[41] Hayashi M, Aso S and Tan A (1989), Fluctuation of heat transfer in shock wave/turbulent boundary layer interaction, *AIAA Journal*, **27**(4), 399-404.

[42] Holden M (1972), Shock wave-turbulent boundary layer interaction in hypersonic flow, *10th Aerospace Science Meeting*, AIAA paper 72-74.

[43] Horstman C, Settles G, Vas I, Bogdonoff S and Hung C (1977), Reynolds number effects on shock-wave turbulent-boundary-layer interactions, *AIAA Journal*, **15**(8), 1152-1158.

[44] Settles G (1975), An experimental study of compressible turbulent boundary-layer separation at high Reynolds number, Ph. D. Dissertation, Aerospace and Mechanical Sciences Dep., Princeton University, Prinston, New Jersey,USA.

[45] Settles G (1976), Details of a shock-separated turbulent boundary layer at a compression corner, *AIAA Journal*, **14**(12), 1709-1715.

[46] Settles G, Fitzpatrick T and Bogdonoff S (1979), Detailed study of attached and separated compression corner flowfields at high Reynolds number supersonic flow, *AIAA Journal*, **17(**6), 579-585.

[47] Tyler D and Shapiro A (1953), Pressure rise required for separation in interaction between turbulent boundary layer and shock wave, *Journal of the Aeronautical Sciences*, **20(**12), 858-860.

[48] Panov Yu A and Shvets A I (1966), Separation of turbulent boundary layer in supersonic flow (In Russian), Prikladnaya mekhanika, **1**.

[49] Zukoski E E (1967), Turbulent boundary layer separation in front of a forward facing step, *AIAA Journal*, **5**(1).

[50] Horstman C (1987), Prediction of hypersonic shock-wave/turbulent-boundary-layer interaction flow, *19th Fluid Dynamics, Plasma Dynamics and Laser Conference*, AIAA Paper 87-1367.

[51] Kuntz D, Amatucci V and Addy A (1987), Turbulent boundary-layer properties downstream of the shock-wave/boundary-layer interaction, *AIAA Journal*, **25**(5), 668-675.

[52] Lange R (1954), Present status of information relative to prediction of shock-induced boundary-layer separation, NACA Technical Note 3065, Langley Aeronautical Laboratory, Langley Field.

[53] Mikulla V and Horstman C (1976), Turbulent measurments in hypersonic shock-wave boundary-layer interaction flows, *AIAA Journal*, **14**(5), 568-575.

[54] Modarress D and Johnson D (1976), Investigation of shock induced separation of a turbulent boundary layer using laser velocimetry, *9th Fluid and Plasma Dynamics Conference*, AIAA Paper 76-374.

[55] Selig M, Andrepoulos J, Muck K, Dussauge J and Smits A (1989), Turbulence structure in a shock wave/turbulent boundary-layer interaction, *AIAA Journal*, **27(**7), 862-869.

[56] Back L and Cuffel R (1970), Changes in heat transfer from turbulent boundary layers interacting with shock waves and expansion waves, Technical note, *AIAA Journal*, **8(**10), 1871-1873.

[57] Back L and Cuffel R (1976), Shock wave/turbulent boundary-layer interactions with and without surface cooling, *AIAA Journal*, **14**(4), 526-532.

[58] Spaid F and Frishett J (1972), Incipient separation of a supersonic, turbulent boundary layer, including effects of heat transfer, *AIAA Journal*, **10**(7), 915-922.

[59] Muck K , Andrepoulos J and Dussauge J (1988), Unsteady nature of shock-wave/turbulent boundary-layer interaction, *AIAA Journal*, **26(**2), 179-187.

[60] Plotkin K (1975), Shock wave oscillation driven by turbulent boundary layer fluctuations, *AIAA Journal*, **13**(8), 1036-1040.

[61] Andreopoulos J and Muck K (1987), Some new aspects of the shock-wave/boundary-layer interaction in compression ramp-flows, *Journal of Fluid Mechanics*, **180**, 405-428.

[62] Coe C, Chyu W and Dods J (1973), Pressure fluctuations underlying attached and separated supersonic turbulent boundary layers and shock waves, *Aero-Acoustics Conference,* AIAA Paper 73-996.

[63] Dolling D and Murphy M (1983), Unsteadiness of the separation shock wave structure in a supersonic compression ramp flowfield, *AIAA Journal*, **21**(12), 1628-1634.

[64] Dolling D and Or C (1985), *Unsteadiness of the shock wave structure in attached and separated compression ramp flows, Experiments in fluids **3(1)***, Springer Verlag, Heidelberg, 24-32.

[65] Erengil M and Dolling D (1991), Unsteady wave structure near separation in a Mach 5 compression ramp interaction, *AIAA Journal,* **29**(5), 728-735.

[66] Erengil M and Dolling D (1991), Correlation of separation shock motion with pressure fluctuations in the incoming boundary layer, *AIAA Journal*, **29(**11), 1868-1877.

[67] Erengil M and Dolling D (1992), Effects of sweepback on unsteady separation in Mach 5 compression ramp interactions, *30th Aerospace Sciences Meeting*, AIAA Paper 92-0430.

[68] Erengil M and Dolling D (1993),Physical causes of separation shock unsteadiness in shock wave/turbulent boundary layer interactions, *AIAA 24th Fluid Dynamics Conference*, AIAA Paper 93-3134.

[69] Kistler M (1964), Fluctuating wall pressure under a separated supersonic flow, *Journal of the Acoustical Society of America*, **36**(3).

[70] Gonsalez J and Dolling D S (1993), Effects of interaction sweepback on the dynamics of shock-induced turbulent separation, *31st Aerospace Science Meeting*, AIAA Paper 93-0776.

[71] Dolling D S (1993), Fluctuating loads in shock wave/turbulent boundary layer interaction: tutorial and update, *31st Aerospace Sciences Meeting & Exhibit*, AIAA Paper 1993-0284.

[72] Smits A and Muck K (1987), Experimental study of three shock wave/turbulent boundary layer interactions, *Journal of Fluid Mechanics*, **182**, 291-314.

[73] Spina E, Smits A and Robinson S (1994), The physics of turbulent boundary layers, *Annual Review of Fluid Mechanics*, **26**, 287-319.

[74] Thomas F, Putnam C and Chu H (1994), On the mechanism of unsteady shock oscillation in the shock wave/ turbulent boundary layer interactions, *Experimental Fluids*, **18**, 69-81.

[75] Dolling D S and Bogdonoff S M (1981), An experimental investigation of the unsteady behaviour of blunt fin-induced shock wave turbulent boundary layer separation, *14th Fluid and Plasma Dynamics Conference*, AIAA Paper 81-1287.

[76] Robertson J E (1971), Prediction of in-flight fluctuating pressure environments including protuberance induced flows, Wyle Laboratories Research Staff Report WR71-10, Wyle Laboratories.

[77] Schmisseur J D and Dolling D S (1994), Fluctuating wall pressures near separation in highly swept turbulent interactions, *AIAA Journal*, 32(6), 1151-1157.

[78] Beresh S J, Clemens N T and Dolling D S (2002), Relationship between upstream turbulent boundary-layer velocity fluctuations and separation shock unsteadiness, *AIAA Journal,* **40**(12), 2412-2422. .

[79] Ünlamais O H (1995), Structure of the supersonic turbulent boundary layer and its influence of unsteady separation, Ph.D. Dissertation, Center for Aeromechanics Research, University of Texas, Austin.

[80] Beresh S (1999), The effect of the incoming turbulent boundary layer on a shock-induced separated flow using particle image velocimetry, Ph.D. Dissertation, University of Texas, Austin.

[81] Beresh S, Clemens N and Dolling D (1999), The relationship between upstream turbulent boundary layer velocity fluctuations and separation shock unsteadiness, *37th Aerospace Meeting*, AIAA Paper 99-0295.

[82] Delery J and Marvin J G (1986), Shock-wave boundary layer interactions, AGARD-AG-280, NATO AGARD, Neuilly sur Seine, France.

[83] Schlichting H, and Gersten K (1997), *Boundary Layer Theory*, Springer, Berlin Heidelberg.

[84] Erdos J and Pallone A (1962), Shock-boundary layer interaction and flow separation, Heat Transfer and Fluid Mechanics Institute Procs., Stanford University Press, Stanford.

[85] Östlund J (2002), Flow processes in rocket engine nozzles with focus on flow separation and side-loads, Licentiate Thesis TRITA-MEK 2002:09, Department of Mechanics, Royal Institute of Technology, Stockholm, Sweden.

[86] Johnson C and Bushnell D (1970), Power-law velocity profile-exponent variation with Reynolds number, wall cooling, and Mach number in a turbulent boundary layer, NASA TN D-5753, National Aeronautics and Space Administration., Langley Research Center, Hampton, VA.

[87] Knight D D and Degrez G (1998), Shock wave boundary layer interactions in high Mach number flows, a critical survey of current numerical prediction capabilities, AGARD Advisor Report 319, Vol II, 1.1-1.35, NATO AGARD.

[88] Knight D Yan H, Panaras A G, Zheltovodov A (2003), Advances in CFD prediction of shock wave turbulent boundary layer interactions, *Progress in Aerospace Sciences*, **39**, 121-184.

[92] Salikuddin M (1992), Unsteady pressures on exhaust nozzle interior surfaces – empirical correlations for prediction, *14th DGLR/AIAA Aeroacoustics Conference*, Proceedings. Vol. 2 (A93-19126 05-71), pp. 873-881, Bonn, Deutsche Gesellschaft fuer Luft- und Raumfahrt..

[93] Darren R and Hidalgo H (1995), Fluctuating pressure analysis of a 2-d SSME nozzle air flow test, *In its Thirteenth Workshop for Computational Fluid Dynamic Applications in Rocket Propulsion and Launch Vehicle Technology*, (SEE N96-29750 11- 34) pp. 723-743.

[94] Forster C and Cowles F (1949), Experimental study of gas flow separation in overexpanded exhaust nozzles for rocket motors, JPL Progress Report 4-103, Jet Propulsion Lab., California Inst. of Tech., Pasadena, CA.

[95] Green L (1953), Flow separation in rocket nozzles, *ARS Journal*, **23**(1).

[96] Summerfield M, Foster C and Swan W (1954), Flow separation in overexpanded supersonic exhaust nozzles, *Jet Propulsion*, **24**.

[97] Campbell C and Farley J (1960), Performance of several conical convergent-divergent rocket type exhaust nozzles, NASA TN D-467, NASA Lewis Research Center, Cleveland OH.

[98] Schilling T W (1962), Flow separation in rocket nozzle, M. S. Thesis, University of Buffalo, New York.

[99] Kalt S and Badal D (1965), Conical rocket nozzle performance under flow separated condition, *Journal of Spacecraft and Rockets*, **2**(3).

[100] Arens, M and Spiegler E (1963), Shock-Induced boundary layer separation in overexpanded conical exhaust nozzles, *AIAA Journal*, **1**(3), 578-581.

[101] Sunley H and Ferriman D (1964), Jet separation in conical nozzles, *Journal of the Royal Aeronautical Society*, **68,** 808-817.

[102] Lawrence R A (1967), Symmetrical and unsymmetrical separation in supersonic nozzles, Ph.d. Thesis, TX. Inst. of Technology, Southern Methodist University, Dallas.

[103] Chen C, Chakravarchy S and Hung C (1994), Numerical investigation of separated nozzle flows, *AIAA Journal*, **32**(9), 1836-1843.

[104] Nasuti F and Onofri M (1996), Viscous and inviscid vortex generation during nozzle flow transients, *34th Aerospace Sciences Meeting & Exhibit*, AIAA Paper 96-0076.

[105] Nasuti F and Onofri M (1998), Viscous and inviscid vortex generation during start-up of rocket nozzles, *AIAA Journal*, **36**(5), 809-815.

[106] Onofri F and Nasuti M (1999), The physical origin of side-loads in rocket nozzles, *35th Joint Propulsion Conference and Exhibit*, AIAA Paper 99-2587.

[107] Östlund J and Jaran M (1999), Assessment of turbulence models in overexpanded rocket nozzle flow simulations, *35th Joint Propulsion Conference and Exhibit*, AIAA Paper 99-2583.

[108] Östlund, J., Damgaard T and Frey M (2002), Side-load phenomena in highly overexpanded rocket nozzles, re-print of paper AIAA-2001-3684 submitted to JPP.

[109] Östlund J, Damgaard T and Frey M (2001), Side-load phenomena in highly overexpanded rocket nozzles, *37th Joint Propulsion Conference and Exhibit*, AIAA Paper 2001-3684.

[110] Nave L H and Coffey G A (1973), Sea-level side-loads in high area ratio rocket engines, *9th Propulsion Conference*, AIAA Paper 73-1284.

[111] Tomita T, Takahashi M, Ueda S, Tamura H and Aoki K (2001), Visualization of the formation of separation bubbles on a bell-shaped nozzle surface in relation to serious side-load, *37th Joint Propulsion Conference and Exhibit*, AIAA Paper 2001-3559.

[112] Gribben B Cantariti F, Badcock K and Richards B (1998), Numerical study of an underexpanded jet, *Proceedings of the 3rd European Symposium on Aerothermodynamics of Space Vehicles*, ESA SP-426, 111-118.

[113] Welsh F (1997), Electron beam fluorescence measurements of shock reflection hysteresis in an underexpanded supersonic jet, *Proceedings of the 21st International Symposium on Shock Waves*, Paper 5950.

[114] NASA (1976), NASA space vehicle design criteria (chemical propulsion), liquid rocket engine nozzles, NASA SP-8120, Lewis Research Center, Cleveland OH.

[115] Schmucker R (1973), Flow processes in overexpanding nozzles of chemical rocket engines (In German), Report TB-7,-10,-14, Technical University Munich, Munich.

[116] Crocco L and Probstein R (1954), The peak pressure rise across an oblique shock emerging from a turbulent boundary layer over a plane surface, Report 254, The James Forrestal Research Center, Princeton University, Princeton NJ.

[117] Carriere P (1966), Comments on computational methods of viscous effects in propulsion nozzles (In French), *DGRR/WGLR Symposium*, also published as ONERA TP 408.

[118] Carrière P, Sirieix M and Solignac J-L (1968), Propértiés de similitude des phénomènes de décollement laminaires ou turbulents en écoulemnt supersonique non uniforme, *12th International Congress of Applied Mechanics*, Stanford University, Stanford, also ONERA TP N° 659F.

[119] Östlund (former Mattsson) J (1999), Test synthesis – reference and polygon modular nozzle, VAC Report SV RE 114 0000 E 2005 VOLV (6600-98-3015), VOLVO AERO CORPORATION, Trollhättan.

[120] Reijass Ph, Morzenski L, Blacodon D and Birkemeyer J (2001), Flow separation experimental analysis in overexpanded subscale rocket nozzles, *37th Joint Propulsion Conference and Exhibit,* AIAA Paper 2001-3556.

[121] Reijass Ph and Birkemeyer J (2001), Semi-empirical flow separation model for subscale nozzles, *4th European Symposium on Aerothermodynamics for Space Vehicles*, ESA SP-487, 407-414.

[122] Lewis J E, Kubota T and Lees L (1968), Experimental investigation of supersonic laminar, two-dimensional boundary layer separation in a compression corner with and without wall cooling, *AIAA Journal*, **6**, 7-14.

[123] Hagemann G, Alting J, Kretschmer J, Terhardt M, Frey M, Ryden R and Stark R (2002), The calorimetric nozzle programme, *38th Joint Propulsion Conference and Exhibit*, AIAA Paper 2002-3998.

[124] Dumnov G E, Nikulin G Z, Voinov A L and Zyuzin V I (1995), Nozzle flow separation and unsteady side-loads, *Conference on Propulsive Flows in Space Transportation System*, pp. 798-816.

[125] Kudryavtsev V M (1975), Fundamentals of theory and calculations of liquid rocket engines (In Russian), Moscow High School, Moscow.

[126] Malik T I and Tagirov R K (1988), A semiempirical method for calculating separated turbulent flow in a conical Laval nozzle in the reexpansion mode (In Russian), *Akademiia Nauk SSSR, Izvestiia, Mekhanika Zhidkosti i Gaza* , 60-66.

[127] Abramovich G N (1963), *The theory of turbulent jets*, The MIT Press, Massachusetts.

[128] Dumnov G E (1996), Unsteady side-loads acting on the nozzle with developed separation zone, *32nd Joint Propulsion Conference and Exhibit,* AIAA Paper 96-3220.

[129] Girard S and Alziary T (1998), Fluctuations measurements in axisymmetric sub-scale nozzle, *ESA CNES European Seminar on Rocket Nozzle Flows*.

[130] Sergienko A A and Kirillov A V (2000), Pulsating loads on propulsive nozzles with flow separation (In Russian), *Aviatsionnaya Thekhnika*, **4**,23-26.

[131] Tuovila W J and Land N S (1968), Experimental study of aeroelastic instability of overexpanded rocket nozzle extensions, NASA TN D-4471, Langley Research Center, Langely Station, Hampton, Va.

[132] Brown A M (2002), Characterization of side load phenomena using measurement of fluid/structure interaction, *38th Joint Propulsion Conference and Exhibit*, AIAA Paper 2002-3999.

[133] Pekkari L-O (1993), Aeroelastic stability of supersonic nozzles with separated flow, *29th Joint Propulsion Conference and Exhibit,* AIAA Paper 93-2588.

[134] Pekkari L-O (1994), Aeroelastic analysis of side-loads in supersonic nozzles with separated flow, *30th Joint Propulsion Conference and Exhibit,* AIAA Paper 94-3377.

[135] Kwan W (2001), Aeroelastic effects on a bended conical nozzle, DLR-IB 645-2001-06, DLR, Lampholdshausen.

[136] Stanke H (1986), Test report on the results on HM60-subscale test series 3, Vulcain Ne Project Report HM RT 110 0000 501, MBB, Ottobrun.

[137] Hagemann G, Alting J and Preclik D (2001), Scalability discussion for rocket nozzle flows based on subscale and full-scale testing, *4th European Symposium on Aerothermodynamics for Space Vehicles*. Also published as Hagemann G, Alting J and Preclik D (2003), Scalability for rocket nozzle flows based on subscale and full-scale testing, *Journal of Propulsion and Power,* **19**(3), 321-331.

[138] Stark R, Kwan W, Quessard F, Hagemann, G and Terhardt M (2001), Rocket nozzle cold-gas test campaigns for plume investigations, *4th European Symposium on Aerothermodynamics for Space Vehicles*, ESA SP-487

[139] Reijasse P, Bouvier F and Servel P (2002), Experimental and numerical investigation of the cap-shock structure in overexpanded thrust-optimized nozzles, *West East High Speed Flow Conference.*

[140] Girard S and Alziary de Roquefort T (1999), Measurements of side-loads in an overexpanded parabolic nozzle, Laboratoire d'Etudes Aérodynamiques, CEAT, Poitiers.

[141] Gramann R and Dolling D S (1988), Detection of turbulent boundary layer separation using fluctuating wall pressure signals, *AIAA/NASA/AFWAL Conference on Sensors and Measurement Techniques for Aeronautical Applications*, AIAA Paper 88-4676.

[142] Reda D C and Wilder M C (2001), Shear-sensitive liquid crystal coating method applied through transparent test surfaces, *AIAA Journal*, **39**(1), 195-197.

[144] Dolling D S and Dussauge J P (1990), Fluctuating wall pressure measurements, A survey of measurements and measuring techniques in rapidly distorted compressible turbulent boundary layers, Ch. 8, Agardograph 315, NATO AGARD.

[145] McLachlan B G and Bell J H (1995), Pressure sensitive paint in aerodynamic testing, *Experimental Thermal and Fluid Science*, **10**(4), 470-485.

[146] Lepicovsky J and Bencic T J (2001), Use of pressure sensitive paints for diagnostics in turbomachinery flows with shocks, *ISOABE, ISABE – 15th International Symposium on Air Breathing Engines*, ISABE-2001-1142.

[147] Taghavi R, Raman G and Bencic T (1999), Pressure sensitive paint demonstrates relationship between ejector wall pressure and aerodynamic performance, *Experiments in Fluids*, **26**(6), 481-487.

[148] Lepicovsky J, Bencic T J and Bruckner R J (1997), Application of pressure sensitive paint to confined flow at Mach number 2.5, *33rd Joint Propulsion Conference and Exhibit*, AIAA Paper 97-3214

[149] Sakaue H, Gregory J W, Sullivan J P and Raghu S (2001), Pressure sensitive paint for unsteady flow fields, *39th Aerospace Sciences Meeting and Exhibit*, AIAA Paper 2001-0554.

[150] Reijass Ph, Morzenski L, Naudin P and Géneau F (2001), Fluctuating side-load measurements in overexpanded subscale rocket-nozzles, *37th Joint Propulsion Conference and Exhibit*, AIAA Paper 2001-3557.

[151] Harris C M and Crede C E (1976), *Shock and vibration handbook*, McGraw-Hill, Inc., New York.

[152] Bendat J S and Piersol A G (2000), *Random data: analysis and measurement procedures, 3rd Edition*, John Wiley & Sons, New York.

[154] Birch S F and Eggers J M (1972), Free turbulent shear flows, NASA SP-321, **1**, 11-40, NASA Langley Research Center, Hampton, VA, United States

[155] Sarkar S and Balakrishnan L (1990), Application of a Reynolds-stress turbulence model to the compressible shear layer, *21st Fluid Dynamics, Plasma Dynamics and Lasers Conference*, AIAA Paper 1990-1465.

[156] Zeman O (1990), Dilataion dissipation: The concept and application in modeling compressible mixing layers, Phys. Fluids, **2**(2), 178-188.

[157] Coakley T J and Huang P G (1992), Turbulence modeling for high speed flows", *30th Aerospace Science Meeting & Exhibit*, AIAA Paper 92-0436.

[158] Aupoix B, Desmet E and Viala S (1993), Hypersonic turbulent boundary layer modelling, Symposium on transitional and turbulent compressible flows, ASME Fluids Engineering Conference.

[159] Wilcox D C (1998), Turbulence modeling for CFD, DWC Industries, Inc., La Canada, CA.

[160] Thivet F, Knight D and Zeltovodov A (2000), Computation of crossing-shock-wave/boundary layer interaction with realizable two-equation turbulence models, In Proceedings of the *International Conference on methods of Aerophysical Research*, Part 1, 195-201.

[161] Schumann U (1977), Realisability of reynolds stress turbulence models, *Phys. Fluids*, **20**, 721-725.

[162] Lumley J L (1978), Computational modeling of turbulent flows, *Advances in Applied Mechanics, Academic Press*, **18**, 123-176.

[163] Thivet F, Knight D D, Zheltovodov A A and Maksimov A I (2000), Some insights in turbulence modeling for crossing shock-wave/boundary-layer interactions, *38th Aerospace Science Meeting & Exhibit*, AIAA Paper 2000-0131.

[164] Moore J G and Moore J (1999), Realizability in two-equation turbulence models, *30th Fluid Dynamics Conference*, AIAA Paper 99-3779.

[165] Durbine P A (1996), On the k-ε stagnation point anomaly, *Int. J. Heat & Fluid Flow*, **17**(1), 89-90.

[166] Behnia M, Parneix S and Durbin P A (1996), Simulation of jet impingment heat transfer with the k-ε -ν2 model, Annual Research Briefs 1996, pp. 3-16, Center for Turbulence Research, California, also at http://ctr.stanford.edu/ResBriefs96/behnia.ps.Z

[167] Coakley T J (1983), Turbulence modeling for Compressible Navier-Stokes equations, *16th Fluid and Plasma Dynamics Conference*, AIAA Paper 83-1693.

[169] Menter F R (1994), Two-equation eddy-viscosity turbulence models for engineering applications, *AIAA Journal*, **32**(8), 1598-1605.

[170] Deck S and Hallard R (2001), Simulations numériques des écoulements décollés dans les tuyères, *37ème colloque d'Aérodynamique Appliquée "Aérodynamique et Propulsion des vèhicules à grande vitesse"*, also publised as ONERA TP 2001-61.

[171] Deck S, Hallard R and Guillen P(2002), Numerical simulations of steady and unsteady separated nozzle flows, *40th AIAA Aerospace Science Meeting and Exhibit*, AIAA Paper 2002-0406.

[172] Yonezawa K, Yokota K, Tsujimoto Y, Sakazume N and Watanabe Y (2002), Threee-dimensional unsteady flow simulation of compressed truncated perfect nozzles, *38th Joint Propulsion Conference and Exhibit*, AIAA Paper 2002-3991.

[173] David E (1993), Modélisation des Écoulements Compressibles et Hypersoniques, Ph.D. Dissertation, Dept. of Engineering, Grenoble Univ., Grenoble, France.

[179] Garnier E, Sagaut P and Deville M (2002), Large eddy simulation of shock/boundary-layer interaction, *AIAA Journal*, **40**(10), 1935-1944.

[181] Frey M, Hagemann G (1999), Critical assessment of dual-bell nozzles, *Journal of Propulsion and Power*, **15**(1),137-143.

[182] Kumakawa A, Tamura H, Niino M, Nosaka M, Yamada H, Konno A, Atsumi M (1999), Propulsion research for rocket SSTOs at NAL/KRC, *35th Joint Propulsion Conference and Exhibit*, AIAA Paper 99-2337.

[183] Immich H, Caporicci M (1997), FESTIP thechnology developments in liquid rocket propulsion for reusable launch vehicles, *33rd Joint Propulsion Conference and Exhibit*, AIAA Paper 97-3311.

[184] Dumnov G, Ponomaryov N B, Voinov A L (1997), Dual-bell nozzles for rocket engines of launch vehicles upper stages and orbital transfer vehicles, *33rd Joint Propulsion Conference and Exhibit*, AIAA Paper 97-3089

[185] Horn M, Fisher S (1994), Dual-bell altitude compensating nozzles, NASA-CR-194719.

[186] Hagemann G, Terhardt M, Haeseler D, Frey M (2002), Experimental and analytical design verification of the dual-bell concept, *Journal of Propulsion and Power*, **18**(1),116-122.

[187] Kusaka K, Kumakawa M, Konno A, Atsumi M (2000), Experimental study on extendible and dual-bell nozzles under high altitude conditions, *36th Joint Propulsion Conference and Exhibit*, AIAA Paper 2000-3303.

[188] Schmucker R (1973), Strömungsvorgänge beim betrieb überexpandierter düsen chemischer raketentriebwerke, Report TB-7,-10,-11,-14, Technical University Munich, Munich.

[189] Luke G D, Adams D E (1992), Use of nozzle trip rings to reduce nozzle separation side forces during staging, *29th Joint Propulsion Conference and Exhibit*, AIAA Paper 1992-3617.

[190] Schmucker R (1973), A procedure for calculation of boundary layer trip protuberences in overexpanded rocket nozzles, NASA TM X-64843, Marshall Space Flight Center, Alabama.

[191] Chiou J, Hung R (1974), A study of forced flow separation in rocket nozzles, Final Report, Alabama University, Huntsville.

[192] Parsley R C, Van Stelle K J (1992), Altitude compensating nozzle evaluation, *28th Joint Propulsion Conference and Exhibit*, AIAA Paper 1992-3456.

[193] Musial N T, Ward J J (1959), Overexpanded performance of conical nozzles with area ratios of 6 and 9 with and without supersonic external flow, NASA TM X-83, NASA Lewis Research Center, Cleveland.

[194] Goncharov N, Orlov V, Rachuk V, Shostak A, Starke R (1995), Reusable launch vehicle propulsion based on the RD-0120 engine, *31st Joint Propulsion Conference and Exhibit*, AIAA Paper 1995-3003.

[195] Brown J L, McIntire Jr. V W (1993), Altitude compensating abaltive stiffining band for rocket motor nozzles, U.S. Patent application No. 08/034,452.

[196] Clayton R, Back L (1986), Thrust improvment with ablative insert nozzle extensions, *Journal of Propulsion and Power* **2**(1), 91-93.

[197] Dumnov G E, Nikulin N B, Ponomaryov N B (1993), Investigation of advanced nozzles for rocket engines, *Space Rocket Engine and Power Plants (published in Russia)* **4**(142).

[198] Bollinger L E, Goldsmith M, Lemmon Jr. A W (1960), *Liquid rockets and propellants, Progress in astronautics and rocketry – Volume 2*, Academic pres inc., New York, 617-645.

[199] Smith-Kent R, Loh H, Chawalowski P (1995), Analytical contouring of pintle nozzle exit cone using computational aerodynamics, *31st Joint Propulsion Conference and Exhibit* , AIAA Paper 1995-2877.

[200] Asbury S C, Hunter C A (1999), Effects of convoluted divergent flap contouring on the performance of a fixed-geometry nonaxisymmetric exhaust nozzle, NASA TP-1999-209093, Langley Research Center, Hampton.

[201] Jameson A (1995), The present status, challenges and future developments in computational fluid dynamics, *Proceedings of 12th Australasian Conference on Fluid Dynamics*.

BIOGRAPHICAL SKETCH

Jan Östlund began his studies at Luleå University of Technology, Sweden, in 1990. He completed his Master of Science degree in mechanical engineering in 1995 with applied mechanics as the field of specialization. After graduation he joined the rocket nozzle development team at the Space Propulsion Division at Volvo Aero Corporation. As an aero design engineer he worked with the technical development of the European launcher nozzles, involving e.g. the Vulcain 2 nozzle's supersonic film cooling technology and design. In 1997 he became the technical manager of novel technologies and responsible of the supersonic flow separation research activities at Volvo. The study of the flow separation phenomenon in overexpanded rocket nozzles became his special interest, and in 1999 Jan Östlund started as a PhD student in a joint research program in the field between Volvo and the Royal Institute of Technology. He earned his Licentiate on the subject in 2002 and is currently finishing this research to obtain his PhD in 2004.

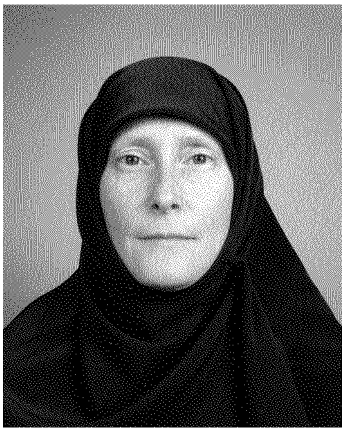

Barbro Muhammad-Klingmann began her studies at the Royal Institute of Technology in Stockholm, Sweden, in 1983, graduated in 1986, and earned her PhD in 1991 on the subject of laminar-turbulent transition. During her post-doc period in Switzerland and Russia she produced a series of contributions on boundary layer stability. She thereafter spent a three years period at Volvo Aero Corp., Space Division, working with the technical development and test logic for rocket engine nozzles, including problems such wall cooling and flow separation in overexpanded nozzles. Since 1997 she has been a senior researcher at the Royal Institute in Stockholm, with a primary interest of turbulent flow separation and the development of new measurement techniques, in particular PIV.